INVESTIGATION OF PLANT CELL WALL PROPERTIES: A STUDY OF CONTRIBUTIONS FROM THE NANOSCALE TO THE MACROSCALE IMPACTING CELL WALL RECALCITRANCE

 $\mathbf{B}\mathbf{y}$

Jacob Dillon Crowe

A DISSERTATION

Submitted to
Michigan State University
in partial fulfillment of the requirements
for the degree of

Chemical Engineering – Doctor of Philosophy

2017

ABSTRACT

INVESTIGATION OF PLANT CELL WALL PROPERTIES: A STUDY OF CONTRIBUTIONS FROM THE NANOSCALE TO THE MACROSCALE IMPACTING CELL WALL RECALCITRANCE

By

Jacob Dillon Crowe

Biochemical conversion of lignocellulosic biomass to fuel ethanol is one of a few challenging, yet opportune technologies that can reduce the consumption of petroleum-derived transportation fuels, while providing parallel reductions in greenhouse gas emissions. Biomass recalcitrance, or resistance to deconstruction, is a major technical challenge that limits effective conversion of biomass to fermentable sugars, often requiring a costly thermochemical pretreatment step to improve biomass deconstruction. Biomass recalcitrance is imparted largely by the secondary cell wall, a complex polymeric matrix of cell wall polysaccharides and aromatic heteropolymers, that provides structural stability to cells and enables plant upright growth. Polymers within the cell wall can vary both compositionally and structurally depending upon plant species and anatomical fraction, and have varied responses to thermochemical pretreatments. Cell wall properties impacting recalcitrance are still not well understood, and as a result, the goal of this dissertation is to investigate structural features of the cell wall contributing to recalcitrance (1) in diverse anatomical fractions of a single species, (2) in response to diverse pretreatments, and (3) resulting from genetic modification.

In the first study, feedstock cell wall heterogeneity was investigated in anatomical (stem, leaf sheaths, and leaf blades) and internode fractions of switchgrass at varying tissue maturities.

Lignin content was observed as the key contributor to recalcitrance in maturing stem tissues only, with non-cellulosic substituted glucuronoarabinoxylans and pectic polysaccharides

contributing to cell wall recalcitrance in leaf sheath and leaf blades. Hydroxycinnamate (i.e., saponifiable *p*-coumarate and ferulate) content along with xylan and pectin extractability decreased with tissue maturity, suggesting lignification is only one component imparting maturity specific cell wall recalcitrance.

In the second study, alkaline hydrogen peroxide and liquid hot water pretreatments were shown to alter structural properties impacting nanoscale porosity in corn stover. Delignification by alkaline hydrogen peroxide pretreatment decreased cell wall rigidity, with subsequent cell wall swelling resulting in increased nanoscale porosity and improved enzymatic hydrolysis compared to limited swelling and increased accessible surface areas observed in liquid hot water pretreated biomass. The volume accessible to a 90 Å dextran probe within the cell wall was found to be positively correlated to both enzyme binding and glucose hydrolysis yields, indicating cell wall porosity is a key contributor to effective hydrolysis yields.

In the third study, the effect of altered xylan content and structure was investigated in irregular xylem (irx) Arabidopsis thaliana mutants to understand the role xylan plays in secondary cell wall development and organization. Higher xylan extractability and lower cellulose crystallinity observed in irx9 and irx15 irx15-L mutants compared to wild type indicated altered xylan integration into the secondary cell wall. Nanoscale cell wall organization observed using multiple microscopy techniques was impacted to some extent in all irx mutants, with disorganized cellulose microfibril layers in sclerenchyma secondary cell walls likely resulting from irregular xylan structure and content. Irregular secondary cell wall microfibril layers showed heterogeneous nanomechanical properties compared to wild type, which translated to mechanical deficiencies observed in stem tensile tests. These results suggest nanoscale defects in cell wall strength can correspond to macroscale phenotypes.

To those who strive to make the world a better place

ACKNOWLEDGEMENTS

I would like to thank my advisor Dr. David Hodge for all his help, and for providing me with this opportunity to contribute to the scientific community. I would also like to thank my committee members Dr. Shi-You Ding, Dr. Ilsoon Lee, and Dr. Bruce Dale for their guidance, advice, and assistance with pursuing this PhD.

To my lab mates, Dr. Ryan Stoklosa, Thanaphong Phongpreecha, Lisaura Maldonado-Pereira, Dr. Daniel Williams, and Dr. Glen Li, I thank you for the friendship and support, and I wish the best in your graduate and post-graduate careers. To my collaborators Dr. Jacob Jensen, Dr. Rebecca Garlock-Ong, Dr. Sivakumar Pattathail, Pengchao Hao, and Cliff Foster, I am grateful to have learned so much while working with you. To the undergraduates Nicholas Feringa, Rachael Zarger, and Henry Pan, it has been a pleasure mentoring you and working countless hours in lab together. I expect you all will do well in your academic endeavors. To all my other colleagues at Michigan State and abroad, I am happy and thankful to have worked with you over these years.

To all my friends, thank you for always being around for support and encouragement. To my family, you have made me the person I am today, I am forever grateful. To Amanda and Maverick, without you two, I would not have made it through graduate school. Thank you for standing by me through this journey.

TABLE OF CONTENTS

LIST OF TABLES	iv
LIST OF FIGURES	v
KEY TO ABBREVIATIONS	xv
Chapter 1: Introduction	1
Motivation: Sustainable biofuels and chemicals	1
Background: General outline of lignocellulosic biomass	5
Structure of lignocellulosic biomass	5 5
Plant cell wall polysaccharides	8
Lignin content and structure	12
Cell wall deconstruction	13
Enzymatic hydrolysis	16
Plant cell wall properties contributing to recalcitrance	18
Cell wall composition	18
Morphological fractionation and tissue maturity	19
Feedstock improvement through genetic manipulation	20
Characterization of biomass properties	21
Hydrophilicity	21
Porosity	24
Crystallinity	25
Microscopy	26
Cell wall extractability	28
REFERENCES	29
Chapter 2: Identification of developmental stage and anatomical fraction contrib	utions to
cell wall recalcitrance in switchgrass	45
Introduction	45
Materials and methods	48
Field conditions and biomass preparation	48
Pretreatment conditions	49
Composition analysis	50
Enzymatic hydrolysis	51
Confocal microscopy	51
Glycome profiling	52
Results	52
Anatomical fraction- and internode-specific recalcitrance	53
Cell wall composition	55
Non-cellulosic glucose and extractable sugar content	58
Cell wall autofluorescence	60
Glycome profiling	65
Glycome profiling for internode specific extractability	68

Discussion	70
Conclusions	75
Acknowledgements	76
APPENDIX	77
APPENDIX A: Supplementary Figures	78
REFERENCES	83
Chapter 3: Relating nanoscale accessibility within plant cell walls to improve enzyments	e
hydrolysis yields in corn stover subjected to diverse pretreatments	90
Introduction	90
Materials and methods	93
Biomass and composition analysis	93
Pretreatments	94
Enzymatic hydrolysis	95
Water retention value	95
Solute exclusion	96
Enzyme binding	97
Results and discussion	98
Composition analysis and enzymatic hydrolysis	98
Cell wall swelling in response to increasing solvent ionic strength	102
Accessible volume distributions determined by solute exclusion	104
Drying-induced pore collapse on cell wall properties and enzymatic	
hydrolysis	107
Enzyme binding	110
Correlation of properties	111
Conclusions	115
APPENDIX	117
APPENDIX B: Supplementary figures and additional results	118
REFERENCES	123
Chapter 4: Impact of impaired xylan biosynthesis on cellulose microfibril organizati	on in
Arabidopsis thaliana secondary cell walls	129
Introduction	129
Materials and methods	134
Plant lines and growth conditions	134
Composition analysis	134
Glycome profiling	135
Wide angle x-ray scattering	135
Tensile test	136
Scanning electron microscopy	136
Atomic force microscopy	137
Results	138
Irx mutant phenotype, composition, and extractability	138
Relative crystallinity index measured by wide angle x-ray scattering	145
Interfascicular ultrastructure is altered in irx mutants	148
Mechanical properties of irx mutants	156
Discussion	160
Conclusions	165

APPENDICES	167
APPENDIX C: Supplementary figures	168
APPENDIX D: Additional irx experiments	178
REFERENCES	184

LIST OF TABLES

Table A.1: Compiled AIR + destarched cell wall polysaccharides, acetate, and lignin content for five internodes of three switchgrass anatomical fractions. Samples are presented	
as an average $(n = 3)$ with standard deviations following in Table A.2	8
Table A.2 : Standard deviations for compiled AIR + destarched cell wall polysaccharides, acetate, and lignin content for five internodes of three switchgrass anatomical fractions.	
Samples are presented as an average $(n = 3)$ with standard deviations following	9
Table 3.1 : Neutral dextran probes used in solute exclusion technique. 9°	7
Table 4.1 : Summary features observed in SEM and AFM height images for irx mutants. 15	1
Table C.1: Roughness analysis and fiber width measurements of delignified irx mutant cell walls using AFM. Roughness parameters for average roughness (R_a) and root-mean-square roughness (R_q) measured on AFM height images at multiple image scales. Roughness is utilized in this case to measure cell wall uniformity. Roughness calculations were performed on three individual images for each scale ($n = 3$), with standard deviations shown in table. P values	
indicate statistical significance compared to wild type from t-test	4

LIST OF FIGURES

Figure 1.1: US primary energy consumption 2016. Taken from [2]
Figure 1.2 : Plant stems examined from different scales using multiple microscopy techniques. (A) Observed whole plant of Arabidopsis thaliana, scale bar 8 cm. (B) Bright field cross section of Arabidopsis lower stem, scale 25 μm. (C) Single sclerenchyma cell from orange region in (B), scale 5 μm. (D) Single parenchyma cell wall from purple region in (B), scale 5 μm. (E) Magnified parenchyma cell, scale 2.5 μm. (F) Sclerenchyma secondary cell wall surface, scale 0.75 μm. (G) Parenchyma primary cell wall surface, scale 500 nm. (H) Sclerenchyma secondary cell wall surface, scale 500 nm. Adapted from [25]
Figure 1.3 : Schematics diagrams of the cell wall. (A) Primary cell wall, and (B) Secondary cell wall. Adapted from [114]
Figure 1.4 : Model of cellulose organization from individual glucan chains to fibril bundles. Adapted from [28]
Figure 1.5 : Schematic representation of hemicellulose xyloglucan structures. Individual bond linkages between polysaccharides shown as lines are glycosidic linkages. Adapted from [30,35]
Figure 1.6 : Schematic representation of hemicellulose xylan structures. Individual bond linkages between polysaccharides shown as lines are glycosidic linkages. Adapted from [30,35].
Figure 1.7 : Schematic representation of hemicellulose mannan structures. Individual bond linkages between polysaccharides shown as lines are glycosidic linkages. Adapted from [30,35].
Figure 2.1 : Schematic of switchgrass tillers used for this study. Tillers were harvested above either the 5 th or 6 th internode, and then separated into internodes, discarding the nodes and panicle. Internodes were further manually subdivided into leaves, leaf sheaths, and stems. Notes: diagram is representative and not to scale
Figure 2.2 : Enzymatic hydrolysis glucose yields of untreated and alkaline pretreatment of anatomical fractions. Enzymatic hydrolysis of untreated biomass was performed on AIR +

destarched biomass, while alkaline pretreatment was performed using 10% w/w NaOH loading at 80°C for 1 hr. Glucose hydrolysis yields are presented as the percent of total cell wall glucan released as monomeric glucose. Enzyme loading was 30 mg protein/g glucan for untreated fractions and 10 mg protein/g glucan for alkaline pretreated fractions with a ratio of 2:1 CTec3 to HTec3. Replicates (n = 3) are displayed as averages with standard deviations
Figure 2.3 : Compositional highlights of (A) lignin (B) hydroxycinnamates (C) minor polysaccharides, and (D) acetate and arabinan in switchgrass fractions with respect to internode. Internodes I ₁ -I ₅ are displayed in ascending order from left to right for each
switchgrass anatomical fraction. All composition values were quantified on an extractives free basis (AIR).
Figure 2.4 : Native switchgrass non-cellulosic sugar composition with respect to internode. Internodes I ₁ -I ₅ are displayed in ascending order from left to right for each switchgrass anatomical fraction. Compositions are represented as a percent of total dry weight. Replicates (n = 3) displayed as average with standard deviations
Figure 2.5: Examples of differences in macroscopic morphology, cell wall organization, and aromatic abundance as shown by autofluorescence between switchgrass anatomical fractions from internode I ₂ . Confocal laser scanning microscopy carried out using laser emission wavelengths of 405nm and 543 nm. Tissue types are denoted from the following notation: Ep – epidermis, Fb – fiber bundles, Vb – vascular bundles, Ph – phloem, X – xylem, Pc – Parenchyma cells. Scale bars represent 200 μm.
Figure 2.6 : Cell wall autofluorescence cross-sections of NaOH-pretreated switchgrass anatomical fractions from internodes I ₂ , I ₃ , and I ₄ . Confocal laser scanning microscopy carried out using an overlay of laser excitation wavelengths of 405 nm and 543 nm. Scale bars represent 200 µm.
Figure 2.7: Abundance of select major non-cellulosic glycan epitopes in chemical extracts from stem, sheath, and leaf anatomical fractions of internodes I ₁ (A), and extracts from stem internodes I ₁ -I ₅ (B). Extracts were screened by ELISA using a comprehensive suite of cell wall glycan-directed mAbs as described in materials and methods. Binding response values are depicted as heat maps with black-red-bright yellow color scheme representing from no binding to strongest binding. The amount of carbohydrate material recovered per gram of AIR is depicted in the bar graphs (green) above the heat maps. The panel on the right-hand side of the heat map shows the groups of mAbs based on the class of cell wall glycan they each recognize

Figure 2.8: Summary of Pearson's correlation coefficients between plant cell wall properties and glucose hydrolysis yields for each anatomical fraction and for pooled samples. Data demonstrate strong correlations between many properties and yields
Figure 2.9: Select correlations between data relationships between either lignin content or ferulic acid against glucose hydrolysis yield represented as scatter plots. (A) 48-hr glucose hydrolysis yields for NaOH-pretreat biomass versus lignin content, (B) ferulate content in relation to total lignin, and 48-hr glucose hydrolysis yield with respect to (C) fucan and (D) arabinan content.
Figure A.1 : Cell wall autofluorescence of switchgrass organ cross-sections from internode I_2 . Confocal laser scanning microscopy carried out using laser excitation wavelengths of 405 nm and 543 nm. Tissue types are denoted from the following notation: Ep – epidermis, Fb – fiber bundles, Vb – vascular bundles, Ph – phloem, X – xylem, Pc – Parenchyma cells. Scale bars represent 200 μ m.
Figure A.2: Heat map abundance of major non-cellulosic glycan epitopes in oxalate, carbonate, 1M KOH, 4M KOH, chlorite, and 4M KOH PC extracts from cell walls of stem, sheath, and leaf samples of internodes I1. Extracts were screened by ELISA using a comprehensive suite of cell wall glycan-directed mAbs as described in materials and methods. Binding response values are depicted as heat maps with black-red-bright yellow color scheme representing from no binding to strongest binding. The amount of carbohydrate material recovered per gram of AIR is depicted in the bar graphs (purple) above the heat maps. The panel on the right-hand side of the heat map shows the groups of mAbs based on the class of cell wall glycan they each recognize.
Figure A.3: Heat map abundance of major non-cellulosic glycan epitopes in oxalate, carbonate, 1M KOH, 4M KOH, chlorite, and 4M KOHPC extracts from stem internodes I ₁ -I ₅ . Extracts were screened by ELISA using a comprehensive suite of cell wall glycan-directed mAbs as described in materials and methods. Binding response values are depicted as heat maps with black-red-bright yellow color scheme representing from no binding to strongest binding. The amount of carbohydrate material recovered per gram of AIR is depicted in the bar graphs (purple) above the heat maps. The panel on the right-hand side of the heat map shows the groups of mAbs based on the class of cell wall glycan they each recognize
Figure 3.1 : Compositional profiles of corn stover subjected to either AHP pretreatment, LHW, or LHW followed by AHP pretreatment. Compositional profiles for xylan, crystalline cellulose, and Klason lignin are shown for alcohol insoluble residue (AIR) corn stover and pretreated biomass. Composition analysis was performed in technical triplicate (n = 3), with standard deviations shown on figure

Figure 3.3 : Cell wall swelling measured using water retention in the absence and presence
of a salt. Water retention value (WRV) of never-dried corn stover at varying pretreatments
measured after incubation in water only (blue bars) or 1 M NaCl (orange bars). Samples were
performed in technical triplicate $(n = 3)$, with standard deviation shown on figure

Figure 3.5: Structural model for pretreatment effect on cell wall organization. Transverse section of cellulose microfibrils for (A) native cell wall, (B) AHP-pretreated cell wall, (C) LHW-pretreated cell wall, and (D) two-stage AHP pretreated LHW cell wall. AHP pretreatment results primarily in reduction in lignin content, promoting the formation of porous regions and inducing cell wall swelling. LHW pretreatment primarily removes xylan and relocalizes lignin, increasing accessible surface area. Two-stage pretreatments contain significant reductions in both xylan and lignin content, increasing porous regions, and in the case of 190°C LHW, sufficient non-cellulosic component removal results in cell wall aggregation. Orange squares representing cellulose microfibrils, green lines representing xylan and gray clouds representing lignin. 107

Figure 3.7 : Bound enzyme fractions of CTec3 on pretreated biomass. Bound enzyme fractions are shown as a percent of bound enzyme to total enzyme loading. Binding

concentrations were performed in technical duplicate, with standard deviations shown on figure.
Figure 3.8: Comparisons between glucose hydrolysis yields, solute exclusion, water retention value, and lignin content. (A,B) Glucose hydrolysis yields taken from Figure 3.2 were from 72 hr total hydrolysis time using an enzyme solution of CTec3 and HTec3. Xylan content is displayed as a range for each linear trend in orange on (A). Accessible volume distributions (C, D) were used from Figure 3.4, and lignin content was taken from Figure 3.1.
Figure 3.9: Comparisons between glucose hydrolysis yields and (A) bound enzyme fractions and (B) water retention value. Glucose hydrolysis yields taken from Figure 3.2 were from 72 hr total hydrolysis time using an enzyme solution of CTec3 and HTec3. WRV were taken from Figure 3.3, and bound enzyme fractions were taken from Figure 3.7
Figure 3.10 : Comparison of inaccessible pore volume to water retention value. Total inaccessible pore volume was determined using solute exclusion at the effective pore size of 560 Å and compared to WRV (0 M NaCl) from Figure 3.3
Figure B.1 : Solute-induced swelling of biomass at multiple salt concentrations. Water retention value (WRV) of never dried and oven dried corn stover at varying pretreatments measured without salt (0 M NaCl), and after soaking in salt solutions (0.25 -1 M NaCl). (A) shows AHP-only pretreatment conditions, (B) shows LHW-only pretreatment conditions, (C) shows two-stage pretreatment conditions, and (D) shows oven-dried pretreatments tested. Samples were performed in technical triplicate (n = 3), with standard deviation shown on figure.
Figure B.2: Enzyme binding curves of CTec3 on never-dried biomass and linear fits for bound enzyme fractions. Bound CTec3 concentrations are displayed as individual data points, with a linear best fit representing the relative ratio of bound enzyme to total enzyme loading. (A) shows AHP-only pretreatment conditions, (B) shows LHW-only pretreatment conditions, and (C) shows two-stage pretreatment conditions. Binding concentrations were performed in technical duplicate $(n = 2)$, with standard deviations shown on figure
Figure B.3 : T₂ NMR relaxation curves of water interacting with pretreated biomass. (A) Relaxation curves of AHP-only pretreatment samples, (B) relaxation curves of 160°C LHW and two-stage pretreatments, and (C) relaxation curves of 190°C LHW and two-stage pretreatments. Samples were performed and fitted in technical duplicate (n = 2), with standard deviations shown on figure.

on figure
Figure B.5: ¹ H-NMR relaxometry of AHP-delignified corn stover showing (A) spin-spin (T ₂) relaxation curves and (B) correlation of monocomponent exponential fits of these relaxation curves to the corresponding WRV and glucose hydrolysis yield
Figure 4.1 : Growth phenotypes of xylan irx mutants. Growth phenotypes were documented at week 6 and 9 as indicated. Arrows in SEM cross-section (lower row, <i>irx9</i> and <i>irx15 irx15-L</i>) indicate the irregular xylem (<i>irx</i>) phenotype of collapsed xylem vessels. Scale bars for overhead growth photos are 1.8 cm, side growth photos are 8 cm, and SEM images are 100μm
Figure 4.2 : Cell wall polysaccharide composition and xylan chain length. (A) Non-cellulosic cell wall neutral monosaccharide content of irx mutant stems determined from TFA hydrolysis. Standard deviations are shown (n = 12, four biological replicates with three technical replicates for wild type, $irx9$, $irx10$, and $irx15$ $irx15$ - L ; n = 6, two biological replicates with three technical replicates for $irx15$ $irx15$ - L $IRX15$ - L and $irx15$ $irx15$ - L $IRX15$ - L). * indicates statistical significance from wild type ($p < 0.05$). (B) Xylan degree of polymerization (DP) percent compared to wild type as reported by prior studies.
Figure 4.3 : Crystalline cellulose, lignin, and glycome profile analysis of cell wall material of <i>irx</i> mutant stems. (A) chemical quantification of crystalline cellulose content (B) and ABSL lignin content of cell wall material. Standard deviations are shown (n = 12, four biological replicates in three technical replicates each for wild type, <i>irx9</i> , <i>irx10</i> , and <i>irx15 irx15-L</i> ; n = 6, two biological replicates with three technical replicates for <i>irx15 irx15-L IRX15-L</i> and <i>irx15 irx15-L OE-IRX15-L</i>). * indicates statistical significance compared to wild type (t-test, p < 0.05). (C) Cell wall material of wild type, <i>irx9</i> , <i>irx10</i> , and <i>irx15 irx15-L</i> inflorescence stems was extracted sequentially with increasing chemical severity using glycome profiling. A selected subset of antibodies and extracts are shown, while the full profile can be found in Figure C.2 143
Figure 4.4 : WAXS diffraction pattern of <i>irx</i> mutant stems and relative crystallinity index. (A), representative WAXS diffraction patterns of wild type, $irx9$, $irx10$, and $irx15$ $irx15$ - L stems showing the diffraction peaks for the [110], [1-10], [200], and [400] crystal faces. (B), relative crystallinity indexes (RCI) of the [200] peak face calculated from the WAXS diffraction pattern, such as the ones in (A). Standard deviations are shown (n = 4, biological replicates for wild type, $irx9$, $irx10$, and $irx15$ $irx15$ - L ; n = 4, two biological and two technical replicates for $irx15$ $irx15$ - L $irx15$ - L and $irx15$ $irx15$ - L

Figure B.4: T₂ NMR relaxation curves monocomponent T₂ relaxation times. Relaxation times were determined from a mono-exponential component fit of each relaxation curve.

Samples were performed and fitted in technical duplicate (n = 2), with standard deviations shown

Figure 4.5: Ultrastructure of <i>irx</i> mutants observed with SEM and AFM. Scanning electron microscopy images of sclerenchyma cell surface texture in native wild type Arabidopsis (A,G,S) <i>irx9</i> (B,H,T), <i>irx10</i> (C,I,U), <i>irx15 irx15-L</i> (D,J,V), <i>irx15 irx15-L IRX15-L</i> (E,K,W), and <i>irx15 irx15-L OE-IRX15-L</i> (F,L,X) stems. Atomic force microscopy images of sclerenchyma cell wall surface texture after delignification in wild type Arabidopsis (M,Y), <i>irx9</i> (N,Z), <i>irx10</i> (O,AA), <i>irx15 irx15-L</i> (P,BB), <i>irx15 irx15-L IRX15-L</i> (Q,CC), and <i>irx15 irx15-L OE-IRX15-L</i> (R,DD) stems. Scale bars are 2 μm for low magnification SEM (A-F), 1 μm for intermediate magnification SEM (G-L), and 200 nm for high magnification SEM (S-X), 500 nm for the 2.5 μm AFM images (M-R), and 200 nm for the 1.0 μm AFM images (Y-DD)
Figure 4.6: Fiber widths measurements of delignified irx mutant secondary cell walls using AFM. Fibril widths were determined from well-resolved features in 2.5 μ m image sizes, using five measurements for each of three individual images for each sample (n = 15). Averages of fiber measurements are displayed as a horizontal bar for each sample on figure
Figure 4.7: Roughness analysis, fiber orientation, and 3D topography measurements of delignified irx mutant cell walls using AFM. (A), Roughness parameters for average roughness (Ra) and root-mean-square roughness (Rq) measured on AFM height images at 0.5 μ m image scale. P values indicate statistical significance compared to wild type from t-test. (B), Microfibri orientations measured by dispersion of fibers distributed throughout an entire image at the 1.0 μ m image scale. Standard deviations for (A) and (B) are shown on figure for three different images (n = 3). (C), 3D surface profiles of wild type and $irx9$ demonstrating fiber alignment in wild type observed at three different image angles compared to $irx9$. Scale bar represents 100 nm and image scale is 0.5 μ m.
Figure 4.8: Height distribution profiles of delignified irx mutant cell walls using AFM. Gaussian distributions highlighting the distribution of height topography of each sample at 1 μ m scale. Distributions of each image triplicates (n = 3) are shown on figure. Gaussian distributions of all image scales can be found in Figure C.11 .
Figure 4.9 : Mechanical strength of xylan <i>irx</i> mutant stems. Tensile stress to breaking of stem tissue measured by universal tensile test. Box and whiskers plot is the result of twenty replicates of one biological batch of stems ($n = 20$). * indicate statistical significance from wild type ($p<0.1$), ** indicates statistical significance from wild type ($p<0.0005$)
Figure 4.10 : Merged nanomechanical AFM imaging of irx mutants. Nanomechanical mapping of modulus (MPa), adhesion (nN), deformation (nm), and dissipation (eV) were scaled to the same absolute intensities for direct comparison of distributions. Groups were designated based upon qualitative features, with <i>irx9</i> , <i>irx10</i> , and <i>irx15 irx15-L</i> placed in group 1, and <i>irx15 irx15-L IRX15-L</i> and <i>irx15 irx15-L OE-IRX15-L</i> placed in group 2. Scale bar represents 200 nm, with all images corresponding to a 1.0 μm size

Figure 4.11 : Schematic of analytical techniques utilized in this study, and proposed connections between individual techniques.
Figure C.1 : SEM images of parenchyma cells surface texture in <i>irx</i> mutants. Wild type (A,G,M), <i>irx9</i> (B,H,N), <i>irx10</i> (C,I,O), <i>irx15 irx15-L</i> (D,J,P), <i>irx15 irx15-L IRX15-L</i> (E,K,Q), and <i>irx15 irx15-L OE-IRX15-L</i> (F,L,R) stems labeled. Scale bars are 2 μm for low magnification (A-E), 1 μm for intermediate magnification (G-L), and 200 nm for high magnification (M-R).
Figure C.2 : Extended dataset of the glycome profile of <i>irx</i> mutants. Glycome profile of Arabidopsis cell wall material extracted sequentially with increasing chemical severity using oxalate, carbonate, 1M KOH, 4M KOH, acidic chlorite, and 4M KOHPC pretreatments as defined in materials and methods. Antibody binding strength is based upon optical density, with binding intensity presented as a color gradient from black (low binding) to red (intermediate binding), and yellow (strongest binding). Green bars on the top indicate the amount of carbohydrate recovered per gram of cell wall AIR for each extraction
Figure C.3: WAXS diffraction curve processing for crystallinity and microfibril diameter calculation. (A), WAXS diffraction curve fitting for quantification of relative crystallinity index with ten Gaussian fits used to fit the major crystal faces and account for amorphous contributions. (B), Relative crystallinity index determined using the peak area method as described in the methods. (C), Sherrer microfibril diameter determined using the width at peak half height of the [200] crystal face
Figure C.4: Additional SEM and AFM images of sclerenchyma cell wall surface texture in Arabidopsis wild type. Scale bars for SEM are 2 μm for low magnification (left column), 1 μm for intermediate magnification (middle column), and 200 nm for high magnification (right column). Scale bars for AFM are 500 nm for the 2.5 μm images (first column), 200 nm for the 1.0 μm images (second column), 100 nm for the 0.5 μm images (third column), and 50 nm for the 0.25 μm images (fourth column).
Figure C.5 : Additional SEM and AFM images of sclerenchyma cell wall surface texture in Arabidopsis <i>irx9</i> . Scale bars for SEM are 2 μm for low magnification (left column), 1 μm for intermediate magnification (middle column), and 200 nm for high magnification (right column). Scale bars for AFM are 500 nm for the 2.5 μm images (first column), 200 nm for the 1.0 μm images (second column), 100 nm for the 0.5 μm images (third column), and 50 nm for the 0.25 μm images (fourth column).

Figure C.6 : Additional SEM and AFM images of sclerenchyma cell wall surface texture in Arabidopsis irx10. Scale bars for SEM are 2 μm for low magnification (left column), 1 μm for

intermediate magnification (middle column), and 200 nm for high magnification (right column). Scale bars for AFM are 500 nm for the 2.5 µm images (first column), 200 nm for the 1.0 µm images (second column), 100 nm for the 0.5 µm images (third column), and 50 nm for the 0.25 µm images (fourth column)
Figure C.7 : Additional SEM and AFM images of sclerenchyma cell wall surface texture in Arabidopsis <i>irx15 irx15-L</i> . Scale bars for SEM are 2 μm for low magnification (left column), 1 μm for intermediate magnification (middle column), and 200 nm for high magnification (right column). Scale bars for AFM are 500 nm for the 2.5 μm images (first column), 200 nm for the 1.0 μm images (second column), 100 nm for the 0.5 μm images (third column), and 50 nm for the 0.25 μm images (fourth column).
Figure C.8 : Additional SEM and AFM images of sclerenchyma cell wall surface texture in Arabidopsis <i>irx15 irx15-L IRX15-L</i> . Scale bars for SEM are 2 μm for low magnification (left column), 1 μm for intermediate magnification (middle column), and 200 nm for high magnification (right column). Scale bars for AFM are 500 nm for the 2.5 μm images (first column), 200 nm for the 1.0 μm images (second column), 100 nm for the 0.5 μm images (third column), and 50 nm for the 0.25 μm images (fourth column)
Figure C.9 : Additional SEM and AFM images of sclerenchyma cell wall surface texture in Arabidopsis <i>irx15 irx15-L OE-IRX15-L</i> . Scale bars for SEM are 2 μm for low magnification (left column), 1 μm for intermediate magnification (middle column), and 200 nm for high magnification (right column). Scale bars for AFM are 500 nm for the 2.5 μm images (first column), 200 nm for the 1.0 μm images (second column),100 nm for the 0.5 μm images (third column), and 50 nm for the 0.25 μm images (fourth column)
Figure C.10 : Distribution profiles of microfibril orientations for an entire image. Sample image distribution profiles for each <i>irx</i> mutant and wild type. Dispersion was calculated based upon the width of the gaussian distribution.
Figure C.11 : Height distribution profiles of delignified <i>irx</i> mutant cell walls using AFM. Gaussian distributions of height ranges at each image scale are displayed as individual plots of three images for each sample.
Figure C.12 : Example calculation of microfibril width. Microfibril widths were calculated using the build in section Tool in Nanoscope. Well resolved microfibril features were used to determine horizontal fibril widths

Figure C.13 : Merged nanomechanical AFM imaging of all *irx* **mutants.** Nanomechanical mapping of modulus (MPa), adhesion (nN), deformation (nm), and dissipation (eV) were scaled

to the same absolute intensities for direct comparison of distributions. Scale bar represents 200 nm, with all images corresponding to a 1.0 μ m size
Figure D.1 : Water retention values and extractive insoluble residue of cell wall material of <i>irx</i> mutants. (A), Water retention values (WRV) of alcohol insoluble residue (AIR) with and without chemical extraction with 1M KOH and extractive insoluble components (EIC) represents solid residue after sequential extraction with 4M KOH after chlorite delignification. (B-D), Composition of neutral monosaccharides, crystalline cellulose, and ABSL lignin content of residue remaining after 4M KOHPC extraction. Standard deviations are shown with two biological replicates with three technical replicates (n = 6).
Figure D.2: Enzymatic digestibility of cell wall material of <i>irx</i> mutant stems. Enzymatic hydrolysis monomeric sugar yields of glucose (A) and xylose (B) of unpretreated AIR on a basis of % monomeric sugar observed per total available polysaccharide ($g/g*100$). Standard deviations are shown ($n = 6$, biological duplicate with technical triplicate)
Figure D.3: Cell wall compositions of Arabidopsis wild type and WAXS relative crystallinity index after chemical extraction. (A) cell wall neutral monosaccharide content determined from TFA hydrolysis, (B) crystalline cellulose content, and (C) ABSL lignin content of wild type AIR, and sequentially extracted with carbonate and 1M KOH. (D) Relative crystallinity indexes of the [200] peak face calculated from the WAXS diffraction patterns in wild type native, AIR, and sequentially extracted with carbonate and 1M KOH. Standard deviations are shown ($n = 3$, biological replicates. * indicates statistical significance compared to wild type (t-test, $p < 0.05$)

KEY TO ABBREVIATIONS

ABSL – acetyl bromide soluble lignin Ac - acetate AFEX- ammonia fiber expansion AFM -atomic force microscopy AG – arabinogalactan AGP – arabinogalactan pectins AHP -alkaline hydrogen peroxide AIR – alcohol insoluble residue Ara- arabinan BSA – bovine serum albumin CBM – carbohydrate binding module CESA – cellulose synthase complexes CI – crystallinity index DI – de-ionized DP – degree of polymerization DSC – differential scanning calorimetry DSC-TP – differential scanning calorimetry thermoporemetry EA – extractive ammonia EIC – extractive insoluble components ELISA – enzyme-linked immunosorbent assay Ep- epidermis ESK - ESKIMO FA – ferulate Fb – fiber bundle

FSP – fiber saturation point

Fuc – fucan

G – guaiacyl

Gal – galactan

GAX – glucuronoarabinoxylan

GFP – green fluorescent protein

GH – glycosyl hydrolase

GHG – greenhouse gas

GlcA – glucuronic acid

GUX – glucuronyl transferases

GX – glucuronoxylan

GXMT – glucuronic acid methyl transferase

H – p-hydroxyphenyl

HG – homogalacturanan

HPLC – high performance liquid chromatography

Irx – irregular xylem

LHW – liquid hot water

LUT – look up table

mAb – monoclonal antibody

Man – mannan

MeGlcA – Methyl glucuronic acid

MLG – mixed linkage glucan

ND – never-dried

NMR – nuclear magnetic resonance

NREL – national renewable energy laboratory

OD – oven-dried

Pc – parenchyma cells

PC – post-chlorite

pCA - p-coumarate

Ph - phloem

RCI -relative crystallinity index

RFS – renewable fuel standard

RG – rhamnogalacturonan

Rha – rhamnan

S-syringyl

SEM – scanning electron microscopy

TBL – TRICHOME BIREFRINGENCE-LIKE

TEM - transmission electron microscopy

TFA - trifluoracetic acid

Vb – vascular bundle

WAXS – wide angle x-ray scattering

WRV – water retention value

X - xylem

XG-xyloglucan

XGA – xylogalacturanan

Xyl - xylan

Chapter 1 : Introduction

Motivation: Sustainable biofuels and chemicals

There exists a growing political, cultural, and economic movement towards pursuing policy and technologies to mitigate the human carbon footprint on climate change. From the 2015 Paris Agreement, predictions of a global reduction of 50% of total greenhouse gas (GHGs) emissions by 2050 are required to limit the mean temperature rise between 2 -2.5°C [1]. Fossil derived energy accounts for 80% of total global energy consumption [2], with both changes to energy utilization and source required to meet the maximum GHG predicted for a limited temperature rise [3]. In 2016, an estimated 10% of total energy consumption was derived from renewables in the United States (**Figure 1.1**), with 15% of total electrical power generated from renewables such as solar and wind. Advances in solar and wind technologies are anticipated to reduce implementation costs in the coming years [4], allowing renewables to compete economically on the electrical grid with fossil sources.

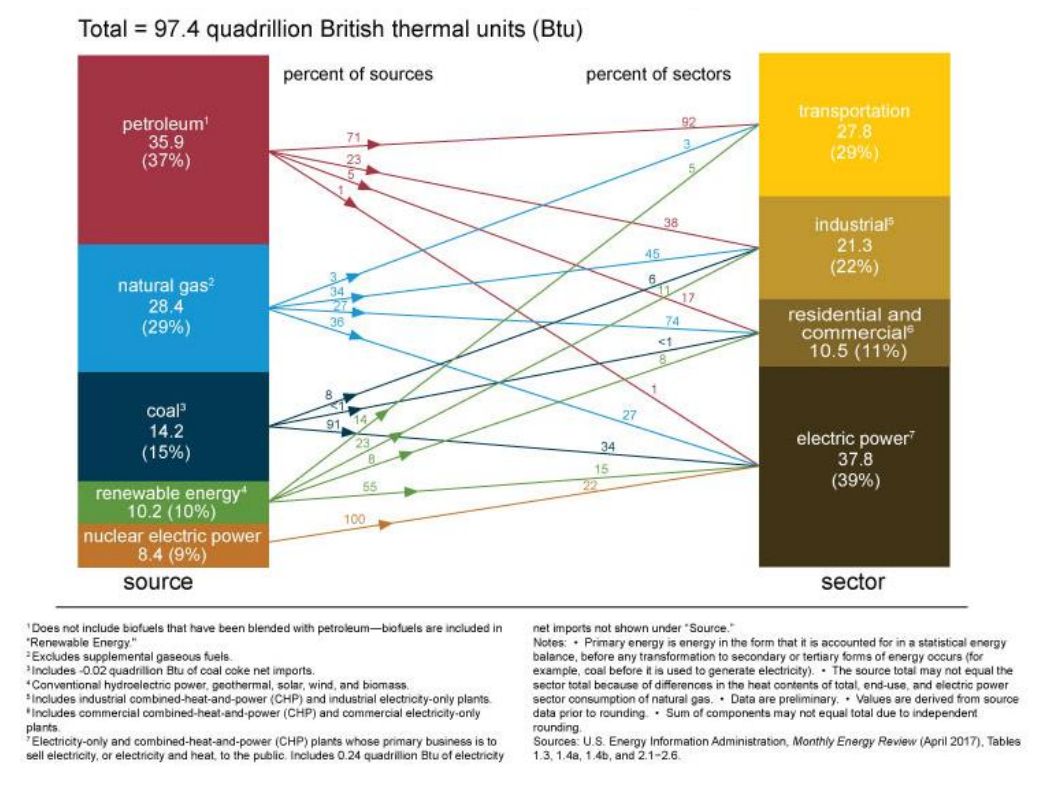


Figure 1.1 : US primary energy consumption 2016. Taken from [2].

Energy for transportation accounts for 29% of total energy consumption in the United States (**Figure 1.1**), with 92% of that energy derived from petroleum sources. Current technological prospects exist to offset energy dense liquid transportation fuels with alternative sources such as electrification of vehicles, hydrogen production, or other non-drop-in fuels [5], however significant advances to energy storage technology, production, and infrastructure for development and distribution are still required for successful implementation of these technologies. Biofuels represent a challenging, yet opportune technology that can supplement petroleum derived transport fuels using existing infrastructure [6], provide reductions in carbon emissions, and improve non-petroleum derived human wealth and development during the global transition away from fossil fuels [7].

The Renewable Fuel Standard (RFS) was implemented as part of the Energy Policy Act of 2005, and expanded under the Energy Independence and Security Act of 2007, setting mandatory volumes of renewable fuels to offset petroleum derived fuels [8]. Current volumes of first generation corn ethanol are near 15.3 billion gallons a year in the US, with an average of 43% reduction in GHG emissions compared to gasoline [9]. Corn ethanol, while establishing logistics and transport infrastructure for ethanol distribution and blending, is volume limited due to land allocation between corn purposed for food production versus ethanol production. Cellulosic ethanol, represents another source of reduced carbon for bioethanol production with the potential for higher reductions of GHGs compared to gasoline, availability of feedstock, with an estimated 1.3 billion tons of economically feasible and sustainable feedstock [10], and is slated for 16 billion gallons of total production in the RFS by 2022 [8]. Cellulosic bioethanol is divided into three major feedstock unit operations to produce cellulosic bioethanol: (1) feedstock pretreatment to improve cell wall accessibility for (2) enzymatic hydrolysis to produce hexose and pentose sugars capable of providing anaerobic microbes a high titer stream of sugars for (3) fermentation of sugars to bioethanol or other value-added products.

Recent progress in cellulosic bioethanol processing has resulted in the construction of pioneer second generation cellulosic ethanol plants [11], however the current predicted volume requirements of cellulosic ethanol set by the RFS are not being met. This is due in part to the difficulties encountered in upstream processing and scale up [12], as well as recent increases in oil and gas drilling in the form of hydraulic fracturing and oil sands reducing petroleum prices and lowering the incentive for investing in alternative forms of energy security [13].

If cellulosic bioethanol is to come to fruition on a large scale, technological improvements need to be implemented to reduce capital costs and improve process economics

such as value-added co-production such as lignin valorization [14, 15]. Pioneer plants have identified key technical challenges associated with continuous upstream production and achieving plant operating capacity, which may be addressed in time through 'learning by doing', however, other challenges outside of the industrial plant still exist [11]. Development and implementation of upstream feedstock supply chains is both a technical and capital investment hurdle; unlike other commodity chemicals with established logistics, lignocellulosic biomass lacks existing infrastructure [12]. In addition, lignocellulosic feedstocks have poor transport and handling properties, with low densities, high moisture content, and poor-flowability characteristics, often necessitating on-field drying and densification for long distance transport [16].

Understanding feedstock properties from the fundamental perspective may provide an avenue for addressing a few outstanding challenges limiting economic feasibility of lignocellulosic bioethanol; biomass heterogeneity is a significant variable impacting upstream feedstock handling properties, as well as downstream biomass conversion economics. At the root of feedstock heterogeneity, the plant cell wall is a complex and diverse structure that is still not fully understood. As a result, the focus of this dissertation will be to investigate factors influencing plant cell wall properties in order to understand and improve cell wall hydrolysis for the production of fermentable sugars. In **Chapter 2**, biomass heterogeneity will be investigated in anatomical and developmentally distinct fractions of a single switchgrass cultivar to understand cell wall variability between fractions. Furthermore, these differences will be investigated in the context of cell wall deconstruction towards improving biomass processing.

In **Chapter 3**, the role of chemical pretreatment impacting nanoscale cell wall properties is investigated to understand cell wall factors impacting cellulose accessibility and enzymatic

digestibility. Nanoscale porosity has shown to play an integral role in improving cell wall deconstruction, and will be investigated in the context of changes to cell wall structure and rigidity.

In **Chapter 4**, the role of individual components impacting secondary cell wall structure is investigated using a series of xylan deficient *irregular xylan (irx)* mutants. The purpose of this work is to examine the role of altered polymer structure to understand the role of higher order interactions impacting cell wall organization, as well as demonstrate synergy between multiple analytical techniques to characterize altered cell wall structure.

Background: General outline of lignocellulosic biomass Structure of lignocellulosic biomass

A large fraction of the total terrestrial plant mass resides in plant cell walls, an integral component of all plant cells. Cell walls are important features of plant cells that perform essential features ranging from defining cell shape and cell type, to providing a physical barrier from extracellular interaction [17]. The general model of plant cell wall is comprised of both a primary and secondary cell wall, with vastly different functions for each.

The primary cell wall makes up a thin physical layer that encapsulates cells and inhibits movement during creep, or expansion of the cell wall during plant growth [18]. Composed primarily of cellulose microfibrils imbedded in a matrix of complex polysaccharides, the primary cell wall resembles a web of fibrous cellulose weaving and forming distinct lamellar layers [19, 20]. Polysaccharides associated with cellulose microfibrils in primary cell wall interact via non-covalent interactions, such as hydrogen bonding or van-der Waals interactions, and form a complex 3D imbedded matrix. Xyloglucans, one class of hemicelluloses within the primary cell wall of dicots, are an essential polysaccharide involved in cell wall loosening during extension.

The primary mechanism of interaction with cellulose microfibrils is hypothesized through association of a series of parallel microfibrils together via a tethered network model, however, recent evidence in xyloglucan deficient *xxt1/xxt2* mutants has put that model into question [21, 22]. Pectins are also present in the primary cell wall, with highly hydrophilic structures likely contributing to reductions in cellulose-cellulose interactions, and promoting inter-microfibril spacing [23].

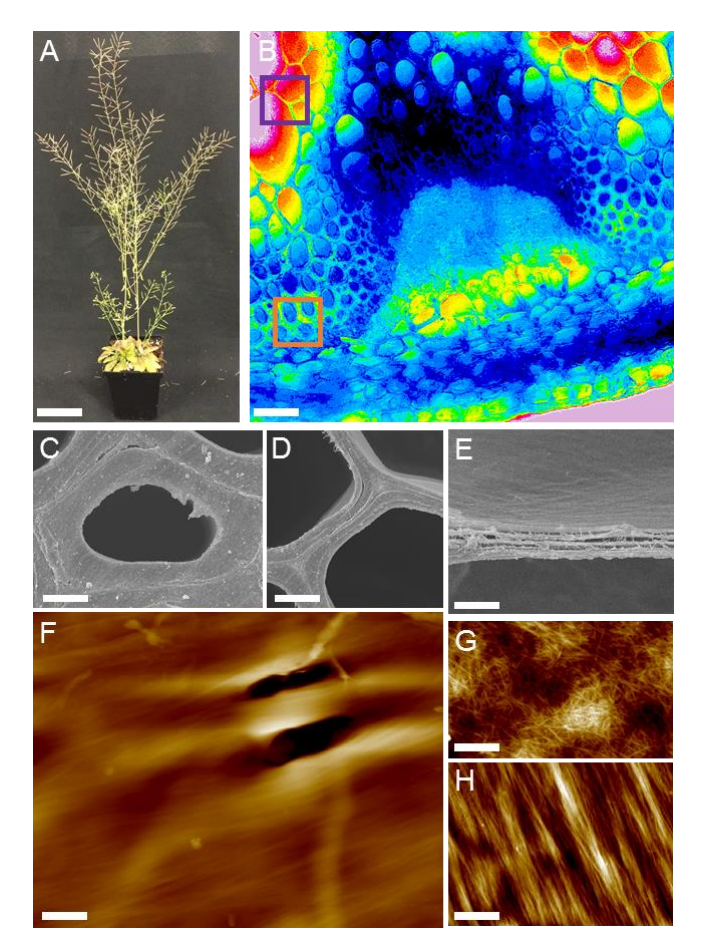


Figure 1.2 : Plant stems examined from different scales using multiple microscopy techniques. (**A**) Observed whole plant of *Arabidopsis thaliana*, scale bar 8 cm. (**B**) Bright field cross section of Arabidopsis lower stem, scale 25 μm. (**C**) Single sclerenchyma cell from orange region in (B), scale 5 μm. (**D**) Single parenchyma cell wall from purple region in (B), scale 5 μm. (**E**) Magnified parenchyma cell, scale 2.5 μm. (**F**) Sclerenchyma secondary cell wall surface, scale 0.75 μm. (**G**) Parenchyma primary cell wall surface, scale 500 nm. (**H**) Sclerenchyma secondary cell wall surface, scale 500 nm. Adapted from [25].

The secondary cell wall is present only in fully developed cells post elongation, and is deposited in certain cell types to provide mechanical strength and resistance to osmotic pressures. Secondary cell walls are significantly thicker than primary cell walls, constitute a large portion of the total cell wall mass, and are composed predominately of cellulose, hemicelluloses, and lignin [24]. There are two types of secondary cell walls, the parenchymatype and the sclerenchyma-type secondary cell wall. Parenchyma-type are usually partially lignified and act as support tissues, while sclerenchyma-type secondary cell walls are found in differentiated treachery elements and sclerenchyma fibers [25]. Sclerenchyma-type secondary cell walls are fully lignified, and formed by alternating layers of sheet-like cellulose microfibrils accompanied by hemicelluloses and separated by lignified layers [26]. Many genes specific to secondary cell wall formation are highly active in sclerenchyma-type secondary cell walls only [24]. Example schematics of both the primary and secondary cell wall are highlighted in Figure 1.3.

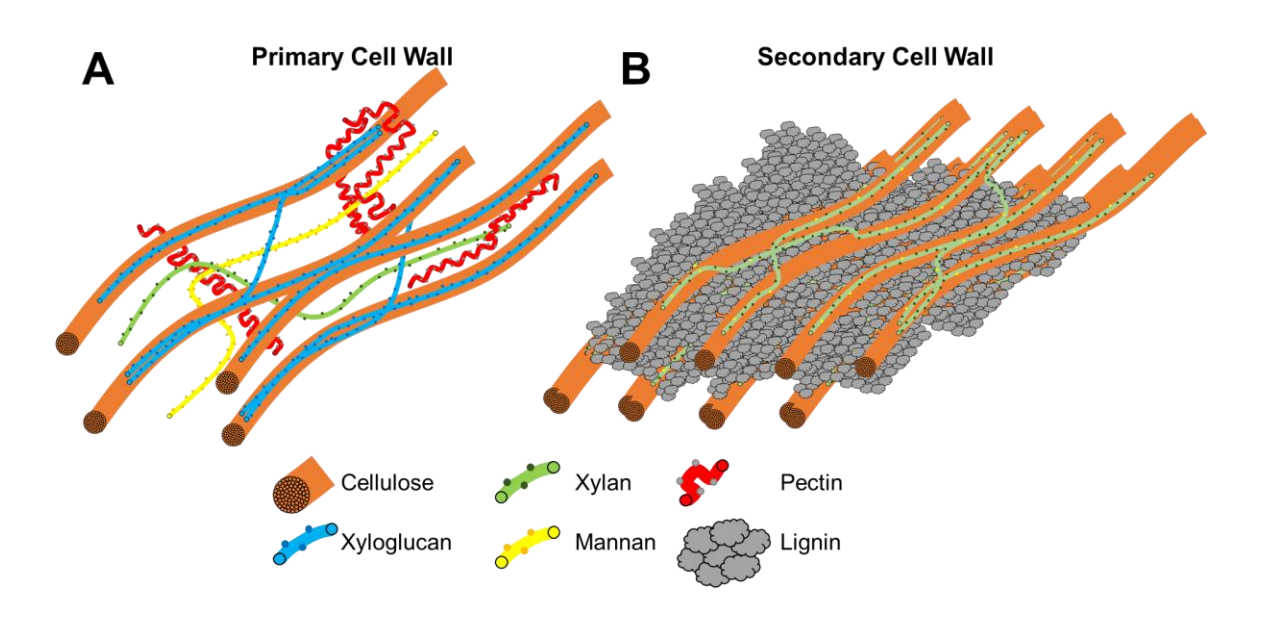


Figure 1.3 : Schematics diagrams of the cell wall. (A) Primary cell wall, and **(B)** Secondary cell wall. Adapted from [114].

Plant cell wall polysaccharides

The major classes of polysaccharides in the cell wall include cellulose, hemicelluloses, and pectins. Cellulose is linear chain of glucosidic β -1,4-linked glucose units comprised of a repeat unit of two anhydroglucose rings, referred to as cellobiose, with a variable chain length anywhere from 10,000-15,000 individual glucose units depending on the source material [27]. Intra-chain hydrogen bonding between hydroxyl groups and adjacent oxygen molecules maintains the linear configuration of cellulose, with interchain hydrogen bonding and van-der Waals between individual cellulose chains resulting in parallel stacking and formation of cellulose elementary fibrils [28]. Elementary fibrils further aggregate and form larger microfibrils through hydrogen bonding. A traditional two-phase model has been used to describe cellulose structure, with regions of highly ordered cellulose crystals formed termed crystalline cellulose, while cellulose microfibrils of low structural order are referred to as amorphous cellulose [29].

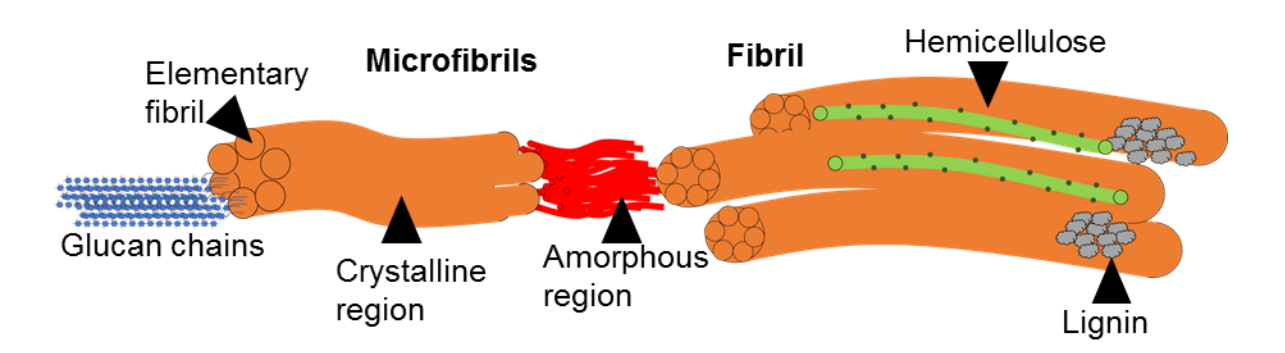


Figure 1.4: Model of cellulose organization from individual glucan chains to fibril bundles. Adapted from [28].

Hemicelluloses compared to cellulose are significantly more heterogeneous, comprised broadly of xyloglucans, xylans, mannans, and mixed linkage glucans. Xyloglucans (XyG) as described earlier are primarily found in the primary cell wall of dicots and are hypothesized to

interact and form cellulose- xyloglucan networks. The predominant xyloglucan structure in dicots is the fucogalactoxyloglucan structure (FucogalactoXyG), while monocots favor the arabinogalactoxyloglucan (arabinogalactoXyG) structure [30]. Xyloglucan backbones are comprised of β -1,4-lined glucose units similar to cellulose, that are substituted at various positions by xylosyl residues depending upon plant species. In most species, xylosyl residues are further substituted with galacturonosyl, arabinoxyl, or other glycosyl residues, with galactosyl residues often further substituted by fucosyl and acetyl units depending upon the species [30].

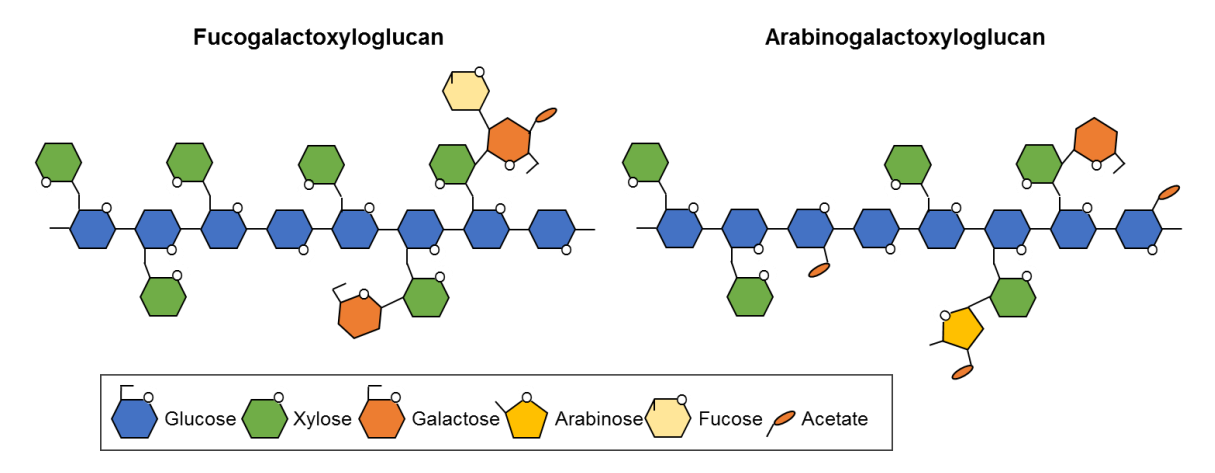


Figure 1.5 : Schematic representation of hemicellulose xyloglucan structures. Individual bond linkages between polysaccharides shown as lines are glycosidic linkages. Adapted from [30,35].

Xylans are the major hemicellulose present in secondary cell walls of monocots and dicots. Glucuronoxylan (GX) is the predominant structure of xylan in dicots, consisting of β -1,4-linked xylosyl residues as the backbone, decorated with α-1,2-linked glucuronic acid (GlcA) and 4-O-methyl-glucuronic acid (MeGlcA) [31], and O-acetyl groups at the O-2 and O-3 position [32]. A tetrasaccharide sequence of 4-β-D-Xyl-(1-4)-β-D-Xyl-(1-3)-α-L-Rha-(1-2)-α-D-Gal-(1-4)-D-Xyl is found in some dicots including Arabidopsis, and is thought to play a terminating role in xylan chain length during biosynthesis [33, 34]. Glucuronoarabinoxylan (GAX) is the main

xylan found in monocot grass primary and secondary walls. In addition to a similar backbone and GlcA and MeGlcA substitution and acetylation patterns, GAX also contains arabinosyl substitutions to the backbone at the α -1,2 and α -1,3 positions [35]. Unique to grass cell walls, arabinosyl units may be further substituted through ester and ether linkage of hydroxycinnimates, acting as an anchor point for lignification [36].

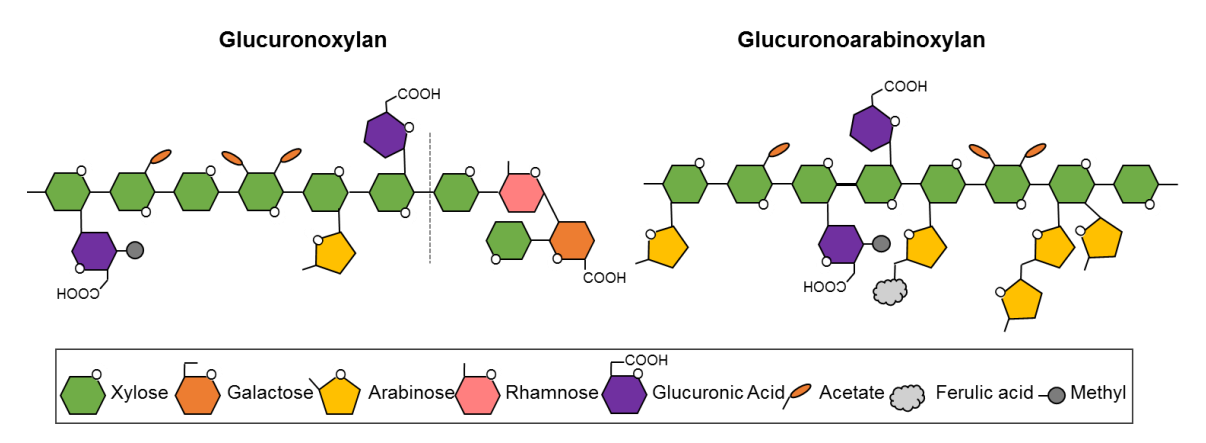


Figure 1.6 : Schematic representation of hemicellulose xylan structures. Individual bond linkages between polysaccharides shown as lines are glycosidic linkages. Adapted from [30,35].

Mannans are the major hemicellulose in secondary cell walls of gymnosperms [37], and are classified into homomannan, glucomannan, galactomannan, and galactoglucomannan [35]. Homomannans and galactomannan have a backbone formed by β -1,4-linked mannosyl units, while glucomannan and galactoglucomannan contain both mannose and glucose units in a β -1,4-linked configuration [30]. Mannosyl residues may be substituted with α -1,6-linked galactosyl units, and can be acetylated at the O-2 and O-3 positions [38, 39]. Mixed linkage glucans (MLGs) are found in the cell walls of grasses, and are thought to play a role as a storage polymer [40]. MLGs are unsubstituted, linear chains of glucose units with randomly distributed β -1,4-linked cellobiose, cellotriose, and cellotetrose sub-units. Although not as prevalent as a

hemicellulose, MLGs can constitute an appreciable fraction of cell polysaccharide in secondary cell walls of grasses [41].

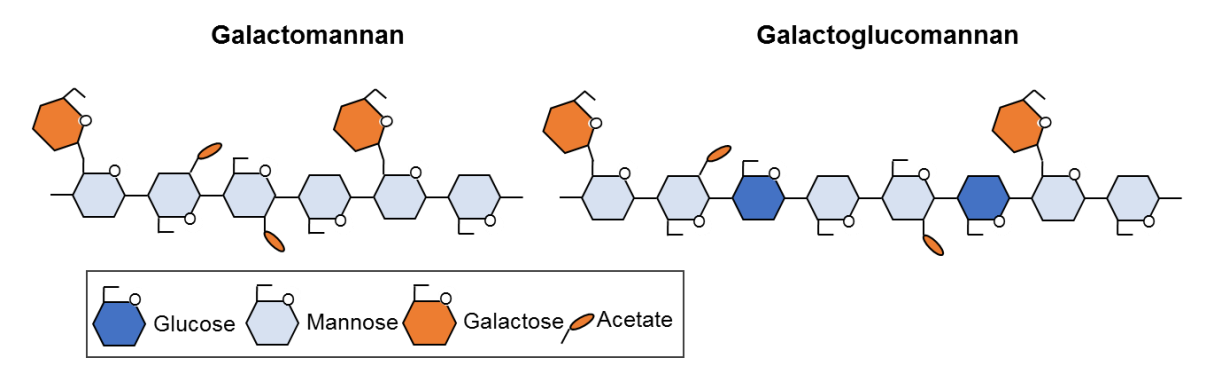


Figure 1.7 : Schematic representation of hemicellulose mannan structures. Individual bond linkages between polysaccharides shown as lines are glycosidic linkages. Adapted from [30,35].

Pectins are the third group of polysaccharides present in the cell wall, and are thought to facilitate cell wall strength through non-covalent and covalent interactions with other cell wall polymers [42]. There are four major groups of pectins in non-aquatic plants, broken into homogalacturanans (HG), xylogalacturanan (XGA), and rhamnogalacturanan I and II (RG I & II). The ratio of pectin structures is highly varied depending upon plant species, however HG is usually the most prevalent pectin, followed by RG I and other pectins constituting smaller fractions [43]. HG is comprised of unbranched α -1,4-linked D-GalUA that can be further substituted with other sugar residues such as xylosyl units in XGA, or with acetyl groups at the O-2 and O-3 positions or methyl esterification at the C-6 carboxyl position. RG II consists of a stretch of HG backbone that is substituted with four complex size chains, containing a total of 12 different types of glycosyl residues [44]. RG II is highly conserved among vascular plants, [45] and likely plays a critical role in maintain cell wall integrity. RG I is the only pectin lacking a HG backbone, and instead is a branched polymer with α -1,4-D-Gal- α -1,2-L-Rha repeat. Rha residues are further substituted with either β -1,4-linked galactan branches that are further

substituted with branched arabinose units, or arabinogalactan side chains, with acetylation of the backbone occurring at the O-3 position [42].

Lignin content and structure

Lignin is a complex heteropolymer found in plant secondary cell walls that provides compression strength, limits cell wall mobility, and prevents extracellular interaction with the cell wall. Lignin content in biomass, although varying considerably depending upon plant species and tissue maturity can range from 10-30% dry weight [46]. Chemically, lignin is derived mainly from three p-hydroyphenyl alcohols, p-coumaryl, coniferyl, and sinapyl alcohols which are precursors for the lignin monolignols p-hydroxyphenyl (H), guaiacyl (G), and syringyl (S) units. Other non-monolignol aromatic monomers such as hydroxycinnimates p-coumatate, ferulate, and sinapate found in grasses, are derived from the lignin biosynthesis pathway are also incorporated into lignin, and can constitute an appreciable fraction of quantifiable lignin monomers depending upon species [47].

Lignin is thought to form within the cell wall through radical oxidative polymerization catalyzed by peroxidases and laccases [48]. A range of bond configurations exist within lignin, however the primary bonds quantified are categorized into labile β -O-4 and α -O-4 aryl-ether bonds, and condensed C-C bonds such as β -5 phenylcoumaran, β - β resinol, and 5-5 aryl-aryl bonds, or 4-O-5 and 5-O-4 biphenyl ethers which are significantly more resistant to chemical degradation [49].

In addition to the bond configurations described, monocot grasses incorporate hydroxycinnimates into lignin through ester and ether bonding. Specifically, ferulate monomers can be incorporated into lignin by various ether and C-C bonds [47], however they are also known to ester bind to arabinosyl residues on GAX, forming covalent linkages between

hemicellulose and lignin [50]. Ferulates may also dimerize, forming diferulates, and may play an important role as initiation sizes for lignin formation or anchoring lignin in grass cell walls [51].

P-coumarates are also in abundance in grass cell walls, and are mainly bonded through esterification to the gamma-position of phenylpropanoid sidechains of S lignin, and unlike ferulate, form few crosslinked structures [52]. P-coumarates are thought to aid in the formation of syringyl-rich lignins during later stages of lignification, however their exact role is unknown [50]. Generally, grasses have a more condensed lignin structure with higher phenolic hydroxyl content compared to dicots [36], and coupled with alkali labile bonds formed from hydroxycinnimates are highly soluble in alkali solution, with large fractions of total lignin soluble at room temperature [53].

Cell wall deconstruction

Biomass recalcitrance, imparted by cell wall structural and compositional features, is a key obstacle in successful employment of lignocellulosic biomass as a feedstock. Limited accessibility of polysaccharide degrading enzymes within the cell wall makes biomass conversion on an industrially relevant time scale unfeasible in native biomass [54], requiring the alteration of biomass feedstock properties through biochemical and mechanical pretreatment approaches. The goal of pretreatment is to remove or alter structural and compositional impediments in order to improve the rate of enzymatic hydrolysis [55]. Approaches to improving enzymatic hydrolysis yields can be classified into modifications of feedstock variables or modification of pretreatment variables. In the case of pretreatment variables, approaches are taken to improve either mass transfer, reaction kinetics, or a combination of both through application of physiochemical conditions to improve feedstock accessible surface area, porosity, or alter substrate affinity and accessibility for depolymerization [56].

Chemical pretreatments can be further classified based upon the general effect on cell wall structure, with acidic pretreatments preferentially solubilizing hemicelluloses and relocalizing lignin and alkaline or oxidative based pretreatments solubilizing or depolymerizing lignin. A third class of pretreatment grouping ionic liquid and organosoly pretreatments physically fractionate cell wall components. Most pretreatments can be further categorized based upon main chemical mode of action and reactant nucleophilicity, as described in the review by Ong. et al. [56]. In general, the following pretreatments presented all are dependent upon similar variables such as reaction temperature, time, pH, catalyst or reactant loading, and solids content, although the importance of each variable may be significantly different depending upon feedstock and pretreatment [55, 57].

Acid pretreatments such as dilute acid are well-studied techniques and have been used commercially in the manufacture of furfural [55], with a main mode of action through electrophilic hydrolysis of ester cross-links and β-ether bonds in lignin, as well as hydrolysis of glycosidic linkages in hemicelluloses to form monomers and oligomers, which can further be dehydrated to form furans [58]. Lignin has been observed to aggregate and localize along the cell wall surface after dilute acid pretreatment [59, 60]. Dilute acid pretreatment may also impact cellulose crystal structure by altering hydrogen bonding interactions between glucan chains [61].

Neutral chemistry hydrothermal pretreatments such as liquid hot water pretreatment (LHW) and steam explosion pretreatment initially utilize hydronium ions derived from water autoionization to liberate weak biomass-derived acids such as acetyl groups, which in turn act as weak acids in solution [62]. Hemicellulose backbone and substitutions are hydrolyzed to a lesser extent, generally released as oligomers, while only labile bonds are broken in lignin [63]. Similar to dilute acid pretreatments, lignin is relocalized as globules on the outer cell walls at high LHW

pretreatment severity [64], although minimal lignin is solubilized and generally increases in total mass fraction significantly after pretreatment [58]. LHW pretreatment may reduce cellulose crystallinity at high temperatures [65], however low to moderate severity pretreatment has shown no significant change in crystallinity [66].

Alkaline and oxidative pretreatments act through either saponification reactions of available esters in lignin and hemicelluloses, as well nucleophilic substitution or oxidation of β -ether bonds [56]. At high alkali loadings, hemicelluloses may also be extracted through peeling reactions [67], although side chain substitutions and acetate can still be extracted at low alkali loadings [68], as well as significant fractions of lignin in grasses, which are particularly susceptible [53] to moderate alkali pretreatment conditions.

Alkaline hydrogen peroxide (AHP) pretreatment is an oxidative pretreatment derived from existing pulp and paper applications [69, 70]. AHP pretreatment is unique in that it is carried out at room temperature [71], targeting mainly lignin bonds and solubilizing a large fraction of lignin from the lignocellulosic matrix. β-ether bonds are cleaved at higher peroxide loadings along with reductions in lignin molecular weight contributing to lignin solubility and removal in grasses [72, 73]. Hemicellulose removal is present due to the caustic nature of pretreatment causing saponification of acetate and ester bonds, increasing hemicellulose solubility [74]. Cellulose content and crystallinity remains relatively unchanged in AHP pretreatment, indicating that the major changes in biomass are associated with loosening of the cell wall matrix [75].

Ammonia Fiber Expansion (AFEX) pretreatment falls generally under alkaline pretreatments, and utilizes anhydrous ammonia under high pressure, followed by an explosive decompression to disrupt cell wall structure [76]. AFEX results in changes to cell wall

ultrastructure [77] through targeting of ester linkages between lignin and hemicelluloses, as well as deacetylation and partial depolymerization of hemicelluloses [78]. In addition, cellulose decrystallization is observed, forming cellulose III allomorphs, which has been shown to increases digestibility significantly [79], and is the basis of newer Extractive Ammonia (EA) pretreatments [80].

Pretreatment technologies that dissolve or fractionate lignocellulose include organosolv pretreatments and ionic liquid pretreatments, which will be briefly mentioned for completeness. The main mode of ionic liquid pretreatment, similar to EA pretreatment is the disruption of cellulose hydrogen bonding and de-crystallization of cellulose and removal from the cell wall [81]. Currently, there exist multiple ionic liquid pairs for application in lignocellulosic biomass pretreatment, which are highlighted in a recent review [82]. Organosolv pretreatment utilizes a combination of organic solvents and aqueous solutions to extract lignin and hemicelluloses from lignocellulose, and similarly to ionic liquids, possess a wide range of organic solvent-aqueous pairings [83]. The majority of organosolv pretreatments delignify through cleavage of β -ether linkages in lignin, followed by reductions in lignin molecular weight. Hemicellulose glycosidic linkages are also targeted, resulting in hemicellulose solubilization, while cellulose dedecrystalization also occurs [84], giving organosolv pretreatments significant similarity with multiple other pretreatments mentioned earlier.

Enzymatic hydrolysis

Following pretreatment, lignocellulosic biomass is subjected to depolymerization to break sugars down from polymers into monomers. The main mode of action in this process is the breaking of glycosidic linkages between individual cellulose and hemicellulose subunits, which can be performed either thermochemically via acid and heat, or enzymatically using enzymes to

target individual bonds. Enzymatic hydrolysis is favored for lignocellulosic processing, due in part to the production of inhibitors in acid hydrolysis limiting fermentability [85], however the presence of a multitude of bond configurations requires multiple enzymes. In nature, microorganisms such as bacteria and fungi produce biomass-degrading enzymes, secreting cellulolytic enzymes from classes of glycoside hydrolases (GH), which work together synergistically to depolymerize polysaccharides [86]. The primary enzymes required for lignocellulosic hydrolysis are cellulases and xylanases, however accessory enzymes play an important role in improving both enzyme dosing and overall hydrolysis yields [71, 87]. In addition, cellulose structure can impact enzymatic hydrolysis yields, with amorphous cellulose having higher digestibility compared to crystalline cellulose [54]. Changes in crystalline cellulose allomorph imparted by pretreatments such as EA [80] also have shown to increase hydrolysis yields [79].

Enzymatic depolymerization effectiveness may be inhibited through either nonproductive adsorption to lignin or other cell wall polymers, product inhibition, limited enzyme
accessibility, or enzyme deactivation [88]. Non-productive adsorption and limited enzyme
accessibility are two factors directly related to feedstock properties, with lignin and to a lesser
extent xylan believed to act as a sheathe and physically occlude cellulase accessibility to
cellulose via steric hindrance [89, 90]. Delignification pretreatments alone have shown marginal
increases in cellulose accessibility, indicating lignin indirectly limits cellulose accessibility
through limiting accessibility to xylan, which in turn limits cellulose accessibility [88, 91]. There
also exists a limit for improving cellulase accessibility through pretreatment, with harsh
pretreatment conditions exhibiting a decrease in enzyme accessibility, likely due to cell wall
collapse or aggregation [92].

Non-productive adsorption is thought to occur due to hydrophobic and electrostatic interactions between lignin and cellulase carbohydrate binding modules (CBM), promoting a high affinity for lignin [93]. Increases in carboxylic acid content and therefore higher net negative charge in lignin has shown decreases in non-productive binding of cellulases [94], while adding negative charges to cellulases can significantly decrease lignin affinity [95, 96].

Approaches using proteins such as Bovine Serum Albumin (BSA) as lignin blockers prior to enzymatic hydrolysis have also reduced non-productive adsorption of cellulases [97], with BSA thought to reduce lignin affinity by interacting with hydrophobic charges. Pretreatment altering lignin properties may also participate in changing non-productive adsorption, and may provide avenues for tailoring pretreatment conditions to minimize non-productive adsorption [94, 98].

Plant cell wall properties contributing to recalcitrance Cell wall composition

Lignin is often cited as the most common cell wall component to inhibit enzymatic digestibility, with strong negative correlations observed before and after pretreatment in multiple pretreatments [73, 99, 100]. Lignin monomer composition has been examined as a variable impacting enzymatic hydrolysis, with some studies showing increased S/G monolignol content positively correlates with yield [99, 101]. This is not a universally observed trend however [56], leading to the conclusion that other properties as well as pretreatment type may impact S/G ratio. Esterified ferulate content in grasses has shown positive correlations with hydrolysis, and may be due to the more labile ester linkages associated with ferulates enabling cell wall loosening [102, 103].

Because the contribution of lignin towards recalcitrance is substantial in most feedstocks, deriving non-lignin correlations to digestibility can be difficult to deconvolute from lignin. The

substitution pattern of arabinan has recently been proposed to impact recalcitrance, with higher abundances of GAX arabinose substitution correlating positively to digestibility [104]. Additionally, substituted xylan has been correlated to increased extractability, which may be an indicated of a less tightly crosslinked cell wall matrix [105]. Similar conclusions have been drawn in a study utilizing sequential extraction of switchgrass, which showed the greatest increase in hydrolysis yield after alkaline extraction has removed significant fractions of substituted xylan [106].

Morphological fractionation and tissue maturity

Biomass morphological fractions and varying tissue maturities can impart significant differences in feedstock composition [105], and present an opportunity for either modifying harvesting methods or employing physical fractionation prior to biomass pretreatment and digestibility. Physical fraction of corn stover to stem pith, stem rind, and leaves resulted with the highest yield in stem pith, followed by leaves, and stem rind for both no pretreatment and liquid hot water pretreatment [107]. Similar conclusions have been observed in physical fractionation of sugarcane stems [108]. In herbaceous feedstocks, multiple studies have all come to similar conclusions that stem fractions are less digestible compared to leaf fractions [109, 110].

Tissue maturity can also impact enzymatic hydrolysis yields. Internode maturity in switchgrass stems decreased in digestibility in more mature internodes [111], as did maize digestibility with stem age [112]. As a general trend, structural carbohydrates and lignification increase in proportion of total biomass with tissue maturity, while soluble sugars and other components decrease [113].

Feedstock improvement through genetic manipulation

The past decade has seen significant strides in understanding the genes and transcription factors involved in plant cell wall biosynthesis and regulation, and are the subject of numerous reviews [24, 114]. Feedstock manipulation aims to improve feedstock sugar yields through reductions in cell wall recalcitrance, while maintaining normal feedstock growth. General approaches to feedstock improvement include modification of cell wall component structure, abundance, or localized expression in tissues, with a few examples of each highlighted in the proceeding text. Modification of cellulose abundance and crystallinity are two approaches that have been taken, however over-expression of CESA complexes resulted in reduced cellulose content due to silencing of other genes [115], while reductions in crystallinity were accompanied by dwarfed phenotypes [116]. Given the essential role cellulose plays in maintaining cell wall strength, approaches manipulating cellulose content and structure may not be advantageous.

Typically, down regulation of major hemicellulose components such as xylan backbone synthesis [24] has resulted in improved sugar digestibility at the expense of severe growth phenotypes; however, regulation of tissue specific expression of xylan biosynthesis to vessel cells xylan deficient mutants *irx7*, *irx8*, and *irx9* has shown rescued phenotypes coupled with increased digestibility [117]. Alteration of xylan side chain substitution, specifically reduction of uronic acid side chains on hemicellulose in the *gux* mutants showed increased digestibility with no noticeable growth phenotypes [118], while reductions in other side chains such as acetylation [38, 119] had dwarfed phenotypes.

Reductions in lignin content follow similar approaches to xylan modification, with severe reductions in lignin causing phenotypic dwarfism. Vessel specific expression of cinnamate 4-hydroxylase in Arabidopsis resulted in reductions in lignin content without sacrificing plant

fitness [120], while the creation of a competitive metabolic pathway reducing shikimate, a key enzyme in the lignin pathway, also significantly reduced yields without dwarfism [121]. Changes to lignin monomer content have also shown some success [122], as have incorporation of chemically labile ester linkages via the design of a novel lignin monomer to improve pretreatment effectiveness [123]. Engineering of lignin structure without sacrificing functionality is an active research field, working to reduce lignin degree of polymerization, reduce lignin hydrophobicity, reduce lignin-carbohydrate covalent bonds, increase chemically labile linkages, and improve lignin valorization [124].

Characterization of biomass properties Hydrophilicity

Water imbedded within the cell walls causes cell walls to swell and soften, acting as a plasticizer and separating individual polymers through hydrogen bonding and electrostatic interactions [125]. Other solvents can swell cell walls; however, hydrogen bond donors show preferential swelling [126]. Individual cell wall components have different affinities for water, with hydrophobic lignin generally having the lowest affinity, followed by cellulose, hemicelluloses, and hydrophilic pectins [127, 128]. Available hydroxyl and carboxylic acid groups found on polysaccharide chains are the predominant cell wall features water bonds with, forming hydrogen bonded layers [129]. In cellulose, water may absorb within a cellulose elementary fibril, with water molecules hydrogen bonded between individual elementary microfibril chains [130].

Because of this phenomenon, cellulose is sometimes thought of as a hydrate, given the native state of cellulose fibers can be expected to contain up to 8% moisture by weight, which is equivalent to one water molecule per glucose unit [125]. Furthermore, initial water added to a

cellulosic fiber immediately adsorbs and hydrogen bonds to elementary fibrils [131]. Water closest to cell wall surfaces has an altered chemical environment due to hydrogen bonding and does not have a freezing point [132], while water beyond the first few molecular layers has a depressed freezing point, which can be used to quantify pore size of nonporous materials [133].

The nature of available chemical bonds on polysaccharide chains also presents the ability for polyelectrolytes to impact biomass-water interactions and impact cell wall swelling. In the case of salts, conversion of hydroxyl groups and carboxyl groups to the salt form can impact the pH of the surrounding solution, as well as induce osmotic diffusion gradients [134]. This phenomenon is most prevalent in carboxymethylated super-absorbent pulps and cellulose gels, however chlorite delignified pulps have exhibited similar changes in cell wall swelling, indicating that unlignified cell walls behave similar to a hydrogel [135]. One hypothesis for hydrolysis effectiveness has been proposed around sufficient delignification inducing loss of cell wall rigidity and subsequent expansion [73], with cell wall swelling in response to polyelectrolytes providing one proxy for measuring cell wall rigidity to osmotic pressure.

Fiber saturation point (FSP) is defined as the water weight where the cell wall of a sample becomes saturated with bound water, and is used as a metric for measuring bulk hydrophilicity. Multiple techniques including pore dilution by solute exclusion, vapor pressure adsorption, or gravimetric filter pad techniques have been employed to precisely measure FSP, with multiple techniques yielding similar values [136, 137].

Differences in feedstock, composition, or tissue type can impact water sorption behavior. In addition, water sorption can be dramatically impacted by chemical pretreatment, depending on the chemical and ultrastructural changes of the cell wall. Water retention value (WRV) is one standardized way of determining the pseudo-FSP, through determination of bound water in a

sample via gravitational separation [138]. Cell wall compositions and response to pretreatment can both contribute to cell wall hydrophilicity, enabling the usage of WRV to represent multiple feedstock properties.

Recent work correlating compositional relationships to WRV in a genotypically diverse group of maize samples concluded that individual contributions from both lignin components and hemicellulose components can be related to WRV, limiting weighting of individual contributions towards overall WRV [103].

WRV has been successfully employed to demonstrate increases in cell wall swelling of AHP delignified and LHW pretreated grasses along with correlate subsequent increases in enzymatic hydrolysis [139]. WRV has also been used to represent cellulose accessibility in fiber sheets, and captured loss in cellulose accessible area imparted by hornification processes [140, 141]. From these studies, it was concluded that WRV represents cell wall response to diverse structural and compositional features which likely impact cellulose accessibility and indirectly impact enzymatic digestibility.

Nuclear magnetic resonance (NMR) relaxometry represents another avenue for measuring biomass-water interactions, using time domain spin-spin (T₂) NMR relaxometry techniques. In addition to gauging general biomass recalcitrance, specific information on the chemical environment of water may be extracted [142]. Water constraint has been proposed as a general term to describe the extent of hydrogen bonding between water and the cell wall, with increased water constraint correlating to increases in accessibility [143, 144]. Relaxation time as a single metric similar to WRV has shown to correlate well with enzymatic hydrolysis yields in model cellulose components [143], and has also been used to describe tissue-specific chemical

states of water in sugarcane [145], however to date has not been directly correlated to enzymatic hydrolysis of lignocellulosic biomass.

Porosity

The idea of cell wall hydrophilicity can be extrapolated to ultrastructural features of the cell wall, namely the presence of void spaces or pores contributing to total cell wall accessible surface area. In the context of lignocellulosic biomass, pore formation may result from chemical pretreatment, altering void spaces and available surface area for enzyme penetration and subsequent hydrolysis. The lamellar structure of plant cell walls allows for the assumption of a simple slit model to define cell wall pores, and has been used in prior studies to define pore geometry [146, 147]. Solute exclusion is one technique to measure pore accessibility of various sizes of probe molecules to obtain a pore size distribution [136].

The technique works through dilution of probe solution indicating interaction with pores, and is based upon the assumptions of equal concentration of probe solution within the pore and surrounding bulk fluid, as well as full accessibility of a probe to a pore. Solute exclusion is limited by irregular pores under-contributing to total pore volumes, known as the 'ink-bottle' effect, or the presence of ionized groups excluding probes via electrostatic interaction [148]. The solute exclusion technique has been successfully utilized to describe pore changes resulting from delignification [149], sulfite pretreatment [150], and hornification [151].

Differential scanning calorimetry thermoporemetry (DSC-TP) is another technique utilized to measure pore distributions, and is based upon changes in freezing point depression of water associated with the cell wall discussed earlier. The relationship between specific melting enthalpy of water associated with the cell wall is related to a specific pore geometry using the Gibbs-Thompson equation. This technique has been successfully employed in observing pore

changes during drying [133], as well as recently to identify the impact of alkaline and autohydrolysis pretreatment on porosity [65]. Cryoporismetry is not limited to DSC-TP, with ¹H NMR cryoporisemetry having been utilized following similar assumptions in dilute acid pretreated corn stover [152]. One of the key advantages of solute exclusion and cryoporisemetry is the ability to measure samples in a wet state, while older techniques for measuring pore distributions such as nitrogen adsorption or mercury porismetry require dry samples, which imparts altered pore properties [147].

Crystallinity

The amount of inter- and intra- molecular hydrogen bonds between cellulose elementary microfibrils gives rise to ordered crystalline cellulose microfibril structures. To date, there are four crystalline cellulose allomorphs, with cellulose I the most abundant and naturally occurring, found as cellulose I α in some bacteria and regenerated pulps, and I β in plant cell walls. Other allomorphs are derived from either chemical treatment with alkali (II) or ammonia (III), coupled with solubilization and regeneration (II), or through heating of cellulose III (IV) [28]. Cellulose crystalline structure and abundance can be observed using X-ray diffraction techniques, or through solid-state 13 C NMR.

As described earlier, amorphous regions of cellulose have less ordered hydrogen bonding and do not contribute to the crystallinity of cellulose, with a ratio of crystalline cellulose to amorphous contribution called crystallinity index (CI) or relative crystallinity index in this text (RCI). RCI is used to interpret changes to cellulose structure after physiochemical or biological treatments, and is a non-destructive way to observe crystalline cellulose changes [29].

The relative amount of crystalline cellulose compared to amorphous cellulose has been linked to reductions in hydrolysis rates, with higher RCI values corresponding to more

crystalline cellulose and slower initial hydrolysis yields [153, 154]. Altering the crystalline hydrogen bond network as mentioned earlier has shown improvements to yield [79], along with de-crystalization of cellulose to amorphous cellulose increasing hydrolysis rates by an order of magnitude [155]. Crystallinity has also shown to have no correlation with overall hydrolysis yields [156], however can still be used to gauge relative cellulose organization.

Native cell wall crystallinity can be affected by perturbations to components within the cell wall during growth, although higher order interactions between individual cell wall components are not well understood. A few notable examples of irregular cellulose include cellulose deficient mutants from KORRIGAN1 [157] and CESA1 and CESA3 mutants [116], reduced crystalline cellulose organization in lignin deficient mutants [158], and disruption in microfibril angle observed in xylan modified mutants [159].

Microscopy

Direct observation of cell wall organization via microscopy techniques is another approach towards characterizing biomass, and enables visualization a cell wall surface and structural features at the micron or nanoscale.

Transmission electron microscopy (TEM) is a widely used microscopy technique that utilizes electrons passing through a sample to derive images, and allows for high-resolution views of the cell walk ultrastructure and of different cell wall layers [148]. One limitation of TEM is sample thickness, limiting analysis of three-dimensional topography that may be present in samples. Scanning electron microscopy (SEM) provides high-resolution topographic information with minimal sample preparation aside from drying and coating. One advantage of SEM over TEM is the ability to examine three-dimensional features of cells often overlooked when taking small cross-sections using TEM.

Atomic force microscopy (AFM) utilizes direct contact between a sample and a probe tip to produce a three-dimensional image. The probe tip is attached to an oscillating cantilever, allowing changes in tip contact height to be observed as a change in cantilever oscillation [160]. AFM also has the advantage of capturing nanomechanical properties of the sample surface through direct contact, allowing for direct measurement of properties such as modulus force, deformation, adhesion force, and dissipation [161]. Alternatively, complex molecules such as a cellulase CBM may be linked to an AFM tip to alter the chemical interaction between the tip and surface, allowing for examination of a sample surface from the perspective of an external probe interaction [162]. The major limitation of AFM is disruption of native sample state during preparation. While AFM sampling can be performed in vacuum, fluid, or air, thin samples of relative height uniformity are required to effectively image, requiring some cutting or sample isolation prior. Additionally, in the case of imaging secondary cell walls, cellulose microfibril layers are imbedded within coated lignin layers, often requiring a chemical pretreatment such as acid-chlorite pretreatment prior to imaging, which will certainly impact native structure and interpretation of results relative to a native perspective [163].

Confocal microscopy is another common microscopy technique, using laser excitation to visualize cell wall surfaces. Often, microscopy is coupled with staining techniques [164], or along with immunohistochemical techniques to highlight local abundance of certain components [165]. Confocal microscopy may also be used to autofluorescence cell walls, and obtain information about chemical makeup [166, 167], however is limited by some lack of specificity between individual components [168]. More recent endeavors using confocal microscopy coupled GFP-labelling of individual cell wall components to obtain special

distribution information [169], or GFP-labelling of proteins involved in cell wall biosynthesis to obtain real-time visualization of cell wall synthesis and organization [170, 171].

Cell wall extractability

Biomass response to deconstruction can also be approached through investigation of cell wall extractability of certain components. Glycome profiling, using a suite of plant cell wall glycan-directed monocolonal antibodies (mAbs) represents one technique to identify cell wall deconstruction patterns and understand cell wall organization [172, 173]. This technique is useful in application for identifying structural differences between feedstocks [106], understanding pleiotropic impacts of gene mutants on cell wall extractability [174], and evaluating pretreatment effectiveness in different feedstocks [175, 176]. More recently, glycome profiling has been used to identify structural changes during tissue maturity [105], as well as understand recalcitrant unhydrolyzed carbohydrates in residual solids after enzymatic hydrolysis [87]. While a powerful technique with multiple applications, glycome profiling is limited to recognizing individual clades of epitopes in most cases, as the specific substitution patterns of many epitopes are not known [175, 177].

REFERENCES

REFERENCES

- 1. Rogelj J, den Elzen M, Höhne N, Fransen T, Fekete H, Winkler H, Schaeffer R, Sha F, Riahi K, Meinshausen M: **Paris Agreement climate proposals need a boost to keep warming well below 2** °C. *Nature*. 2016, **534**:631-639.
- 2. Administration USEI: **Monthly Energy Review**. 2017.
- 3. Meinshausen M, Meinshausen N, Hare W, Raper SCB, Frieler K, Knutti R, Frame DJ, Allen MR: **Greenhouse-gas emission targets for limiting global warming to 2 degrees** C. *Nature*. 2009, **458**:1158-1196.
- 4. MacDonald AE, Clack CTM, Alexander A, Dunbar A, Wilczak J, Xie YF: Future cost-competitive electricity systems and their impact on US CO2 emissions. *Nat Clim Chang.* 2016, **6**:526-531.
- 5. Arent D, Verrastro F, Bovair J, Peterson E: **Alternative transportation fuels and vehicle technologies**. 2009.
- 6. Fulton LM, Lynd LR, Körner A, Greene N, Tonachel LR: **The need for biofuels as part of a low carbon energy future**. *Biofuel Bioprod Bior*. 2015, **9**:476-483.
- 7. Dale BE, Ong RG: Energy, wealth, and human development: Why and how biomass pretreatment research must improve. *Biotechnol progr.* 2012, **28**:893-898.
- 8. Schnepf R, Yacobucci BD: **Renewable fuel standard (RFS): Overview and issues**. 2013.
- 9. Flugge M, J. Lewandrowski, J. Rosenfeld, C. Boland, T. Hendrickson, K. Jalgo, S. Kolansky, K. Moffroid, M. Riley-Gilbert, and D. Pape: A life-cycle analysis of the greenhouse gas emissions of corn-based ethanol. 2017.
- 10. Perlack RD, Eaton LM, Turhollow Jr AF, Langholtz MH, Brandt CC, Downing ME, Graham RL, Wright LL, Kavkewitz JM, Shamey AM: **US billion-ton update: biomass supply for a bioenergy and bioproducts industry**. 2011.
- 11. Lynd LR, Liang X, Biddy MJ, Allee A, Cai H, Foust T, Himmel ME, Laser MS, Wang M, Wyman CE: **Cellulosic ethanol: status and innovation**. *Curr Opin Biotech*. 2017, **45**:202-211.
- 12. Dale B: A sober view of the difficulties in scaling cellulosic biofuels. *Biofuel Bioprod Bior*. 2017, **11**:5-7.

- 13. Wallington TJ, Anderson JE, Kleine RD, Kim HC, Maas H, Brandt AR, Keoleian GA: When comparing alternative fuel-vehicle systems, life cycle assessment studies should consider trends in oil production. *J Ind Ecol.* 2017, 21:244-248.
- 14. Ragauskas AJ, Beckham GT, Biddy MJ, Chandra R, Chen F, Davis MF, Davison BH, Dixon RA, Gilna P, Keller M *et al*: **Lignin valorization: improving lignin processing in the biorefinery**. *Science*. 2014, **344**:709-711.
- 15. Beckham GT, Johnson CW, Karp EM, Salvachua D, Vardon DR: **Opportunities and challenges in biological lignin valorization**. *Curr Opin Biotech*. 2016, **42**:40-53.
- 16. Hoefnagels R, Searcy E, Cafferty K, Cornelissen T, Junginger M, Jacobson J, Faaij A: Lignocellulosic feedstock supply systems with intermodal and overseas transportation. *Biofuel Bioprod Bior*. 2014, **8**:794-818.
- 17. Keegstra K: **Plant cell walls**. *Plant Physiol*. 2010, **154**:483-486.
- 18. Cosgrove DJ: **Growth of the plant cell wall**. *Nat Rev Mol Cell Bio*. 2005, **6**:850-861.
- 19. Ding S-Y, Zhao S, Zeng Y: Size, shape, and arrangement of native cellulose fibrils in maize cell walls. *Cellulose*. 2014, **21**:863-871.
- 20. Zhang T, Zheng Y, Cosgrove DJ: **Spatial organization of cellulose microfibrils and matrix polysaccharides in primary plant cell walls as imaged by multichannel atomic force microscopy**. *Plant J.* 2016, **85**:179-192.
- 21. Park YB, Cosgrove DJ: Changes in cell wall biomechanical properties in the xyloglucan-deficient xxt1/xxt2 mutant of Arabidopsis. *Plant Physiol.* 2012, **158**:465-475.
- 22. Park YB, Cosgrove DJ: A revised architecture of primary cell walls based on biomechanical changes induced by substrate-specific endoglucanases. *Plant Physiol.* 2012, **158**:1933-1943.
- 23. Cosgrove DJ: **Re-constructing our models of cellulose and primary cell wall assembly**. *Curr Opin in Plant Biol*. 2014, **22**:122-131.
- 24. Kumar M, Campbell L, Turner S: **Secondary cell walls: biosynthesis and manipulation**. *J Exp Bot*. 2016, **67**:515-531.
- 25. Ding S-Y: **Nanoscale structure of biomass**. In: *Reaction Pathways and Mechanisms in Thermocatalytic Biomass Conversio n I: Cellulose Structure, Depolymerization and Conversion by Heterogeneous Catalysts*. Edited by Schlaf M, Zhang ZC. Singapore: Springer Singapore; 2016: 1-14.

- 26. Ding S-Y, Liu Y-S, Zeng Y, Himmel ME, Baker JO, Bayer EA: **How does plant cell wall nanoscale architecture correlate with enzymatic digestibility?** *Science.* 2012, **338**:1055-1060.
- 27. Somerville C: Cellulose synthesis in higher plants. *Annu Rev Cell Dev Biol* 2006, **22**:53-78.
- 28. Moon RJ, Martini A, Nairn J, Simonsen J, Youngblood J: **Cellulose nanomaterials review: structure, properties and nanocomposites**. *Chem Soc Rev.* 2011, **40**:3941-3994.
- 29. Park S, Baker JO, Himmel ME, Parilla PA, Johnson DK: Cellulose crystallinity index: measurement techniques and their impact on interpreting cellulase performance. *Biotechnol Biofuels*. 2010, **3**:10.
- 30. Pauly M, Gille S, Liu L, Mansoori N, Souza A, Schultink A, Xiong G: **Hemicellulose biosynthesis**. *Planta*. 2013, **238**:627-642.
- 31. Ebringerova A, Hromadkova Z, Heinze T: **Hemicellulose**. In: *Polysaccharides 1: Structure, Characterization and Use*. Edited by Heinze T; 2005, **186**:1-67.
- 32. Gille S, Pauly M: **O-Acetylation of Plant Cell Wall Polysaccharides**. *Front Plant Sci.* 2012, **3**:12.
- 33. Pena MJ, Zhong R, Zhou G-K, Richardson EA, O'Neill MA, Darvill AG, York WS, Ye Z-H: Arabidopsis irregular xylem8 and irregular xylem9: Implications for the complexity of glucuronoxylan biosynthesis. *Plant Cell* 2007, **19**:549-563.
- 34. York WS, O'Neill MA: **Biochemical control of xylan biosynthesis which end is up?** *Curr Opin Plant Biol.* 2008, **11**:258-265.
- 35. Scheller HV, Ulvskov P: **Hemicelluloses**. *Annu Rev Plant Biol.*. 2010, **61**:263-289.
- 36. Vogel J: Unique aspects of the grass cell wall. Curr Opin Plant Biol. 2008, 11:301-307.
- 37. Pauly M, Keegstra K: Cell-wall carbohydrates and their modification as a resource for biofuels. *Plant J.* 2008, **54**:559-568.
- 38. Xiong G, Cheng K, Pauly M: **Xylan O-Acetylation Impacts Xylem Development and Enzymatic Recalcitrance as Indicated by the Arabidopsis Mutant tbl29**. *Mol Plant*. 2013, **6**:1373-1375.
- 39. Pawar PMA, Koutaniemi S, Tenkanen M, Mellerowicz EJ: **Acetylation of woody lignocellulose: significance and regulation**. *Front Plant Sci.* 2013, **4**:118.

- 40. Buckeridge MS, Rayon C, Urbanowicz B, Tine MAS, Carpita NC: **Mixed linkage** (1 -> 3),(1 -> 4)-beta-D-glucans of grasses. *Cereal Chem.* 2004, 81:115-127.
- 41. Vega-Sanchez ME, Verhertbruggen Y, Scheller HV, Ronald PC: **Abundance of mixed linkage glucan in mature tissues and secondary cell walls of grasses**. *Plant Signal Behav*. 2013, **8**:e23143.
- 42. Harholt J, Suttangkakul A, Vibe Scheller H: **Biosynthesis of pectin**. *Plant Physiol*. 2010, **153**:384-395.
- 43. Mohnen D: **Pectin structure and biosynthesis**. Curr Opin Plant Biol. 2008, **11**:266-277.
- 44. Caffall KH, Mohnen D: **The structure, function, and biosynthesis of plant cell wall pectic polysaccharides**. *Carbohyd Res.* 2009, **344**:1879-1900.
- 45. O'Neill MA, Ishii T, Albersheim P, Darvill AG: **Rhamnogalacturonan II: Structure** and function of a borate cross-linked cell wall pectic polysaccharide. *Annu Rev Plant Biol.* 2004, **55**:109-139.
- 46. McKendry P: **Energy production from biomass (part 1): overview of biomass**. *Bioresource Technol.* 2002, **83**:37-46.
- 47. Ralph J: **Hydroxycinnamates in lignification**. *Phytochem Rev* 2010, **9**:65-83.
- 48. Ralph J, Lundquist K, Brunow G, Lu F, Kim H, Schatz PF, Marita JM, Hatfield RD, Ralph SA, Christensen JH: **Lignins: natural polymers from oxidative coupling of 4-hydroxyphenyl-propanoids**. *Phytochem Rev* 2004, **3**:29-60.
- 49. Vanholme R, Demedts B, Morreel K, Ralph J, Boerjan W: Lignin biosynthesis and structure. *Plant Physiol.* 2010, **153**:895-905.
- 50. Grabber JH, Ralph J, Lapierre C, Barrière Y: **Genetic and molecular basis of grass cell-wall degradability. I. Lignin–cell wall matrix interactions**. *C R Biol*. 2004, **327**:455-465.
- 51. Grabber JH, Hatfield RD, Lu F, Ralph J: Coniferyl ferulate incorporation into lignin enhances the alkaline delignification and enzymatic degradation of cell walls. *Biomacromolecules* 2008, **9**(9):2510-2516.
- 52. Ralph J, Hatfield RD, Quideau S, Helm RF, Grabber JH, Jung H-JG: **Pathway of p-coumaric acid incorporation into maize lignin As revealed by NMR**. *J Am Chem Soc*. 1994, **116**:9448-9456.
- 53. Hartley RD: **Degradation of cell walls of forages by sequential treatment with sodium hydroxide and a commercial cellulase preparation**. *J Sci Food Agr.* 1983, **34**:29-36.

- 54. Jeoh T, Ishizawa CI, Davis MF, Himmel ME, Adney WS, Johnson DK: Cellulase digestibility of pretreated biomass is limited by cellulose accessibility. *Biotechnol Bioeng.* 2007, **98**:112-122.
- 55. Mosier N, Wyman C, Dale B, Elander R, Lee YY, Holtzapple M, Ladisch M: **Features of promising technologies for pretreatment of lignocellulosic biomass**. *Bioresource Technol*. 2005, **96**:673-686.
- Ong RG, Chundawat SPS, Hodge DB, Keskar S, Dale BE: Linking plant biology and pretreatment: Understanding the structure and Organization of the Plant Cell Wall and Interactions with Cellulosic Biofuel Production. In: *Plants and BioEnergy*. Edited by McCann MC, Buckeridge MS, Carpita NC. New York, NY: Springer New York; 2014: 231-253.
- 57. Hendriks A, Zeeman G: Pretreatments to enhance the digestibility of lignocellulosic biomass. *Bioresource Technol.* 2009, **100**:10-18.
- 58. Hu F, Ragauskas A: **Pretreatment and lignocellulosic chemistry**. *Bioenerg Res.* 2012, **5**:1043-1066.
- 59. Donohoe BS, Decker SR, Tucker MP, Himmel ME, Vinzant TB: Visualizing lignin coalescence and migration through maize cell walls following thermochemical pretreatment. *Biotechnol Bioeng.* 2008, **101**:913-925.
- 60. Selig MJ, Viamajala S, Decker SR, Tucker MP, Himmel ME, Vinzant TB: **Deposition of lignin droplets produced during dilute acid pretreatment of maize stems retards enzymatic hydrolysis of cellulose**. *Biotechnol Progr.* 2007, **23**:1333-1339.
- 61. Pingali SV, Urban VS, Heller WT, McGaughey J, O'Neill H, Foston M, Myles DA, Ragauskas A, Evans BR: **Breakdown of cell wall nanostructure in dilute acid pretreated biomass**. *Biomacromolecules*. 2010, **11**:2329-2335.
- 62. Garrote G, Dominguez H, Parajo J: **Hydrothermal processing of lignocellulosic materials**. *Eur J Wood Wood Prod*. 1999, **57**:191-202.
- 63. Garlock RJ, Balan V, Dale BE, Ramesh Pallapolu V, Lee YY, Kim Y, Mosier NS, Ladisch MR, Holtzapple MT, Falls M *et al*: Comparative material balances around pretreatment technologies for the conversion of switchgrass to soluble sugars. *Bioresource Technol.* 2011, **102**:11063-11071.
- 64. Mosier N, Hendrickson R, Ho N, Sedlak M, Ladisch MR: **Optimization of pH** controlled liquid hot water pretreatment of corn stover. *Bioresource Technol.* 2005, **96**:1986-1993.

- 65. Pihlajaniemi V, Sipponen MH, Liimatainen H, Sirviö JA, Nyyssölä A, Laakso S: Weighing the factors behind enzymatic hydrolyzability of pretreated lignocellulose. *Green Chem.* 2016, **18**:1295-1305.
- 66. Xiao L-P, Sun Z-J, Shi Z-J, Xu F, Sun R-C: Impact of hot compressed water pretreatment on the structural changes of woody biomass for bioethanol production. *Bioresources*. 2011, **6**:1576-1598.
- 67. Knill CJ, Kennedy JF: **Degradation of cellulose under alkaline conditions**. *Carbohyd Polym*. 2003, **51**:281-300.
- 68. Karp EM, Resch MG, Donohoe BS, Ciesielski PN, O'Brien MH, Nill JE, Mittal A, Biddy MJ, Beckham GT: **Alkaline Pretreatment of Switchgrass**. *ACS Sustain Chem Eng*. 2015, **3**:1479-1491.
- 69. Gould JM: Studies on the mechanism of alkaline peroxide delignification of agricultural residues. *Biotechnol Bioeng.* 1985, **27**:225-231.
- 70. Gould MJ: Enhanced polysaccharide recovery from agricultural residues and perennial grasses treated with alkaline hydrogen peroxide. *Biotechnol Bioeng.* 1984, 27:893-896.
- 71. Banerjee G, Car S, Scott-Craig JS, Hodge DB, Walton JD: **Alkaline peroxide** pretreatment of corn stover: effects of biomass, peroxide, and enzyme loading and composition on yields of glucose and xylose. *Biotechnol Biofuels* 2011, 4:16.
- 72. Mittal A, Katahira R, Donohoe BS, Black BA, Pattathil S, Stringer JM, Beckham GT: Alkaline peroxide delignification of corn stover. *ACS Sustain Chem Eng.* 2017, 5:6310-6321.
- 73. Li M, Foster C, Kelkar S, Pu Y, Holmes D, Ragauskas A, Saffron C, Hodge D: Structural characterization of alkaline hydrogen peroxide pretreated grasses exhibiting diverse lignin phenotypes. *Biotechnol Biofuels* 2012, 5:38.
- 74. Kerley MS, Fahey GC, Jr., Berger LL, Gould JM, Lee Baker F: **Alkaline hydrogen peroxide treatment unlocks energy in agricultural by-products**. *Science*. 1985, **230**:820-822.
- 75. Martel P, Gould JM: Cellulose stability and delignification after alkaline hydrogen peroxide treatment of straw. *J Appl Polym Sci.* 1990, **39**:707-714.
- 76. Balan V, Bals B, Chundawat SP, Marshall D, Dale BE: **Lignocellulosic biomass** pretreatment using AFEX. *Biofuels: Methods and Protocols.* 2009, 61-77.
- 77. Chundawat SPS, Donohoe BS, da Costa Sousa L, Elder T, Agarwal UP, Lu F, Ralph J, Himmel ME, Balan V, Dale BE: **Multi-scale visualization and characterization of**

- lignocellulosic plant cell wall deconstruction during thermochemical pretreatment. *Energ Environ Sci.* 2011, **4**:973-984.
- 78. Harun S, Balan V, Takriff MS, Hassan O, Jahim J, Dale BE: **Performance of AFEXTM** pretreated rice straw as source of fermentable sugars: the influence of particle size. *Biotechnol Biofuels*. 2013, **6**:40.
- 79. Chundawat SPS, Bellesia G, Uppugundla N, da Costa Sousa L, Gao D, Cheh AM, Agarwal UP, Bianchetti CM, Phillips GN, Langan P *et al*: **Restructuring the crystalline cellulose hydrogen bond network enhances its depolymerization rate**. *J Am Chem Soc.* 2011, **133**:11163-11174.
- 80. da Costa Sousa L, Jin M, Chundawat SPS, Bokade V, Tang X, Azarpira A, Lu F, Avci U, Humpula J, Uppugundla N *et al*: **Next-generation ammonia pretreatment enhances cellulosic biofuel production**. *Energ Environ Sci.* 2016, **9**:1215-1223.
- 81. Sun L, Li C, Xue Z, Simmons BA, Singh S: **Unveiling high-resolution, tissue specific dynamic changes in corn stover during ionic liquid pretreatment**. *RSC Adv.* 2013, **3**:2017-2027.
- 82. Brandt A, Grasvik J, Hallett JP, Welton T: **Deconstruction of lignocellulosic biomass** with ionic liquids. *Green Chem.* 2013, **15**:550-583.
- 83. Zhao X, Cheng K, Liu D: **Organosolv pretreatment of lignocellulosic biomass for enzymatic hydrolysis**. *Appl Microbiol Biot*. 2009, **82**:815.
- 84. Zhang Z, Harrison MD, Rackemann DW, Doherty WOS, O'Hara IM: **Organosolv pretreatment of plant biomass for enhanced enzymatic saccharification**. *Green Chem.* 2016, **18**:360-381.
- 85. Jönsson LJ, Martín C: **Pretreatment of lignocellulose: Formation of inhibitory by- products and strategies for minimizing their effects**. *Bioresource Technol*. 2016, **199**:103-112.
- 86. Yang B, Dai Z, Ding S-Y, Wyman CE: **Enzymatic hydrolysis of cellulosic biomass**. *Biofuels*. 2011, **2**:421-449.
- 87. Gunawan C, Xue S, Pattathil S, da Costa Sousa L, Dale BE, Balan V: Comprehensive characterization of non-cellulosic recalcitrant cell wall carbohydrates in unhydrolyzed solids from AFEX-pretreated corn stover. *Biotechnol Biofuels*. 2017, 10:82.
- 88. Kumar R, Wyman CE: Cellulase adsorption and relationship to features of corn stover solids produced by leading pretreatments. *Biotechnol Bioeng.* 2009, **103**:252-267.

- 89. Chang VS, Holtzapple MT: **Fundamental factors affecting biomass enzymatic reactivity**. *Appl Biochem Biotech*. 2000, **84**:5-37.
- 90. Mansfield SD, Mooney C, Saddler JN: **Substrate and enzyme characteristics that limit cellulose hydrolysis**. *Biotechnol Progr.* 1999, **15**:804-816.
- 91. Teixeira LC, Linden JC, Schroeder HA: **Alkaline and peracetic acid pretreatments of biomass for ethanol production**. *Appl Biochem Biotech*. 1999, **77**:19-34.
- 92. Ishizawa CI, Jeoh T, Adney WS, Himmel ME, Johnson DK, Davis MF: Can delignification decrease cellulose digestibility in acid pretreated corn stover? *Cellulose*. 2009, **16**:677-686.
- 93. Börjesson J, Engqvist M, Sipos B, Tjerneld F: **Effect of poly (ethylene glycol) on enzymatic hydrolysis and adsorption of cellulase enzymes to pretreated lignocellulose**. *Enzyme Microb Tech.* 2007, **41**:186-195.
- 94. Nakagame S, Chandra RP, Kadla JF, Saddler JN: **Enhancing the enzymatic hydrolysis** of lignocellulosic biomass by increasing the carboxylic acid content of the associated lignin. *Biotechnol Bioeng.* 2011, **108**:538-548.
- 95. Strobel KL, Pfeiffer KA, Blanch HW, Clark DS: **Structural insights into the affinity of Cel7A carbohydrate-binding module for lignin**. *J Biol Chem.* 2015, **290**:22818-22826.
- 96. Whitehead TA, Bandi CK, Berger M, Park J, Chundawat SPS: **Negatively** supercharging cellulases render them lignin-resistant. *ACS Sustain Chem Eng.* 2017, 5:6247-6252.
- 97. Yang B, Wyman CE: **BSA treatment to enhance enzymatic hydrolysis of cellulose in lignin containing substrates**. *Biotechnol Bioeng*. 2006, **94**:611-617.
- 98. Rahikainen JL, Martin-Sampedro R, Heikkinen H, Rovio S, Marjamaa K, Tamminen T, Rojas OJ, Kruus K: **Inhibitory effect of lignin during cellulose bioconversion: the effect of lignin chemistry on non-productive enzyme adsorption**. *Bioresource Technol*. 2013, **133**:270-278.
- 99. Zhang Y, Culhaoglu T, Pollet B, Melin C, Denoue D, Barriere Y, Baumberger S, Méchin V: Impact of lignin structure and cell wall reticulation on maize cell wall degradability. *J Agr Food Chem.* 2011, **59**:10129-10135.
- 100. Zeng Y, Zhao S, Yang S, Ding S-Y: Lignin plays a negative role in the biochemical process for producing lignocellulosic biofuels. *Curr Opin Biotech.* 2014, **27**:38-45.
- 101. Mechin V, Argillier O, Menanteau V, Barriere Y, Mila I, Pollet B, Lapierre C: Relationship of cell wall composition to in vitro cell wall digestibility of maize inbred line stems. *J Sci Food Agr.* 2000, **80**:574-580.

- 102. Casler MD, Jung H-JG: **Relationships of fibre, lignin, and phenolics to in vitro fibre digestibility in three perennial grasses**. *Anim Feed Sci Tech.* 2006, **125**:151-161.
- 103. Li M, Heckwolf M, Crowe JD, Williams DL, Magee TD, Kaeppler SM, de Leon N, Hodge DB: Cell-wall properties contributing to improved deconstruction by alkaline pre-treatment and enzymatic hydrolysis in diverse maize (Zea mays L.) lines. *J Exp Bot.* 2015. **66**:4305-4315.
- 104. Costa THF, Vega-Sanchez ME, Milagres AMF, Scheller HV, Ferraz A: **Tissue-specific** distribution of hemicelluloses in six different sugarcane hybrids as related to cell wall recalcitrance. *Biotechnol Biofuels*. 2016, **9**:99.
- 105. da Costa RMF, Pattathil S, Avci U, Lee SJ, Hazen SP, Winters A, Hahn MG, Bosch M: A cell wall reference profile for Miscanthus bioenergy crops highlights compositional and structural variations associated with development and organ origin. New Phytol. 2017, 213:1710-1725.
- 106. DeMartini JD, Pattathil S, Miller JS, Li HJ, Hahn MG, Wyman CE: **Investigating plant cell wall components that affect biomass recalcitrance in poplar and switchgrass**. *Energ Environ Sci.* 2013, **6**:898-909.
- 107. Zeng M, Ximenes E, Ladisch MR, Mosier NS, Vermerris W, Huang C-P, Sherman DM: Tissue-specific biomass recalcitrance in corn stover pretreated with liquid hotwater: Enzymatic hydrolysis (part 1). *Biotechnol Bioeng*. 2012, **109**:390-397.
- 108. Allen SG, Kam LC, Zemann AJ, Antal MJ: **Fractionation of sugar cane with hot, compressed, liquid water**. *Ind Eng Chem Res.* 1996, **35**:2709-2715.
- 109. Garlock RJ, Chundawat SPS, Balan V, Dale BE: **Optimizing harvest of corn stover** fractions based on overall sugar yields following ammonia fiber expansion pretreatment and enzymatic hydrolysis. *Biotechnol Biofuels*. 2009, **2**:29.
- 110. Duguid K, Montross M, Radtke C, Crofcheck C, Wendt L, Shearer S: **Effect of anatomical fractionation on the enzymatic hydrolysis of acid and alkaline pretreated corn stover**. *Bioresource Technol*. 2009, **100**:5189-5195.
- 111. Shen H, Fu CX, Xiao XR, Ray T, Tang YH, Wang ZY, Chen F: **Developmental control** of lignification in stems of lowland switchgrass variety alamo and the effects on saccharification efficiency. *Bioenerg Res.* 2009, **2**:233-245.
- 112. Jung H, Casler M: Maize stem tissues: cell wall concentration and composition during development. *Crop Sci.* 2006, **46**:1793-1800.
- 113. Dien BS, Jung HJG, Vogel KP, Casler MD, Lamb JFS, Iten L, Mitchell RB, Sarath G: Chemical composition and response to dilute-acid pretreatment and enzymatic

- saccharification of alfalfa, reed canarygrass, and switchgrass. *Biomass Bioenerg*. 2006, **30**:880-891.
- 114. Loqué D, Scheller HV, Pauly M: **Engineering of plant cell walls for enhanced biofuel production**. *Curr Opin Plant Biol*. 2015, **25**:151-161.
- 115. Joshi CP, Thammannagowda S, Fujino T, Gou J-Q, Avci U, Haigler CH, McDonnell LM, Mansfield SD, Mengesha B, Carpita NC *et al*: **Perturbation of wood cellulose synthesis causes pleiotropic effects in transgenic aspen**. *Mol Plant*. 2011, **4**:331-345.
- Harris DM, Corbin K, Wang T, Gutierrez R, Bertolo AL, Petti C, Smilgies DM, Estevez JM, Bonetta D, Urbanowicz BR *et al*: Cellulose microfibril crystallinity is reduced by mutating C-terminal transmembrane region residues CESA1(A903V) and CESA3(T942I) of cellulose synthase. *P Natl Acad Sci USA*. 2012, 109:4098-4103.
- 117. Petersen PD, Lau J, Ebert B, Yang F, Verhertbruggen Y, Kim JS, Varanasi P, Suttangkakul A, Auer M, Loqué D *et al*: **Engineering of plants with improved properties as biofuels feedstocks by vessel-specific complementation of xylan biosynthesis mutants**. *Biotechnol Biofuels*. 2012, **5**:84.
- 118. Mortimer JC, Miles GP, Brown DM, Zhang Z, Segura MP, Weimar T, Yu X, Seffen KA, Stephens E, Turner SR *et al*: **Absence of branches from xylan in Arabidopsis gux mutants reveals potential for simplification of lignocellulosic biomass**. *P Natl Acad Sci USA*. 2010, **107**:17409-17414.
- 119. Xiong G, Dama M, Pauly M: Glucuronic acid moieties on xylan are functionally equivalent to O-acetyl-substituents. *Mol Plant.* 2015, 8:1119-1121.
- 120. Yang F, Mitra P, Zhang L, Prak L, Verhertbruggen Y, Kim JS, Sun L, Zheng K, Tang K, Auer M: **Engineering secondary cell wall deposition in plants**. *Plant Biotechnol J*. 2013, **11**:325-335.
- 121. Eudes A, Sathitsuksanoh N, Baidoo EEK, George A, Liang Y, Yang F, Singh S, Keasling JD, Simmons BA, Loqué D: Expression of a bacterial 3-dehydroshikimate dehydratase reduces lignin content and improves biomass saccharification efficiency. *Plant Biotechnol J.* 2015, **13**:1241-1250.
- 122. Ciesielski PN, Resch MG, Hewetson B, Killgore JP, Curtin A, Anderson N, Chiaramonti AN, Hurley DC, Sanders A, Himmel ME *et al*: **Engineering plant cell walls: tuning lignin monomer composition for deconstructable biofuel feedstocks or resilient biomaterials**. *Green Chem.* 2014, **16**:2627-2635.
- 123. Wilkerson CG, Mansfield SD, Lu F, Withers S, Park JY, Karlen SD, Gonzales-Vigil E, Padmakshan D, Unda F, Rencoret J *et al*: **Monolignol ferulate transferase introduces chemically labile linkages into the lignin backbone**. *Science*. 2014, **344**:90-93.

- 124. Mottiar Y, Vanholme R, Boerjan W, Ralph J, Mansfield SD: **Designer lignins:** harnessing the plasticity of lignification. *Curr Opin Biotech.* 2016, **37**:190-200.
- Hubbe MA RO: Colloidal stability and aggregation of lignocellulosic materials in aqueous suspension: A review. *Bioresources*. 2008, **3**:1419-1491.
- 126. Nayer AN, Hossfeld RL: **Hydrogen bonding and the swelling of wood in various organic liquids**. *J Am Chem Soc*. 1949, **71**:2852-2855.
- 127. Lund K, Sjöström K, Brelid H: **Alkali extraction of kraft pulp fibers: Influence on fiber and fluff pulp properties**. *J Eng Fiber Fabr*. 2012, **7**.
- 128. Weber CW, Kohlhepp EA, Idouraine A, Ochoa LJ: **Binding capacity of 18 fiber sources for calcium**. *J Agric Food Chem*. 1993, **41**:1931-1935.
- 129. Olsson AM, Salmen L: **The association of water to cellulose and hemicellulose in paper examined by FTIR spectroscopy**. *Carbohydr Res.* 2004, **339**:813-818.
- 130. Kocherbitov V, Ulvenlund S, Kober M, Jarring K, Arnebrant T: **Hydration of** microcrystalline cellulose and milled cellulose studied by sorption calorimetry. *J Phys Chem B*. 2008, **112**:3728-3734.
- 131. Watanabe A, Morita S, Ozaki Y: A study on water adsorption onto microcrystalline cellulose by near-infrared spectroscopy with two-dimensional correlation spectroscopy and principal component analysis. *Appl Spectrosc.* 2006, **60**:1054-1061.
- Weise U, Maloney T, Paulapuro H: **Quantification of water in different states of interaction with wood pulp fibres**. *Cellulose*. 1996, **3**:189-202.
- 133. Park S, Venditti RA, Jameel H, Pawlak JJ: Changes in pore size distribution during the drying of cellulose fibers as measured by differential scanning calorimetry. *Carbohyd Polym.* 2006, **66**:97-103.
- 134. Grignon J, Scallan AM: **Effect of pH and neutral salts upon the swelling of cellulose gels**. *J Appl Polym Sci*. 1980, **25**:2829-2843.
- 135. Carlsson G, Kolseth P, Lindstrom T: **Poly-electrolyte swelling behavior of chlorite delignfied sprice wood fibers.** *Wood Sci Technol.* 1983, **17**:69-73.
- 136. Stone JE, A. M. Scallan: The effect of component removal upon porous structure of cell wall of wood: Swelling in water and fiber saturation point. *Tappi*. 1967, **50**.
- 137. Scallan AM, Carles JE: Correlation of water retention value with fiber saturation point. Sven Papperstidn. 1972, 75:699-&.

- 138. Andreasson B, Forsstrom J, Wagberg L: **The porous structure of pulp fibres with different yields and its influence on paper strength**. *Cellulose*. 2003, **10**:111-123.
- 139. Williams D, Hodge D: Impacts of delignification and hot water pretreatment on the water induced cell wall swelling behavior of grasses and its relation to cellulolytic enzyme hydrolysis and binding. *Cellulose*. 2014, **21**:221-235.
- 140. Luo XL, Zhu JY, Gleisner R, Zhan HY: **Effects of wet-pressing-induced fiber hornification on enzymatic saccharification of lignocelluloses**. *Cellulose*. 2011, **18**:1055-1062.
- 141. Luo X, Zhu JY: **Effects of drying-induced fiber hornification on enzymatic saccharification of lignocelluloses**. *Enzyme Microb Tech*. 2011, **48**:92-99.
- 142. Weiss ND, Thygesen LG, Felby C, Roslander C, Gourlay K: **Biomass-water** interactions correlate to recalcitrance and are intensified by pretreatment: An investigation of water constraint and retention in pretreated spruce using low field NMR and water retention value techniques. *Biotechnol Progr.* 2-17, **33**:146-153.
- 143. Selig MJ, Thygesen LG, Felby C: Correlating the ability of lignocellulosic polymers to constrain water with the potential to inhibit cellulose saccharification. *Biotechnol Biofuels*. 2014, 7:10.
- 144. Selig MJ, Hsieh C-WC, Thygesen LG, Himmel ME, Felby C, Decker SR: Considering water availability and the effect of solute concentration on high solids saccharification of lignocellulosic biomass. *Biotechnol Progr.* 2012, **28**:1478-1490.
- 145. Tsuchida J, Rezende C, Oliveira-Silva R, Lima M, D'Eurydice M, Polikarpov I, Bonagamba T: **1H NMR Investigation of water accessibility in cellulose of pretreated sugarcane bagasse**. *Biotechnol Biofuels*. 2014, **7**:127.
- 146. Stone JE, E. Treiber, B. Abrahamson: **Accessibility of regenerated cellulose to solute molecules**. *Tappi*. 1969, **52**:108-110.
- 147. Stone JE, A. M. Scallan: A structural model for the cell wall of water swollen wood pulp fibres based on their accessibility to macromolecules. *Cell Chem Technol*.1968, 2:343-358.
- 148. Beecher JF, Hunt CG, Zhu JY: **Tools for the characterization of biomass at the nanometer scale**. In: *The Nanoscience and Technology of Renewable Biomaterials*. John Wiley & Sons, Ltd; 2009: 61-90.
- 149. Junior CS, Milagres AMF, Ferraz A, Carvalho W: **The effects of lignin removal and drying on the porosity and enzymatic hydrolysis of sugarcane bagasse**. *Cellulose*. 2013, **20**:3165-3177.

- 150. Wang QQ, He Z, Zhu Z, Zhang YH, Ni Y, Luo XL, Zhu JY: Evaluations of cellulose accessibilities of lignocelluloses by solute exclusion and protein adsorption techniques. *Biotechnol Bioeng.* 2012, **109**:381-389.
- Hui L, Liu Z, Ni Y: Characterization of high-yield pulp (HYP) by the solute exclusion technique. *Bioresource Technol.* 2009, **100**:6630-6634.
- 152. Ishizawa CI, Davis MF, Schell DF, Johnson DK: **Porosity and its effect on the digestibility of dilute sulfuric acid pretreated corn stover**. *J Agr Food Chem.* 2007, **55**:2575-2581.
- 153. Fan L, Lee YH, Beardmore DH: Mechanism of the enzymatic hydrolysis of cellulose: effects of major structural features of cellulose on enzymatic hydrolysis. *Biotechnol Bioeng.* 1980, 22:177-199.
- 154. Sasaki T, Tanaka T, Nanbu N, Sato Y, Kainuma K: Correlation between X-ray diffraction measurements of cellulose crystalline structure and the susceptibility to microbial cellulase. *Biotechnol Bioeng.* 1979, 21:1031-1042.
- 155. Zhang YHP, Lynd LR: **Toward an aggregated understanding of enzymatic hydrolysis of cellulose: noncomplexed cellulase systems**. *Biotechnol Bioeng*. 2004, **88**:797-824.
- 156. Yu Z, Jameel H, Chang H-m, Park S: **The effect of delignification of forest biomass on enzymatic hydrolysis**. *Bioresource Technol*. 2011, **102**:9083-9089.
- 157. Takahashi J, Rudsander UJ, Hedenström M, Banasiak A, Harholt J, Amelot N, Immerzeel P, Ryden P, Endo S, Ibatullin FM *et al*: **KORRIGAN1** and its Aspen homolog **PttCel9A1** decrease cellulose crystallinity in Arabidopsis stems. *Plant Cell Physiol*. 2009, **50**:1099-1115.
- 158. Liu JL, Kim JI, Cusumano JC, Chapple C, Venugopalan N, Fischetti RF, Makowski L: The impact of alterations in lignin deposition on cellulose organization of the plant cell wall. *Biotechnol Biofuels*. 2016, 9.
- 159. Derba-Maceluch M, Awano T, Takahashi J, Lucenius J, Ratke C, Kontro I, Busse-Wicher M, Kosik O, Tanaka R, Winzell A *et al*: **Suppression of xylan endotransglycosylase PtxtXyn10A affects cellulose microfibril angle in secondary wall in aspen wood**. *New Phytol*. 2015, **205**:666-681.
- 160. Tetard L, Passian A, Farahi RH, Kalluri UC, Davison BH, Thundat T: **Spectroscopy and atomic force microscopy of biomass**. *Ultramicroscopy*. 2010, **110**:701-707.
- 161. Bischel M, Vanlandingham M, Eduljee R, Gillespie J, Schultz J: **On the use of nanoscale indentation with the AFM in the identification of phases in blends of linear low density polyethylene and high density polyethylene**. *J Mater Sci.* 2000, **35**:221-228.

- 162. Zhang M, Chen G, Kumar R, Xu B: Mapping out the structural changes of natural and pretreated plant cell wall surfaces by atomic force microscopy single molecular recognition imaging. *Biotechnol Biofuels*. 2013, 6:147.
- 163. Eaton P, West P: **Atomic force microscopy**: Oxford University Press; 2010.
- 164. O'brien T, Feder N, McCully ME: **Polychromatic staining of plant cell walls by toluidine blue O**. *Protoplasma*. 1964, **59**:368-373.
- 165. Hahn MG: Immunological approaches to cell wall/biomass characterization. 2010.
- 166. Hutzler P, Fischbach R, Heller W, Jungblut TP, Reuber S, Schmitz R, Veit M, Weissenböck G, Schnitzler J-P: **Tissue localization of phenolic compounds in plants by confocal laser scanning microscopy**. *J Exp Bot*. 1998, **49**:953-965.
- 167. Lee KJ, Marcus SE, Knox JP: **Cell wall biology: perspectives from cell wall imaging**. *Mol Plant*. 2011, **4**:212-219.
- 168. Donaldson L: **Softwood and hardwood lignin fluorescence spectra of wood cell walls in different mounting media**. *IAWA Journal*. 2013, **34**:3-19.
- 169. Tobimatsu Y, Wagner A, Donaldson L, Mitra P, Niculaes C, Dima O, Kim JI, Anderson N, Loque D, Boerjan W *et al*: **Visualization of plant cell wall lignification using fluorescence-tagged monolignols**. *Plant J*. 2013, **76**:357-366.
- 170. Li S, Bashline L, Zheng Y, Xin X, Huang S, Kong Z, Kim SH, Cosgrove DJ, Gu Y: Cellulose synthase complexes act in a concerted fashion to synthesize highly aggregated cellulose in secondary cell walls of plants. *P Natl Acad Sci USA*. 2016, 113:11348-11353.
- 171. Watanabe Y, Meents M, McDonnell L, Barkwill S, Sampathkumar A, Cartwright H, Demura T, Ehrhardt D, Samuels A, Mansfield S: **Visualization of cellulose synthases in Arabidopsis secondary cell walls**. *Science*. 2015, **350**:198-203.
- 172. DeMartini JD, Pattathil S, Avci U, Szekalski K, Mazumder K, Hahn MG, Wyman CE: **Application of monoclonal antibodies to investigate plant cell wall deconstruction for biofuels production**. *Energ Environ Sci.* 2011, **4**:4332-4339.
- 173. Pattathil S, Avci U, Baldwin D, Swennes AG, McGill JA, Popper Z, Bootten T, Albert A, Davis RH, Chennareddy C *et al*: A comprehensive toolkit of plant cell wall glycandirected monoclonal antibodies. *Plant Physiol.* 2010, **153**:514-525.
- 174. Shen H, Poovaiah CR, Ziebell A, Tschaplinski TJ, Pattathil S, Gjersing E, Engle NL, Katahira R, Pu Y, Sykes R *et al*: **Enhanced characteristics of genetically modified switchgrass (Panicum virgatum L.) for high biofuel production**. *Biotechnol Biofuels*. 2013, **6**:71.

- 175. Pattathil S, Hahn MG, Dale BE, Chundawat SPS: **Insights into plant cell wall structure**, **architecture**, **and integrity using glycome profiling of native and AFEXTM-pre-treated biomass**. *J Exp Bot*. 2015, **66**:4279-4294.
- 176. Li M, Pattathil S, Hahn MG, Hodge DB: **Identification of features associated with** plant cell wall recalcitrance to pretreatment by alkaline hydrogen peroxide in diverse bioenergy feedstocks using glycome profiling. *RSC Adv.* 2014, 4:17282-17292.
- 177. Pattathil S, Avci U, Miller JS, Hahn MG: **Immunological approaches to plant cell wall and biomass characterization: glycome profiling**. In: *Biomass Conversion*. Springer; 2012: 61-72.

Chapter 2: Identification of development stage and anatomical fraction contributions to cell wall recalcitrance in switchgrass

This work has been published as original research in July 2017, in Biotechnology for Biofuels, Volume 10, Issue 1, Page 184.

Introduction

Development of renewable sources of fuels and chemicals is necessary to improve energy security and mitigate climate change effects resulting from greenhouse gas emissions [1, 2]. Lignocellulosic biomass, which includes dedicated bioenergy crops and agricultural residues, is a widely available and largely untapped source of reduced carbon in the production of renewable fuels and chemicals [3]. A current major challenge in deconstructing plant cell walls are plant-evolved mechanisms for resisting microbial and animal degradation of plant cell walls, termed biomass recalcitrance [4]. Within a feedstock, abundance and density of cell type, structure and substitution of cell wall polymers, and organization of polymers within the cell wall can all contribute to biomass recalcitrance [4].

Plant cell walls account for the majority of lignocellulosic feedstock dry mass, and are comprised of primary and in some cases secondary cell walls depending upon the tissue type. Primary cell walls are found in growing cells, and contain cellulose microfibrils, pectins, and hemicellulose polysaccharides. Secondary cell walls are significantly thicker than primary cell walls, provide mechanical strength and structural reinforcement to the cells, and are found predominantly in fiber and vascular cells post cell enlargement [5], and represent the majority of the mass of lignocellulosic feedstocks. Secondary cell walls contain cellulose microfibils, hemicelluloses, and lignin, an aromatic heteropolymer comprised of phenylpropanoid subunits.

In monocot grasses, the primary hemicellulose components are glucuronoarabinoxylans ("xylans") containing arabinosyl, acetyl, and uronosyl substitutions on a β-1,4 linked xylan backbone [6]. The arabinofuranosyl residues in grass xylans can also be covalently linked via ferulic acid ester crosslinks to lignin or other xylans, and this phenomenon has been hypothesized to play an important role in promoting cell wall rigidity and decelerating expansion [7]. Mixed-linkage glucan and xyloglucans are also present as minor hemicellulose components in cell walls, and may account for a minor fraction of non-cellulosic glucan found in mature tissues [6, 8]. Lignin content and composition is often cited as one of the predominant contributors of cell wall recalcitrance [9], however there also exists a body of literature that has examined the role of hemicelluloses [10], structural pectins [11], and polymer interactions within the cell wall as other significant contributors to cell wall recalcitrance [12].

Switchgrass (*Panicum virgatum* L.) is a well-studied C₄ perennial grass envisioned as a promising herbaceous feedstock to supply North American cellulosic biorefineries along with other monocot grasses such as miscanthus (*Miscanthus x giganteus*), and corn stover (*Zea mays*) [13, 14]. Switchgrass is an attractive feedstock due to high production yields, low energy and nutrient inputs, wide adaptability, and short growing time [15]. Switchgrass grows as a clonal modular organism, with the tiller forming the main clonal module and phytomers consisting of multiple shoot meristems. Shoots are comprised of leaf blades, sheath leaves, stem nodes and internodes, auxiliary buds, and ligules [16]. Grasses such as switchgrass grow through elongation of stem internodes, each of which is linked at the base node to a single leaf sheath and blade.

Analysis of individual internodes, as opposed to bulk plant material, is useful as internodes represent sequential stages of maturity during plant development, affecting cell wall composition and abundance of cell type within biomass [17]. Basal internodes tend to have greater lignin and

cellulose content coupled with lower digestibility compared to internodes near the top of a single tiller [18]. Tissue maturity in relation to harvest times may impact switchgrass digestibility [19], including time left on field post maturation [20]. In addition, there are significant differences in compositions of stem, sheath, and leaf anatomical fractions, with the stem generally containing more lignin and being less digestible compared to the leaf [21, 22]. The distribution, structure, and extractability of non-cellulosic cell wall glycans in miscanthus stem and leaf organs sampled at distinct maturities indicated that hemicellulose structure and extractability varied with tissue maturity, and may account for significant non-lignin contributions to recalcitrance [23].

Within-plant heterogeneity for graminaceous feedstocks such as switchgrass has important impacts on several important processing variables for a biorefining process. Ranges of particle size distribution, composition, hygroscopicity and drainability, chemical pretreatment effectiveness, and extent of enzymatic hydrolysis can all result from differing responses of biomass to comminution. Physical fractionation, employed either on-field during harvest or at the biorefinery, is one potential route to addressing feedstock challenges to potentially improve agronomic, logistics, and processing-conversion outcomes. Limited work has been published on biomass fractionation in the context of pretreatment and hydrolysis. In one study, disc refining followed by air classification of corn stover yielded pith and depithed stover fractions that were subjected to dilute acid pretreatment or mild base pretreatment, quantifying mass losses and sugar release response during acid treatment [24]. Other work identified significant differences in enzymatic hydrolysis response of corn stover stems compared to other fractions [25-27].

Studies investigating tissue-specific responses have been assessed for liquid hot water pretreatment of corn stover [28] and wheat straw [29], although the only industrially-relevant fractionation approach that have been studied are alteration of leaf-stem ratio in wheat straw

[30]. With AFEX pretreatment, the impact of knife-milling and sieving of corn stover [31] as well manual separation of stem, sheath, leaf, and cob have been assessed [32], and found to yield fractions with differing compositions and responses to deconstruction.

The objective of this study is to characterize within-plant heterogeneity by identifying key compositional differences between switchgrass anatomical fractions at different internode maturities and relating compositional differences to enzymatic digestibility response following mild alkaline pretreatment. Structural differences are evaluated by localization of phenolics within tissue cross-sections before and after alkaline pretreatment using confocal microscopy, while hemicellulose and pectin structure and extractability are evaluated using glycome profiling following chemical extraction.

Materials and methods

Field conditions and biomass preparation

Switchgrass (var. "Forestburg", upland ecotype) was manually harvested post-anthesis above either the 5th or 6th internode Figure 2.1 from a field at Michigan State University (East Lansing, MI; 42°42'48.80" N by 84°28'1.41"W) between 17-19 September, 2014. During harvest, intact harvested tillers were dried indoors at room temperature. After harvest was completed all tillers were dried overnight in a 45°C oven. Internodes were then manually separated into leaves, leaf sheaths, and stems, while the nodes and panicle were discarded **Figure 2.1.** Whole fractions were air dried to a moisture content of ~5% (g H₂O/g total), and particle size was reduced using a Wiley Mini-Mill (Thomas Scientific, Swedesboro, NJ) to pass a 30-mesh screen. Samples were stored in dry, airtight bags until further use.

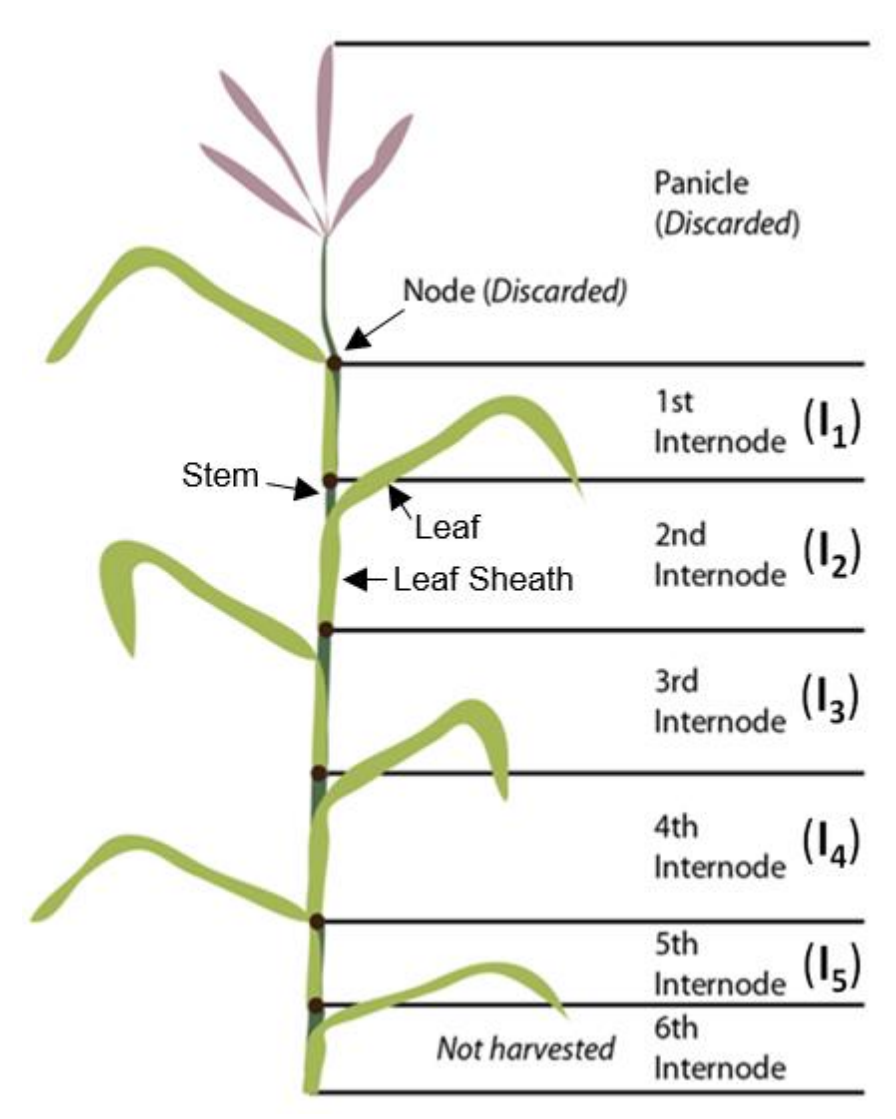


Figure 2.1 : Schematic of switchgrass tillers used for this study. Tillers were harvested above either the 5^{th} or 6^{th} internode, and then separated into internodes, discarding the nodes and panicle. Internodes were further manually subdivided into leaves, leaf sheaths, and stems. Notes: diagram is representative and not to scale.

Pretreatment conditions

Alkaline pretreatment was performed in 8 mL borosilicate glass tubes (Thermo Fisher Scientific, Waltham, MA) with rubber lined caps. Alkali loading was performed at a 10% (g NaOH/g dry biomass) loading at 10% (g biomass/g solution) loading, giving a 0.25 M NaOH concentration. Samples were vortexed and immersed in an 80°C water bath for 1 hr, with mixing every 15 min. After the elapsed pretreatment time, solids were separated from the alkaline liquor

and washed with de-ionized water until pH neutral. Following washing, samples were rinsed with absolute ethanol and allowed to air dry at 45°C to a moisture content <5%, with mass loss following pretreatment determined gravimetrically.

Composition analysis

Extractives-free cell wall material (*i.e.*, alcohol insoluble residue or "AIR") was isolated following extraction and de-starching according to Foster et al. [33]. All composition procedures were performed on de-starched AIR, except for the determination of extractable sugars. Minor polysaccharide content (rhamnan, mannan, galactan, fucan, non-cellulosic glucan) was determined using the alditol acetate method with minor changes [33]. Cell wall acetate, glucan, xylan, arabinan, and Klason lignin content were determined for AIR using the NREL/TP 510-42618 protocol [34] with minor modifications [35]. Thioacidolysis was used to determine lignin monolignol yields [36]. Extractable free glucose, sucrose, and starch were determined on the original untreated biomass as described by Santoro et al. [37].

Alkaline saponification was used to determine the *p*-hydroxycinnimic acid content, as described previously [38], with modifications to the quantification method. Briefly, 0.5 g of biomass was treated with 25 mL of 3 M NaOH in a sealed pressure tube at 121°C for 1 hr to release esterified *p*-coumarate (*p*CA) and esterified or etherified ferulate (FA). Liquid samples were centrifuged at 13000 x g for 3 min. Next, 1 mL of alkaline liquor was taken, and pH adjusted to pH 1.5 using concentrated H₂SO₄ (Sigma-Aldrich Corp., St. Louis, MO). Samples were centrifuged at 13000 x g for 3 min to remove any precipitated solids, and subsequently analyzed by HPLC (Agilent 1100 Series) with an Aminex HPX-87H column (Bio-Rad, Hercules, CA, USA) using a mobile phase of 5 mM H₂SO₄ with a 10% (v/v) ACN organic modifier. Quantification was performed using a diode-array detector with a UV wavelength of 210 nm.

Standards containing FA and pCA ranged from 0.05 mg/mL to 1 mg/mL. To account for precipitation of pCA and FA with pH adjustment, solubility with respect to pH curves were determined, with R^2 linear coefficients of 0.999 for both FA and pCA observed from the range of pH 1.4 - 1.8. Samples were analyzed in biological triplicate for reproducibility.

Enzymatic hydrolysis

Enzymatic hydrolysis was performed at 2.5% solids loading (g AIR biomass/g solution) in 1.5 mL microcentrifuge tubes (Posi-Click, Denville Scientific, Holliston, MA). Enzymatic hydrolysis was performed using 10 mg protein/g glucan for pretreated biomass and 30 mg protein/g glucan for untreated, de-starched, extractives-free biomass using CTec3 and HTec3 (Novozymes A/S Bagsværd, Denmark), at a CTec3:HTec3 ratio of 2:1. A buffer solution of 50 mM citric acid (pH 5.20) was used to maintain pH, and samples were incubated at 50°C with orbital mixing at 180 rpm for either 6 hr or 48 hr. Samples were centrifuged at 13000 x g for 3 min post-incubation and filtered using 22 μm mixed cellulose-ester filters (EMD Millipore, Billerica, MA). Glucose and xylose were quantified by HPLC (Agilent 1100 Series) with an Aminex HPX-87H column (Bio-Rad, Hercules, CA, USA) with a mobile phase of 5 mM H₂SO₄. Glucose yield was determined based on quantified glucose released compared to total AIR cell wall glucan available (as glucose), including non-cellulosic glucan.

Confocal microscopy

Air dried whole samples were sectioned by hand using a platinum tipped razor blade and prepared for imaging by washing with 50 mL of de-ionized water prior to immersing in water buffered at a pH of 7.0 by 20 mM Na₂PO₄ overnight. Pretreated samples were generated by NaOH pretreatment at 0.10 g NaOH/g biomass of whole cross-sections, followed by washing with de-ionized water until pH neutral, and immersion in water buffered at a pH of 7.0 by 20

mM Na₂PO₄ overnight. Confocal fluorescent images were collected on an Olympus FluoView FV1000 Confocal Laser Scanning Microscope (Olympus America, Inc., Center Valley, PA), configured on a fully automated Olympus IX81 inverted microscope. Images were recorded with a 10x UPlanFLN objective (NA 0.30). Blue and red autofluorescence signals were sequentially recorded, as shown **Figure 2.10**in Appendix A. Blue autofluorescence was excited using a 405 nm diode laser and emission was recorded using a 430-470 nm band pass emission filter. The red autofluorescence was excited using a 543 nm helium neon laser and emission was recorded using a 560 nm long pass emission filter. A series of confocal images (XYZ) were recorded through the thickness of each sample (approximately 50 μm). Images were collected in 10 μm intervals when using the 10x objective. Each confocal series was then compressed into a maximum intensity projection image and recorded in a TIF format. The color look-up table (LUT) for all images was modified with the blue display rescaled from 0-4095 to 350-800 and the red display rescaled from 0-4095 to 0-1200 to brighten images. All further processing was performed in ImageJ (http://imagej.nih.gov/ij/).

Glycome profiling

Sequential cell wall extractions and glycome profiling of switchgrass anatomical fractions were carried out as described previously [39, 40] on AIR biomass. Plant glycan-directed mAbs were from laboratory stocks (CCRC,JIM, and MAC series) available at the Complex Carbohydrate Research Center [41]. A complete description of the mABs used in this study can be found in our prior work [42].

Results

Switchgrass anatomical fractions sampled at different internodes throughout the plant representing differing levels of maturity were utilized in this work to develop an improved understanding of the impacts of within-plant heterogeneity in switchgrass on a potential

cellulosic biofuels conversion process. Switchgrass samples were characterized with respect to composition and assessed for response to pretreatment and enzymatic hydrolysis with the goals of (1) identifying cell wall properties contributing to observed differences in cell wall recalcitrance, (2) understanding how differences in composition and recalcitrance are distributed throughout the plant, and (3) potentially use this understanding to inform both plant breeding and harvesting strategies to optimally couple the plant feedstock to a conversion process.

Anatomical fraction- and internode-specific recalcitrance

Enzymatic hydrolysis before or after mild NaOH pretreatment was performed on extractives-free (AIR), de-starched cell wall material from three switchgrass anatomical fractions (leaves, leaf sheath, stem) as a function of internode (**Figure 2.2**).

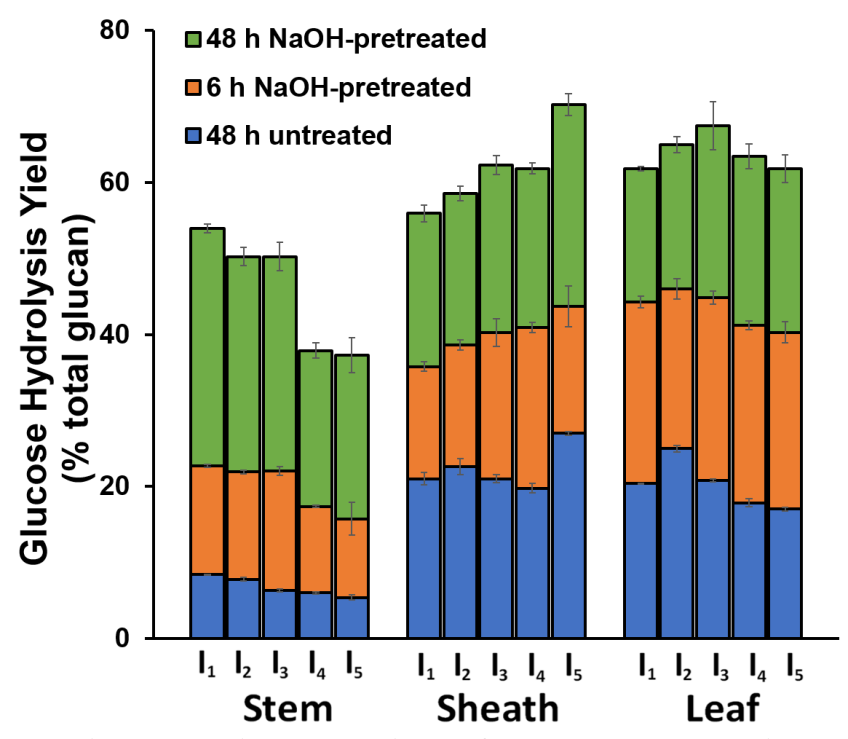


Figure 2.2 : Enzymatic hydrolysis glucose yields of untreated and alkaline pretreatment of anatomical fractions. Enzymatic hydrolysis of untreated biomass was performed on AIR + destarched biomass, while alkaline pretreatment was performed using 10% w/w NaOH loading at 80°C for 1 hr. Glucose hydrolysis yields are presented as the percent of total cell wall glucan released as monomeric glucose. Enzyme loading was 30 mg protein/g glucan for untreated fractions and 10 mg protein/g glucan for alkaline pretreated fractions with a ratio of 2:1 CTec3 to HTec3. Replicates (n = 3) are displayed as averages with standard deviations.

From the results in **Figure 2.2**, lower glucose yields for both untreated and NaOH-pretreated cases of stem internodes indicate that stem fractions are significantly more recalcitrant compared to leaf sheath (referred to as sheath) and leaf internodes. Previous work using liquid hot water pretreatment of switchgrass also found that pretreated leaves were more digestible than stem internodes [43]. Also of note, the mass of above-ground biomass in switchgrass is known to be primarily leaves, with stems and leaf sheaths each comprising on the order of half the mass of the leaves [43]. Stem internodes also demonstrated a clear decrease in enzymatic hydrolysis yields with increasing tissue maturity (*i.e.*, from I₁ to I₅) for both the untreated and NaOH-pretreated cases [44], although similar trends were not as clearly observed in the untreated yields of leaf sheath and leaf internodes and indicate cell wall recalcitrance increases with maturity in stem only.

NaOH-pretreated leaf sheaths again showed significantly different trends compared to stem, with a trend of increasing hydrolysis yields with increasing internode in both the 6-hr and 48-hr hydrolysis yield cases. Leaf hydrolysis yields became similar between internodes in the 48-hr yields for the NaOH-pretreated case, contrasting the general trend of decreasing yields with increasing internode seen in the untreated and 6-hr hydrolysis yield for the NaOH-pretreated cases. From these observations, the application of alkaline pretreatment resulted in a change in recalcitrance between internodes in both leaf sheath and leaf fractions, although differences in the 6-hr and 48-hr hydrolysis yield trends in leaf internodes suggest pretreatment also influenced hydrolysis rate as well. The contributions of composition and cell wall biopolymer structure to these differences in recalcitrance are described in the subsequent sections.

Cell wall composition

The content of major cell wall biopolymers (cellulose, xylan, lignin), minor hemicelluloses (non-cellulosic glucan) and minor hemicellulose sugars (Rha, Ara, Man, Gal, Fuc), alkali-labile hydroxycinnamic acids (*p*-coumarate, ferulate), and lignin composition (syringyl and guaiacyl monomer yields by thioacidolysis) were quantified for stem, sheath, and leaf internodes. Key results that highlight observed trends found are presented in **Figure 2.3**, while the complete data set can be found in **Table 2.1** in Appendix A.

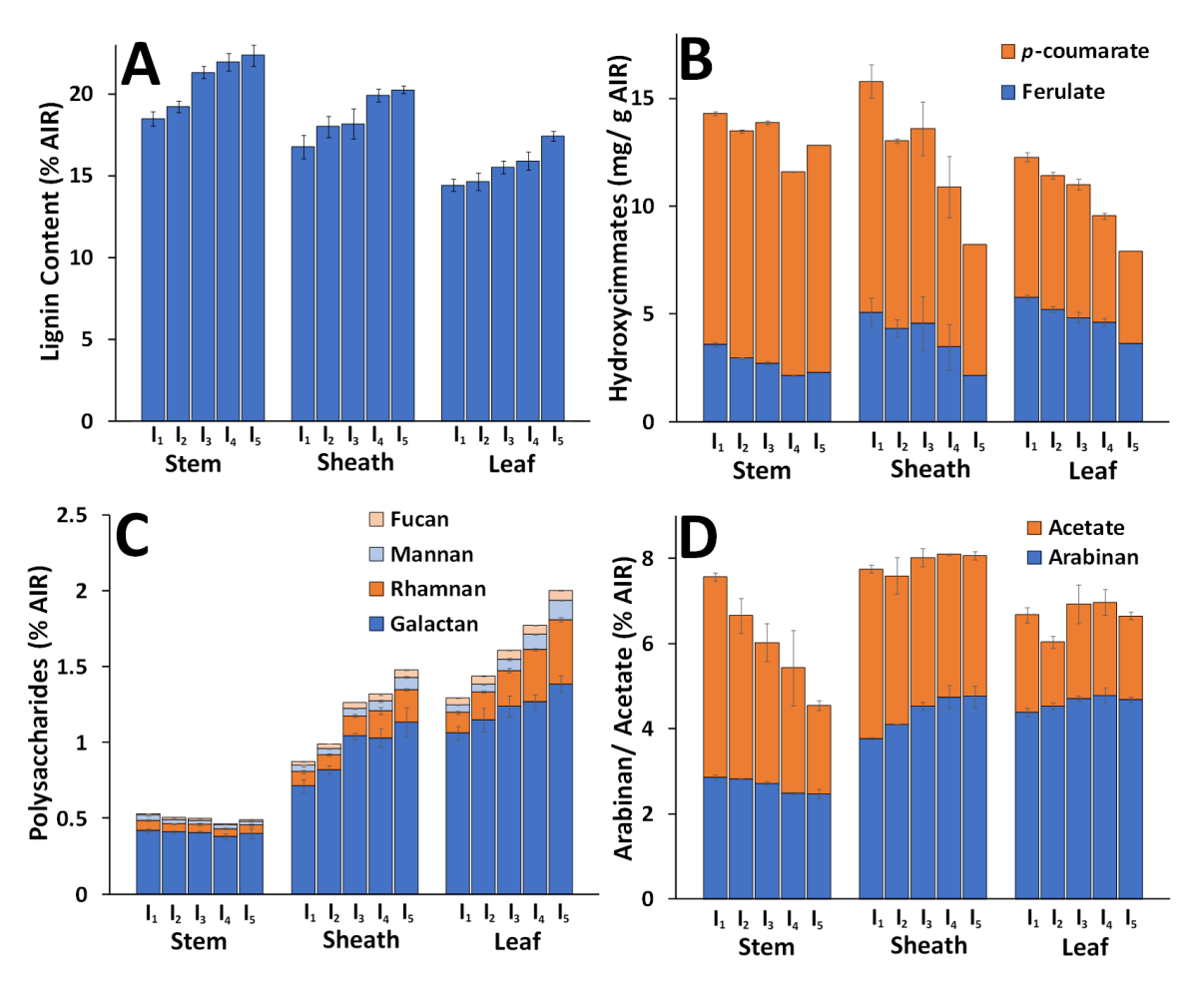


Figure 2.3 : Compositional highlights of (A) lignin (B) hydroxycinnamates (C) minor polysaccharides, and (D) acetate and arabinan in switchgrass fractions with respect to internode. Internodes I_1 - I_5 are displayed in ascending order from left to right for each switchgrass anatomical fraction. All composition values were quantified on an extractives free basis (AIR).

The Klason lignin content demonstrated a clear increase with respect to internode for stem, sheath, and leaf (**Figure 2.3A**), with results presumably corresponding to increasing maturation and development of secondary cell wall tissues following cell elongation and differentiation in older fractions. Overall, stem lignin content was higher compared to sheath and leaf, which is expected due to the abundance of sclerenchyma and xylem cells providing structural support for both upright growth and normal vascular transport [5]. It should be noted that ash was not quantified independently in this study, and may represent a portion of the quantified lignin [45]. However, ash content has been shown to be higher in abundance in leaf fractions when compared to stem and sheath fractions [43], likely limiting ash impact on trends observed in this study.

Alkali-labile hydroxycinnamic acids also varied significantly with internode, with both pCA and FA content decreasing between internodes I_1 - I_5 for all switchgrass anatomical fractions (**Figure 2.3B**). Decreases in pCA content with increasing internode maturity ranged from a 19% decrease from I_1 to I_5 in stem samples, to 53% and 45% in sheath and leaf samples, respectively. FA content also demonstrated the same trend between internodes I_1 - I_5 with decreases of 47%, 65%, and 48% for stem, sheath, and leaf, respectively. Combined with the trend for lignin content (**Figure 2.3A**), the inverse relationship between FA content and lignin content suggest that crosslinking of cell wall biopolymers via ferulates is an important feature of cell wall organization in tissues with less secondary cell wall lignification [18]. Prior work has concluded that total FA content decreases with increasing maturity (based on harvest date) concurrent with increasing lignin content in switchgrass [45], and is in agreement with the results of the present work in which maturity is based on internode rather than harvest date.

Composition analysis of polysaccharide content revealed a similar content of xylan between internodes (average content of 24.4% for stem and sheath and 19.8% for leaf), while galactan, mannan, rhamnan, and fucan, representing minor hemicellulose and structural pectin polysaccharides were higher in sheath and leaf fractions compared to stem and showed clear trends of increased abundance with tissue maturity in sheath and leaf internodes (**Figure 2.3C**). Functionally, this indicates in maturing stem internodes, pectic and minor hemicellulosic polysaccharides represent a smaller fraction of total cell wall polysaccharides, and the decreases in total compositional fraction suggest minimal continued synthesis of these polysaccharides during tissue maturation. Conversely, increased overall composition content in more mature sheath and leaf internodes suggest continued synthesis and accumulation of minor polysaccharides during maturation. The exception to this trend, non-cellulosic glucan, showed an increase with respect to internode in all three anatomical fractions as well as similar overall content of non-cellulosic glucan (2.5% overall for all samples), indicating increases in either β-glucan or xyloglucan content with internode maturation (**Table 2.1** in Appendix A).

Stem arabinan content, indicative of glucuronoarabinoxylan (GAX), arabinogalactan (AG), and rhamnogalacturonan I (RG I) pectin side chains decreased slightly in stem internodes, while increasing only in leaf sheaths (**Figure 2.3D**). Given the small decrease in overall xylan content between internodes, it can be hypothesized that increases in arabinan content correspond to an increase in GAX or RG I side chain abundance in leaf sheath cell walls [23]. Many cell wall polysaccharides are known to be O-acetylated, including pectins, xyloglucans, and xylans. Cell wall acetyl content (**Figure 2.3D**) decreased significantly with stem internode maturity, with only minor decreases observed with respect to sheath and leaf internode maturity, indicating

similarity in acetylated cell wall components between sheath and leaf internodes compared to stem.

Non-cellulosic glucose and extractable sugar content

The accumulation of soluble sugars in the stems of grasses is of paramount importance to agriculturally important crops such as sugarcane (*Saccharum* spp.) and sweet sorghum (*Sorghum bicolor*). Soluble sugar abundance in other grasses used as feedstocks for cellulosic biofuels can be a significant fraction of total dry weight [50], with both genetic and environmental drivers responsible for starch and extractable sugar accumulation [46]. For example, soluble sugar synthesis in plants has been shown to be environment responsive, with significant accumulation of soluble sugars accompanying reduced structural carbohydrate and lignin content in switchgrass harvests subjected to drought conditions [47].

Notably these sugars are often overlooked in many biomass-to-fuels studies or analyses and can present both processing and analytical challenges. Soluble sugars may mask structural polysaccharides in cell walls [48] resulting in false positives for carbohydrate content in screening techniques relating feedstock digestibility to biomass physical characteristics or high throughput digestibility studies that do not remove soluble sugars and starches before analysis [49]. As a processing challenge, contents of extractable sugars and starch can be degraded during many pretreatments (*e.g.*, dilute acid or AFEX) representing a potentially significant loss of value sugars. Furthermore, sugar degradation products can present additional challenges to the biological conversion of sugars to biofuels or bioproducts. For example, in recent work using AFEX pretreatment on switchgrass subjected to drought environmental stress, imidazoles and pyrazines were formed by the reaction of ammonia with soluble sugars in high enough

concentrations to significantly inhibit fermentation compared to switchgrass harvests not subjected to drought [47].

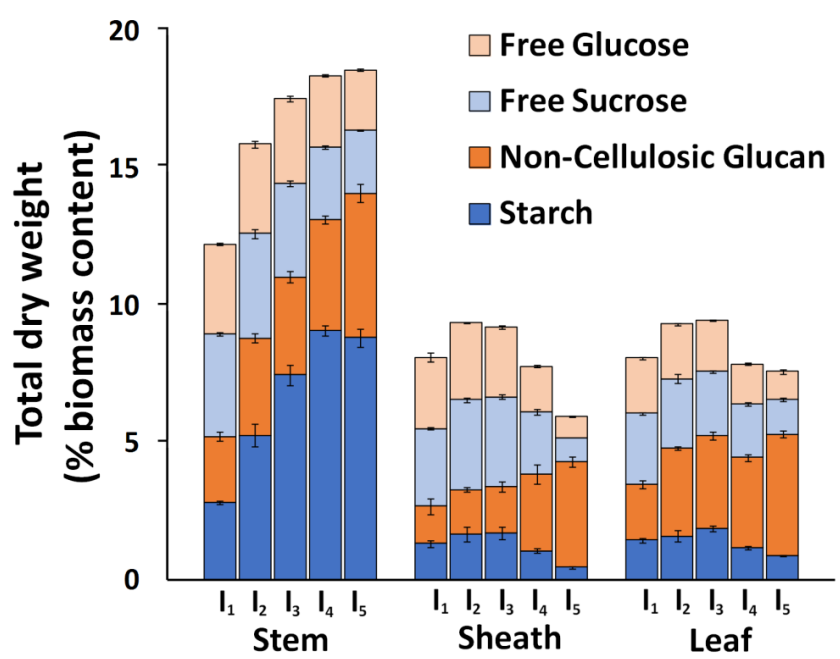


Figure 2.4 : Native switchgrass non-cellulosic sugar composition with respect to internode. Internodes I₁-I₅ are displayed in ascending order from left to right for each switchgrass anatomical fraction. Compositions are represented as a percent of total dry weight. Replicates (n = 3) displayed as average with standard deviations.

In the present work, non-cellulosic glucan (presumably as xyloglucan and β-glucan) and extractable such as sucrose, fructose, free glucose, and starches sugar contents were determined (**Figure 2.4**) and represent a non-trivial fraction of overall feedstock mass. Stem internodes were observed to have significantly more soluble sugars compared to similar sheath and leaf internode contents, with soluble sugars combined with non-cellulosic glucan constituting between 12% to 18% of total dry weight. Starch content was dramatically different in stem internodes, accumulating to up to 8% of total biomass dry weight in internode I₅. Comparatively, sheath and leaf starch content accounted for up to 2% dry weight, and decreased with internode maturity. One likely reason for such a high stem extractible sugar content was due to sample harvesting during grain filling [50].

Non-cellulosic glucan, presumably in the form of xyloglucans, β -glucans, and glucomannans, were observed to accumulate from internode I_1 through I_5 for all three anatomical fractions. Although comprising a small percentage of total biomass, β -glucans are generally more easily digested compared to cellulose, while xyloglucans may be closely associated to cellulose in the primary cell wall [51]. It can also be observed that the differences in the non-cellulosic glucan can be correlated to differences in most of the minor hemicellulose and pectin sugars (*i.e.*, Fuc, Rha, Man, Gal as presented in

Figure 2.3C).

Cell wall autofluorescence

At both the macroscopic and microscopic scales as seen in **Figure 2.5**, switchgrass stem, sheath, and leaf exhibit obvious significant differences in overall morphology, tissue organization, and cell type abundance. Structural (and compositional) heterogeneity across fractions has important implications for biomass recalcitrance. As one example, sclerenchyma secondary cell wall types in stems have significantly thicker cell walls and contain a high ratio of lignified secondary cell walls compared to partially lignified parenchyma type cells [45], resulting in anatomical fractions containing high contents of sclerenchyma cells expecting to have higher recalcitrance compared to parenchyma rich fractions.

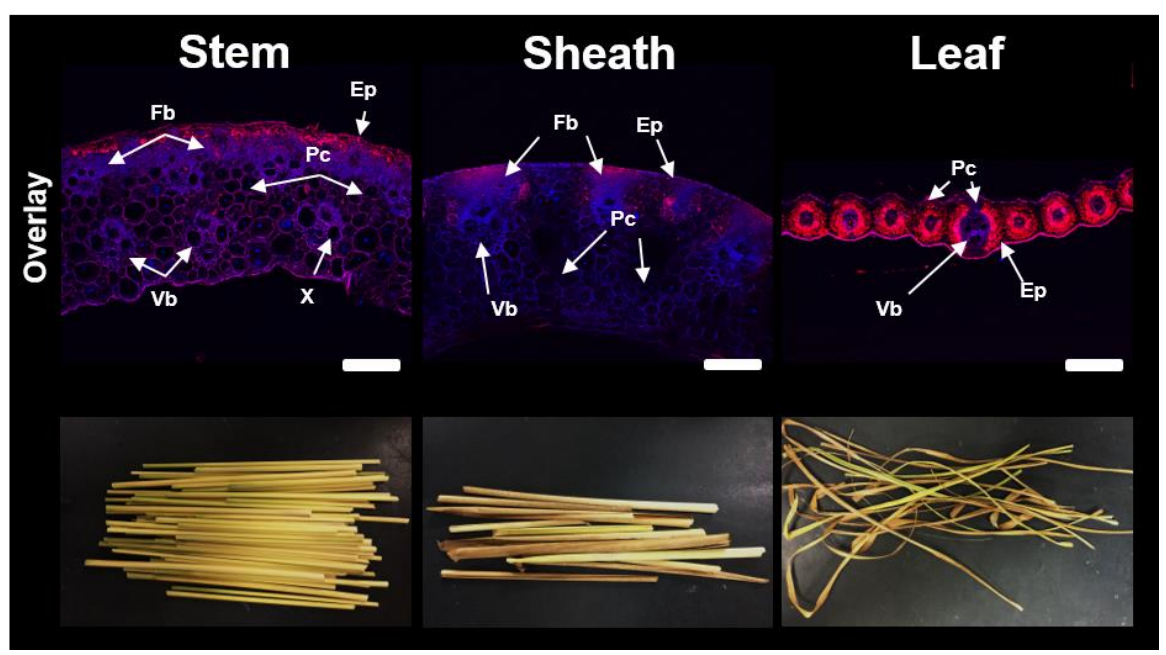


Figure 2.5: Examples of differences in macroscopic morphology, cell wall organization, and aromatic abundance as shown by autofluorescence between switchgrass anatomical fractions from internode I₂. Confocal laser scanning microscopy carried out using laser emission wavelengths of 405nm and 543 nm. Tissue types are denoted from the following notation: Ep – epidermis, Fb – fiber bundles, Vb – vascular bundles, Ph – phloem, X – xylem, Pc – Parenchyma cells. Scale bars represent 200 µm.

Analysis of cell wall phenolics using confocal microscopy often employs combinations of fluorescence tagging, chemical labels, and autofluorescence techniques to characterize the cell wall landscape at the micron-scale resolution [52, 53]. Using phenolic autofluorescence alone, general trends in phenolic localization and abundance can be obtained, however the wide range of emission spectrums of phenolic compounds can limit deconvolution of specific phenolic components [54-56]. With a low-field excitation using a diode laser at 405 nm, hydroxycinnimates have an emission spectrum of around 420 – 460 nm (shown and denoted as blue) along with alkaloids, flavonoids, and other phenyl propanoids [56]. Using a helium neon laser excitation at 543 nm, most phenolics fluoresce with an emission spectrum of 600-650 nm (shown and denoted as red), however hydroxycinnimates do not [55]. One convoluting factor in this technique resides in the autofluorescence of chlorophyll. With an emission spectrum in the

600-700 nm region [56], chlorophyll will certainly provide signal contribution to the red emission spectrum from chlorophyll rich tissues such as epidermal and bundle sheath regions of leaf (**Figure 2.5** and **Figure 2.6**).

Overlay of both autofluorescence channels of whole biomass cross sections revealed several noticeable features of each organ (**Figure 2.5**). Stem and sheath cross-sections displayed similar architecture, with atactostele patterned vascular bundles, distinct regions of fiber bundles, and similar overall thickness [57]. The only notable difference resided in distribution of fiber cells between epidermal located vascular bundles in the sheath cross-section. Both displayed blue and red emission patterns in all tissue types, however signal intensity was much stronger in secondary cell wall abundant regions such as sclerenchyma cell fiber bundles, and vascular bundles. Leaf cross-section architecture was significantly different, with vascular bundles surrounded by a bundle sheath of parenchyma cells, and a highly lignified lower midrib region. Leaf autofluorescence showed a blue emission pattern in the vascular bundles along with some epidermal tissues, while the red emission spectrum was localized to the lower midrib and bundle sheath, and was most likely due to chlorophyll autofluorescence.

The impact of NaOH pretreatment on autofluorescence signature was examined for multiple internodes to gauge both organ and internode response to pretreatment (**Figure 2.6**). In stem and leaf sheath cross-sections, the red emission spectrum was localized to secondary cell wall tissue such as vascular tissue and fiber bundles, while the blue emission spectrum was observed predominantly in parenchyma cells.

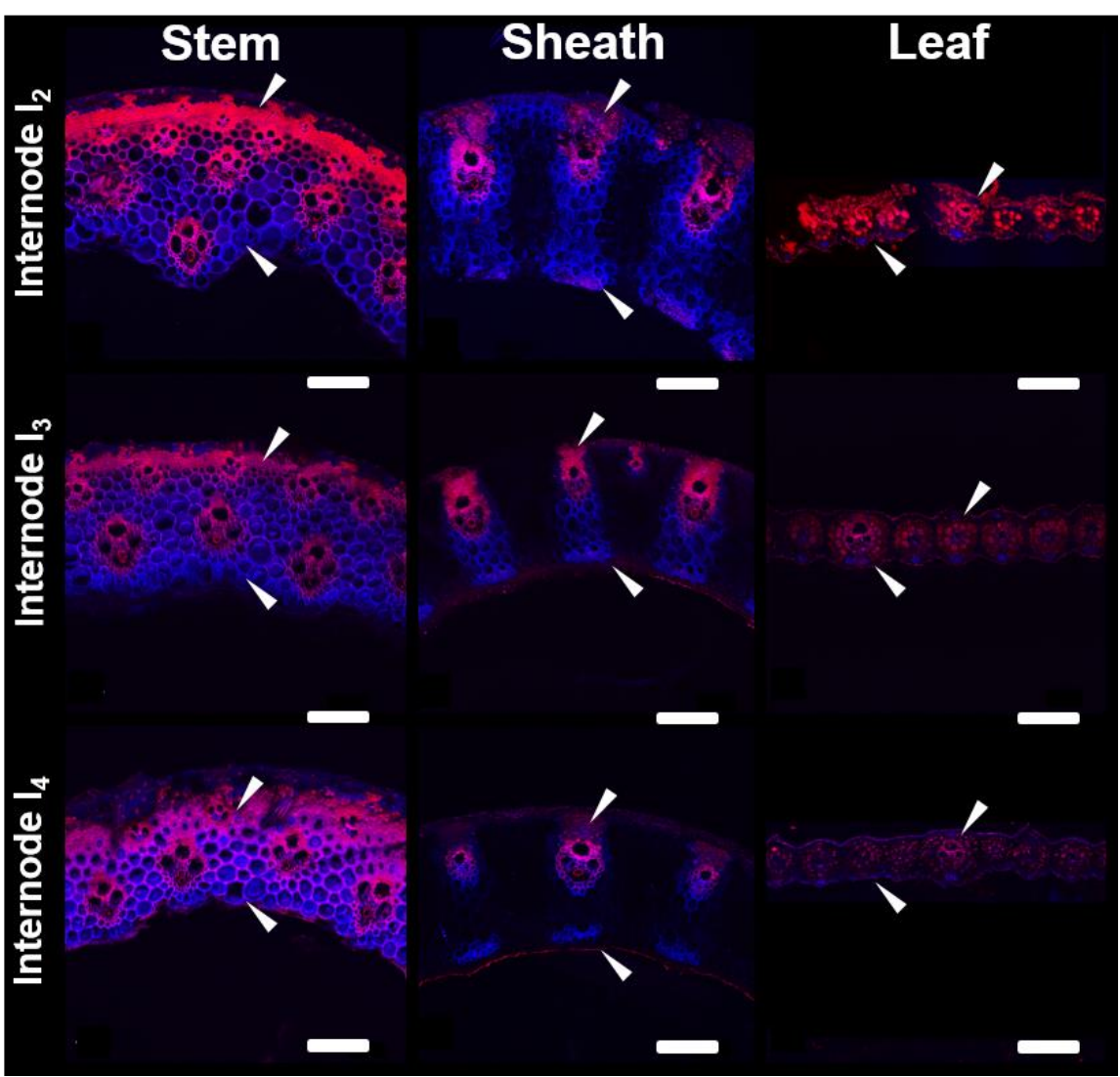


Figure 2.6 : Cell wall autofluorescence cross-sections of NaOH-pretreated switchgrass anatomical fractions from internodes I₂, I₃, and I₄. Confocal laser scanning microscopy carried out using an overlay of laser excitation wavelengths of 405 nm and 543 nm. Scale bars represent 200 μ m.

Comparing cross-sections of stem internodes I₂ to I₄, there was a clear increase of the blue emission spectrum in the fiber bundles, while in leaf sheaths cross-sections sampled from internodes I₂ to I₄, there was a clear decrease of the blue emission spectrum in the parenchyma cells. Signal intensity from the red emission spectrum decreased in fiber and vascular cells in both stem and leaf sheaths from internode I₂ to I₄. In addition to changes in signal intensity, cell wall thickening was also observed in the parenchyma and interfascicular tissues of stem

internode cross-sections, corresponding to a maturation of tissues [18]. Similar thickening was not as apparent in sheath or leaf cross-sections.

These results suggest that following NaOH pretreatment, components that fluoresced red in the stem cross-sections were either preferentially extracted due to pretreatment, or were observed in lower abundance relative to other components in more mature internodes. This may also suggest that following alkaline pretreatment, there were regions of hydroxycinnimates that remained unextracted or were more recalcitrant in stem internodes, as evidenced by the change in ratio of blue emission to red emission spectrum. The loss of both emission spectrum signals with internode maturity in sheath cross-sections suggests either the removal of both components with alkaline pretreatment, or the loss of accessibility of both components for autofluorescence.

From the perspective of secondary cell wall development, more mature internode crosssections may have hydroxycinnimates in all cell types, while in younger stem internode crosssections, potential locations of hydroxycinnimates might be restricted predominantly to
developing parenchyma cells. In sheath cross-sections, younger internodes had potential
locations of hydroxycinnimates in all cell types, with the eventual observance of the blue
emission spectrum only in the vascular bundle regions. Leaf internodes following NaOH
pretreatment had a noticeable decrease in both emission signal intensities, with the blue emission
spectrum localized to the outer parenchyma and epidermal cells, and the red emission spectrum
localized to the bundle sheath and epidermal cells. Given the autofluorescence of chlorophyll in
the red emission spectrum, the decrease in red signal can be largely attributed to either
chlorophyll removal from alkaline extraction, or a decrease in chlorophyll in more mature leaf
internodes following senescence.

Glycome profiling

Glycome profiling was performed to assess organ-specific variations in the cell wall glycan composition and extractability across individual internodes of each anatomical fraction, I₁-stem, I₁-sheath, and I₁-leaf. In **Figure 2.7A**, selected regions of glycome profiles highlight abundancies of xylan and pectin epitopes in cell wall extracts, while the full glycome profile results can be found in **Figure 2.11** in Appendix A.

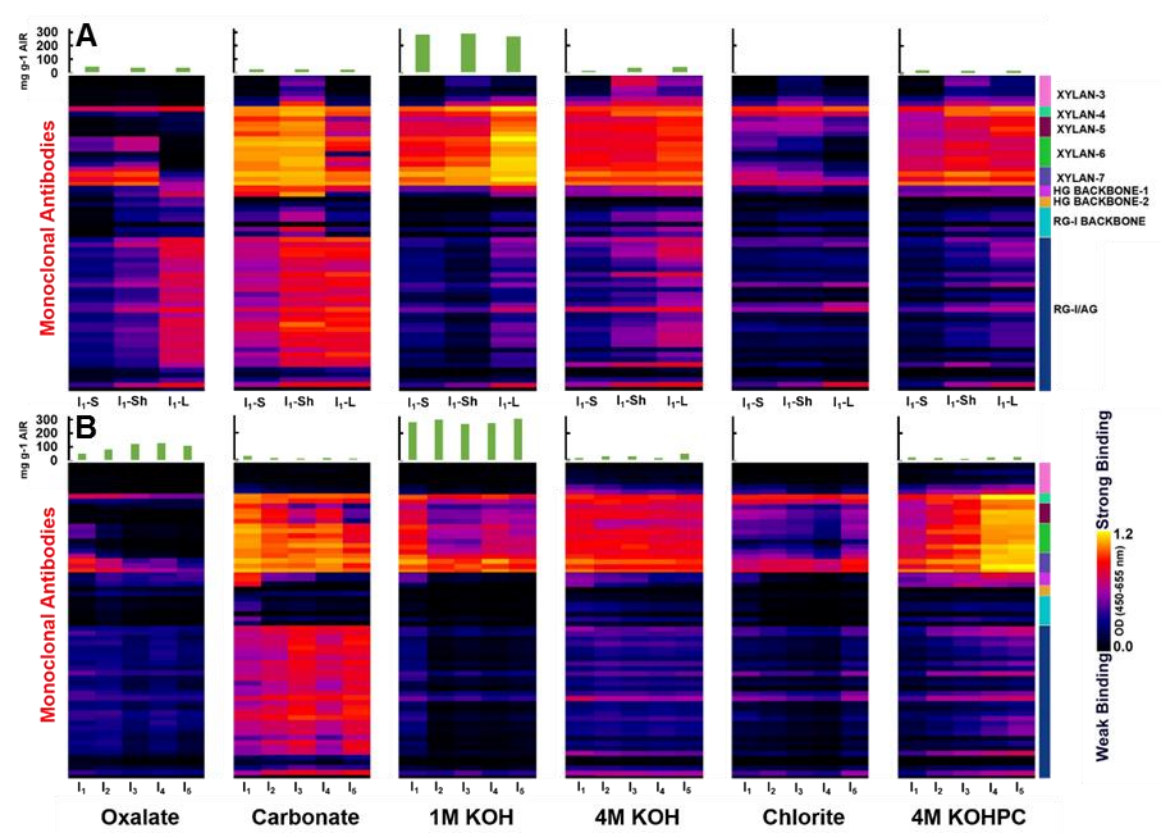


Figure 2.7: Abundance of select major non-cellulosic glycan epitopes in chemical extracts from stem, sheath, and leaf anatomical fractions of internodes I₁ (A), and extracts from stem internodes I₁-I₅ (B). Extracts were screened by ELISA using a comprehensive suite of cell wall glycan-directed mAbs as described in materials and methods. Binding response values are depicted as heat maps with black-red-bright yellow color scheme representing from no binding to strongest binding. The amount of carbohydrate material recovered per gram of AIR is depicted in the bar graphs (green) above the heat maps. The panel on the right-hand side of the heat map shows the groups of mAbs based on the class of cell wall glycan they each recognize.

With the oxalate extracts, extractability of xylan epitopes varied across anatomical fractions. For instance, both I₁-stem and I₁-sheath exhibited similar xylan epitope extractability patterns with significant abundance of arabinosylated xylan epitopes recognized by mAb CCRC-M154 of xylan-4 clade [58], unsubstituted xylan epitopes recognized by several mAbs from xylan-6 clade, and unsubstituted xylan epitopes recognized by all mAbs from xylan-7 clades. The I₁-leaf oxalate extract was significantly different, showing an abundance of only arabinosylated xylan epitopes recognized by mAb CCRC-M154 of xylan-4 clade along with significantly reduced abundance of unsubstituted xylan epitopes recognized by mAbs from xylan-7 clades. Differences across anatomical fractions were also observed in the carbonate extract, with all three carbonate extracts containing most classes of xylan epitopes from unsubstituted and substituted regions. The I₁-leaf sample again exhibited differences in the pattern of extractability with a marginal reduction in the overall abundancies of these epitopes, namely the Me-GlcA substituted xylan epitopes (xylan-5) and complete absence of xylan-6 epitopes. Xylan-3 epitopes were observed only in the I₁-sheath, while all xylan clades were observed in the I₁-stem extract.

Likely due to grass susceptibility to alkaline pretreatment [38], the 1M KOH extract showed the largest portion of total carbohydrates released, with significant xylan epitope abundance in all three sample extracts. I₁-leaf exhibited the strongest binding intensity for xylan epitopes 4 through 7 in the 1M KOH extract, and this trend was mirrored in the 4M KOH fraction. Similar patterns of xylan epitopes composition and extractability were recognized in the 4M KOH extract, however at this point binding intensities across samples were largely similar and were probably the residual alkaline susceptible xylans that remained after the 1M KOH extract [42]. The chlorite and subsequent 4M KOH PC extracts were used to determine

carbohydrates more tightly bound with lignin. Interestingly, the chlorite extract showed overall similar epitope recognition patterns for all three extracts as the oxalate extract, with the I₁-leaf containing only xylan-4 and xylan-7 epitopes. Subsequent 4M KOH PC extraction showed similar overall epitope extractability patterns and binding intensity as the 1M KOH extract, with I₁-sheath and I₁-leaf extracts having the most intense binding for xylan-4 to xylan-7 epitopes.

From these results, it can be hypothesized that xylan integration within the cell walls of each anatomical fraction are not equivalent. Specifically, xylan association in the leaf fraction appeared to be more tightly integrated within the cell wall, as leaf xylan required a more severe basic 1M KOH extract to observe significant xylan epitopes. Recognition of xylan-5 epitopes in the carbonate and 1M KOH fraction was unexpected, as more substituted xylans such as arabinoxylan are thought to exist in primary cell walls, while less substituted and branched xylans are associated with the secondary cell wall [59]. This result may indicate an abundance in arabinosylation of leaf xylans compared to stem xylan in these switchgrass fractions [60]. Furthermore, higher xylan epitope recognition in the 4M KOH PC suggests that xylan is more integrated with lignin in the leaf fraction, which may be a result of hemicelluloses in the leaf contributing more towards leaf internode recalcitrance compared to higher lignin containing fractions such as stem and sheath.

In terms of pectin epitope trends, while I₁-stem and I₁-sheath displayed marginal pectin epitope abundancies in the oxalate extract, the majority of recognized epitopes and highest abundancies was in the I₁-leaf extract. Specifically, epitopes of the homogalacturonan backbone (HG backbone 1 & 2) and pectic arabinogalactan epitopes (RG-I/AG) were broadly recognized in the I₁-leaf extract, with weak to moderate binding also occurring in the I₁-sheath extract. More intense binding and recognition for the pectic arabinogalactan epitopes was observed in the

carbonate extract for I₁-sheath and I₁-leaf, with a moderate amount of recognition in the I₁-stem extract. In addition, HG 1 epitopes were observed in high intensity for all three extracts, and rhamnogalacturanan-I backbone (RG-I backbone) was recognized highest in the I₁-sheath extract. Overall, a higher abundance of pectin backbone and pectic arabinogalactan (AG) epitopes was noted in I₁-leaf samples in 1M, 4M KOH and 4M KOH PC extracts, while patterns in chlorite extracts were largely similar across samples.

From the pectin epitope recognition patterns, it is clear the stem anatomical fraction generally had lower overall pectin content that was also less recalcitrant. Sheath and leaf anatomical fractions displayed similar epitope recognition, suggesting similar pectin structures, however, differential epitope binding intensity suggests that each anatomical fraction has a unique organization of pectin in the cell wall. Pectic AGs are the major galactose containing pectin found in grasses [61], with the higher content of galactan found in the cell walls of leaf extracts suggesting higher overall pectic AGs content compared to stem samples [23].

Glycome profiling for internode specific extractability

Stem internodes I₁- I₅ were subjected to glycome profiling to examine trends in the non-cellulosic polysaccharide extractability and structure with respect to tissue maturity. As earlier, selected epitope profiles for xylan and pectins are shown in **Figure 2.7B**, while the complete glycome profile can be found in **Figure 2.12** in Appendix A.

Oxalate and carbonate extracts showed binding of xylan-4 and xylan-7 epitopes in all internodes, with the significantly enhanced appearance of xylan-6 epitopes in the carbonate fraction. There was a trend of reduced xylan-5 epitope abundance in the more mature internodes, corresponding to a decrease in extractable Me-GlcA substituted xylans in oxalate, carbonate, and 1M KOH extracts. The 1M KOH extract showed significant epitope extractability of xylan-4 and

xylan-7, indicating that a large fraction of the total polysaccharides released in the 1M KOH extracts were unsubstituted xylans or arabinoxylated xylans. The 4M KOH fraction showed similar abundance of xylan-4, xylan-5, xylan-6, and xylan-7 epitopes among all developmental stages of internodes, while the 4M KOH PC extracts showed an increasing trend of xylan mAb extractability in more mature internodes.

Taken together, these results indicate that internode maturity impacts xylan deconstruction and extractability. Specifically, higher abundance of xylans were recognized in less severe chemical extracts for younger internodes, while harsh extractions after chlorite delignification showed the opposite trend, indicating lignification plays a greater role in xylan recalcitrance in more mature internodes [62]. Pectin epitope abundance was largely observed in the carbonate and 4M KOH PC extracts, with an increase in binding intensity of pectic AG epitopes with maturing internodes. In addition, a clear trend in decreasing binding strength was observed with the epitopes for the HG backbone 1, which is an indication of a transition from an abundance of primary cell walls to the development of secondary cell wall thickening [63]. In the 4M KOH PC extracts, a similar trend was observed for the pectic AG as in the carbonate fraction, however, the HG backbone 1 epitope abundance increased with internode maturity. Pectin trends indicate that less severe extracts result in more extractable pectins from more mature internodes, which would indicate that pectins more closely associate within the cell wall in less mature internodes or are more easily liberated compared to xylans. At the same time, however, the trend observed post chlorite delignification suggests that there is a second fraction of pectins that are closely associated with lignin, as indicated by the increased pectin and pectin backbone abundance in more mature internodes. Pectin-lignin associations have been proposed in grasses in prior studies [23, 64].

Discussion

Results for plant cell wall composition together with cell wall susceptibility to deconstruction by a coupled alkaline pretreatment and enzymatic hydrolysis demonstrate different switchgrass anatomical fractions possess significant differences both within fractions of varying maturity, and between different anatomical fractions. These trends are shown as a summary of Pearson's correlation coefficients between cell wall properties and hydrolysis yields for either individual anatomical fractions or for all pooled fractions are presented in **Figure 2.8**, while data from a few illustrative identified correlations are plotted in **Figure 2.9**.

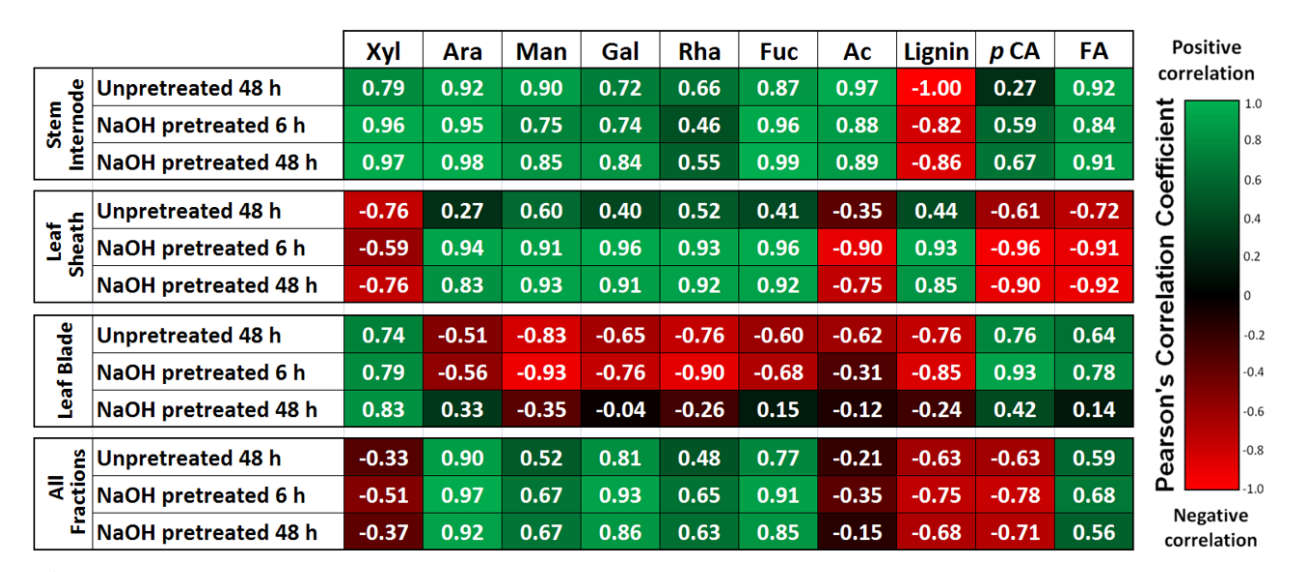


Figure 2.8: Summary of Pearson's correlation coefficients between plant cell wall properties and glucose hydrolysis yields for each anatomical fraction and for pooled samples. Data demonstrate strong correlations between many properties and yields.

First, lignin content was found to exhibit a negative correlation with untreated and pretreated in stems and leaves (**Figure 2.8**), while demonstrating a strong, significant negative correlation when all anatomical fractions are pooled for 48 hr hydrolysis yields following pretreatment (R = -0.68; p-value = 0.005; **Figure 2.8** and **Figure 2.9A**). As similar trends are observed for untreated hydrolysis yields and pretreated hydrolysis yields, indicating the trend is

related to anatomical fraction structure and maturation rather than pretreatment response. Stems contain the highest content of lignin of any of the anatomical fractions (

Figure 2.3A), with tissue maturity-dependent lignification and cell wall thickening [18] observed in confocal microscopy cross-sections (Figure 2.6). These results together suggest lignin is a defining feature of recalcitrance in the cell walls of developing stems. Notably, lignin is a well-known contributor to cell wall recalcitrance, and as one example, our previous work in diverse maize lines demonstrated that initial lignin content was a strong predictor of glucose hydrolysis yields for no pretreatment, while lignin content after mild NaOH pretreatment was a strong predictor of glucose hydrolysis yields comparable to what was performed in the present work [38]. Glycome profiling results do suggest that hemicelluloses may play a parallel role in inhibiting cell wall deconstruction, as a noted decrease in xylan epitope extractability was observed in maturing stem internodes until alkaline extraction post chlorite delignification (Figure 2.7), however higher lignification reducing xylan accessibility to extraction may have contributed to the observed trends.

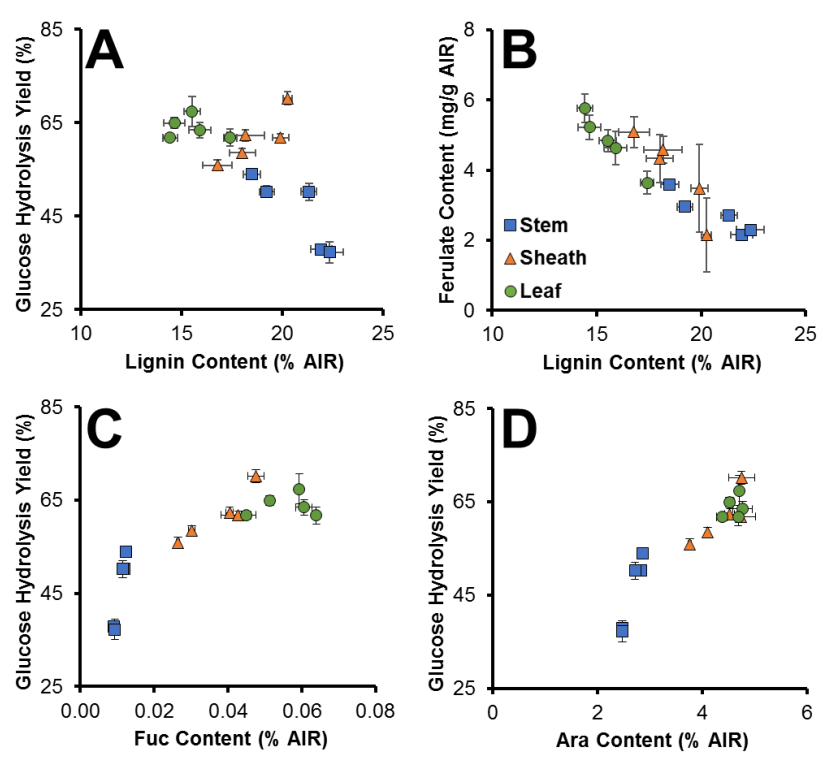


Figure 2.9: Select correlations between data relationships between either lignin content or ferulic acid against glucose hydrolysis yield represented as scatter plots. (A) 48-hr glucose hydrolysis yields for NaOH-pretreat biomass versus lignin content, (B) ferulate content in relation to total lignin, and 48-hr glucose hydrolysis yield with respect to (C) fucan and (D) arabinan content.

Variability in lignin composition may also play a significant role in anatomical fraction-specific differences of recalcitrance. A strong negative correlation was observed between lignin and ferulate content for all fractions, shown in **Figure 2.9B** ($R^2 = 0.923$; p-value = 10^{-8}). Coupled with the observed decrease in ferulate content with increasing internodes shown in

Figure 2.3B and as reported previously in switchgrass stem internodes [18], suggesting that ferulate content within the cell wall is dependent upon both tissue maturity and lignin content. Ester crosslinking of cell wall biopolymers via ferulates is considered to be one of the major contributing features cell wall recalcitrance in low-lignin grass cell walls [7, 65]. Notably, ester crosslinks are susceptible to saponification during mild alkaline pretreatment relative to

ether linkages between other monolignols, and may potentially contribute significantly to enzymatic hydrolysis yields following alkaline pretreatment.

Similar to stem internode composition, lignification increased in maturing leaf sheath cell walls, however, the positive correlation between 48-hr glucose hydrolysis yields following NaOH pretreatment and lignin content in leaf sheath samples (**Figure 2.9A**) suggests that other cell wall components, such as hemicellulose substitution, pectin abundance, and polysaccharide-lignin associations may be a more significant contributor to cell wall recalcitrance. In the leaf sheath, significant positive correlations were observed between minor polysaccharide sugars (Rha, Ara, Fuc, Gal, Man) and hydrolysis yields following pretreatment (**Figure 2.8**; **Figure 2.9C** and **Figure 2.9D**), and considering the leaf sheath cell wall composition of each of these minor sugars can be more than double that in stem internodes (

Figure 2.3C), indicating these polymers may play a more important role in cell wall recalcitrance. Of note, arabinan, which is present as substitutions on the xylan backbone in GAX and to a substantially lesser extent as arabinogalactan (AG), is substantially higher in leaf sheath cell walls than in stem internodes and exhibits a strong positive correlation to glucose hydrolysis yields in pretreated biomass (Figure 2.9D). The implications of this are that increased substitution of xylan with arabinosyl substitutions suggests a less tightly crosslinked cell wall matrix that may be more accessible to enzymatic deconstruction [21,66]. This finding is in agreement with the work of Costa et al [62], who found that the Ara:Xyl ratio in different anatomical fractions isolated from sugarcane stems was a strong predictor of enzymatic hydrolysis yields in un-pretreated biomass.

Although possessing similar arabinan content, the same trend was not observed in leaf internodes; lower cellulose, xylan, and lignin content in leaf internodes suggest that due to

limited lignification in leaf internodes compared to stem internodes (**Figure 2.2**), structural pectins and minor hemicellulose components with lower overall compositions playing a more significant role in cell wall recalcitrance. Results suggest that a relatively internode-independent, uniform response was observed in leaf cross-section phenolic autofluorescence to alkaline pretreatment (**Figure 2.6**), corresponding to similar response to lignin removal. The effectiveness of enzymatic hydrolysis of leaf internodes following NaOH pretreatment further suggests that alkaline susceptible cell wall components did not have a differential effect upon leaf cell wall digestibility. Although displaying comparable yields to alkaline pretreated leaf sheaths, leaf cell walls may be more susceptible to a pretreatment that predominantly removes more polysaccharide components, such as liquid hot water pretreatment, which has shown to dramatically improve leaf digestibility [67].

Technologies for biomass fractionation or extraction employed either on-field or at a centralized processing facility offer the potential to simultaneously improve agronomic, logistics, and processing outcomes. As an example, on-site field fractionation of switchgrass could capitalize on more recalcitrant stem internodes residing at the bottom of the tiller, harvesting upper less mature internodes while leaving mature internodes on-field for soil coverage and nutrient retention. Given stem and sheath leaf fractions constitute half of leaf dry weight in prior reporting [43], loss of biomass yield would have to be weighed against increases in downstream sugar yields due to less recalcitrant materials representing a larger total fraction of biomass.

Additionally, grass stems can accumulate a substantial amount of soluble sugars in storage parenchyma cells surrounding the vascular tissues [68]. Given that soluble sugars can represent more than 10% of the switchgrass total dry weight in this study, water extraction may be proposed as a route to yield a stream rich in fermentable sugars. Sugarcane undergoes

mechanical fractionation coupled with counter-current hot water extraction to remove soluble, fermentable sugars. Flow-through liquid hot water pretreatments are well-established pretreatment technologies [69]; counter-current processing configurations can be envisioned that integrate soluble sugar extraction with liquid hot water pretreatment, each taking place at their respective optimal temperatures.

Conclusions

In this work, we were able to demonstrate that significant heterogeneity in cell wall structure, composition, properties within switchgrass results in substantially different feedstocks response to processing in a cellulosic biorefinery. Feedstock heterogeneity may offer the potential to either tailor harvest approach, harvest time, or employ physical fractionation during processing to optimize processing outcomes such as sugar yield. Using switchgrass physically fractionated by anatomical fraction and internode, we identified compositional differences that impact recalcitrance and related results to macroscopic observations. Specifically, we showed that while all anatomical fractions experienced different extents of lignification between internodes; stem internode, leaf sheath, and leaf blade fractions were shown to have different structural features that dominate cell wall recalcitrance. Lignin content was identified as exhibiting a strong correlation to cell wall recalcitrance in stem internodes and initial recalcitrance in leaves. Leaf sheath and leaf cell wall recalcitrance were also shown to be impacted significantly by hemicellulose content and substitution, as well as structural pectin content. Ferulate and p-coumarate content were inversely correlated to lignin content in all fractions and decreased significantly with increasing internode maturity. Additionally, soluble sugars can account for a non-trivial fraction of total switchgrass dry weight, and represent a potential avenue to generate an enriched stream of easily extracted sugars to improve process economics.

Acknowledgements

The authors would like to thank Dr. Melinda Frame (Michigan State University) for assistance with confocal microscopy sample preparation and image collection.

APPENDIX

APPENDIX A: Supplementary figures

	Stem							Sheath			Leaf					
	I ₁	l ₂	I ₃	I ₄	I ₅	I ₁	l ₂	I ₃	I ₄	I ₅	I ₁	l ₂	I ₃	l ₄	I ₅	
Cellulose (% AIR)	43.93	50.96	50.51	50.33	46.42	40.07	48.12	47.90	42.97	42.59	35.78	36.72	36.22	37.27	36.69	
Xylan (% AIR)	25.41	25.56	25.25	22.79	23.09	24.39	25.37	25.03	24.59	22.78	19.59	20.33	20.37	19.86	18.79	
Arabinan (% AIR)	2.85	2.83	2.72	2.47	2.47	3.76	4.10	4.53	4.75	4.75	4.38	4.53	4.71	4.77	4.69	
Mannan (% AIR)	0.03	0.03	0.03	0.02	0.03	0.04	0.04	0.05	0.07	0.08	0.05	0.05	0.07	0.1	0.13	
Galactan (% AIR)	0.42	0.41	0.41	0.38	0.4	0.72	0.82	1.04	1.03	1.14	1.06	1.15	1.24	1.27	1.38	
Rhamnan (% AIR)	0.07	0.05	0.05	0.05	0.05	0.09	0.10	0.13	0.18	0.21	0.13	0.18	0.23	0.35	0.43	
Fucan (% AIR)	0.01	0.01	0.01	0.01	0.01	0.03	0.03	0.04	0.04	0.05	0.04	0.05	0.06	0.06	0.06	
Non-cellulosic glucan (% AIR)	1.80	2.06	2.68	3.02	3.05	1.92	2.00	2.36	2.74	2.81	2.31	2.39	2.64	3.22	3.68	
Acetate (% AIR)	4.72	3.83	3.31	2.95	2.07	3.99	3.49	3.49	3.35	3.32	2.30	1.51	2.22	2.19	1.96	
Lignin (% AIR)	18.49	19.23	21.33	21.94	22.35	16.78	18.01	18.18	19.92	20.26	14.43	14.65	15.53	15.91	17.42	
P-coumaric acid yield (mg/g AIR)	10.71	10.54	11.16	9.45	10.51	10.71	8.70	9.02	7.42	6.09	6.51	6.20	6.17	4.92	4.29	
Ferulic acid yield (mg/g AIR)	3.59	2.95	2.71	2.15	2.3	5.08	4.33	4.58	3.48	2.15	5.77	5.22	4.84	4.63	3.64	
Syringyl (S) monomer unit (mg/g AIR)	1.55	1.84	1.87	1.88	2.38	0.87	0.72	0.73	0.63	0.65	0.43	0.42	0.41	0.52	0.69	
Guaiacyl (G) monomer unit (mg/g AIR)	3.20	3.59	3.55	3.78	4.76	2.48	2.23	2.13	2.00	2.09	1.33	1.26	1.24	1.50	2.13	
P-hydroxyphenyl (H) monomer unit (mg/g AIR)	0.15	0.16	0.14	0.16	0.17	0.10	0.09	0.10	0.09	0.10	0.08	0.08	0.07	0.09	0.10	

Table 2.1 : Compiled AIR + destarched cell wall polysaccharides, acetate, and lignin content for five internodes of three switchgrass anatomical fractions. Samples are presented as an average (n = 3) with standard deviations following in **Table 2.2.**

	Stem					Sheath						Leaf					
	I ₁	l ₂	I ₃	I ₄	I ₅	I ₁	l ₂	I ₃	I ₄	I ₅	I ₁	l ₂	I ₃	I ₄	I ₅		
Cellulose (% AIR)	1.71	4.87	3.32	4.34	5.26	6.02	4.41	4.77	5.51	2.03	1.19	1.87	2.59	0.80	4.43		
Xylan (% AIR)	0.16	0.16	0.19	0.16	0.34	0.30	0.08	0.17	0.36	0.19	0.16	0.06	0.15	0.12	0.13		
Arabinan (% AIR)	0.81	0.55	0.64	0.74	1.17	0.49	0.39	0.51	1.19	1.62	0.52	0.89	0.41	1.32	0.73		
Mannan (% AIR)	0.07	0.01	0.04	0.03	0.11	0.03	0.01	0.09	0.27	0.25	0.10	0.09	0.06	0.19	0.06		
Galactan (% AIR)	0.00	0.00	0.00	0.00	0.00	0.01	0.00	0.00	0.01	0.01	0.00	0.00	0.01	0.00	0.00		
Rhamnan (% AIR)	0.01	0.01	0.01	0.02	0.03	0.04	0.03	0.02	0.06	0.09	0.04	0.08	0.07	0.05	0.06		
Fucan (% AIR)	0.01	0.01	0.01	0.00	0.01	0.01	0.01	0.01	0.02	0.01	0.01	0.01	0.02	0.01	0.02		
Non-cellulosic glucan (% AIR)	0.00	0.00	0.00	0.00	0.00	0.00	0.00	0.00	0.00	0.00	0.00	0.00	0.00	0.00	0.00		
Acetate (% AIR)	0.09	0.41	0.45	0.90	0.11	0.09	0.42	0.22	0.02	0.10	0.18	0.14	0.45	0.30	0.09		
Lignin (% AIR)	0.43	0.36	0.39	0.53	0.66	0.73	0.64	0.92	0.41	0.23	0.36	0.53	0.41	0.55	0.31		
P-coumaric acid yield (mg/g AIR)	0.04	0.10	0.07	0.09	0.01	0.53	0.77	0.11	1.25	1.41	0.25	0.21	0.17	0.25	0.14		
Ferulic acid yield (mg/g AIR)	0.06	0.08	0.03	0.08	0.04	0.43	0.68	0.39	1.26	1.05	0.16	0.13	0.14	0.23	0.18		
Syringyl (S) monomer unit (mg/g AIR)	0.09	0.13	0.07	0.11	0.07	0.06	0.05	0.05	0.02	0.05	0.01	0.01	0.03	0.03	0.02		
Guaiacyl (G) monomer unit (mg/g AIR)	0.18	0.22	0.12	0.27	0.12	0.10	0.12	0.11	0.04	0.03	0.04	0.07	0.08	0.05	0.04		
P-hydroxyphenyl (H) monomer unit (mg/g AIR)	0.01	0.00	0.01	0.01	0.01	0.00	0.00	0.00	0.01	0.00	0.00	0.00	0.00	0.01	0.00		

Table 2.2: Standard deviations for compiled AIR + destarched cell wall polysaccharides, acetate, and lignin content for five internodes of three switchgrass anatomical fractions. Samples are presented as an average (n = 3) with standard deviations following.

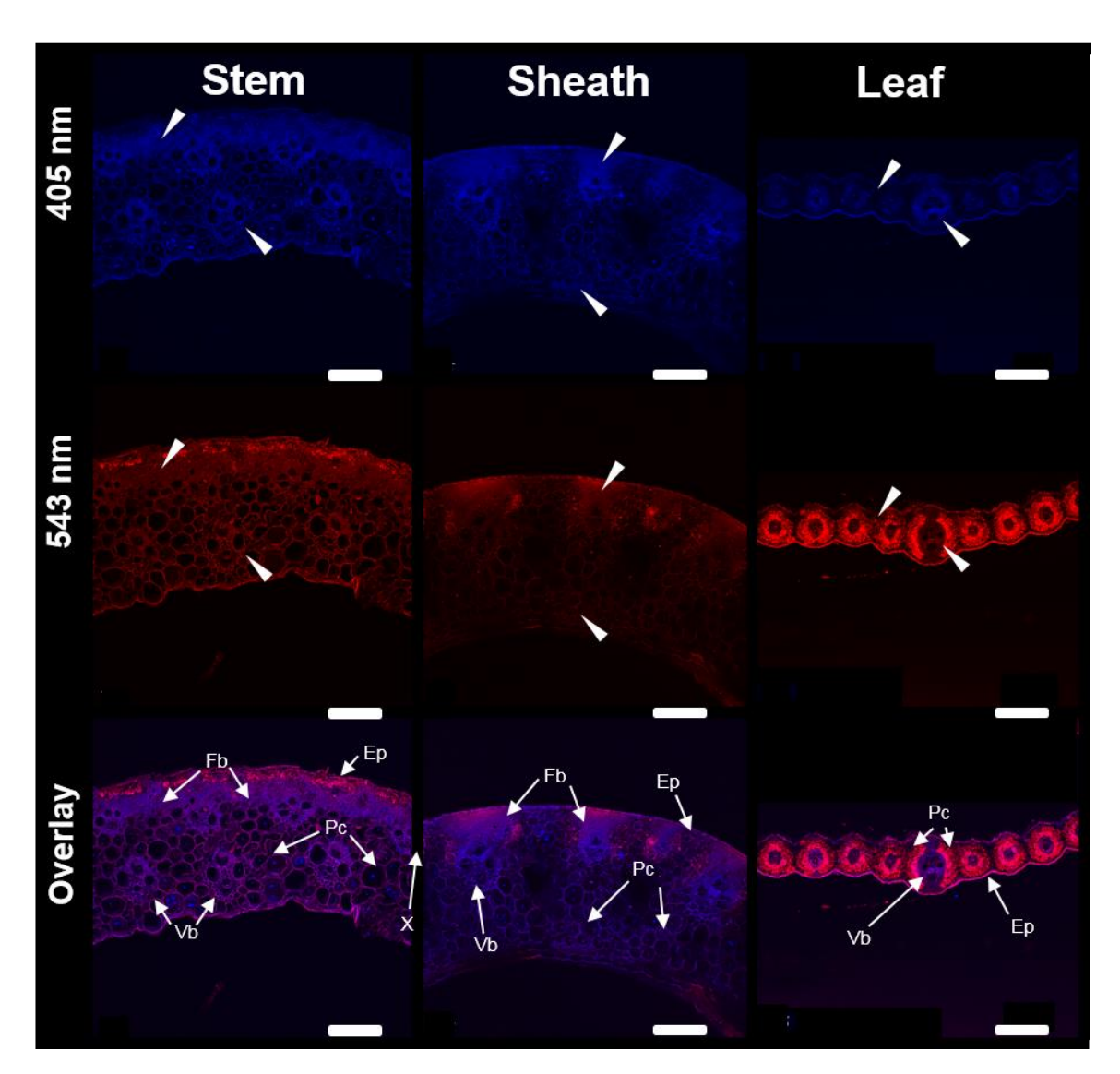


Figure 2.10 : Cell wall autofluorescence of switchgrass organ cross-sections from internode I₂. Confocal laser scanning microscopy carried out using laser excitation wavelengths of 405 nm and 543 nm. Tissue types are denoted from the following notation: Ep – epidermis, Fb – fiber bundles, Vb – vascular bundles, Ph – phloem, X – xylem, Pc – Parenchyma cells. Scale bars represent 200 μ m.

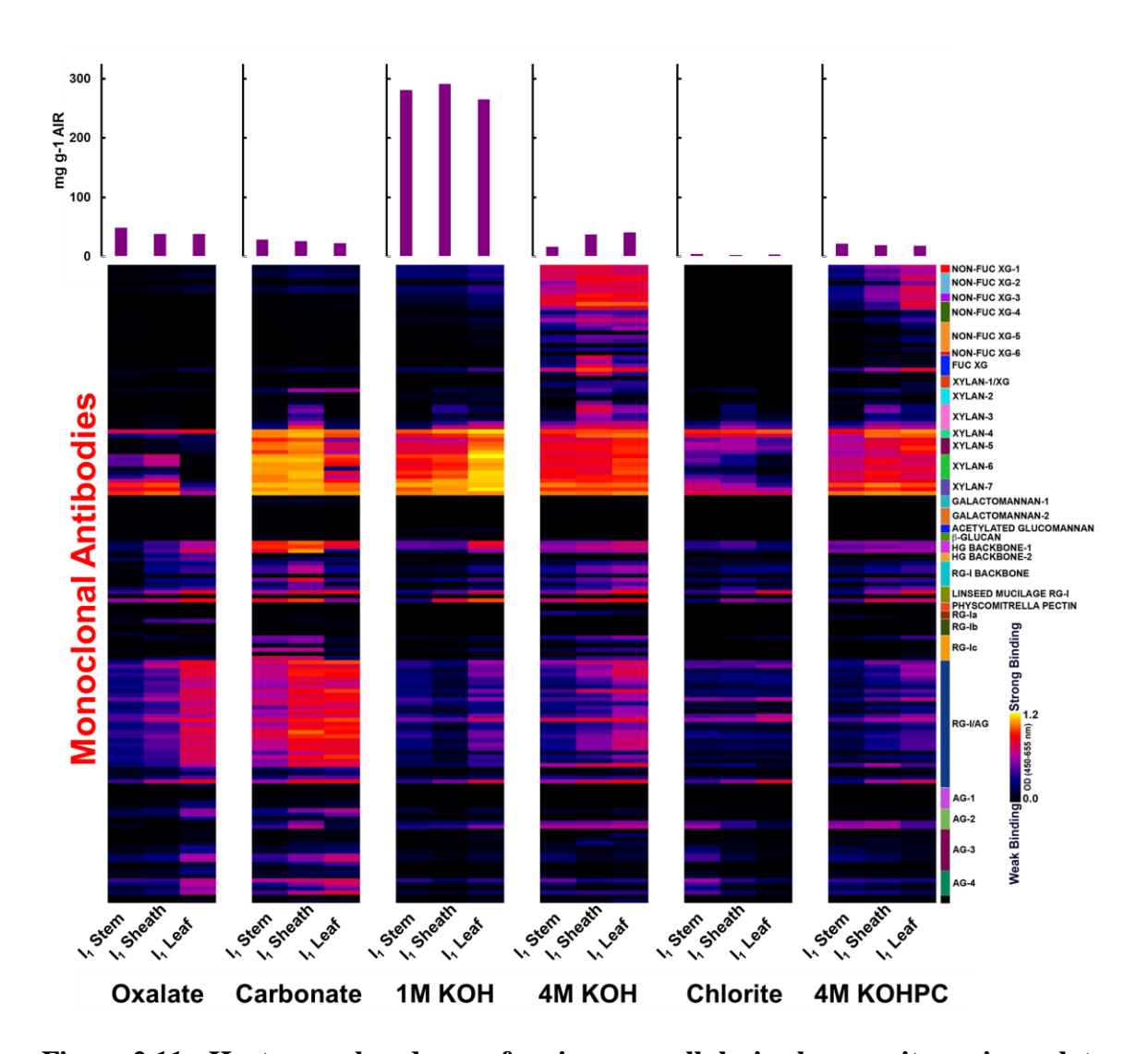


Figure 2.11: Heat map abundance of major non-cellulosic glycan epitopes in oxalate, carbonate, 1M KOH, 4M KOH, chlorite, and 4M KOH PC extracts from cell walls of stem, sheath, and leaf samples of internodes I1. Extracts were screened by ELISA using a comprehensive suite of cell wall glycan-directed mAbs as described in materials and methods. Binding response values are depicted as heat maps with black-red-bright yellow color scheme representing from no binding to strongest binding. The amount of carbohydrate material recovered per gram of AIR is depicted in the bar graphs (purple) above the heat maps. The panel on the right-hand side of the heat map shows the groups of mAbs based on the class of cell wall glycan they each recognize.

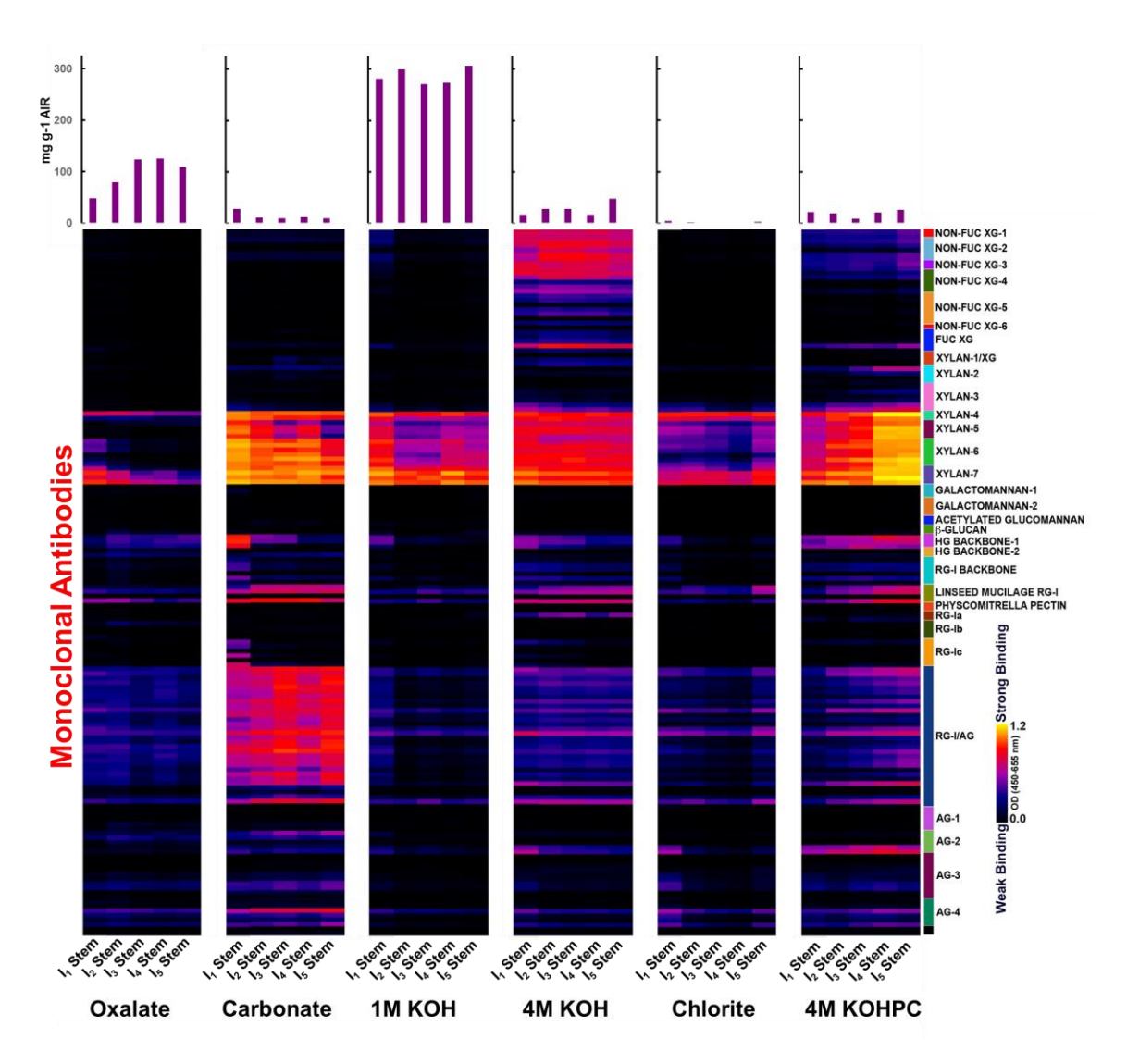


Figure 2.12: Heat map abundance of major non-cellulosic glycan epitopes in oxalate, carbonate, 1M KOH, 4M KOH, chlorite, and 4M KOHPC extracts from stem internodes I₁-I₅. Extracts were screened by ELISA using a comprehensive suite of cell wall glycan-directed mAbs as described in materials and methods. Binding response values are depicted as heat maps with black-red-bright yellow color scheme representing from no binding to strongest binding. The amount of carbohydrate material recovered per gram of AIR is depicted in the bar graphs (purple) above the heat maps. The panel on the right-hand side of the heat map shows the groups of mAbs based on the class of cell wall glycan they each recognize.

REFERENCES

REFERENCES

- 1. Melillo JM., Richmond TC, Yohe GW: Climate change impacts in the United States: The third national climate assessment. US Global Change Research Program, 2014:841.
- 2. Tilman D, Socolow R, Foley JA, Hill J, Larson E, Lynd L, Pacala S, Reilly J, Searchinger T, Somerville C, *et al*: Beneficial biofuels-The food, energy, and environment trilemma. *Science*. 2009, 325:270-271.
- 3. U.S. Department of Energy. U.S. Billion-ton Update: Biomass Supply for a Bioenergy and Bioproducts Industry. D. Perlack and B.J. Stokes (Leads), ORNL/TM-2011/224. Oak Ridge National Laboratory, Oak Ridge, TN. 2011.
- 4. Himmel ME, Ding SY, Johnson DK, Adney WS, Nimlos MR, Brady JW, Foust TD: Biomass recalcitrance: Engineering plants and enzymes for biofuels production. *Science*. 2007, 315:804-807.
- 5. Albersheim PD, Roberts K, Sederoff R, Staehelin A: **Plant Cell Walls**: Garland Science, Taylor & Francis Group, LLC, New York, 1st ed., 2011.
- 6. Pauly M, Gille S, Liu L, Mansoori N, Souza A, Schultink A, Xiong G: **Hemicellulose biosynthesis**. *Planta*. 2013, **238**:627-642.
- 7. Grabber JH, Ralph J, Lapierre C, Barrière Y: **Genetic and molecular basis of grass cellwall degradability. I. Lignin–cell wall matrix interactions**. *C R Biol*. 2004, **327**:455-465.
- 8. Scheller HV, Ulvskov P: **Hemicelluloses**. *Annu Rev Plant Biol*. 2010, **61**:263-289.
- 9. Wilkerson CG, Mansfield SD, Lu F, Withers S, Park JY, Karlen SD, Gonzales-Vigil E, Padmakshan D, Unda F, Rencoret J, *et al*: **Monolignol ferulate transferase introduces chemically labile linkages into the lignin backbone**. *Science*. 2014, **344**:90-93.
- 10. DeMartini JD, Pattathil S, Miller JS, Li HJ, Hahn MG, Wyman CE: **Investigating plant cell wall components that affect biomass recalcitrance in poplar and switchgrass**. *Energy Environ Sci.* 2013, **6**:898-909.
- 11. Lionetti V, Francocci F, Ferrari S, Volpi C, Bellincampi D, Galletti R, D'Ovidio R, De Lorenzo G, Cervone F: Engineering the cell wall by reducing de-methyl-esterified homogalacturonan improves saccharification of plant tissues for bioconversion. *Proc Natl Acad Sci USA*. 2010, **107**:616-621.
- 12. Cass CL, Lavell AA, Santoro N, Foster CE, Karlen SD, Smith RA, Ralph J, Garvin DF, Sedbrook JC: Cell wall composition and biomass recalcitrance differences within a

- genotypically diverse set of *Brachypodium distachyon* inbred lines. *Front Plant Sci.* 2016, 7:16.
- 13. McLaughlin SB, Kszos LA: **Development of switchgrass** (*Panicum virgatum*) as a bioenergy feedstock in the United States. *Biomass Bioenerg*. 2005, **28**:515-535.
- 14. Somerville C, Youngs H, Taylor C, Davis SC, Long SP: Feedstocks for lignocellulosic biofuels. *Science*. 2010, **329**:790-792.
- 15. Parrish DJ, Casler MD, Monties A: **The evolution of switchgrass as an energy crop**. In: *Switchgrass: A Valuable Biomass Crop for Energy*. Monties A, editor: Springer London; 2012. p. 1-28
- 16. Bouton JH: **Molecular breeding of switchgrass for use as a biofuel crop**. *Curr Opin Genet Dev*. 2007, **17**:553-558.
- 17. Jung HG, Casler MD: **Maize stem tissues: cell wall concentration and composition during development**. *Crop Sci* 2006, **46**:1793-1800.
- 18. Sarath G, Baird LM, Vogel KP, Mitchell RB: **Internode structure and cell wall composition in maturing tillers of switchgrass** (*Panicum virgatum*. L). *Bioresource Technol*. 2007, **98**:2985-2992.
- 19. Dien BS, Jung HJG, Vogel KP, Casler MD, Lamb JFS, Iten L, Mitchell RB, Sarath G: Chemical composition and response to dilute-acid pretreatment and enzymatic saccharification of alfalfa, reed canarygrass, and switchgrass. *Biomass Bioenerg*. 2006, 30:880-891.
- 20. Sarath G, Mitchell RB, Sattler SE, Funnell D, Pedersen JF, Graybosch RA, Vogel KP: **Opportunities and roadblocks in utilizing forages and small grains for liquid fuels**. *J Ind Microbiol Biotechnol*. 2008, **35**:343-354.
- 21. Vogel KP, Casler MD, Dien BS: Switchgrass biomass composition traits and their effects on its digestion by ruminants and bioconversion to ethanol. *Crop Sci.* 2016, **57**:275-281.
- 22. Sarath G, Dien B, Saathoff AJ, Vogel KP, Mitchell RB, Chen H: **Ethanol yields and cell wall properties in divergently bred switchgrass genotypes**. *Bioresource Technol*. 2011, **102**:9579-9585.
- 23. da Costa RMF, Pattathil S, Avci U, Lee SJ, Hazen SP, Winters A, Hahn MG, Bosch M: A cell wall reference profile for Miscanthus bioenergy crops highlights compositional and structural variations associated with development and organ origin. *New Phytol.* 2016, 213:1710-1725.
- 24. Bootsma JA, Shanks BH: **Hydrolysis characteristics of tissue fractions resulting from mechanical separation of corn stover**. *Appl Biochem Biotechnol*. 2005, **125**:27-39.

- 25. Crofcheck CL, Montross MD: **Effect of stover fraction on glucose production using enzymatic hydrolysis**. *Trans Am Soc Agric Eng.* 2004, **47**:841-844.
- 26. Montross MD, Crofcheck CL: **Effect of stover fraction and storage method on glucose production during enzymatic hydrolysis**. *Bioresource Technol*. 2004, **92**:269-274.
- 27. Hansey CN, Lorenz AJ, de Leon N: Cell wall composition and ruminant digestibility of various maize tissues across development. *Bioenerg Res.* 2010, **3**:28-37.
- 28. Ding SY, Liu YS, Zeng Y, Himmel ME, Baker JO, Bayer EA: **How does plant cell wall nanoscale architecture correlate with enzymatic digestibility?** *Science.* 2012, **338**:1055-1060.
- 29. Hansen MA, Hidayat BJ, Mogensen KK, Jeppesen MD, Jørgensen B, Johansen KS, Thygesen LG: Enzyme affinity to cell types in wheat straw (*Triticum aestivum* L.) before and after hydrothermal pretreatment. *Biotechnol Biofuels*. 2013, **6**:54.
- 30. Zhang H, Fangel J, Willats WGT, Selig MJ, Lindedam J, Jorgensen H, Felby C: **Assessment of leaf/stem ratio in wheat straw feedstock and impact on enzymatic conversion**. *GCB Bioenergy*. 2014, **6**:90-96.
- 31. Chundawat SPS, Balan V, Dale BE: **Effect of particle size based separation of milled corn stover on AFEX pretreatment and enzymatic digestibility**. *Biotechnol Bioeng*. 2007, **96**:219-231.
- 32. Garlock RJ, Chundawat SPS, Balan V, Dale BE: **Optimizing harvest of corn stover** fractions based on overall sugar yields following ammonia fiber expansion pretreatment and enzymatic hydrolysis. *Biotechnol Biofuels.* 2009, **2**:29.
- 33. Foster CE, Martin TM, Pauly M: Comprehensive compositional analysis of plant cell walls (lignocellulosic biomass) part II: carbohydrates. *J Vis Exp.* 2010, 37:e1837
- 34. Sluiter JB, Ruiz RO, Scarlata CJ, Sluiter AD, Templeton DW: Compositional analysis of lignocellulosic feedstocks. 1. Review and description of methods. *J Agric Food Chem*. 2010, **58**:9043-9053.
- 35. Li M, Foster C, Kelkar S, Pu Y, Holmes D, Ragauskas A, Saffron C, Hodge D: **Structural characterization of alkaline hydrogen peroxide pretreated grasses exhibiting diverse lignin phenotypes**. *Biotechnol Biofuels*. 2012, **5**:38.
- 36. Foster CE, Martin TM, Pauly M: Comprehensive compositional analysis of plant cell walls (Lignocellulosic biomass) part I: lignin. *J Vis Exp.* 2010, **37**:e1745
- 37. Santoro N, Cantu SL, Tornqvist C-E, Falbel TG, Bolivar JL, Patterson SE, Pauly M, Walton JD: A high-throughput platform for screening milligram quantities of plant biomass for lignocellulose digestibility. *Bioenerg Res.* 2010, **3**:93-102.

- 38. Li M, Heckwolf M, Crowe JD, Williams DL, Magee TD, Kaeppler SM, de Leon N, Hodge DB: Cell-wall properties contributing to improved deconstruction by alkaline pretreatment and enzymatic hydrolysis in diverse maize (*Zea mays L.*) lines. *J Exp Bot*. 2015, **66**:4305-4315.
- 39. DeMartini JD, Pattathil S, Avci U, Szekalski K, Mazumder K, Hahn MG, Wyman CE: **Application of monoclonal antibodies to investigate plant cell wall deconstruction for biofuels production**. *Energy Environ Sci.* 2011, **4**:4332-4339.
- 40. Pattathil S, Avci U, Miller JS, Hahn MG: Immunological approaches to plant cell wall and biomass characterization: Glycome profiling. In: *Biomass Conversion*. Springer; 2012: 61-72.
- 41. Pattathil S, Avci U, Baldwin D, Swennes AG, McGill JA, Popper Z, Bootten T, Albert A, Davis RH, Chennareddy C, *et al*: **A comprehensive toolkit of plant cell wall glycan-directed monoclonal antibodies**. *Plant Physiol*. 2010, **153**:514-525.
- 42. Pattathil S, Hahn MG, Dale BE, Chundawat SP: **Insights into plant cell wall structure**, architecture, and integrity using glycome profiling of native and AFEXTM-pre-treated biomass. *J Exp Bot.* 2015, **66**:4279-4294.
- 43. Hu ZJ, Foston M, Ragauskas AJ: Comparative studies on hydrothermal pretreatment and enzymatic saccharification of leaves and internodes of alamo switchgrass. *Bioresource Technol.* 2011, **102**:7224-7228.
- 44. Shen H, Fu CX, Xiao XR, Ray T, Tang YH, Wang ZY, Chen F: **Developmental control of lignification in stems of lowland switchgrass variety Alamo and the effects on saccharification efficiency**. *Bioenerg Res.* 2009, **2**:233-245.
- 45. Grabber J, Jung G, Hill R: Chemical composition of parenchyma and sclerenchyma cell walls isolated from orchardgrass and switchgrass. *Crop Sci* 1991, **31**:1058-1065.
- 46. Chuck GS, Tobias C, Sun L, Kraemer F, Li C, Dibble D, Arora R, Bragg JN, Vogel JP, Singh S, *et al*: **Overexpression of the maize Corngrass1 microRNA prevents flowering, improves digestibility, and increases starch content of switchgrass**. *Proc Natl Acad Sci USA*. 2011, **108**:17550-17555.
- 47. Ong RG, Higbee A, Bottoms S, Dickinson Q, Xie D, Smith SA, Serate J, Pohlmann E, Jones AD, Coon JJ, *et al*: **Inhibition of microbial biofuel production in drought-stressed switchgrass hydrolysate**. *Biotechnol Biofuels*. 2016, **9**:237.
- 48. Garlock RJ, Balan V, Dale BE, Ramesh Pallapolu V, Lee YY, Kim Y, Mosier NS, Ladisch MR, Holtzapple MT, Falls M, *et al*: Comparative material balances around pretreatment technologies for the conversion of switchgrass to soluble sugars. *Bioresource Technol*. 2011, **102**:11063-11071.

- 49. Decker SR, Carlile M, Selig MJ, Doeppke C, Davis M, Sykes R, Turner G, Ziebell A: **Reducing the effect of variable starch levels in biomass recalcitrance screening**. In: *Biomass Conversion: Methods and Protocols, Methods in Molecular Biology*. Himmel ME, editor: Springer; 2012.
- 50. Slewinski TL: Non-structural carbohydrate partitioning in grass stems: A target to increase yield stability, stress tolerance, and biofuel production. *J Exp Bot.* 2012, **63**:4647-4670.
- 51. Park YB, Cosgrove DJ: A Revised architecture of primary cell walls based on biomechanical changes induced by substrate-specific endoglucanases. *Plant Physiol.* 2012, **158**:1933-1943.
- 52. Tobimatsu Y, Wagner A, Donaldson L, Mitra P, Niculaes C, Dima O, Kim JI, Anderson N, Loque D, Boerjan W, *et al*: **Visualization of plant cell wall lignification using fluorescence-tagged monolignols**. *Plant J*. 2013, **76**:357-366.
- 53. O'brien T, Feder N, McCully ME: **Polychromatic staining of plant cell walls by toluidine blue O**. *Protoplasma*. 1964, **59**:368-373.
- 54. Donaldson L: **Softwood and hardwood lignin fluorescence spectra of wood cell walls in different mounting media**. *IAWA J.* 2013, **34**:3-19.
- 55. García-Plazaola JI, Fernández-Marín B, Duke SO, Hernández A, López-Arbeloa F, Becerril JM: **Autofluorescence: Biological functions and technical applications**. *Plant Sci.* 2015, **236**:136-145.
- 56. Hutzler P, Fischbach R, Heller W, Jungblut TP, Reuber S, Schmitz R, Veit M, Weissenböck G, Schnitzler J-P: **Tissue localization of phenolic compounds in plants by confocal laser scanning microscopy**. *J Exp Bot*. 1998, **49**:953-965.
- 57. Matos DA, Whitney IP, Harrington MJ, Hazen SP: Cell walls and the developmental anatomy of the *Brachypodium distachyon* stem internode. *Plos One.* 2013, **8**:9.
- 58. Schmidt D, Schuhmacher F, Geissner A, Seeberger PH, Pfrengle F: **Automated synthesis of arabinoxylan-oligosaccharides enables characterization of antibodies that recognize plant cell wall glycans**. *Chem Eur J.* 2015, **21**:5709-5713.
- 59. Suzuki K, Kitamura S, Kato Y, Itoh T: **Highly substituted glucuronoarabinoxylans** (hsGAXs) and low-branched xylans show a distinct localization pattern in the tissues of *Zea mays* L. *Plant Cell Physiol.* 2000, **41**:948-959.
- 60. de Souza AP, Leite DCC, Pattathil S, Hahn MG, Buckeridge MS: Composition and structure of sugarcane cell wall polysaccharides: Implications for second-generation bioethanol production. *Bioenerg Res.* 2013, **6**:564-579.
- 61. Mohnen D: Pectin structure and biosynthesis. Curr Opin Plant Biol. 2008, 11:266-277.

- 62. Costa THF, Vega-Sanchez ME, Milagres AMF, Scheller HV, Ferraz A: **Tissue-specific** distribution of hemicelluloses in six different sugarcane hybrids as related to cell wall recalcitrance. *Biotechnol Biofuels*. 2016, **9**:99.
- 63. Cosgrove DJ: Growth of the plant cell wall. Nat Rev Mol Cell Biol. 2005, 6:850-861.
- 64. Shen H, Poovaiah CR, Ziebell A, Tschaplinski TJ, Pattathil S, Gjersing E, Engle NL, Katahira R, Pu Y, Sykes R *et al*: Enhanced characteristics of genetically modified switchgrass (*Panicum virgatum L.*) for high biofuel production. *Biotechnol Biofuels*. 2013, **6**:71.
- 65. Ralph J: **Hydroxycinnamates in lignification**. *Phytochemistry Rev.* 2010, **9**:65-83.
- 66. Busse-Wicher M, Grantham NJ, Lyczakowski JJ, Nikolovski N, Dupree P: **Xylan** decoration patterns and the plant secondary cell wall molecular architecture. *Biochem Soc Trans*. 2016, **44**:74-78.
- 67. Zeng M, Ximenes E, Ladisch MR, Mosier NS, Vermerris W, Huang C-P, Sherman DM: Tissue-specific biomass recalcitrance in corn stover pretreated with liquid hot-water: Enzymatic hydrolysis (part 1). *Biotechnol Bioeng*. 2012, **109**:390-397.
- 68. Rae AL, Grof CP, Casu RE, Bonnett GD: Sucrose accumulation in the sugarcane stem: Pathways and control points for transport and compartmentation. *Field Crops Res.* 2005, **92**:159-168.
- 69. Mosier N, Wyman C, Dale B, Elander R, Lee YY, Holtzapple M, Ladisch M: **Features of promising technologies for pretreatment of lignocellulosic biomass**. *Bioresource Technol*. 2005, **96**:673-686.

Chapter 3: Relating nanoscale accessibility within plant cell walls to improved enzyme hydrolysis yields in corn stover subjected to diverse pretreatments

This work has been submitted as original research in July 2017 to the Journal of Agricultural and Food Chemistry

Introduction

Lignocellulosic biomass is a promising feedstock for the production of renewable fuels and chemicals. One key challenge limiting effective utilization of biomass resides in plant-evolved cell wall recalcitrance [1], or resistance to degradation imparted by the higher order structure of plant cell walls. The physical structure of the plant cell wall matrix can be considered a nanostructured composite material, with networks of cellulose fibril bundles and matrix polymers forming cell wall layers [2]. Networks of microfibrils are associated and potentially cross-linked with amorphous hemicellulose polysaccharides through non-covalent interactions [3]. In lignified secondary cell walls, this network can contain lignin, which is deposited to impart structural rigidity, reduce water and solute permeability, and limit extracellular interactions [4]. Thermochemical pretreatment can be applied to improve the deconstruction of plant cell wall polysaccharides by cellulolytic enzymes [5], with the goals of pretreatment to reduce recalcitrance by removing or redistributing hemicellulose and lignin, disrupting the crystalline structure of cellulose, or disrupting the cell wall ultrastructure. Pretreatments often have the net effect of increasing cellulose accessibility to cellulolytic enzymes [6,7].

While cellulose accessibility can be considered as the ability for an enzyme to bind to cellulose and hydrolyze a glycosidic bond, this property is often indirectly assessed as accessible surface area defined by a combination of particle size, porosity, and pore volume [8]. Porosity in

the context of the plant cell wall matrix can be considered to be due to a combination of composition and structural features impacting the rigidity and internal surface area of the composite polymer network. Lignin is a hydrophobic component when sufficiently removed from the cell wall has been directly associated with loss of cell wall rigidity [9]. Xylan removal is also associated with increases in cell wall porosity, but is also coupled to a certain level of lignin removal depending on pretreatment [10]. The removal or relocalization of cell wall components alters the structural integrity of the cell wall matrix, allowing swelling and contraction in response to the solvent, exhibiting behavior like a hydrogel. It is with this model in mind, that porosity is a dynamic term that defines both structural features, as well as the cell wall response to environmental conditions.

Techniques to measures properties of porosity include metrics to measure bulk properties of the cell wall such as water-cell wall associations using water retention value (WRV) [11], measuring cell wall surface adsorption with dyes of known hydrodynamic radii to determine accessible substrate area using the Simons' Stain technique [12] or of fluorescent-labeled enzymes for direct enzyme accessibility measurements [13]. Water constraint measured using T₂ NMR relaxometry provides information on the extent of water-cell wall hydrogen bonding, with increased water constraint associated with increased water accessibility within the cell wall [14]. Pore volume is a specific characteristic of porosity, defined by the porous nature of the cell wall in an idealized slit model. In the idealized slit model, the cell wall thought of as a series of variably spaced lamellae that contain distinct pore size, and therefore pore volume characteristics [15]. The effect of cell wall component removal or re-localization during pretreatment can be associated to changes in the cell wall ultrastructure inducing 3D topographical changes in the form of induction of pore formation or voids [16]. Techniques to measure cell wall pore

distributions quantify the interaction of water within the pores to determine pore distributions. Solute exclusion utilizes the availability of porous water to influence diffusion of a probe of known hydrodynamic radii into a pore of equal or larger diameter [15], however is dependent upon uniform pore sizes for accurate pore volume determination [17]. Differential scanning calorimetry-thermoporometry quantifies heat endotherms associated with freezing point depression of water closely associated with an interface [18], while ¹H NMR cryoporosimetry quantifies water content through similar thermochemical assumptions [19], however requires assumed pore geometries to extract meaningful pore distributions.

The relationship between pore volume and enzymatic hydrolysis has been investigated in multiple studies. Originally observed as differences in the initial rates of glucose hydrolysis for acid-pretreated hardwoods and softwoods [20], a positive correlation between pore volume and enzymatic hydrolysis has also been determined in other pretreatment and feedstock systems such as chlorite-delignified sugarcane bagasse [21]. Other studies have not observed similar trends, with dilute acid pretreatment of corn stover showing no discernable relationship between pretreatment severity, hydrolysis yield, and pore volume [19]. Different methods of measuring pore properties such as Simons' Stain coupled with differential scanning calorimetry-thermoporometry have been recently used to evaluate alkali, autohydrolysis, and multi-stage pretreatments of wheat straw, concluding that delignification increases pore accessibility, while autohydrolysis increased cellulose accessibility at the expense of restricted pore accessibility [22]. Our prior work has also demonstrated relationships between water sorption, water retention and settling volume as predictors for enzyme binding and enzymatic hydrolysis using alkaline hydrogen peroxide and liquid hot water pretreatment of corn stover and switchgrass [11].

The goals of this study are to investigate corn stover subjected to a range of pretreatment conditions that include alkaline hydrogen peroxide (AHP) delignification and liquid hot water (LHW) pretreatment. These pretreatment-modified feedstocks are used to assess the impact of pretreatment on cell wall structural properties and to highlight key relationships between cell wall properties and enzymatic hydrolysis. The role of nanoscale porosity as a key structural property is investigated in the context of both solute exclusion measured accessible pore volumes, WRV determined accessible water-cell wall surface area, and solute-induced cell wall swelling. Correlations derived from both these chemical and physical changes in the cell wall are developed and these properties are then related to enzyme accessibility and enzymatic hydrolysis of cell wall polysaccharides.

Materials and methods

Biomass and composition analysis

Corn stover (*Zea mays* L. Pioneer hybrid 36H56) harvested in 2012 was milled with a Wiley Mini-mill (Thomas Scientific) to pass a 5 mm screen, and air-dried to a moisture content of approximately 5% prior to any pretreatments. Milled material was sieved, and a particle size distribution between 425 micron and 1 mm was selected for use in all pretreatments and subsequent experiments. Cell wall lignocellulosic material was isolated following extraction and de-starching procedure outlined [23] three sequential washes of 70% ethanol, 1:1 methanol-chloroform, and acetone to obtain alcohol insoluble residue (AIR). AIR was de-starched using 50 µg Amylase /mL H₂O (*Bacillus* sp., Catalog # A7595, Sigma-Aldrich St. Louis, MO) and 18.7 units of Pullulanase (*Bacillus acidopullulyticus*, Catalog # P9286 Sigma-Aldrich, St. Louis, MO) in a 0.01% sodium azide solution, with rotary mixing (Intelli-Mixer, ELMI-tech, Newbury Park, CA) at 37°C overnight. The non-cellulosic neutral monosaccharide content of the wall matrix polysaccharides was determined following trifluoracetic acid (TFA) hydrolysis of the de-

starched AIR followed by derivatization of the monosaccharides as alditol acetate method by GC/MS according to Foster et al [23]. Lignin content was determined on AIR biomass using the NREL/TP 510-42618 protocol [24] with minor modifications as described in Li et al [9]. Composition analysis was performed in technical triplicate.

Pretreatments

AHP pretreatment was performed using four different H₂O₂ to biomass loadings, 0, 0.06, 0.12, and 0.25 g H₂O₂/g biomass, at an insoluble solid loading of 15% (mass biomass per total liquid volume). Samples were prepared in 250-mL Erlenmeyer flasks, sealed with parafilm to allow expansion due to O₂ evolution, and placed in an incubator at 30°C with shaking at 180 rpm for 24 hr. The pH was maintained at 11.5 during pretreatment, with adjustments at 3 and 6 hr using 3 M NaOH [11]. LHW pretreatments were performed in a 5 L M/K Systems digester (M/K Systems, Inc., Peabody, MA, USA). Using 100-mL pressure tubes (Ace Glass, Sigma-Aldrich, St. Louis, MO), 6.0 g of biomass was loaded with 70 mL of de-ionized water, yielding a solids content of 8.5% (mass biomass per total liquid volume). Pretreatment conditions were specified at either 160°C for 30 minutes or 190°C for 5 minutes, with a heat-up rate of 1.0°C/min and a cool-down rate of approximately 1.0°C/min. All biomass following pretreatment was washed until clear, vacuum filtered with a 200 mesh Buchner filter to a moisture content of approximately 85% measured gravimetrically, and stored at 4°C. AHP pretreatment on LHWpretreated material for two-stage pretreatments was performed under identical conditions as described previously, using thoroughly washed LHW pretreated material dried to a moisture content of about 5% and sieved to ensure similar particle sizes as the initial AIR material. Material drying for hornification measurements was performed in a temperature-controlled oven (Isotemp, Fisher Scientific) at 105°C.

Enzymatic hydrolysis

Enzymatic hydrolysis was performed on never-dried pretreated material in 250-mL Erlenmeyer flasks using 5% (insoluble mass biomass per total liquid volume) dry solids loading with the moisture content of the never-dried material determined separately to achieve the target solids loading. Reaction media was buffered pH 5.2 using 50 mM sodium citrate buffer, with pH adjustments occurring after 6-hr and 24-hr hydrolysis times. Tetracycline and cycloheximide at a total concentration of 40 µg/mL each were used as antimicrobials during hydrolysis. Enzyme loading was performed using Cellic CTec3 and HTec3 (Novozymes A/S, Bagsværd, Denmark) at 20 mg protein / g glucan for CTec3 loading, and 10 mg protein/ g glucan for HTec3 loading when HTec3 was added. Hydrolysis was performed at 50°C with orbital shaking at 180 rpm and sampling was taken at 6-hr and 72-hr total hydrolysis times. Samples were centrifuged at 13000 x g for 2 min post-incubation and filtered using 22 µm mixed cellulose-ester filters (EMD Millipore, Billerica, MA). Samples were quantified by HPLC (Agilent 1100 Series) equipped with an Aminex HPX-87H column (Bio-Rad, Hercules, CA, USA) using a mobile phase of 5 mM H₂SO₄ at 65°C. Glucose yields were determined based on quantified glucose (as glucan) relative to total glucan available, including non-cellulosic glucan. All hydrolysis runs were performed in technical triplicate.

Water retention value

Water retention values (WRVs) were determined according to a modified version of TAPPI UM 256, as previously described [11], with a centrifuge speed of 4000 x g for 15 min. Briefly, approximately 2.5 g of wet pre-washed biomass samples were soaked in about 150 mL of either de-ionized water, or one of four NaCl solutions (0.25 M, 0.5 M, 0.75 M, and 1.0 M). After soaking for 1 hr, samples were rinsed with around 200 mL of de-ionized water to remove salts

and vacuum filtered using a 200-mesh Buchner filter. Washed biomass was inserted into a spin-column (Handee Spin Column Cs4, Thermo Scientific) with a 200-mesh stainless steel membrane. Biomass was added to form a circular cake devoid of large spaces, with care taken to avoid inducing drainage of biomass from pressing into column. Non-bound water was drained via centrifugation at 4000 x g for 15 min. The mass of the drained biomass was determined using tared aluminum trays, and dried in an oven at 105°C for at least 3 hr, then weighed again. The WRV was determined as the ratio of the mass of water remaining in the biomass after centrifuging divided by the mass of dry biomass. WRV was determined in technical triplicate.

Solute exclusion

Solute exclusion was performed following the original protocol outlined by Stone and Scallon [25], using a series of neutral dextran probes of increasing molecular weight, with some minor modifications to the procedure. **Table 3.1** lists the probes used in this study, which were obtained from Sigma-Aldrich. For this, approximately 5.0 g of wet, or 1.0 g of oven dried biomass was added to tared 50-mL centrifuge tubes and re-weighed after biomass addition.

About 10 mL 0.4% (w/v) dextran solution by was added to each tube, and reweighed. Tubes were vortexed for thorough mixing, and stored at 4°C for 48 hr, with periodic vortexing. A 1 mL sample was taken, centrifuged at 13,000 x g for 2 min, and transferred to a sealed vial for HPLC (Agilent 1100 Series) analysis. Biomass solids were thoroughly washed to remove the dextran probes in centrifuge tubes through dilution with water followed by centrifugation and solid-liquid separation, which was repeated three times. Centrifugation was performed at 900 x g for 3 min, with washed biomass dried overnight in a 105°C oven to determine oven dry biomass weight. Probe concentration was quantified using refractive index on the HPLC, with no column attached as described previously [19]. Blanks were used to determine any background or non-

dextran probe contributions to the refractive index signal. Inaccessible pore volume was determined as previously outlined [17]. Samples were performed in technical triplicate.

Probe Molecules	Mol. Mass ^a (Da)	Mol. Diameter ^b (Å)
D-(+)-Cellobiose	352	8
Dextran 6k	6000	39
Dextran 40k	40000	90
Dextran 70k	70000	110
Dextran 100k	100000	136
Dextran 450-650k	550000	310
Dextran 2000k	2000000	560

^a from the manufacturer. ^b Interpolated from Stone and Scallon ¹⁵.

Table 3.1: Neutral dextran probes used in solute exclusion technique.

Enzyme binding

Enzyme binding experiments were performed on never-dried biomass using 0.2 g biomass (dry basis)/ 10 mL solution buffer solution containing a cellulase cocktail (Cellic CTec3).

Binding isotherms were determined for protein concentrations over a range of 0 to 3.0 mg/mL (protein content determined using nitrogen adsorption) in a 50 mM Na-citrate buffer solution at pH 5.2. Samples were mixed overnight at 4°C using rotary mixing (Intelli-Mixer, ELMI-tech, Newbury Park, CA). Bound protein mass was determined from the difference between unbounded protein in free solution to total initial protein concentration determined using the Bradford method [26]. Bound protein fraction was determined using a standard calibration curve of initial protein concentrations. Bound enzyme fractions were determined from linear fit of bound enzyme for the linear region of the Langmuir adsorption isotherm as described in our previous work [11]. Samples were performed in technical duplicate.

Results and discussion

Composition analysis and enzymatic hydrolysis

Composition profiles of residual solids after AHP delignification, LHW pretreatment, and combinations of the two as shown in **Figure 3.1**. These conditions were selected to generate three distinct feedstock groups with significantly different residual solids compositions that exhibit a wide range of materials for properties testing.

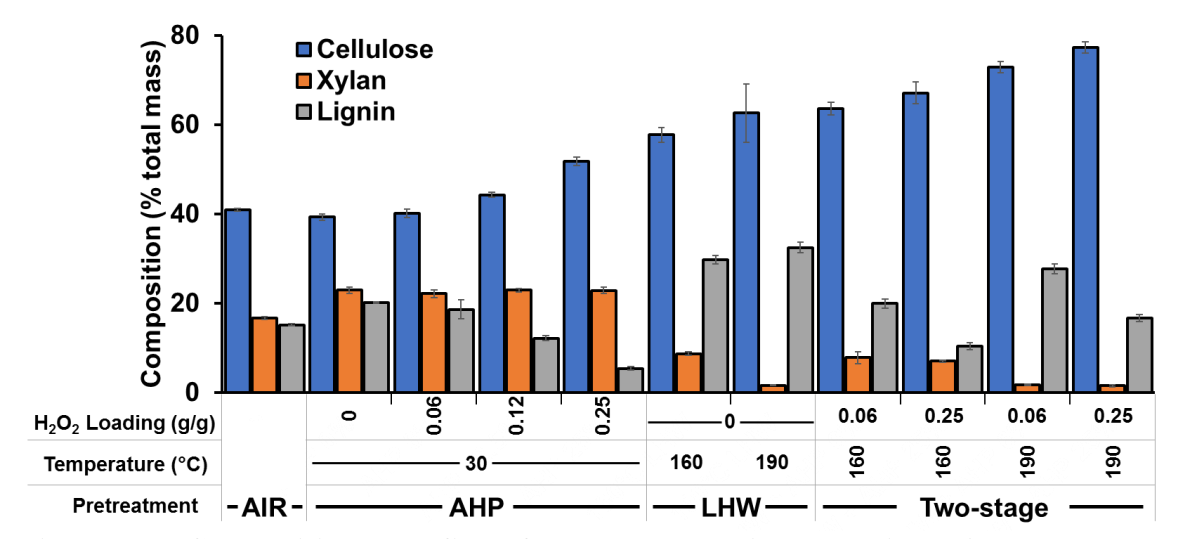


Figure 3.1 : Compositional profiles of corn stover subjected to either AHP pretreatment, LHW, or LHW followed by AHP pretreatment. Compositional profiles for xylan, crystalline cellulose, and Klason lignin are shown for alcohol insoluble residue (AIR) corn stover and pretreated biomass. Composition analysis was performed in technical triplicate (n = 3), with standard deviations shown on figure.

The results show that AHP-delignified biomass demonstrated a clear trend of increasing lignin removal with increasing H₂O₂ loading (**Figure 3.1**) while retaining most of the xylan as demonstrated in our previous work [27]. The LHW-pretreated biomass showed significant xylan removal through solubilization, with the 160°C condition containing about 8% residual xylan by mass, while the 190°C LHW condition had near complete removal of xylan. Residual biomass was enriched in cellulose and lignin content for both conditions [28]. The combination of LHW pretreatment followed by AHP delignification was performed at two AHP loadings (0.06 and

 $0.25~g~H_2O_2/g~biomass)$ for both LHW pretreatment conditions to generate pretreated feedstocks with modified xylan and lignin content. These pretreatment combinations represent a wide range of altered cell wall composition, with cellulose accounting for up to 80% total mass for the most severe pretreatment condition (**Figure 3.1**). Interestingly, the lowest H_2O_2 loading for AHP delignification ($0.06~H_2O_2/g~biomass$) for both LHW-pretreated biomass at both $160^{\circ}C$ and $190^{\circ}C$ resulted in significantly higher removal of lignin compared to the same AHP delignification conditions, and may be due to lignin relocalization associated with LHW pretreatment above the glass transition temperature increasing lignin accessibility to removal by AHP after LHW pretreatment.

Subsequent enzymatic hydrolysis was performed on never-dried pretreated biomass using either a cellulase cocktail (Cellic CTec3) or a combined cellulase/hemicellulase cocktail (CTec3 + HTec3) to measure the impact of cell wall composition and, indirectly, the modification of the higher order structure of the cell wall matrix by pretreatment, to the rate and extent of cellulose enzymatic hydrolysis. Results for 6-hr and 72-hr glucose hydrolysis yields, representing initial rate and final extent of hydrolysis respectively, are shown in **Figure 3.2**.

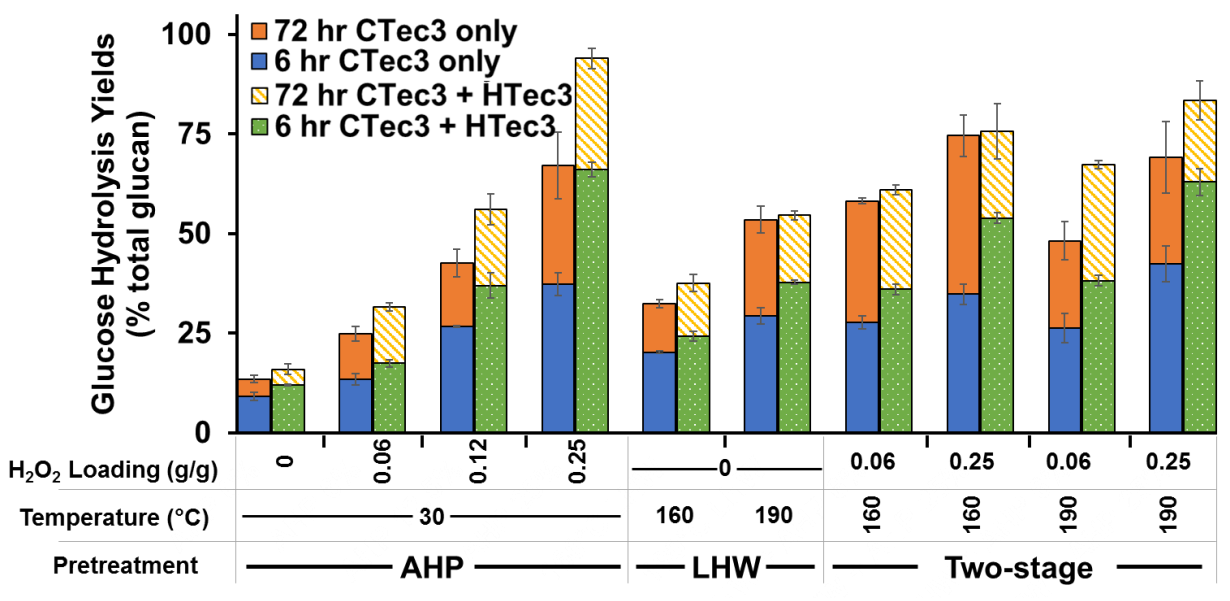


Figure 3.2 : Enzymatic hydrolysis glucose yields of pretreated corn stover samples. Results of never-dried hydrolysis of pretreated samples for 6 hr total hydrolysis time are plotted in blue and dotted green, while 72 hr total hydrolysis times are plotted above in orange and striped gold. Solid bars represented hydrolysis conditions using only 20 mg protein/g glucan cellulase loading, while patterned bars represent hydrolysis conditions using both 20 mg protein/g glucan and 10 mg protein / g glucan hemicellulase loading. Analysis was performed in technical triplicate.

These results show that enzymatic hydrolysis using a cellulase and hemicellulase cocktail on the AHP-only pretreated biomass resulted in high (94%) glucose hydrolysis yields at the highest H₂O₂ loading, while LHW-pretreated biomass achieved only a 54% glucose yield at the highest severity. Interestingly, a glucose yield of only 83% was observed for the highest severity two-stage pretreatment, which can be attributed to cell wall structural changes from the two-stage pretreatment limiting enzymatic hydrolysis. Reductions in cellulose accessibility resulting from cellulose aggregation induced by sufficient removal of non-cellulosic components in the cell wall would explain both reduced hydrolysis kinetics, as well as limited cellulose hydrolysis [29].

The cellulase enzyme cocktail used in this study (*i.e.*, CTec3) has been shown to contain a suite of accessory enzymes including xylanase and pectinase activities [30]. Furthermore, this cocktail is capable of effectively hydrolyzing pretreated biomass with low to moderate

hemicellulose content without any additional accessory enzymes [30]; however, significantly lower yields are observed in pretreated feedstocks containing a substantial fraction of the original xylan, such as the AHP-only samples [31]. In the AHP-only case, delignification may increase enzymatic hydrolysis effectiveness, however as reported in prior studies, cellulose accessibility is likely inhibited by both lignin and xylan content [32], with lignin limiting accessibility to xylan-coated cellulose microfibrils. Therefore, for AHP-only pretreated biomass, we can hypothesize that without removal of xylan, significant regions of the cell wall matrix remain partially inaccessible to cellulase binding. This result is further exemplified by the similar yields observed between the cellulase only and cellulase plus hemicellulase for the 160°C LHW twostage pretreatments (Figure 3.2), which contain significantly lower xylan content compared to the AHP-only pretreatments. Enzymatic hydrolysis using only the cellulase cocktail also resulted in notable lower 6-hr glucose hydrolysis yields for all samples, indicating that lack of xylanase and pectinase hinders initial hydrolytic rate of cellulases due to xylan limiting cellulose accessibility. This conclusion is further supported by higher initial yields associated with highly delignified samples, with delignification acting as an alternative avenue to increase enzyme accessibility [33].

Non-productive adsorption may also play a role in limiting enzymatic hydrolysis effectiveness, as there was a noted increase in enzymatic hydrolysis yields between the cellulase only and cellulase plus hemicellulose cases for the two-stage 190°C LHW-pretreated biomass, as xylan content accounted for less than 2% of total cell wall mass. This result indicates higher overall enzyme loading may limit the effect of non-specific binding of enzymes to lignin by providing more protein for adsorption to the charged surface of lignin, effectively neutralizing the lignin surface and promoting cellulase adsorption to cellulose.

Cell wall swelling in response to increasing solvent ionic strength

Water retention value is a property that can be used to capture a number of different structural features of the cell wall matrix as they relate to cell wall association with water. As demonstrated in our recent work, WRV can be used to predict enzymatic hydrolysis in two different alkaline pretreatments under a range of conditions [34], with WRV able to capture higher order changes in the cell wall associated with nanoscale porosity and cellulose accessibility in compositionally diverse pretreated samples. WRV is used similarly in this study to understand changes in higher order structure, however WRV are lower in this work due to changes in methodology increasing the amount of dewatering compared to prior work [11].

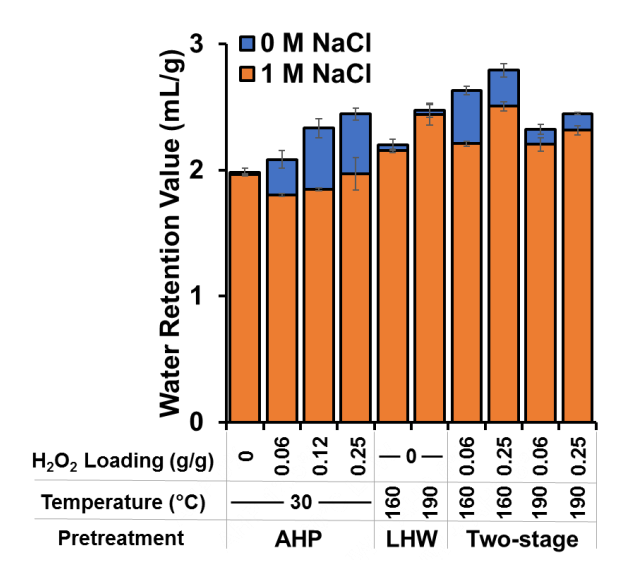


Figure 3.3 : Cell wall swelling measured using water retention in the absence and presence of a salt. Water retention value (WRV) of never-dried corn stover at varying pretreatments measured after incubation in water only (blue bars) or 1 M NaCl (orange bars). Samples were performed in technical triplicate (n = 3), with standard deviation shown on figure.

In the present work, the WRV without an added solute was found to increase with increasing H_2O_2 loading in the AHP-only pretreatment case, as well as increasing severity for LHW pretreatment (**Figure 3.3**). Increases in WRV were also observed between low and high H_2O_2 loading for individual two-stage pretreatments. These results indicate delignification by

AHP and xylan removal by LHW pretreatment can increase the amount of water associated with the cell wall matrix. A noted decrease in WRV in the 190°C LHW two-stage pretreatments may be attributed to two contributions; the first suggesting delignification in low-xylan cell walls removes sufficient spacer components that could be hypothesized to result in cellulose aggregation and collapse of the cell wall matrix, limiting available sites for water entrapment. The second contribution may be due to lignin content making up a larger composition fraction of the 190°C LHW two-stage pretreatments compared to the AHP-only and 160°C LHW two-stage pretreatment, and subsequently limiting the amount of cell wall swelling.

The values for WRV in the presence of an added solute showed noted decreases for the high H₂O₂ loading AHP-only samples, as well as 160°C LHW two-stage pretreatments, while no decrease in WRV was observed in the 0 g/g H₂O₂ AHP-only sample or the LHW only samples. The impact of increasing solvent ionic strength on cell wall water retention has been investigated largely in the context of pulp and paper applications [35]. From our results, delignification appears to be the primary contributor to solute-induced changes in WRV, and can be interpreted as a change in cell wall rigidity. Within the secondary cell walls of grasses, lignin forms a rigid matrix, with ferulate-mediated cross-links between within lignin and between lignin and xylans preventing physical cell wall expansion in response to the solvent environment [36.37]. Lignin content within the cell wall correlates to the extent of enzymatic hydrolysis in grasses, with greater than 50% cell wall delignification associated with high (>80%) hydrolysis yields [9]. Disruption of lignin structure through sufficient cleavage of cross-links and solubilization can be proposed to contribute to a loss of cell wall rigidity, allowing the cell wall to exhibit hydrogel-like behavior in the presence of solutes.

The equilibrium swelling of hydrogels is known to depend on factors that include the cross-link and charge densities of the polymer networks, while increases in the number of ionic groups in hydrogels can increase the swelling capacity by increasing osmotic pressure that driving the infiltration of solvent into the polymer network [38]. This behavior has been observed in carboxymethyl cellulose gels and to a lesser extent sulfite pulps, which exhibited changes in WRV corresponding roughly to the content of acidic groups [35]. AHP pretreatment has been shown to increase the cell wall carboxylate content [11], which would explain the swelling behavior of AHP-delignified biomass, although solute-induced changes in WRVs are not as pronounced as prior work using chlorite-delignified pulps [39]. The extent of non-covalent physical association of cell wall components contributes to the ability of the cell wall to swell, as cell wall swelling not as pronounced in the two-stage 190°C LHW-pretreated biomass, which can be hypothesized to be due to partial cell wall coalescence.

Accessible volume distributions determined by solute exclusion

A set of dextran probes was next employed to assess the accessible nanoscale volume within the pretreated biomass. Accessible volume distributions were determined by subtraction of inaccessible volumes from the inaccessible volume at the largest probe size (560Å), representing the total volume for a sample [15]. It should be noted that these volumes are not direct measurements of cell wall pores, rather effective pore diameter based upon idealized probe diameter in solution [40]; and thus, will be referred to as probe diameter in this work, shown in **Figure 3.4**.

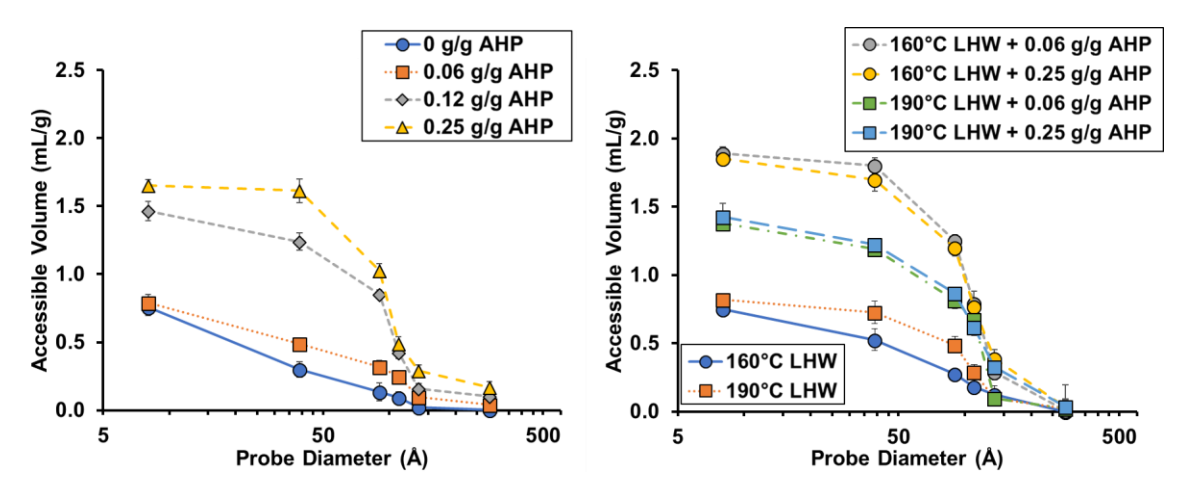


Figure 3.4: Accessible volume distributions measured by solute exclusion. Accessible volumes of never dried corn stover were determined using neutral dextran probes of average molecular weight range (see **Table 3.1**), giving a range of effective hydrodynamic radiuses. (A) AHP-only pretreatment conditions and (B) LHW and the two-stage pretreatments are shown on the right figure. Samples were performed in technical triplicate (n = 3), with standard deviation shown on figure.

From these results, there are clear differences in accessible volumes between AHP-only, LHW-only, and two-stage pretreatments. In the AHP-only samples, accessible volume was restricted to only smaller (<12 Å) probe sizes for the 0 g/g H₂O₂ pretreated sample, while increasing H₂O₂ loading resulted in significant increases in accessible volumes for both small and large probes, indicating the formation of larger (>39 Å) porous voids [15]. Studies using chlorite-delignified sugarcane bagasse have yielded highly similar accessible volume distributions to the AHP-only pretreated samples in this work, indicating that delignification of diverse graminaceous biomass feedstocks results in similar cell wall responses, and that lignin removal may result in the formation of water-accessible surfaces within the cell wall [21].

Accessible volume distributions in the LHW samples showed some noted increases accessible volumes for probes between 39-136 Å between the 160°C LHW and 190°C LHW condition, however larger probe volumes were similar to the 0 g/g AHP-only pretreated sample. In addition, overall accessible volumes were considerably lower compared to AHP-only

pretreated samples, indicating limited accessible volume formation in LHW-only samples. One explanation for the limited accessible volumes observed in LHW only samples may be due melting and relocalization of lignin during pretreatment from spaces between cellulose microfibrils to the cell wall surface [41] together with xylan solubilization that may result in coalescence of cellulose microfibrils, decreasing the enzyme accessibility of the cellulose (**Figure 3.5C**).

For sequential two-stage pretreatment, low H₂O₂ loading coupled with the 160°C LHW pretreatment condition resulted in accessible volume distributions comparable to the highest H₂O₂ loading for AHP-only pretreatment condition. Increased H₂O₂ loading of the 160°C LHW condition resulted in higher accessible volumes for the larger probes coupled to minimal increases in smaller probe accessible volumes. This trend was also observed between the low and high H₂O₂ loading for the 190°C LHW condition, and likely indicates the formation of larger porous regions with increased H₂O₂ loading rather than the formation of more porous regions in the cell wall as observed in the AHP-only conditions. Smaller probe (<136 Å) accessible volumes were also considerably lower in the 190°C LHW two-stage pretreatments compared to the 160°C LHW conditions, and support the previously proposed mechanism of either a collapse of inter-lamellar layers within the cell wall at high overall pretreatment severity, or through cellulose aggregation reducing cell wall porosity due to the lack of xylan to act as a spacer [29]. Based upon results from enzymatic hydrolysis, WRV, and solute exclusion, the following model (Figure 3.5) was derived for cell wall changes resulting from pretreatment.

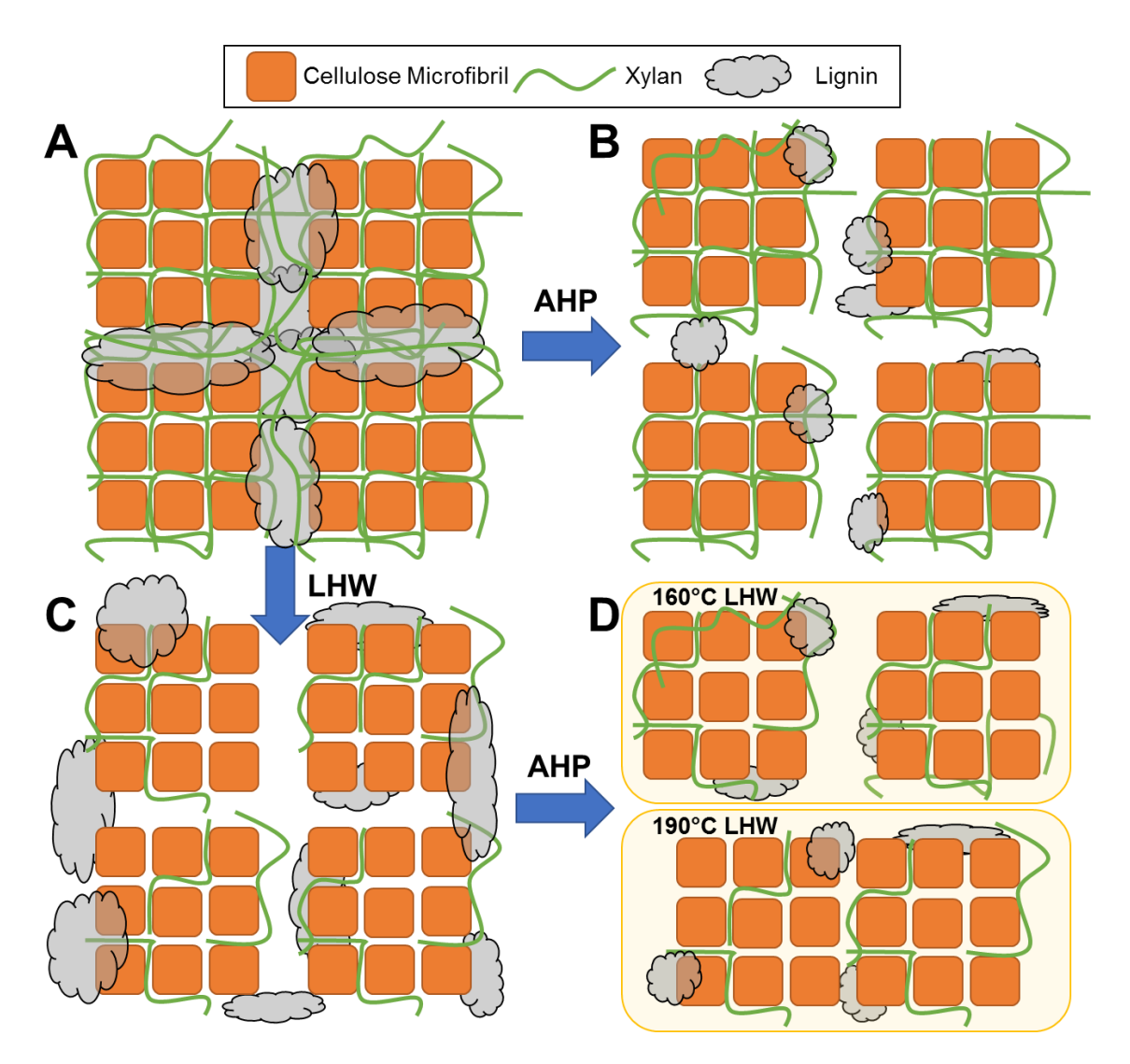


Figure 3.5: Structural model for pretreatment effect on cell wall organization. Transverse section of cellulose microfibrils for (A) native cell wall, (B) AHP-pretreated cell wall, (C) LHW-pretreated cell wall, and (D) two-stage AHP pretreated LHW cell wall. AHP pretreatment results primarily in reduction in lignin content, promoting the formation of porous regions and inducing cell wall swelling. LHW pretreatment primarily removes xylan and relocalizes lignin, increasing accessible surface area. Two-stage pretreatments contain significant reductions in both xylan and lignin content, increasing porous regions, and in the case of 190°C LHW, sufficient non-cellulosic component removal results in cell wall aggregation. Orange squares representing cellulose microfibrils, green lines representing xylan and gray clouds representing lignin.

Drying-induced pore collapse on cell wall properties and enzymatic hydrolysis

Drying-induced hornification was investigated for select pretreatment conditions to determine the impact that changes in higher order structure of pretreatment-modified cell walls

have on cell wall swelling, accessible volumes, and enzymatic hydrolysis yields in compositionally diverse samples.

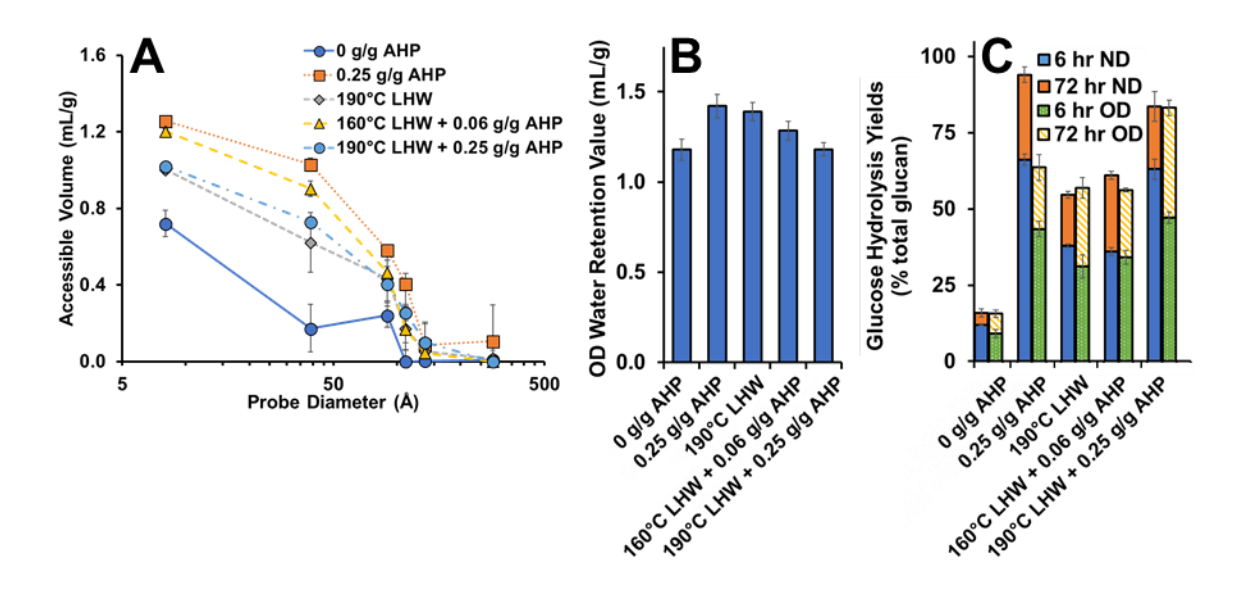


Figure 3.6: Impact of oven drying on cell wall properties and enzymatic hydrolysis. (A) Accessible volumes of oven-dried and rehydrated corn stover were performed similarly to Figure 3.4. (B) Water retention value (WRV) of oven dried corn stover at varying pretreatments. (C) Hydrolysis yields for oven-dried (OD) samples with 6-hr total hydrolysis time are plotted in blue, and 72-hr total hydrolysis time are plotted in orange. Comparative hydrolysis yields for never-dried (ND) 6-hr and 72-hr total hydrolysis time from Figure 3.2 are shown as green dotted and yellow striped bars respectively. Hydrolysis conditions used 20 mg protein/g glucan CTec3 and 10 mg protein / g glucan HTec3 loading. Experiments were all performed in technical triplicate, with standard deviations are shown on each figure.

The results show that oven-drying resulted in significant changes in accessible volume distributions (**Figure 3.6A**), with decreases in accessible volume observed to some extent for all samples relative to the never-dried samples. There was however, a stark contrast in how significantly accessible volumes decreased, with samples subjected to AHP delignification, demonstrating highly altered accessible volumes compared to 0 g H_2O_2 / g biomass AHP and $190^{\circ}C$ LHW only pretreated biomass, which demonstrated only minimal loss of accessible

volumes [42]. Furthermore, there was a noted decrease in volumes accessible to larger probes in samples subjected to AHP delignification. These results can be related to the structural model presented in **Figure 3.5**, with drying resulting in the collapse of larger porous regions within the cell wall (**Figure 3.5B**), while samples containing higher fractions of lignin (**Figure 3.5C**) maintained their ability to sorb water within nanoscale pores [43].

WRVs were also observed to substantially decrease (Figure 3.6B), with all samples experiencing at least a 40% decrease in WRV after drying and exhibited a closer distribution of WRV between pretreated biomass compared to the never-dried WRV. Hornification has been demonstrated to reduce accessible internal surface area within delignified wood fibers that limits water sorption [44,45]. This can be visualized in **Figure 3.5D**, with oven-drying removing water and resulting in the irreversible coalescence of some cell wall components [46]. For the enzymatic hydrolysis yields after oven-drying, the biomass delignified at high H₂O₂ loadings demonstrated the largest decrease in 6-hr hydrolysis yields (Figure 3.6C), followed by less significant decreases for the other pretreated samples. The 72-hr hydrolysis yields were only significantly lower in the 0.25 g/g AHP-only pretreated biomass. As the AHP-delignified biomass is the sample most impacted by drying-induced hornification, this indicates that the hydrated spaces within the cell wall of these samples, presumably containing mostly xylan, are most susceptible to irreversible coalescence. Interestingly, prior work using 0.50 g/g H₂O₂ AHPdelignification followed by lyophilization resulted in no differences in final hydrolysis yields [31]. Different methods of drying have been shown to influence extent of hornification, and have been explored in the context of altered cell wall properties [47].

Enzyme binding

As noted earlier, the commercial cellulase cocktail contains a number of accessory enzyme activities other than cellulase. As a result, the observed bound protein curves represent general protein binding rather than for binding of a specific cellulase. In addition, contributions from cell wall biopolymers other than cellulose (*i.e.*, hemicellulose and lignin) can contribute to the observed adsorption behavior through non-specific or non-productive binding [48]. However, binding isotherms are useful for assessing the impact of pretreatment on enzyme-accessible surfaces.

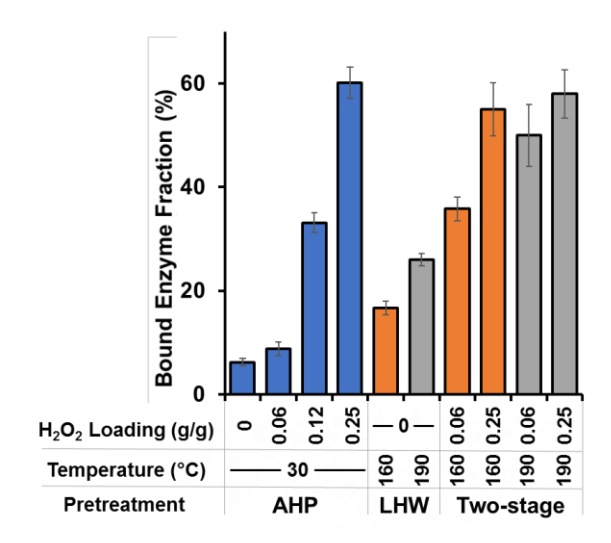


Figure 3.7 : Bound enzyme fractions of CTec3 on pretreated biomass. Bound enzyme fractions are shown as a percent of bound enzyme to total enzyme loading. Binding concentrations were performed in technical duplicate, with standard deviations shown on figure.

The results in **Figure 3.7** show the percent of bound enzyme measured as a fraction of total enzyme in solution for a linear range of enzyme loadings representing the linear, low-concentration region of the binding isotherm. The percentage of bound enzyme increased with increasing H₂O₂ loading for AHP-only pretreated biomass, comparable to results published in our prior work [11]. The LHW-only pretreated biomass had a lower percentage of bound enzyme

compared to the higher severity AHP-only pretreated biomass, indicating that structural changes induced by LHW pretreatment alone do not impact enzyme adsorption the same extent as AHP-delignification. The two-stage pretreatments showed increases in the fraction of bound enzyme with both H_2O_2 loading, and to a lesser extent with LHW pretreatment severity, however low H_2O_2 loadings were still comparable or higher than all but the highest H_2O_2 loading AHP-only pretreated biomass.

Correlation of properties

By correlating compositional and structural properties of pretreatment-modified plant cell walls to hydrolysis yields, a number of important trends can be identified that provide insight into the system.

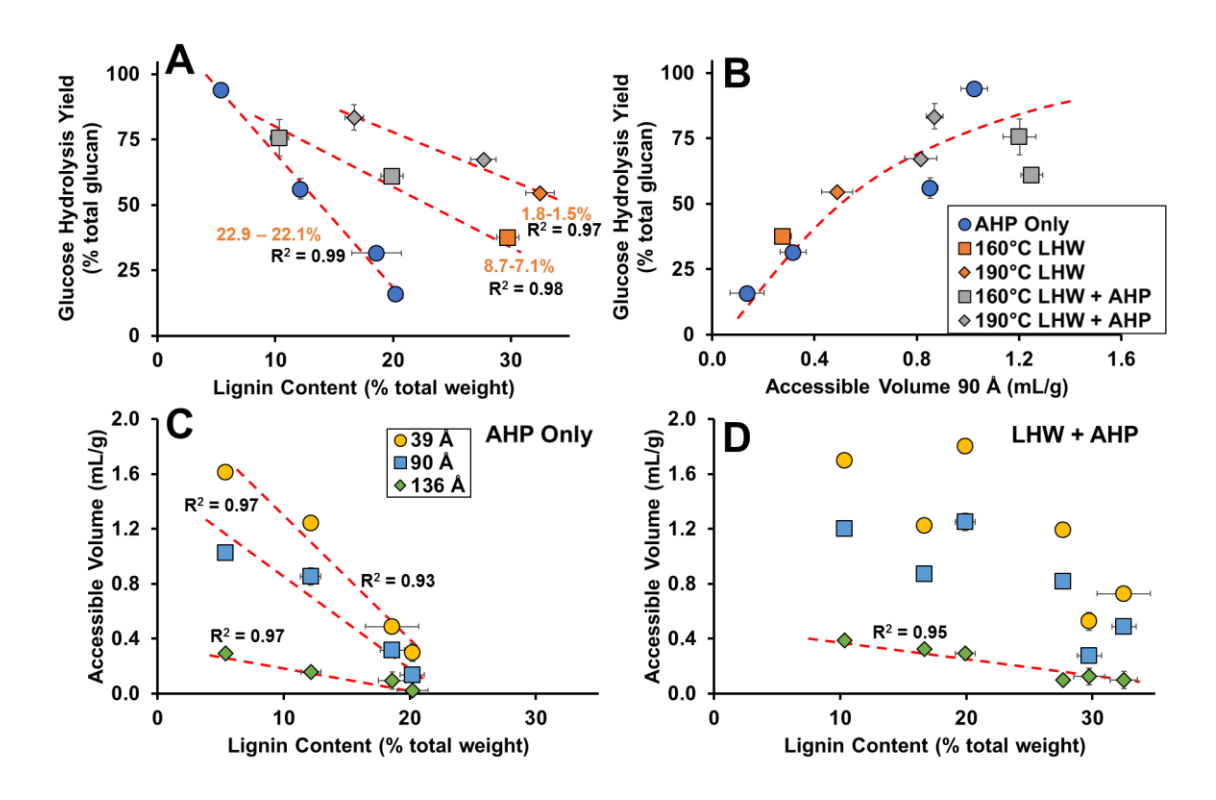


Figure 3.8 : Comparisons between glucose hydrolysis yields, solute exclusion, water retention value, and lignin content. (A,B) Glucose hydrolysis yields taken from **Figure 3.2** were from 72 hr total hydrolysis time using an enzyme solution of CTec3 and HTec3. Xylan content is displayed as a range for each linear trend in orange on (A). Accessible volume distributions (C, D) were used from **Figure 3.4**, and lignin content was taken from **Figure 3.1**.

The first major trend that can be observed is that comparing 72-hr glucose hydrolysis yields to lignin content (**Figure 3.8A**) shows three distinct linear relationships between AHP-only, and each LHW condition. From this, lignin content can be shown correlated to hydrolysis in the context of increased H₂O₂ loading, and therefore extent of delignification result in increased enzymatic hydrolysis yields. The major compositional difference between each grouping in **Figure 3.8A** is the amount of xylan present (shown as a range for each grouping on **Figure 3.8A**), which can be taken as a proxy for the extent of cell wall modification during LHW pretreatment.

Next it was observed was that glucose hydrolysis yields were positively correlated with 90 Å probe accessible volumes (Figure 3.8B). Cell wall volumes accessible to the 90 Å dextran probe were selected to correlate with hydrolysis yields, as 90 Å corresponds to a slightly larger probe size than necessary for reasonable estimation of typical cellulase (e.g., TrCel7A) [49]. Notably, as the accessible volumes increased, the 72-hr hydrolysis yields were observed to approach saturation. This trend is reasonable, because although accessible volumes may indicate increased accessibility within the cell wall for cellulases, there is likely a limit to the extent accessibility plays in increased enzymatic hydrolysis relative to other intrinsic factors [50]. Interestingly, for this data set the accessible volumes across multiple probe sizes were shown to directly correlate to lignin content, with AHP-delignified biomass exhibiting a strong negative correlation with accessible volumes at 39 Å, 90 Å, and 136 Å probe sizes (Figure 3.8C), while LHW-only and two-stage pretreated biomass accessible volumes correlated only to the 136 Å probe size (**Figure 3.8D**). These correlations indicate that for biomass subjected to AHP delignification, increases in the nanoscale probe-accessible volumes can be directly related to the extent of delignification as proposed in the schematic in **Figure 3.5B**. Accessible volumes

observed in AHP-delignified biomass also likely contribute to enzyme penetration within the cell wall, with prior correlations between enzyme binding and accessible pore volumes shown in sulfite pretreated hardwoods [49] and alkali-delignified hardwoods [51].

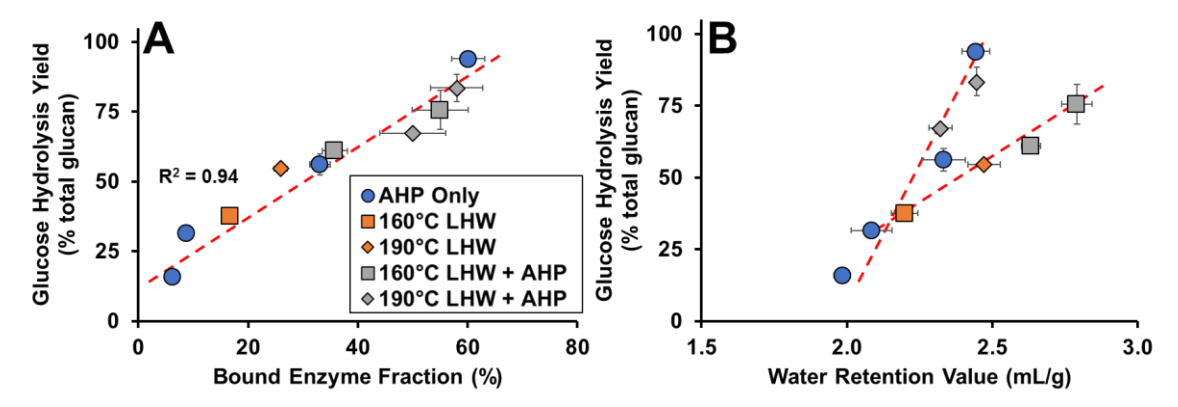


Figure 3.9 : Comparisons between glucose hydrolysis yields and (A) bound enzyme fractions and (B) water retention value. Glucose hydrolysis yields taken from **Figure 3.2** were from 72 hr total hydrolysis time using an enzyme solution of CTec3 and HTec3. WRV were taken from **Figure 3.3**, and bound enzyme fractions were taken from **Figure 3.7**.

The fraction of bound enzyme was demonstrated to exhibit a strong positive correlation to glucose hydrolysis yields irrespective of pretreatment conditions or composition (**Figure 3.9A**). This result is not surprising as cellulase binding and glucose hydrolysis yields are well-known to be correlated in diverse feedstocks subjected to diverse compositional changes resulting from pretreatment [11,32]. Correlation plots of WRV versus 72-hr hydrolysis yields two distinct trends (**Figure 3.9B**), with the AHP-only pretreatment resulting in a clear linear trend between WRV and hydrolysis yields as demonstrated in our prior work [11,34], while a second trend with a different slope was observed for the two-stage 160°C LHW-pretreated biomass. No trend was observed for the two-stage 190°C LHW-pretreated biomass followed by AHP delignification (**Figure 3.9B**), and based upon these results, there appears to be some relationship between glucose hydrolysis yields with water-accessible surface area in pretreated biomass not exhibiting cell wall coalescence due to significant non-cellulosic component removal. In addition, these

distinct, pretreatment-dependent trends are comparable to what we identified in our prior work with AFEX-pretreated corn stover or switchgrass exhibiting distinct trends for at different ammonia loadings [34].

As a final correlation between properties, WRV has also been proposed as a proxy for measuring fiber saturation point (FSP) [52], which is generally defined as the total inaccessible volume at 560 Å [15]. Additionally, WRV and FSP are hypothesized to measure similar properties in pulps [53]. Linear comparisons between the WRVs and FSPs for never-dried and oven-dried pretreated biomass measured show distinct linear trends (**Figure 3.10**).

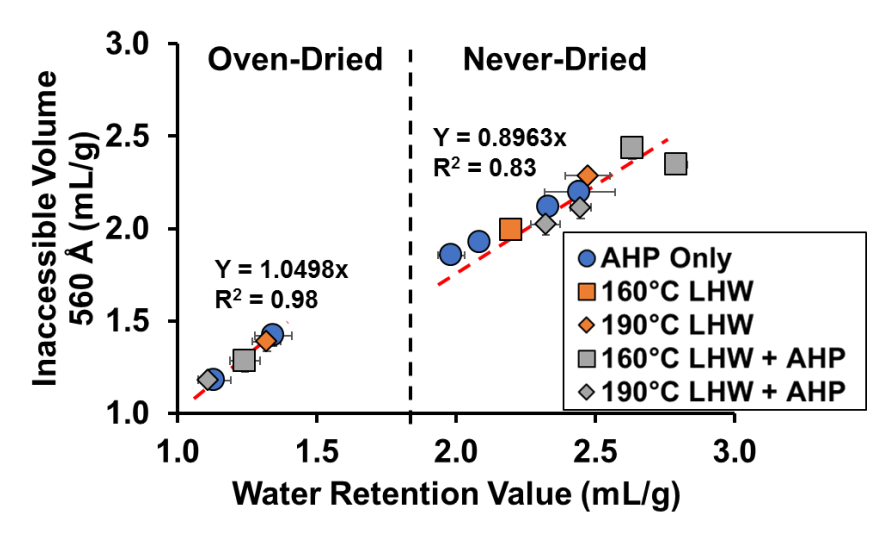


Figure 3.10 : Comparison of inaccessible pore volume to water retention value. Total inaccessible pore volume was determined using solute exclusion at the effective pore size of 560 Å and compared to WRV (0 M NaCl) from **Figure 3.3.**

In the never-dried samples, the slope of the linear relationship was less than one, indicating WRV measurements were higher than the equivalent inaccessible volume measurement. This is important, because one of the limitations of the solute exclusion method resides in the inability for water in porous regions with non-uniform or narrow openings to interact with the dextran probes during the solute exclusion technique [17], while WRV accounts for water localized within porous regions of irregular geometries [25]. After oven drying, the slope between

inaccessible volume and WRV was effectively unity, indicating that the solute exclusion and WRV techniques quantify similar cell wall properties after oven drying. The substantial drop in these properties is clearly attributed to hornification, resulting in the collapse of certain cell wall porous regions and reductions in accessible surfaces shown previously (Figure 3.6). Based upon this comparison, WRV likely over-measures total accessible surface area compared to the FSP in the never-dried case, which may be due to WRV also incorporating water-cell wall binding in the form of intra-lamellar water association within cellulose microfibrils or between microfibrils not be quantified by the FSP. Based upon the two-stage LHW pretreated biomass exhibiting higher WRV relative to FSP (Figure 3.10) compared to the AHP-delignified only biomass, this may be an appropriate evaluation, as xylan removal could increase water-cellulose microfibril interactions [54], while still being inaccessible to quantification by the solute exclusion method.

Conclusions

In summary, AHP delignification and LHW pretreatment of corn stover in this study yielded a series of compositionally diverse feedstocks exhibiting significantly different cell wall properties that were used to assess how both compositional and structural features impact cell wall recalcitrance to enzymatic hydrolysis. Specifically, we were clearly able to demonstrate that, while the mechanisms by which AHP and LHW pretreatment improve cellulose accessibility are dramatically different, both pretreatment types were shown to increase hydrolysis yields, enzyme sorption, and WRV. AHP delignification was shown to result in the substantial increase in the accessible volume to a series dextran probes, while LHW pretreatment resulted in only changes to smaller pore distributions. Solute-induced cell wall swelling measured by WRV showed AHP-delignified pretreatments displayed partial loss of cell wall rigidity, which may explain in part larger accessible volume distributions and increased porosity in AHP-delignified biomass. Overall, this study highlights the importance that cell wall

organization and its modification during processing during biorefining can have on feedstock response to enzymatic hydrolysis.

APPENDIX

APPENDIX B: Supplementary figures and additional results

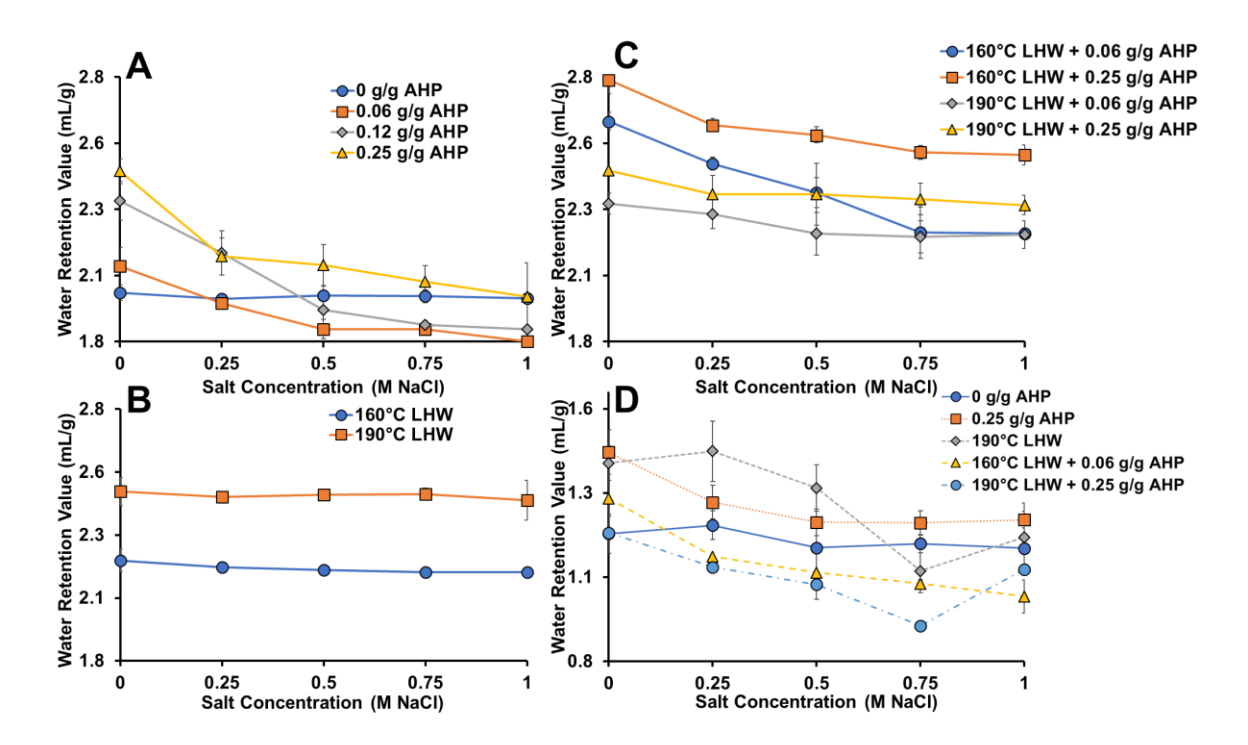


Figure 3.11 : Solute-induced swelling of biomass at multiple salt concentrations. Water retention value (WRV) of never dried and oven dried corn stover at varying pretreatments measured without salt (0 M NaCl), and after soaking in salt solutions (0.25 -1 M NaCl). (**A**) shows AHP-only pretreatment conditions, (**B**) shows LHW-only pretreatment conditions, (**C**) shows two-stage pretreatment conditions, and (**D**) shows oven-dried pretreatments tested. Samples were performed in technical triplicate (n = 3), with standard deviation shown on figure.

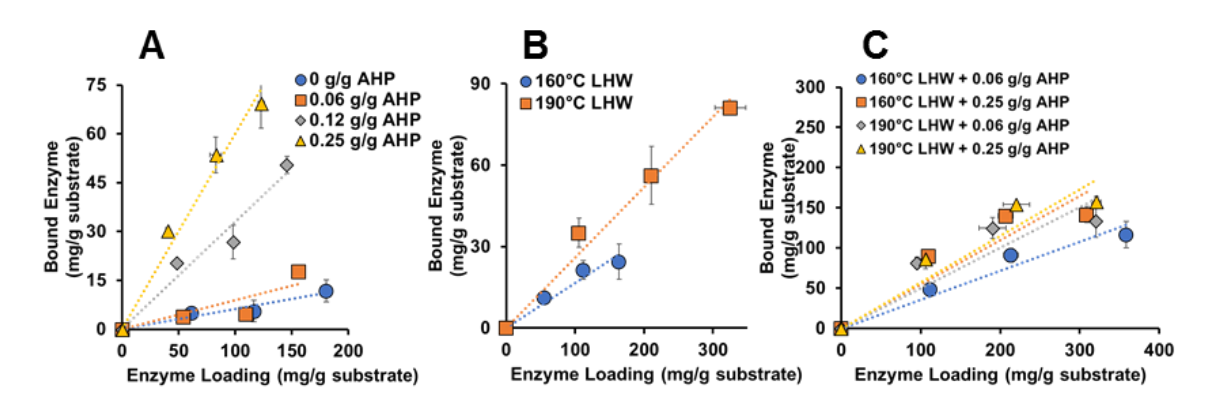


Figure 3.12: Enzyme binding curves of CTec3 on never-dried biomass and linear fits for bound enzyme fractions. Bound CTec3 concentrations are displayed as individual data points, with a linear best fit representing the relative ratio of bound enzyme to total enzyme loading. (A) shows AHP-only pretreatment conditions, (B) shows LHW-only pretreatment conditions, and (C) shows two-stage pretreatment conditions. Binding concentrations were performed in technical duplicate (n = 2), with standard deviations shown on figure.

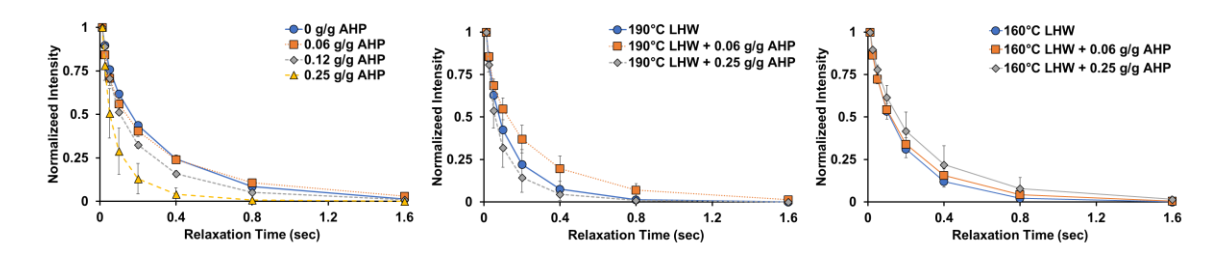


Figure 3.13: T2 NMR relaxation curves of water interacting with pretreated biomass. (A) Relaxation curves of AHP-only pretreatment samples, (B) relaxation curves of 160° C LHW and two-stage pretreatments, and (C) relaxation curves of 190° C LHW and two-stage pretreatments. Samples were performed and fitted in technical duplicate (n = 2), with standard deviations shown on figure.

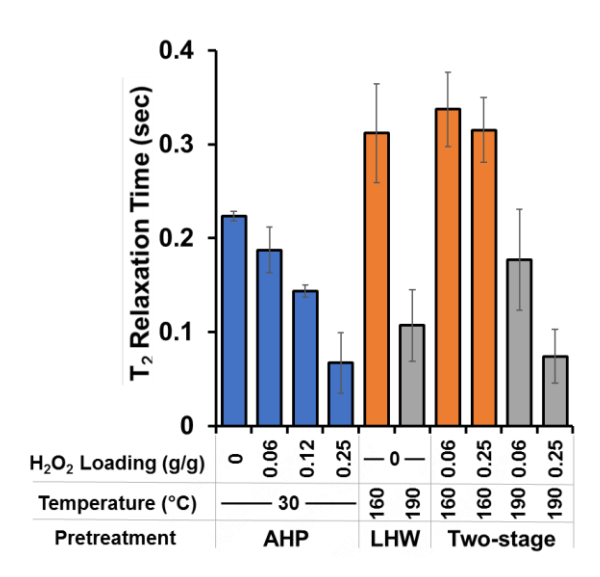


Figure 3.14: T_2 NMR relaxation curves monocomponent T_2 relaxation times. Relaxation times were determined from a mono-exponential component fit of each relaxation curve. Samples were performed and fitted in technical duplicate (n = 2), with standard deviations shown on figure.

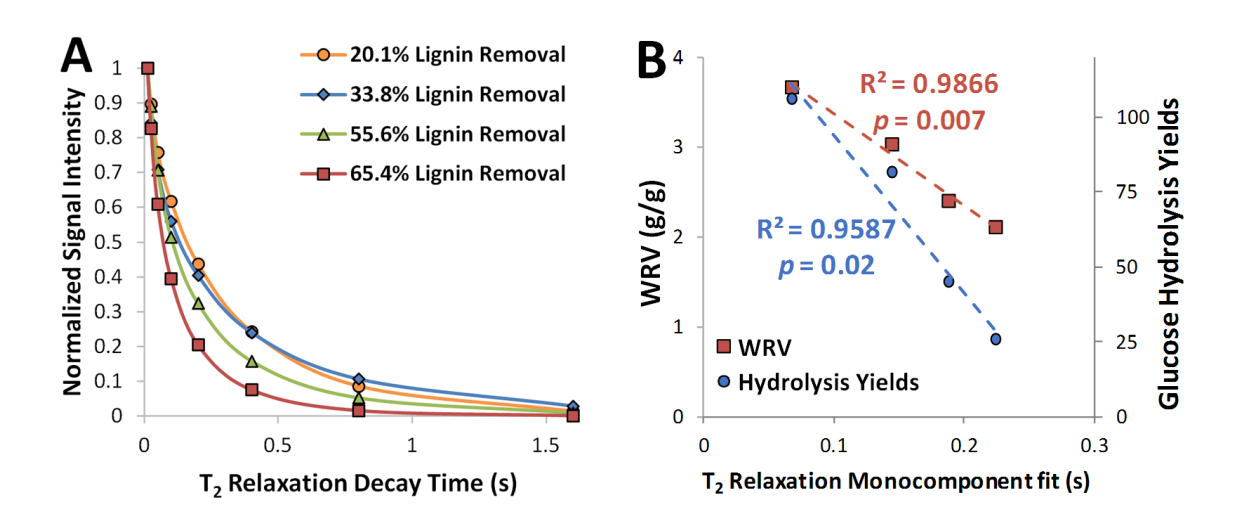


Figure 3.15: ¹H-NMR relaxometry of AHP-delignified corn stover showing (A) spin-spin (T₂) relaxation curves and (B) correlation of monocomponent exponential fits of these relaxation curves to the corresponding WRV and glucose hydrolysis yield.

The following was published as part of an original research paper submitted to Bioresource Technology. It is of note that the data used in this study is not the same data presented earlier in

this supplementary, rather from earlier work performed. However, the methods and objectives were similar, and therefore included in the Appendix.

 1 H spin-spin (T₂) NMR measurements were carried out in a Bruker static probe at frequencies of 300.103MHz on a Varian 300 MHz NMR interfaced with a Dell Precision T3500 desktop running CentOS 5.6 with VnmrJ 3.2A. Spin-spin relation times were determined using a standard 2D Carr-Purcell-Meiborn-Gill (CPMG) sequence with a 5 μs (90°) 1 H pulse, 10 μs (180°) 1 H pulses, 16 scans, 10 s recycle delay and $\tau = 0.0002$. Eight data points were recorded with 4 to 1024 echoes, and data was analyzed and reported as a monocomponent exponential fit of the data [6]. Technical replicates were performed at a constant temperature (25 °C) and a sample total solids content of 25% (wt sample per wt total).

Another approach to measure physical and chemical environment involves using T₂ NMR relaxometry to assess water constraint. Similar to DSC, T₂ NMR relaxometry provides a quantifiable relationship between biomass-water interactions, and results are dependent on both the physical and chemical environment experienced by the solvent, with more solvent constraint resulting in shorter T₂ relaxation curves. Monocomponent exponential decay curves from CGMG T₂ relaxation studies for AHP-delignified corn stover (**Figure 3.15A**) showed a general trend of increased chemical constraint with increasing extent of delignification. Relaxometry curves were similar for low and moderate lignin removal, however become increasingly more constrained as more lignin was removed.

Increased water constraint is an indication of increased hydrogen bonding associated with biomass, and may be due to delignification increasing available hydroxyl content and carboxyl content [11] or due to increased accessibility to cellulose for hydrogen bonding rather than changes in surface area or particle size affecting porosity [14]. These conclusions are further

supported by the correlation between T₂ monocomponent exponent fits and enzymatic hydrolysis yields (**Figure 3.15B**), indicating that systems with more constrained water, have greater cellulose accessibility and result in higher enzymatic hydrolysis yields. The linearity between WRV and T₂ monocomponent exponent fits (**Figure 3.15B**) indicates that WRV and T₂ NMR relaxometry likely quantify the same biomass properties in AHP-delignified samples.

REFERENCES

REFERENCES

- 1. Himmel, M. E.; Ding, S. Y.; Johnson, D. K.; Adney, W. S.; Nimlos, M. R.; Brady, J. W.; Foust, T. D: **Biomass recalcitrance: Engineering plants and enzymes for biofuels production**. *Science*. 2007, **315**:804-807.
- 2. Ding, S.-Y.; Liu, Y.-S.; Zeng, Y.; Himmel, M. E.; Baker, J. O.; Bayer, E. A: **How does** plant cell wall nanoscale architecture correlate with enzymatic digestibility? *Science*. 2012, **338**:1055-1060.
- 3. Pauly, M.; Gille, S.; Liu, L.; Mansoori, N.; Souza, A.; Schultink, A.; Xiong, G: **Hemicellulose biosynthesis**. *Planta*. 2013, **238**:627-642.
- 4. Vanholme, R.; Demedts, B.; Morreel, K.; Ralph, J.; Boerjan, W: Lignin biosynthesis and structure. *Plant Physiol.* 2010, **153**:895-905.
- 5. Ong, R. G.; Chundawat, S. P. S.; Hodge, D. B.; Keskar, S.; Dale, B. E: Linking Plant Biology and Pretreatment: Understanding the Structure and Organization of the Plant Cell Wall and Interactions with Cellulosic Biofuel Production. In *Plants and BioEnergy*. McCann, M. C.; Buckeridge, M. S.; Carpita, N. C., Eds. Springer New York: New York, NY, 2014; pp 231-253.
- 6. Meng, X.; Foston, M.; Leisen, J.; DeMartini, J.; Wyman, C. E.; Ragauskas, A. J: Determination of porosity of lignocellulosic biomass before and after pretreatment by using Simons' stain and NMR techniques. *Bioresource Technol.* 2013, 144:467-476.
- 7. Jeoh, T.; Ishizawa, C. I.; Davis, M. F.; Himmel, M. E.; Adney, W. S.; Johnson, D. K: Cellulase digestibility of pretreated biomass is limited by cellulose accessibility. *Biotechnol Bioeng.* 2007, **98**:112-22.
- 8. Zhao, X.; Zhang, L.; Liu, D: **Biomass recalcitrance. Part I: the chemical compositions and physical structures affecting the enzymatic hydrolysis of lignocellulose**. *BioFPR*. 2012, **6**:465-482.
- 9. Li, M.; Foster, C.; Kelkar, S.; Pu, Y.; Holmes, D.; Ragauskas, A.; Saffron, C.; Hodge, D: Structural characterization of alkaline hydrogen peroxide pretreated grasses exhibiting diverse lignin phenotypes. *Biotechnol Biofuel.* 2012, **5**:38.
- 10. Leu, S.-Y.; Zhu, J. Y: Substrate-related factors affecting enzymatic saccharification of lignocelluloses: Our recent understanding. *BioEnerg Res.* 2013, 6:405-415.
- 11. Williams, D.; Hodge, D: Impacts of delignification and hot water pretreatment on the water induced cell wall swelling behavior of grasses and its relation to cellulolytic enzyme hydrolysis and binding. *Cellulose*. 2014, **21**:221-235.

- 12. Chandra, R.; Ewanick, S.; Hsieh, C.; Saddler, J. N: The characterization of pretreated lignocellulosic substrates prior to enzymatic hydrolysis, Part 1: A modified Simons' staining technique. *Biotechnol Prog.* 2008, 24:1178-1185.
- 13. Liu, H.; Zhu, J. Y.; Chai, X. S: In situ, rapid, and temporally resolved measurements of cellulase adsorption onto lignocellulosic substrates by UV-vis spectrophotometry. *Langmuir.* 2011, **27**:272-8.
- 14. Weiss, N. D.; Thygesen, L. G.; Felby, C.; Roslander, C.; Gourlay, K: **Biomass-water** interactions correlate to recalcitrance and are intensified by pretreatment: An investigation of water constraint and retention in pretreated spruce using low field NMR and water retention value techniques. *Biotechnol Prog.* 2017, **33**:146-153.
- 15. Stone, J. E., A. M. Scallan: A structural model for the cell wall of water swollen wood pulp fibres based on their accessibility to macromolecules. *Cellul Chem Technol.* 1968, 2:343-358.
- 16. Stone, J. E., A. M. Scallan: The Effect of Component Removal Upon the Porous Structure of the Cell Wall of Wood. *Pulp Pap Mag Can.* 1968, **69**:69-74.
- 17. Beecher, J. F.; Hunt, C. G.; Zhu, J. Y: **Tools for the Characterization of Biomass at the Nanometer Scale**. In *The Nanoscience and Technology of Renewable Biomaterials*. John Wiley & Sons, Ltd: 2009; pp 61-90.
- 18. Park, S.; Venditti, R. A.; Jameel, H.; Pawlak, J. J : Changes in pore size distribution during the drying of cellulose fibers as measured by differential scanning calorimetry. *Carb Polym.* 2006, **66**:97-103.
- 19. Ishizawa, C. I.; Davis, M. F.; Schell, D. F.: **Johnson, D. K., Porosity and Its Effect on the Digestibility of Dilute Sulfuric Acid Pretreated Corn Stover**. *J Agric Food Chem.* 2007, **55**:2575-2581.
- 20. Grethlein, H. E: The effect of pore-size distribution on the rate of enzymatic-hydrolysis of cellulosic substrates. *Nat Biotechnol.* 1985, **3**:155-160.
- 21. Junior, C. S.; Milagres, A. M. F.; Ferraz, A.; Carvalho, W: The effects of lignin removal and drying on the porosity and enzymatic hydrolysis of sugarcane bagasse. *Cellulose*. 2013, **20**:3165-3177.
- 22. Pihlajaniemi, V.; Sipponen, M. H.; Liimatainen, H.; Sirviö, J. A.; Nyyssölä, A.; Laakso, S: Weighing the factors behind enzymatic hydrolyzability of pretreated lignocellulose. *Green Chem.* 2016, **18**:1295-1305.
- 23. Foster, C. E.; Martin, T. M.; Pauly, M: Comprehensive compositional analysis of plant cell walls (lignocellulosic biomass) part II: carbohydrates. *J Vis Exp.* 2010, 37.

- 24. Sluiter, J. B.; Ruiz, R. O.; Scarlata, C. J.; Sluiter, A. D.; Templeton, D. W: Compositional Analysis of Lignocellulosic Feedstocks. 1. Review and Description of Methods. *J Agric Food Chem.* 2010, **58**:9043-9053.
- 25. Stone, J. E., A. M. Scallan: The Effect of Component Removal Upon Porous Structure of Cell Wall of Wood: Swelling in Water and Fiber Saturation Point. *TAPPI J.* 1967, 50:496-501.
- 26. Bradford, M. M: A rapid and sensitive method for the quantitation of microgram quantities of protein utilizing the principle of protein-dye binding. *Anal Biochem.* 1976, 72:248-254.
- 27. Banerjee, G.; Car, S.; Liu, T. J.; Williams, D. L.; Meza, S. L.; Walton, J. D.; Hodge, D. B: Scale-up and integration of alkaline hydrogen peroxide pretreatment, enzymatic hydrolysis, and ethanolic fermentation. *Biotechnol Bioeng.* 2012, **109**:922-931.
- 28. Mosier, N.; Hendrickson, R.; Ho, N.; Sedlak, M.; Ladisch, M. R: **Optimization of pH controlled liquid hot water pretreatment of corn stover**. *Bioresour Technol*. 2005, **96**:1986-1993.
- 29. Ishizawa, C. I.; Jeoh, T.; Adney, W. S.; Himmel, M. E.; Johnson, D. K.; Davis, M. F: Can delignification decrease cellulose digestibility in acid pretreated corn stover? *Cellulose*. 2009, **16**:677-686.
- 30. Sun, F. F.; Hong, J.; Hu, J.; Saddler, J. N.; Fang, X.; Zhang, Z.; Shen, S: Accessory enzymes influence cellulase hydrolysis of the model substrate and the realistic lignocellulosic biomass. *Enz MicrobTechnol.* 2015, **79**:42-48.
- 31. Banerjee, G.; Car, S.; Scott-Craig, J. S.; Hodge, D. B.; Walton, J. D: Alkaline peroxide pretreatment of corn stover: effects of biomass, peroxide, and enzyme loading and composition on yields of glucose and xylose. *Biotechnol Biofuel*. 2011, 4:16.
- 32. Kumar, R.; Wyman, C. E: Cellulase adsorption and relationship to reatures of corn stover solids sroduced by leading pretreatments. *Biotechnol Bioeng.* 2009, **103**:252-267.
- 33. Lu, Y. P.; Yang, B.; Gregg, D.; Saddler, J. N.; Mansfield, S. D: Cellulase adsorption and an evaluation of enzyme recycle during hydrolysis of steam-exploded softwood residues. *Appl Biochem Biotechnol.* 2002, **98**:641-654.
- 34. Williams, D. L.; Crowe, J. D.; Ong, R. G.; Hodge, D. B: Water sorption in AFEX- and AHP-pretreated grasses as a predictor of enzymatic hydrolysis yields. *Bioresource Technol.* in review.
- 35. Grignon, J.; Scallan, A. M: Effect of pH and neutral salts uppon the swelling of cellulose gels. *J Appl Polym Sci.* 1980, **25**:2829-2843.

- 36. Ralph, J: **Hydroxycinnamates in lignification**. *Phytochem Rev.* 2010, **9**:65-83.
- 37. Boerjan, W.; Ralph, J.; Baucher, M: Lignin biosynthesis. *Annu Rev Plant Biol.* 2003, **54**:519-546.
- 38. Okay, O: **General properties of hydrogels**. In *Hydrogel sensors and actuators*. Springer: 2009, pp 1-14.
- 39. Carlsson, G.; Kolseth, P.; Lindstrom, T: **Polyelectrolyte swelling behavior of chlorite delignified spruce wood fibers**. *Wood Sci Technol*. 1983, **17**:69-73.
- 40. Grethlein, H. E: The effect of pore-size distribution on the Rate of Enzymatic Hydrolysis of Cellulosic Substrates. Nature *Biotechnol*. 1985, 3:155-160.
- 41. Selig, M. J.; Viamajala, S.; Decker, S. R.; Tucker, M. P.; Himmel, M. E.; Vinzant, T. B: Deposition of lignin droplets produced during dilute acid pretreatment of maize stems retards enzymatic hydrolysis of cellulose. *Biotechnol Prog.* 2007, 23:1333-1339.
- 42. Stone, J. E., E. Treiber, B. Abrahamson: Accessibility of Regenerated Cellulose to Solute Molecules. *TAPPI J.* 1969, pp 108-110.
- 43. Fernandes Diniz, J. M. B.; Gil, M. H.; Castro, J. A. A. M: Hornification—its origin and interpretation in wood pulps. *Wood Sci Technol.* 2004, **37**:489-494.
- 44. Luo, X. L.; Zhu, J. Y.; Gleisner, R.; Zhan, H. Y: Effects of wet-pressing-induced fiber hornification on enzymatic saccharification of lignocelluloses. *Cellulose*. 2011, **18**:1055-1062.
- 45. Luo, X.; Zhu, J. Y: Effects of drying-induced fiber hornification on enzymatic saccharification of lignocelluloses. *Enz Microb Technol.* 2011, **48**:92-99.
- 46. Pönni, R.; Vuorinen, T.; Kontturi, E: **Proposed nano-scale coalescence of cellulose in chemical pulp fibers during technical treatments**. *Bioresources*. 2012, **7**:6077-6108.
- 47. Wong, K. K.; Deverell, K. F.; Mackie, K. L.; Clark, T. A.; Donaldson, L. A: **The** relationship between fiber-porosity and cellulose digestibility in steam-exploded Pinus radiata. *Biotechnol Bioeng.* 1988, **31**:447-456.
- 48. Strobel, K. L.; Pfeiffer, K. A.; Blanch, H. W.; Clark, D. S: **Structural insights into the affinity of Cel7A carbohydrate-binding module for lignin**. *J Biol Chem*. 2015, **290**:22818-22826.
- 49. Wang, Q. Q.; He, Z.; Zhu, Z.; Zhang, Y. H.; Ni, Y.; Luo, X. L.; Zhu, J. Y: Evaluations of cellulose accessibilities of lignocelluloses by solute exclusion and protein adsorption techniques. *Biotechnol Bioeng.* 2012, **109**:381-389.

- 50. Mooney, C. A.; Mansfield, S. D.; Touhy, M. G.; Saddler, J. N: **The effect of initial pore volume and lignin content on the enzymatic hydrolysis of softwoods**. *Bioresource Technol*. 1998, **64**:113-119.
- 51. Meng, X.; Wells, T., Jr.; Sun, Q.; Huang, F.; Ragauskas, A: Insights into the effect of dilute acid, hot water or alkaline pretreatment on the cellulose accessible surface area and the overall porosity of Populus. *Green Chem.* 2015, 17:4239-4246.
- 52. Hui, L.; Liu, Z.; Ni, Y: Characterization of high-yield pulp (HYP) by the solute exclusion technique. *Bioresource Technol.* 2009, **100**:6630-6634.
- 53. Scallan, A. M.; Carles, J. E: Correlation of water retention value with fiber saturation point. *Svensk Papperstid.* 1972, **75**:699.
- 54. Olsson, A. M.; Salmen, L: The association of water to cellulose and hemicellulose in paper examined by FTIR spectroscopy. *Carbohydr Res.* 2004, **339**:813-818.

Chapter 4: Impact of impaired xylan biosynthesis on cellulose microfibril organization in Arabidopsis thaliana secondary cell walls

Introduction

Secondary cell walls represent a key biological and biomechanical component integral to vasculature, strength, and development in land plants. With the main role of primary cell walls to control cell elongation and determine cell shape, secondary cell walls are deposited after cell wall growth to impart mechanical strength and promote upright growth of the plant [1]. The secondary cell wall is generally comprised of three major classes of polymers, cellulose, hemicelluloses, and lignin, which together form a three-dimensional cell wall matrix.

Cellulose is the major biopolymer present in both primary and secondary cell walls, and is composed of linear chains of (1,4)-linked-β-D-glucosyl residues, which stack together with other cellulose chains via inter- and intra- hydrogen bond networks and van der Waals forces to form cellulose elementary microfibrils [2]. Cellulose is synthesized at the plasma membrane by cellulose synthase enzymes that are organized into multi-protein cellulose synthase complexes (CESA), with 10 CESA isoforms in *Arabidopsis thaliana*. Three distinct CESA isoforms are required for normal synthesis, with CESA1, CESA3, and CESA6 involved in primary cell wall synthesis [3], while CESA4, CESA7, and CESA8 are required for secondary cell wall synthesis [4]. Specific cellulose orientation in parallel arrays within the cell wall is thought to be for structural strength, imparted by cortical microtubules [5], however recent evidence has shown cortical microtubules are not necessary to maintain directionality [6]. Live cell imaging of CSCs during secondary cell wall formation indicate that dense formations of CSC complexes contribute to the assembly of closely associated cellulose microfibril sheets and move in

unidirectional concerted fashion [6] in epidermal cells transdifferentiated into secondary cell wall-synthesizing xylem-like cells [7].

In higher plants, the structure of xylans are comprised of a β -(1-4)-linked xylosyl backbone with a multitude of side chain modifications, resulting in arabinoxylans, glucuronoxylans, (arabino)glucuronoxylan, (glucurono)arabinoxylan, and heteroxylans [8]. In dicots such as Arabidopsis, glucuronoxylan (GX) is the predominant xylan in the secondary cell wall, containing glucuronic (GlcA) or 4-O-methyl glucuronic acid (MeGlcA) substituted at the Xyl O-2 position on a xylosyl backbone [9], as well as acetylation at some O-2 and O-3 positions [10]. A reducing end terminal tetrasaccharide group of xylan comprised of a 4- β -D-Xyl-(1,4)- β -D-Xyl-(1,3)- α -L-Rha-(1,2)- α -D-Gal-(1,4)-D-Xyl is found in some dicots including Arabidopsis, and is thought to play a terminating role in xylan chain length during biosynthesis [11, 12].

Recent advances have identified many proteins involved in xylan biosynthesis and functional group addition, however the exact function of many of these genes is still unknown. Notably, synthesis of the xylosyl backbone is impaired when proteins of the glycosyltransferase family GT43 (IRX9, IRX9-L, IRX14, IRX14-L) or GT47 (IRX10, IRX10-L) gene families are mutated [13-15]. While the inferred function of these genes is xylan synthase activity, to date only IRX10, IRX10-L, and homologs of these exhibited xylan synthase activity *in vitro* by heterologous expression and purification [16, 17]. IRX9 function has been hypothesized as a non-catalytic role as a membrane anchor for a hypothetical larger xylan synthase complex, analogous to some pectin biosynthesis proteins [18]. In addition, likely methyl transferases from the DUF579 family of genes have been shown to affect xylan biosynthesis, with *IRX15 IRX15-L* genes identified to significantly reduce both xylan content, and average chain length [19, 20]. Together with *irx9* and *irx10* mutants, reductions in xylan chain length correspond to parallel

observations of higher than wild type ratios of MeGlcA/GlcA in all three mutants, and has been hypothesized to relate to GlcA methylation rate keeping pace with reduced glucuronoxylan backbone synthesis rate, resulting in the methylation of nearly all GlcA units in GX backbone mutants in *irx9* [11]. Glycosyl transferases from the families GT47 (FRA8 and FRA8H) and GT8 (IRX8 and PARVUS) mutations have been shown to impact the terminating tetrasaccharide group occurrence, resulting in dispersed distribution of glucuronoxylan chain lengths, and a reduction in amount of glucuronoxylan chains [11, 21, 22]. GlcA is substituted to the xylan backbone by the GT8 family GUX proteins (GUX1-5) [23]. Acetylation of xylan occurs via members of the ESKIMO1/TRICHOME BIREFRINGENCE-LIKE (ESK1/TBL29) protein family including ESK1 [17]. Knockout of xylan acetyltransferses result in reductions in xylan corresponding to collapsed xylem and dwarfed phenotype [24]. Methylation of glucuronic acid side units is controlled by GXMT proteins [25].

Many xylan mutants are categorized as part of a larger group of irregular xylem (*irx*) mutants, that represents a category of Arabidopsis mutants that have collapsed and deformed xylem vessels [26], and are attributed to perturbations of genes involved in secondary cell wall biosynthesis. To date, there are fifteen *irx* mutant phenotypes identified and excluding a collapsed xylem phenotype, a wide range of enzymes or transcription factors involved in the synthesis of all secondary cell wall components, giving *irx* mutants a diverse range of characteristics [27]. In addition, some mutants display pleiotropic effects, which convolute identification of cell wall response to gene perturbations. One hypothesis for irregular or collapsed xylem observed in *irx* mutants is due to the inability of the cell wall to organize spatially in a way conducive resist compressive forces during stem development [26], which may

be a result of reductions in cell wall components, or alterations to the molecular architecture of components.

The role of xylan structure and interactions with other polymers within the secondary cell wall matrix is not fully understood, however as the main hemicellulose in secondary cell walls of dicots, the loss of plant fitness with perturbations to both xylan structure and abundance suggests that xylan plays a crucial role in promoting normal plant growth and development. Xylan has been proposed to non-covalently coat cellulose microfibrils and crosslink cellulose microfibrils and covalently bind to other polymers [18]. Recent elucidations of substitution patterns [28, 29] coupled with molecular simulations [30] and direct NMR evidence [31] indicate that xylan hydrogen bonds to cellulose in a twofold helical screw confirmation (one 360° twist every two glycosidic bonds) in the secondary cell wall. Both cellulose structure [31] and xylan substitution patterns [32] impact xylan-cellulose binding patterns, as well as the availability for covalent interactions with lignin [27]. Electrostatic charge of xylan substitution may also impact hydrogen bonding interactions, as glucurosylation was shown to rescue the growth phenotype of acetyl deficient *tbl29* mutants [33].

Model systems such as bacterial cellulose synthesis have been employed to understand cellulose-polymer interactions during cellulose synthesis, with prior studies indicating that both xylan [34] and xyloglucan [35] can impact cellulose crystallization. Substituted mannans can also induce differential levels of cellulose fibril organization, with varying extent of microfibril non-covalent cross-links between individual fibrils depending upon mannan substitution frequency [36]. Mixed-linked glucans likely play a similar role to xyloglucans in primary cell walls as evidenced by mixed-linked glucan deficient rice mutants exhibiting fewer cellulose microfibril cross-links, likely resulting in a weakened cell wall [37]. Lignin perturbations in

Arabidopsis resulted in varied degrees of cellulose disorganization related to the severity of the lignin phenotype [38], and indicated cellulose microfibril organization within the secondary cell wall is likely dependent in part on electrostatic interactions imparted by non-cellulosic components. Furthermore, disrupted cell wall structure has been associated with reductions in stem mechanical strength, and indicates cell wall strength is directly related to secondary cell wall organization and regularity to maintain cell wall fitness [23].

While notable strides have been made in characterizing many genes and proteins associated with secondary cell wall synthesis, less focus has been placed on identifying the underlying structural mechanisms maintain cell wall regularity, with descriptors for cell wall phenotypes often limited to cell specific descriptors (i.e. *irx* - irregular xylem mutants). One major reason for limited information on the structural mechanisms resides in the difficulty of directly observing higher order interactions within the secondary cell wall, requiring indirect metrics to characterize cell wall organization through microscopy techniques or chemical analysis. In the case of xylan integration within the cell wall, molecular simulations and NMR evidence have implicated xylan side chain structure significantly impacts xylan-cellulose interactions, however the importance of xylan structure in promoting normal cellulose organization within the cell wall has not been directly observed to date. As such, there currently exists a barrier in the literature between understanding fundamental cell wall biosynthesis from the molecular perspective and translation of knowledge to observed macroscopic ultrastructural features.

The goals of this study are to characterize secondary cell wall organization in a series of altered xylan mutants to (1) demonstrate synergy between non-direct techniques of cell wall characterization and direct cell wall visualization to identify phenotypes and (2) explore the

fundamental role that xylan-cellulose interactions play in secondary cell wall organization and translate nanoscale cell wall observations to macroscopic properties; relating cell wall architecture and organization to function at the cellular and whole plant scale.

Materials and methods

Plant lines and growth conditions

Plant genotypes used were Arabidopsis wild type (*Col-0*) and T-DNA insertion mutants *irx9* (Salk_057033) [11], *irx10* (Salk_055673) [39], *irx15 irx15-L* (GK_735E12,FLAG_532A08) [20] and *irx15 irx15-L* complementation lines, *irx15 irx15-L IRX15-L* (Line #1) [20] and *irx15 irx15-L OE-IRX15-L* (Line #6) [20]. Seeds were planted in wet peat pellets and cold treated for 48 hours at 4 °C, then transfer to growth chamber. Light/dark period was 16/8 hours at light intensity 150 mE with light/dark temperature set at 23/20 °C. Humidity was not controlled. After three weeks in the peat, pellets plants and pellets were transferred to individual pots 8x8x12 cm with SureMix soil (Surefill, http://www.surefill.com/) and 3-4 plants per pot. Stems were harvested post senesce and lyophilized to moisture content 5% (g H₂O/g biomass). Samples post-milling were stored in air-tight containers for further use. Particle size reduction for water retention, wide angle x-ray scattering, and enzymatic hydrolysis was performed using a Wiley Mini-Mill (Thomas Scientific, Swedesboro, NJ) with a 30-mesh screen.

Composition analysis

Cell wall lignocellulosic material was isolated following extraction and de-starching procedure outlined [40] using three sequential washes of 70% ethanol, 1:1 methanol-chloroform, and acetone to obtain alcohol insoluble residue (AIR). AIR was destarched using 50 µg Amylase /ml H₂O (Bacillus species, Sigma-Aldrich, St. Louis, MO) and 18.7 units of Pullinase (*Bacillus acidopullulyticus*, Sigma-Aldrich, St. Louis, MO) in a 0.01% sodium azide solution, with rotary mixing at 37°C overnight.

Non-cellulosic neutral monosaccharide content of the wall matrix polysaccharides was obtained by treating de-starched AIR with trifluoracetic acid (TFA) followed by derivatization using the alditol acetate method with minor changes [40]. Crystalline cellulose content was isolated following TFA extraction using Updegraff reagent, followed by cellulose hydrolysis with 72% sulfuric acid and quantification of the subsequent monosaccharide with the anthrone colormetric assay. Acetyl bromide soluble lignin (ABSL) was determined as described previously [41]. Samples were performed in technical triplicate and biological quadruplicate (n = 12) unless otherwise specified.

Glycome profiling

Previously milled stem samples were further ball-milled with a TissueLyser II (Qiagen Inc., Germantown, MD) in preparation for sequential extraction. Sequential cell wall extractions and glycome profiling of switchgrass organs were carried out as described previously [42, 43] on AIR biomass. Plant glycan-directed monoclonal antibodies (mAbs) were from laboratory stocks (CCRC,JIM, and MAC series) available at the Complex Carbohydrate Research Center [44]. A description of the mABs used in this study can be found in the supplementary materials of prior work [45].

Wide angle x-ray scattering

XRD measurement were performed on a Bruker Davinci Diffractometer system (Bruker, Camarillo, CA). The diffracted intensity of Cu K α radiation (with Nickel filter; λ = 1.5418 Å; 40 kV and 40 mA) was measured in a 2 Theta range between 5° and 50° with Global Mirror method (Primary optics: 1.2 mm). The detector is in LYNXEYE ID mode and with a 3 mm slit. Milled sample mass for XRD measurement was about 1.5 g of total lower stem for each run. Sample collection was performed for 5 hours total time at 0.0128° step sizes with 10 seconds of exposure

at each step. Samples were performed in biological quadruplicate (n = 4). Extraction of cell wall components were performed using the same methodology as described in the Glycome profiling results. Relative crystallinity index (RCI) was determined following the peak difference method and peak area methods outlined [46] using Matlab v2012a (Mathworks, Natick, MA) for peak fitting with gaussian distributions for crystalline and amorphous peak contributions.

Tensile test

Air dried nine-week-old stem samples were selected from the first internode from the bottom for tensile testing. Diameters were measured using a digital micrometer at the bottom and top of each stem sample, giving an overall average. Tensile testing was performed on a United SFM-20 load frame (United Testing Systems Inc., Huntington Beach, California) using a 9.07-kg load cell. Samples were immobilized with an opposite twist 2.54 cm grip lined with 0.127 cm of self-adhesive, 0.127 cm of flexible poly-vinyl carbide, and self-adhesive 320 grit sandpaper, with a 2.54 cm rip separation. Testing to failure was performed at 0.127 cm/min using Datum 5i (United Testing Systems Inc., Huntington Beach, California) software to plot force versus elongation. Samples were performed with 20 biological replicates of stems (n = 20).

Scanning electron microscopy

Fresh nine-week stems were cut with a double-edged razor blade and fixed at 4C for 1-2 hours in 4% glutaraldehyde buffered with 0.1M sodium phosphate at pH 7.4. Following a brief rinse in the buffer, samples were dehydrated in an ethanol series (25%,50%,75%,95%) for 15 minutes at each gradation and with three 15 minutes changes in 100% ethanol. Samples were critical point dried in a Leica Microsystems model EM CPD300 critical point dryer (Leica Microsystems, Vienna, Austria) using carbon dioxide as the transitional fluid. Samples were mounted on aluminum stubs using high vacuum carbon tabs (SPI Supplies, West Chester, PA),

and System Three Quick Cure 5 epoxy glue (System Three Resins, Inc. Auburn, WA). Samples were coated with osmium (~10 nm thickness) in a NEOC-AT osmium CVD (chemical vapour deposition) coater (Meiwafosis Co., Ltd., Osaka, Japan). Samples were examined in a JEOL 7500F (field emission emitter) scanning electron microscope (JEOL Ltd., Tokyo, Japan). Samples were prepared using three biological stems for each sample, and images were acquired in triplicate (n = 3) at 200x, 14000x and 22000x magnification.

Atomic force microscopy

Air dried nine-week old stem samples were selected from the first internode from the bottom for analysis. Longitudinal samples were prepared by hand-cutting using a platinum tipped razor blade in a petri dish, and delignified using a solution of 0.1 N HCl with 10% NaClO₂ at 1% (w/v) biomass loading. Delignification occurred overnight at room temperature. After delignification, samples were thoroughly washed with double distilled H₂O until pH neutral. Samples were transferred wet to clean mica surface and allowed to air dry at room temperature.

Image collection was performed using a Bruker Dimension FastScan (Bruker, Camarillo, CA) equipped with an Acoustic and Vibration Isolation Enclosure, FastScan Scanner, Ultra-Stable High-Resonance Microscope Base, and a Nanoscope V Stage Controller and HV Amplifier. Scanning was performed using the PeakForce Mapping mode in air, with SCANASYST-AIR probes (Bruker, Camarillo, CA). Tips were silicon nitride with a nominal tip radius of 2 nm, a resonant frequency of 70 kHz, and a spring constant of 0.4 N/m, which was appropriate for the range of modulus tested in this study.

AFM operation and image pre-processing was performed in Nanoscope Analysis V1.5. All images were taken at 512 x 512 pixels, with four different scan sizes (2.5 μ m, 1.0 μ m, 0.5

 μ m, and 0.25 μ m) for each scan area, and at least three different scan areas measured for each sample (n = 3). All images were fitted with a third order flatten prior to analysis to center data, remove tilt, and remove bow caused by an uneven cell surface. Image roughness, fibril width measurements, and height distribution profiles were all calculated in NanoScope Analysis V1.5 software using the Roughness, Section, and Particle Analysis tools respectively.

Microfibril orientation and dispersion were measured using Directionality analysis based upon local gradient orientation on grayscale images using the Fiji is just ImageJ version of software (https://fiji.sc/). Nanomechanical properties (elastic modulus, adhesion, deformation, dissipation) were standardized to the same z-axis properties for direct comparison of image intensities. Elastic modulus is calculated based upon the Derjaguin-Muller-Toporov model [47]. Deformation represents to maximum penetration depth during tip-cell wall contact, and can be related to the elastic modulus [48]. The adhesion force represents the absolute value of the negative force during tip release from the surface [49]. Dissipation is calculated by integrating the area between the extension and retraction curves, and represents the difference in energy imparted from the AFM tip to the sample [50].

Results

Irx mutant phenotype, composition, and extractability

The mutants chosen for this study were three xylan *irx* mutants with T-DNA insertions in different genes with known specific expression in the secondary cell wall of xylem and interfascicular fibers. Individual mutants were selected to frame extent of mutants affecting xylan backbone chain elongation; *irx9* was used to represent a xylan synthase mutant with a strong growth phenotype, while *irx10* was used to represent a mutant with a weak phenotype. *Irx15 irx15-L* is a proposed methyl transferase that impacts xylan content and structure, as well as displays similar phenotypes to xylan synthase deficient mutants. Two *IRX15-L*

complementation lines of the *irx15 irx15-L* double mutant were also included to represent a single mutant *irx15* phenotype, which has shown wild type structure in prior work [20]. Complementation expressions had one line with 1-5 times wild type *IRX15-L* expression level, *irx15 irx15-L IRX15-L* (line 1, [20]), and one over-expressing *IRX15-L* 5-30 times, *irx15 irx15-L OE-IRX15-L* (line 6, [20]). All three mutants and complementation line have well-characterized reductions in xylan backbone chain length (**Figure 4.2B**) and altered ratios of MeGlcA/ GlcA; both features which may impact xylan interaction within the secondary cell wall.

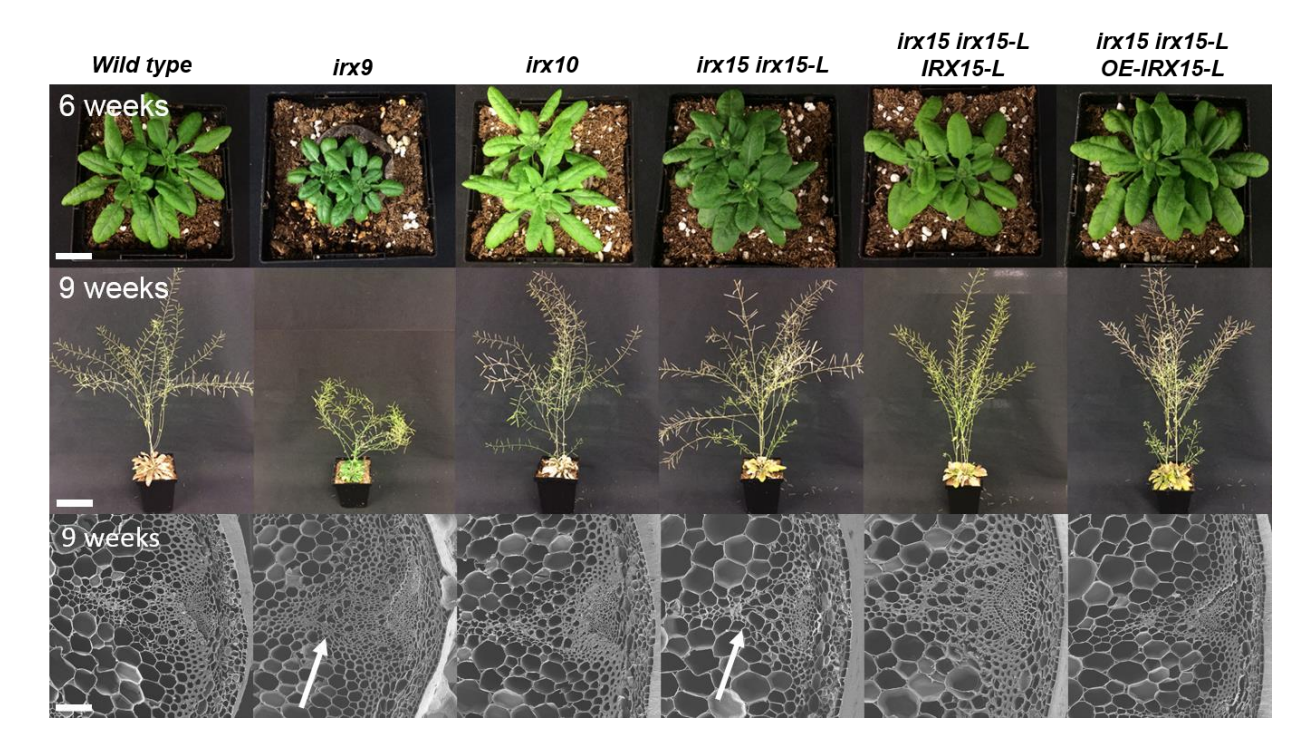


Figure 4.1 : Growth phenotypes of xylan *irx* **mutants.** Growth phenotypes were documented at week 6 and 9 as indicated. Arrows in SEM cross-section (lower row, irx9 and irx15 irx15-L) indicate the irregular xylem (irx) phenotype of collapsed xylem vessels. Scale bars for overhead growth photos are 1.8 cm, side growth photos are 8 cm, and SEM images are $100\mu m$.

Together with the wild type, these five genotypes were grown in parallel in several batches (**Figure 4.1**), and examined using SEM for phenotypic analysis. SEM analysis of stem cross-sections revealed collapsed xylem in *irx9*, along with significant reduction of secondary cell wall thickness, corresponding to prior reporting of up to 60% reduction in thickness

observed via TEM [11]. Reductions in secondary cell wall thickness were observed to a lesser extent in *irx15 irx15-L*, along with normal xylem cell shape and irregular interfascicular cell surface as reported previously [20]. *Irx10* is reported to exhibit minor phenotypic dwarfism and a moderate irregular xylem phenotype [39] which was not observed in our growth batches. This discrepancy may be due to *IRX10* and *IRX10-L* acting as functionally redundant genes, with IRX10-L compensating for a loss of IRX10 and suppressing the phenotype to an extent [15]. Complementation line *irx15 irx15-L IRX15-L* displayed a reversion to wild type interfascicular cell shape and size, as did *irx15 irx15-L OE-IRX15-L* at the SEM scale shown. No noticeable differences were observed in the cell structure of parenchyma-type secondary cell walls, indicating localization of mutant phenotype to vascular and interfascicular tissue (**Figure 4.12**) as previously reported [19, 20].

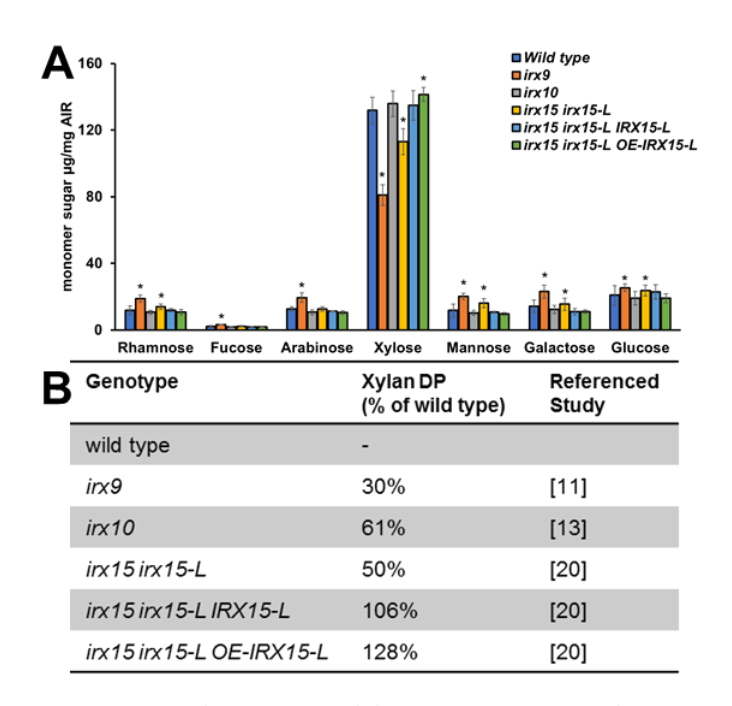


Figure 4.2 : Cell wall polysaccharide composition and xylan chain length. (**A**) Non-cellulosic cell wall neutral monosaccharide content of irx mutant stems determined from TFA hydrolysis. Standard deviations are shown (n = 12, four biological replicates with three technical replicates for wild type, irx9, irx10, and irx15 irx15-L; n = 6, two biological replicates with three technical replicates for irx15 irx15-L irx15-L and irx15 irx15-L irx15-L). * indicates statistical significance from wild type (p < 0.05). (**B**) Xylan degree of polymerization (DP) percent compared to wild type as reported by prior studies.

Chemical composition analysis was also used to confirm the phenotype (**Figure 4.2A**), with reductions in xylan content corresponding to 61% xylan content in *irx9* and 85% in *irx15 irx15-L* compared to wild type, as documented prior in *irx9* [11], and *irx15 irx15-L* [19, 20]. In *irx9*, increases in rhamnose, arabinose, mannose and galactose suggest a higher presence of pectin or arabinogalactopectins (AGP). This could be a consequence of increased ratios of primary cell wall compared to secondary cell wall, or a compensation mechanism by the plant to supplement for lost function of xylan. Increased rhamnose and galactose content observed in *irx15 irx15-L* likely are due to increased proportion of reducing end tetrasaccharide structure resulting from shortened xylan chains. Overexpression of IRX15-L in *irx15 irx15-L OE-IRX15-L*

resulted in a 7% increase in xylan content compared to wild type, which has not been reported previously.

Another characteristic of *irx* mutants is the altered xylan chain length, or degree of polymerization (DP) presumably due to altered xylan synthase activity. Xylan DPs have been reported in individual mutants and complementation lines in previous studies, and were used in this study based upon prior reporting. **Figure2B** highlights the percent decrease in chain length reported in prior literature, along with the literature reference. To supplement visual cell wall characterizations as well as investigate the pleotropic effects of these mutants, crystalline cellulose (**Figure 4.3A**) and lignin contents (**Figure 4.3B**) were determined. To more comprehensively document the effect of *irx* mutants on cell wall deconstruction and extractability, glycome profiling was performed on *irx9*, *irx10*, and *irx15 irx15-L* (**Figure 4.3C**).

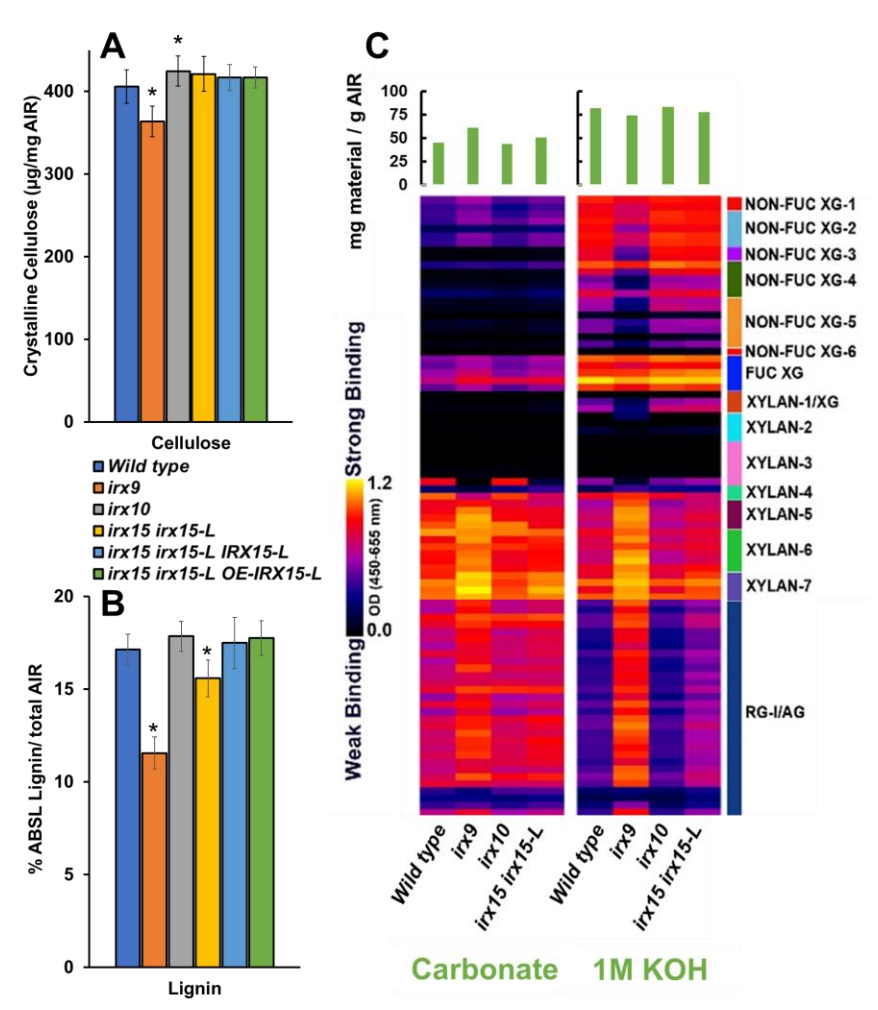


Figure 4.3 : Crystalline cellulose, lignin, and glycome profile analysis of cell wall material of *irx* **mutant stems.** (**A**) chemical quantification of crystalline cellulose content (**B**) and ABSL lignin content of cell wall material. Standard deviations are shown (n = 12, four biological replicates in three technical replicates each for wild type, irx9, irx10, and irx15 irx15-L; n = 6, two biological replicates with three technical replicates for irx15 irx15-L irx15-L and irx15 irx15-L indicates statistical significance compared to wild type (t-test, p < 0.05). (**C**) Cell wall material of wild type, irx9, irx10, and irx15 irx15-L inflorescence stems was extracted sequentially with increasing chemical severity using glycome profiling. A selected subset of antibodies and extracts are shown, while the full profile can be found in **Figure 4.13**

Crystalline cellulose content and lignin content were both significantly lower in *irx9* (90% of wild type cellulose and 65% of wild type lignin) compared to wild type, while only lignin content was moderately lower in *irx15 irx15-L* (91% of wild type lignin). Decreased lignin content corresponded to the observed reductions in secondary cell wall thickness, while reduction crystalline cellulose in *irx9* correspond to stunted growth and is not a direct

consequence of lost gene function [51]. *Irx10* displayed a small, but statistically significant increase in crystalline cellulose content (105% of wild type), indicating some level of phenotypic deviation from the wild type.

Glycome profiling was employed on sequentially extracted cell wall material to identify cell wall polysaccharide structure using a series of carbohydrate-specific antibodies. Glycome profiling is useful in identifying cell wall polysaccharide deconstruction patterns when subjected to increasing harsh chemical extraction, and can elucidate features relating to cell wall matrix organization and integration of cell wall polysaccharides. Glycome profiling results from carbonate and 1M KOH extracts revealed an overrepresentation of pectin and xylan epitopes in *irx9* and to a lesser extent *irx15 irx15-L* fractions, while *irx10* extractability was nearly identical to wild type. Specifically, xylan epitope extractability varied between *irx9* and *irx15 irx15-L*, with a higher presence of mAbs for Xylan4-7 clades in the carbonate fraction of *irx15 irx15-L* compared to wild type. Extractability of Xylan4-7 clades increased for *irx15 irx15-L* in the 1M KOH extract compared to wild type, indicating xylan may be more integrated into the cell wall, requiring harsher chemical extraction to remove from *irx15 irx15-L* cell walls compared to *irx9*, but more easily extracted compared to wild type or *irx10* xylan.

RG-I/AG pectic arabinogalactan epitopes were significantly higher in *irx9* compared to wild type in both carbonate and 1M KOH extracts, while noticeable differences between *irx15 irx15-L* and wild type pectins were identified only in the 1M KOH fraction. Xyloglucan epitope recognition was shown to differ only in *irx9*, and interestingly, the lack of individual xyloglucan epitope clades in *irx9*, indicating *irx9* most likely has structurally different xyloglucan compared to the wild type.

Relative crystallinity index measured by wide angle x-ray scattering

Differences in composition and extractability suggest changes to the cell wall organization that may result from deficiencies in cell wall components. Examining cellulose microfibril crystallinity using wide angle x-ray scattering (WAXS) is one non-destructive technique for probing the structure of cellulose and quantifying the relative crystalline order within a sample [52], and has been used previously to quantify changes in cellulose crystal order and size [53].

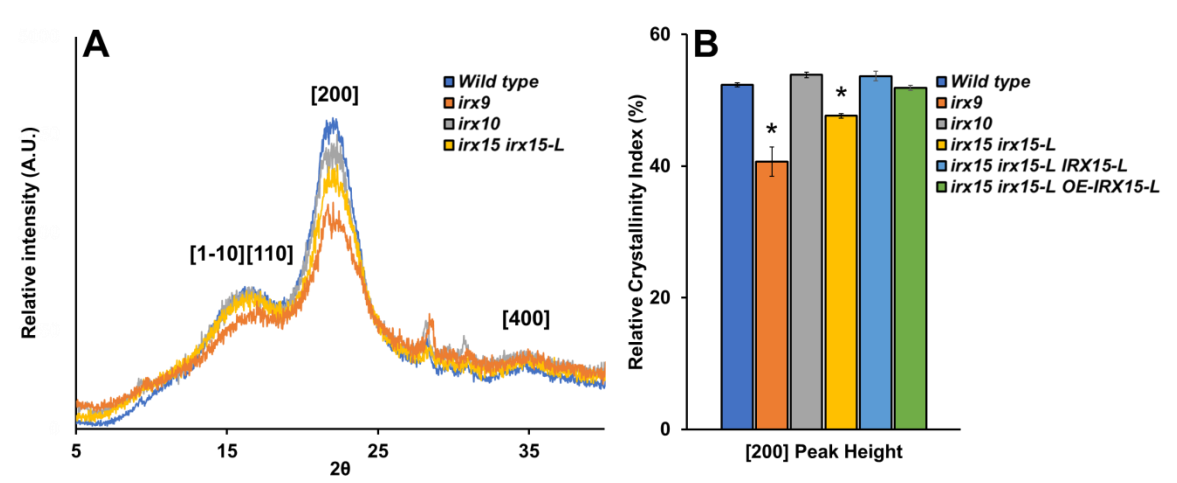


Figure 4.4 : WAXS diffraction pattern of *irx* **mutant stems and relative crystallinity index.** (**A**), representative WAXS diffraction patterns of wild type, irx9, irx10, and irx15 irx15-L stems showing the diffraction peaks for the [110], [1-10], [200], and [400] crystal faces. (**B**), relative crystallinity indexes (RCI) of the [200] peak face calculated from the WAXS diffraction pattern, such as the ones in (A). Standard deviations are shown (n = 4, biological replicates for wild type, irx9, irx10, and irx15 irx15-L; n = 4, two biological and two technical replicates for irx15 irx15-L irx15

WAXS diffraction patterns (**Figure 4.4A**) show qualitatively distinct tends in *irx9* and *irx15 irx15-L* compared to wild type, with a clear decrease in the [200] crystal face is observed relative to the [1-10] and [110] crystal faces, as well as a reduction in prominence of the [1-10] and [110] crystal faces compared to the amorphous baseline in only *irx9*. Quantification of relative crystallinity index (RCI) (**Figure 4.4B**) by the peak difference method [46] revealed a lower calculated RCI of the [200] crystal face in irx9 (22% lower) and *irx15 irx15-L* (9% lower)

compared to wild type. Reductions in RCI can be attributed to either a reduction in crystalline chains, or an increase in crystallite size [5, 54, 55]. In the case of *irx9*, reduced crystalline cellulose content measured chemically (**Figure 4.3A**) could account for the reduction in RCI, however cellulose content does not account for the RCI reduction observed in *irx15 irx15-L*.

Crystallinity measurements made in other mutant systems have indicated KORRIGAN1 Aspen Homolog PttCel9A1 impacts cellulose crystallinity through either increasing the relative amount of amorphous cellulose able to interact with hemicelluloses due to cellulose chains under tension during *endo*-hydrolysis, or through reduction of crystallite size [54]. Arabidopsis knockout studies of domains for CESAs such as, rsw2 [56], any1 [57], and CESA1aegeus/ CESA3^{ixr1-2} [53] have all shown reduced crystallinities attributed to reduced CESA glucan polymerization velocities, and would be expected to result in deficient cellulose due to modification of the CESA synthase. Studies examining higher order cellulose crystallinity due to non-cellulosic cell wall component modification have received significantly less attention, likely due to the limited knowledge of higher order interactions within the cell wall. Modifications in poplar to lignin syringyl content showed no changes to cellulose crystallinity, however inducing the formation of tension wood did significantly increase cellulose crystallinity, with increased crystallization likely due in part as a stress response [58]. Hemicellulose-cellulose crystallinity relationships have been observed in bacterial celluloses as mentioned earlier, however to date no study has observed cellulose crystallinity impacted by xylan within the secondary cell wall, and have mostly focused on cellulose orientation in primary cell walls due to multiple hemicelluloses [37, 48].

One of the hypothesized roles of xylan within the cell wall matrix is to act as an electrostatic spacer, associating via hydrogen bonding along the linear regions of the

polysaccharide chain with other hydrophilic polysaccharides such as cellulose and other xylans. Alterations to xylan structure and content may result in changes to inter-hydrogen bonding between cellulose microfibrils, resulting in more amorphous regions of cellulose compared to normal xylan. Conversely, sufficient removal of xylan may promote increases in crystallinity due to an absence of steric hindrance between cellulose microfibrils normally imparted by xylan. Hemicellulose chain length can impact hemicellulose-cellulose affinity, with shorter xylan chains have lower equilibrium concentration binding with bacterial celluloses compared to longer chain xylan [59]. This is important, as shorter xylan chain length is characteristic of *irx9* [11] and *irx15 irx15-L* [20], and may implicate altered xylan-cellulose interactions which correspond to altered cellulose crystallinity. However, lower xylan DP may only result in noted changes in cellulose crystallinity if accompanied by reduced xylan content, as no noted reductions in crystallinity were observed in *irx10*, or the *irx15 irx15-L* complementation lines.

For completeness and transparency, relative crystallinity index using the peak area method was calculated as well, yielding similar conclusions for irx9 and irx15 irx15-L (**Figure 4.14**), albeit the difficulty of fitting all peaks resulted higher errors associated with the technique. Relative crystallite size of the [200] face determined using the Sherrer correlation [60] were found to be around 4.3 nm on average for all samples, which was comparable to prior studies [61, 62] and indicated no significant change in crystallite size (**Figure 4.14C**). Similar calculated crystallite sizes indicate that changes in cellulose were limited to changes in cellulose crystalline chain abundance rather than crystallite size, which is reasonable given the ability for changes in hydrogen bonding networks to impact cellulose crystallinity [63].

Interfascicular ultrastructure is altered in *irx* mutants

To more thoroughly investigate the ultrastructural organization of the secondary cell wall, SEM and AFM were performed as complimentary microscopy techniques [64]. SEM was performed on native, freshly harvested stems that were dehydrated and coated with osmium (~10 nm), providing information on native cell wall shape and surface features, while AFM was performed on chlorite-delignified, air dried samples to directly examine the cellulose microfibril layers of the secondary cell wall. Metal coating in SEM likely renders features observed at the nm scale smaller or unresolved, while AFM requires chemical modification of the surface, but provides nanoscale resolution. Interfascicular cells were examined as model cells for the impact of *irx* mutants on secondary cell wall biosynthesis [65]. Direct comparison of SEM and AFM images at similar scale are shown in **Figure 4.5**, highlighting comparable ultrastructural scales observed by two different techniques.

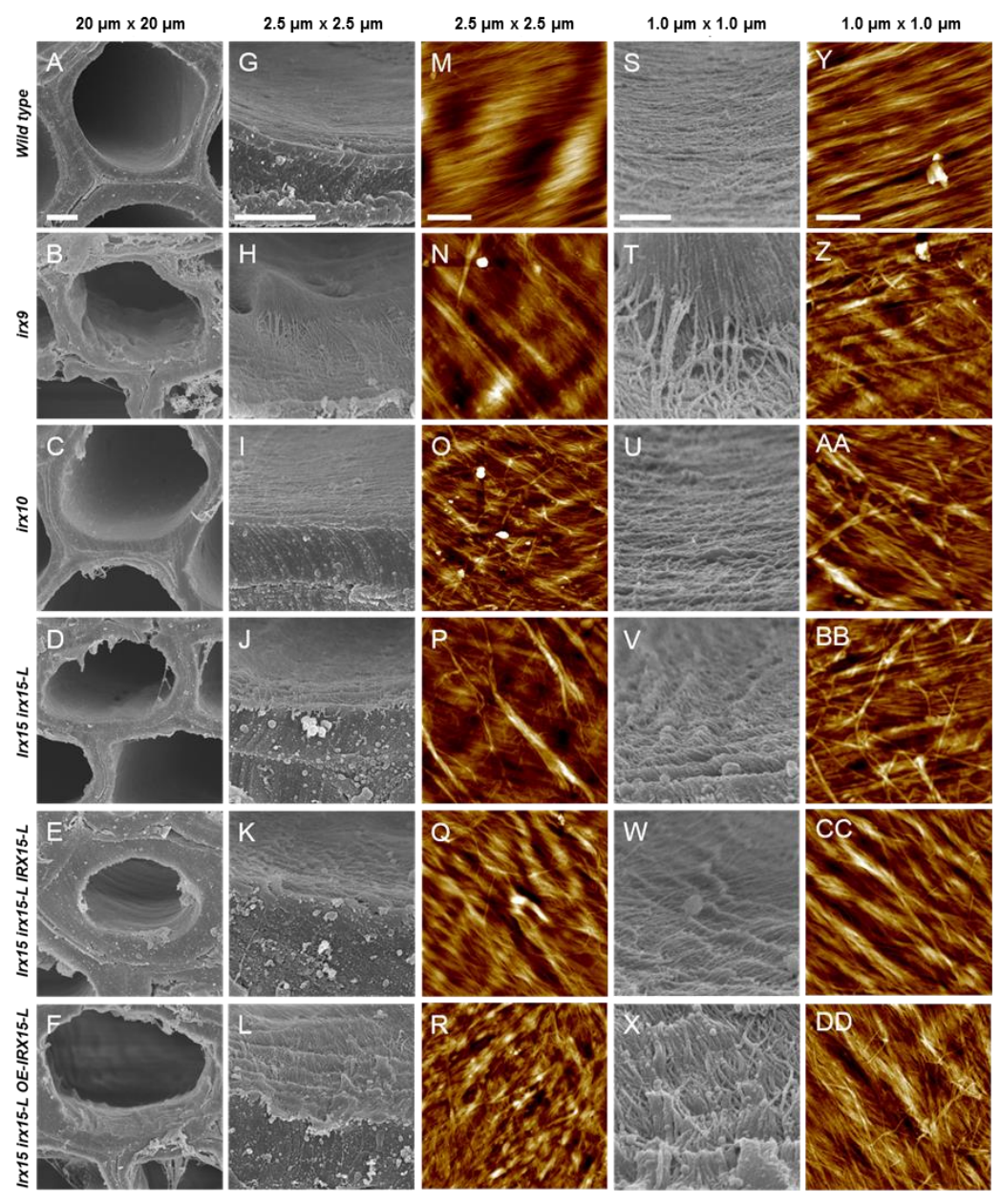


Figure 4.5 : Ultrastructure of *irx* mutants observed with SEM and AFM. Scanning electron microscopy images of sclerenchyma cell surface texture in native wild type Arabidopsis (**A,G,S**), *irx9* (**B,H,T**), *irx10* (**C,I,U**), *irx15 irx15-L* (**D,J,V**), *irx15 irx15-L IRX15-L* (**E,K,W**), and *irx15 irx15-L OE-IRX15-L* (**F,L,X**) stems. Atomic force microscopy images of sclerenchyma cell wall surface texture after delignification in wild type Arabidopsis (**M,Y**), *irx9* (**N,Z**), *irx10* (**O,AA**), *irx15 irx15-L* (**P,BB**), *irx15 irx15-L IRX15-L* (**Q,CC**), and *irx15 irx15-L OE-IRX15-L* (**R,DD**) stems. Scale bars are 2 μm for low magnification SEM (A-F), 1 μm for intermediate magnification SEM (G-L), and 200 nm for high magnification SEM (S-X), 500 nm for the 2.5 μm AFM images (M-R), and 200 nm for the 1.0 μm AFM images (Y-DD).

Consistent with previous literature, irregular cell shape was observed in SEM at the whole cell cross-sections (**Figure 4.5A-F**) in *irx9* [11] and *irx15 irx15-L*, with a return to wild type cell shape in irx15 irx15-L IRX15-L [20], while no discernable difference in cell wall thickness was observed for irx10. Interestingly, the overexpressed complementation line irx15irx15-L OE-IRX15-L had similar cell thickness to wild type, but exhibited irregular features similar to irx15 irx15-L. Examination of individual cell wall cross-sections with SEM at the 2.5 µm scale (Figure 4.5G-L) revealed normal secondary cell wall and warty layer organization with smooth cell inner cell wall surfaces in wild type (Figure 4.5G) and irx10 (Figure 4.5I) only, while rough, non-uniform features were observed in the other irx mutants (**Figure 4.5H,J,K,L**). These rough features were also accompanied by fibril-like features coating the inner secondary cell wall and in some cases peeling away from the cell wall, shown predominantly in irx9 (Figure 4.5T), irx15 irx15-L (Figure 4.5V), irx15 irx15-L OE-IRX15-L (**Figure 4.5X**), and to a lesser extent in *irx15 irx15-L IRX15-L* (**Figure 4.5W**), indicating an incomplete phenotypic compliment at the microscale not observed in prior literature. Interestingly, irx10 also showed slight rough features at the high magnification scale (**Figure 4.5U**), indicating that all mutants expressed some ultrastructural difference compared to wild type (**Figure 4.5S**) at the highest magnification.

Similar to SEM, comparative AFM images revealed nanoscale differences in the cell wall ultrastructure for all mutants compared to wild type. After chlorite delignification, cellulose microfibril layers in the secondary cell wall were exposed, revealing cellulose microfibril organization and orientation with respect to an individual cell wall layer [66]. Qualitatively, at the 2.5 µm scale (**Figure 4.5M-R**), the cellulose microfibril surface in wild type (**Figure 4.5M**)

resembled a smooth sheet, with uniform orientation similar to prior work with maize secondary cell walls [66]. Contrary to wild type smoothness, large clusters of microfibril bundles were observed in *irx9* and *irx15 irx15-L* (Figure 4.5N,P), and an uneven smoothness was observed in the *irx15 irx15-L* complementation lines (Figure 4.5Q,R). To some degree, the microfibril organization and uniformity was disrupted in *irx10* (Figure 4.5O), however the features were not as dramatic as the other mutants. At higher resolution, AFM images in *irx9* and *irx15 irx15-L* (Figure 4.5Z, BB) show the formation of microfibril bundles originating from the microfibril sheet layer, indicating irregular microfibril features are associated in some part to microfibril layer synthesis during secondary cell wall thickening, however, may also be imparted by chlorite delignification inducing aggregation. A summary of qualitative observation, including AFM image scales not shown in Figure 4.5 are described in Table 4.1. Furthermore, the images in Figure 4.5 were chosen as representative samples for describing interfascicular cell shape and AFM surface features, with additional replicates for SEM and AFM images of each sample found in Figure 4.15-9.

Image Size	20 μm	2.5 μm	1.0 µm	0.5 µm	0.25 μm
Wild type	SEM: thickened secondary cell wall, smooth cell shape	SEM: Smooth warty layer AFM: Smooth microfibril layer, uniform microfibril direction	SEM: Uniform surface AFM: Microfibrils unidirectional, no defects present	AFM: No microfibril overlap, smooth layer	AFM: Even microfibril spacing
irx9	SEM: thin secondary cell wall, irregular cell shape	SEM: Rough warty layer AFM: Aggregation of microfibril bundles, non-uniform orientation	SEM: Fibrous structures, peeling from warty layer AFM: Microfibril aggregates originating from microfibril layer, defects overlapping microfibril layer	AFM: Significant microfibril overlap, rough layer	AFM: Uneven microfibril spacing
irx10	SEM: slightly thinner secondary cell wall, smooth cell shape	SEM: Smooth warty layer AFM: Minor microfibril defects, non-uniform orientation	SEM: Minor grooves, mostly uniform AFM: Minor microfibril aggregation of defects, defects overlapping microfibril layer	AFM: Microfibril overlap, moderately uniform flat layer	AFM: Uneven microfibril spacing
irx15 irx15-L	SEM: thickened secondary cell wall, irregular cell shape	SEM: Rough warty layer AFM: Aggregation of microfibril bundles, non-uniform orientation	SEM: Fibrous structures, peeling from warty layer AFM: Microfibril aggregates originating from microfibril layer, defects overlapping microfibril layer	AFM: Significant microfibril overlap, rough layer	AFM: Uneven microfibril spacing
irx15 irx15-L IRX15-L	SEM: thickened secondary cell wall, smooth cell shape	SEM: Rough warty layer AFM: Smooth microfibril layer, minor microfibril defects	SEM: Some fibrous structures, mostly uniform AFM: Microfibrils unidirectional, minor defects present	AFM: Microfibril overlap, smooth surface	AFM: Uneven microfibril spacing
irx15 irx15-L OE- IRX15-L	SEM: thickened secondary cell wall, irregular cell shape	SEM: Rough warty layer AFM: Rough microfibril layer, uniform spacing	SEM: Fibrous structures, peeling from warty layer AFM: Nonuniform cell wall flatness, defects overlapping microfibril layer present	AFM: Significant microfibril overlap, rough surface	AFM: Uneven microfibril spacing

Table 4.1: Summary features observed in SEM and AFM height images for irx mutants.

While features at the 2.5 µm SEM and AFM images were generally comparative, chlorite delignification certainly impacts microfibril surfaces observed via AFM to some extent. However, based upon the stark contrast between wild type and mutants, there is a likely a strong connection between observed features and native microfibril organization, with chlorite delignification only partially contributing to observed differences.

Visual inspection of microfibril size at the 2.5 µm AFM scale (**Figure 4.5M-R**) show clear formations of large macrofibril-like features in *irx9* and *irx15 irx15-L* originating from the microfibril sheet. To capture the variability in microfibril bundling, fiber widths of well resolved features were calculated and presented as a distribution (**Figure 4.6**), similar to prior studies of primary and secondary cell walls [48, 62]. Example calculation of fibril diameters can be found in **Figure 4.23.**

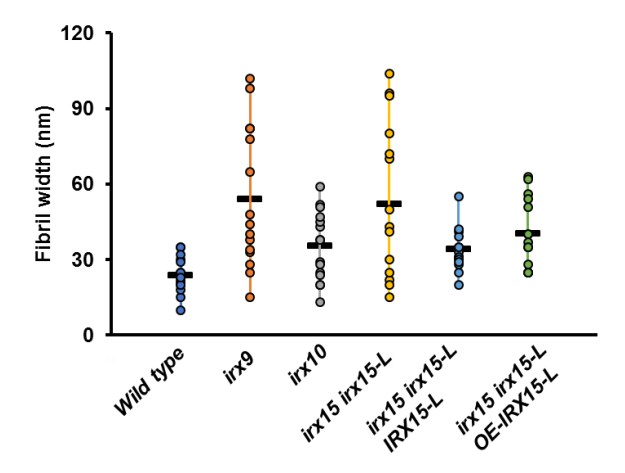


Figure 4.6: Fiber widths measurements of delignified *irx* mutant secondary cell walls using **AFM.** Fibril widths were determined from well-resolved features in 2.5 μ m image sizes, using five measurements for each of three individual images for each sample (n = 15). Averages of fiber measurements are displayed as a horizontal bar for each sample on figure.

Fibril widths down to individual elementary fibrils were generally not resolved due to the proximity of fibers within the secondary cell wall as well as the hydration state during sampling (air dried) impacting elementary fibril size [62], however larger features were captured. From the

distribution, *irx9* and *irx15 irx15-L* showed similar patterns of macrofibril size distributions, with some bundles reaching 100 nm in width. *Irx10* and the complementation line *irx15 irx15-L OE-IRX15-L* had less distinct bundling, indicating limited aggregation aside from visual microfibril breaks from the microfibril surface. *Irx15 irx15-L IRX15-L* showed similar distribution compared to wild type. Wild type average microfibril size was slightly higher than prior fibril measurements made on wild type primary cell wall in Arabidopsis [48], however the distribution was somewhat similar with the exception of single fibril measurements (3-4 nm) not observed in **Figure 4.6**.

Roughness analysis was performed as well as microfibril orientation to assess cellulose microfibril sheet spatial distributions (**Figure 4.7**). Roughness is a term used to describe irregularities of surface features from a mean plane, with larger irregularities corresponding to higher roughness, and is dependent upon both sample scale and measurement size [67]. Microfibril orientation is used in this context to determine directionality of microfibrils within an image, with dispersion measuring the deviation from the mean angle of orientation.

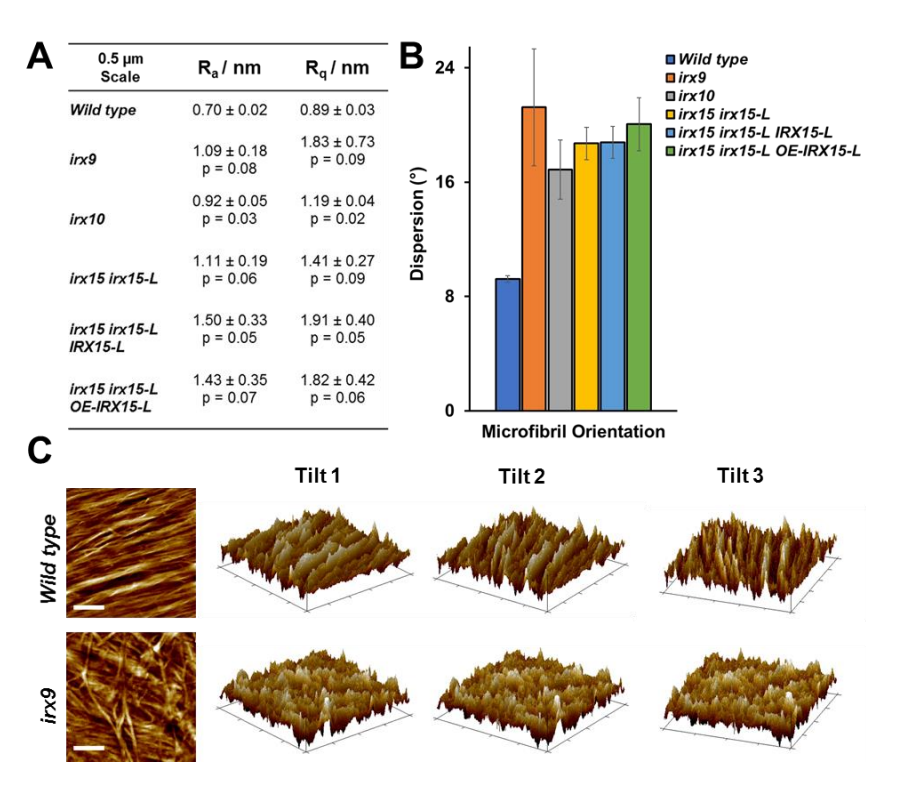


Figure 4.7: Roughness analysis, fiber orientation, and 3D topography measurements of delignified irx mutant cell walls using AFM. (A), Roughness parameters for average roughness (Ra) and root-mean-square roughness (Rq) measured on AFM height images at 0.5 μ m image scale. P values indicate statistical significance compared to wild type from t-test. (B), Microfibril orientations measured by dispersion of fibers distributed throughout an entire image at the 1.0 μ m image scale. Standard deviations for (A) and (B) are shown on figure for three different images (n = 3). (C), 3D surface profiles of wild type and irx9 demonstrating fiber alignment in wild type observed at three different image angles compared to irx9. Scale bar represents 100 nm and image scale is 0.5 μ m.

The average roughness (Ra) and root-mean-square roughness (Rq) were used to quantify average image roughness, and deviation from mean roughness respectively [68], with roughness analysis (**Figure 4.7A**, full analysis in **Table 4.2**) indicating to varying degrees of statistical significance that all mutant microfibril surfaces were rougher compared to the wild type. In particular, *irx9* and *irx15 irx15-L* grouped similarly, as did the complementation lines, whose roughness was most likely determined based upon the uneven wavy surfaces (**Figure 4.5CC,DD**) and not irregular microfibril deviation. *Irx10* was also statistically different from the

wild type, although was less pronounced in roughness and had the lowest deviation from the mean.

Microfibril orientations were revealed in wild type images, fibril orientation dispersion was less than 10 degrees for a single microfibril layer, indicating a narrow range of directionality changes within the microfibril plane. Comparatively, all mutants showed some extent of dispersion deviating from the wild type, with *irx9* showing the largest deviation. Factors contributing to dispersion were attributed to microfibril bends, breaks, out of plane features [69], or microfibril weaving between an individual layer which is generally attributed to primary cell wall tissue [48]. An example plot of the distribution of all microfibril orientations within a single image can be found in **Figure 4.21**. A combined visual approach using 3D surface topography (**Figure 4.7C**), clearly shows the combination of roughness distribution and microfibril orientation.

Both the wild type and *irx9* clearly show rough features, with the intensity of wild type appearing more evenly distributed (**Figure 4.7C Tilt1**). Analysis of the same images at different orientations (**Figure 4.7C Tilt2-3**) reveal patterned fiber alignments in the wild type that are likely not fully captured in the roughness analysis, but are captured in the microfibril orientation analysis. Likewise, microfibril orientation may not accurately capture fiber orientation in the presence of wide range of changes in 3D topography, such as in the *irx15 irx15-L* complementation lines, highlighted in the height distribution profiles (**Figure 4.8**).

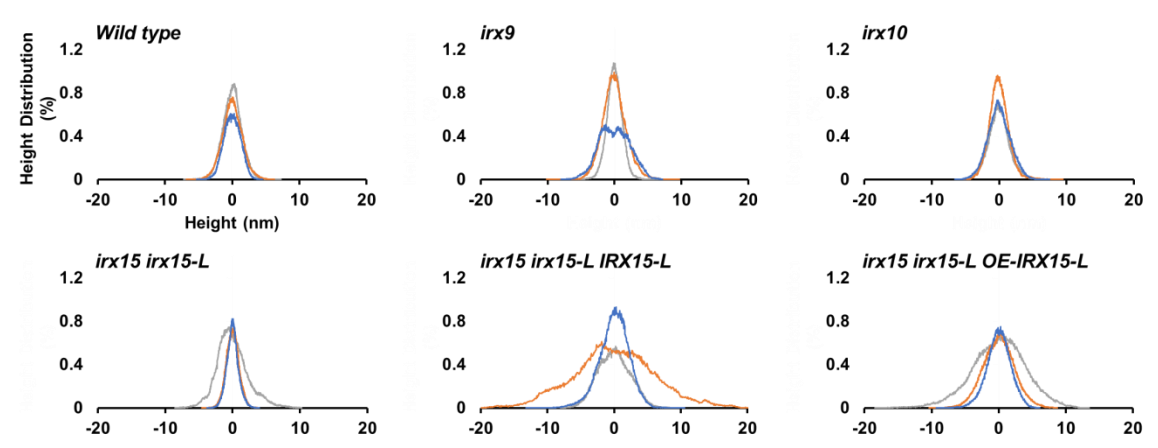


Figure 4.8: Height distribution profiles of delignified *irx* mutant cell walls using AFM. Gaussian distributions highlighting the distribution of height topography of each sample at 1 μ m scale. Distributions of each image triplicates (n = 3) are shown on figure. Gaussian distributions of all image scales can be found in **Figure 4.22**.

Height distributions on an ideal flat surface represent the frequency of particle diameters [70], however in the case of secondary cell wall surfaces, cellulose microfibril layers may not be flat and normally distributed. As a result, the height distribution likely represents the range of observed diameters corresponding to a general understanding of surface flatness, and will be used in this context to understand variations on microfibril surface topography. From **Figure 4.8**, a few conclusions can be drawn about the height profile distributions for each sample. In correspondence with roughness calculations, *irx9* and *irx15 irx15-L* were similarly grouped, as were the complementation lines. Wild type and *irx10* exhibited somewhat similar Gaussian distributions, while significant deviations in distribution were shown in the other *irx* mutants. Specifically, the complementation lines highlight the heterogeneity in height distributions, which are likely due to a different mechanism of disorganization causing non-flat height profiles, and are captured by the other AFM characterization techniques (**Figure 4.5Q,R**).

Mechanical properties of *irx* mutants

One of the major functions of the secondary cell wall is to provide mechanical strength to the individual cell and at the level of tissue and organ of the plant. *Irx* mutants are characterized

by mechanical failure at the individual cell level in the form of irregular xylem vessels in the stem, which directly impact nutrient transport and resistance to osmotic pressures [26, 27]. In parallel, interfascicular cells which are generally associated with stem strengthening, and from the prior analysis performed in this study, have documented altered cellulose microfibril organization at multiple levels. The altered ultrastructure of the secondary cell wall in these cells are therefore likely to impact physical properties of the stem related to maintaining an erect position, e.g. bending, breaking, and tensile strength.

Stem tensile strength was measured for lower stems as a metric for overall stem mechanical strength, with results indicating lower tensile strength in irx9, irx15 irx15-L (p< 0.0005), and to a lesser extent irx15 irx15-L OE-IRX15-L (p<0.1) compared to wild type, shown in **Figure 4.9.**

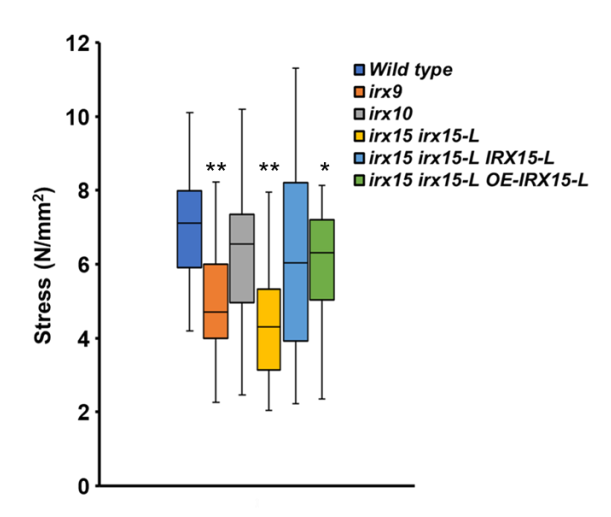


Figure 4.9 : Mechanical strength of xylan *irx* **mutant stems.** Tensile stress to breaking of stem tissue measured by universal tensile test. Box and whiskers plot is the result of twenty replicates of one biological batch of stems (n = 20). * indicate statistical significance from wild type (p < 0.1), ** indicates statistical significance from wild type (p < 0.0005).

From the tensile strength test, results indicate that cell wall structure impacts stem strength. The role of xylan within the cell wall has not been directly implicated in providing mechanical strength within the cell wall, with cellulose microfibrils providing a significantly

higher contribution to cell wall strength [1], however in pulp and paper applications, xylan is a desirable property in wood pulp for producing paper with higher tensile properties, providing pulp fracture stiffness [71]. Molecular dynamic simulation work has shown one reason for improved fiber strength resides in hydrogen bonding between xylan and cellulose stabilizing the cellulose chain by limiting disruption of hydrogen bonding between cellulose chains [72]. Xylan-cellulose films have shown improved mechanical properties can result from the incorporation of cellulose into xylan films, and cited similar conclusions [73].

The severe stem mechanical phenotype observed in *irx15 irx15-L* was comparable to mechanical strength observed in *irx9*, however, significant differences in xylan content between the two suggests that in the case of mutants exhibiting both reduced xylan content and altered structure, xylan structure likely plays a stronger role in dictating phenotype. This is supported by somewhat similar observations made for *irx9* and *irx15 irx15-L* for all techniques, however a fundamental examination of xylan chain length with respect to cellulose microfibril strength would need to be explored to confirm this hypothesis.

Altered xylan as observed in the SEM and AFM images does result in irregular cell shape and at the nanoscale level disruptions in cellulose microfibril organization. Therefore, irregular cell wall organization observed in *irx9* and *irx15 irx15-L*, and irx15 irx15-L OE-IRX15-L specifically, and may be the underlying reason for reductions in stem strength. To further probe the role of cell wall organization in mechanical properties, qualitative nanomechanical mapping of modulus, deformation, adhesion and dissipation was recorded for each pixel along each of the topology AFM scans (**Figure 4.10**), generating spatial distribution maps of each property (full figure can be found in **Figure 4.24**). In the context of nanomechanical properties, elastic modulus is a force based upon contact deformation between the AFM tip and cellulose

microfibril surface [47], with high modulus regions representing stiff surfaces and corresponding to lower deformation distances of surfaces. Adhesion force represents the absolute value of the negative force during tip release from the surface [49]. Dissipation is measured based upon electrostatic discharge, and may be representative of electrochemical surface heterogeneity [74] of soft matter.

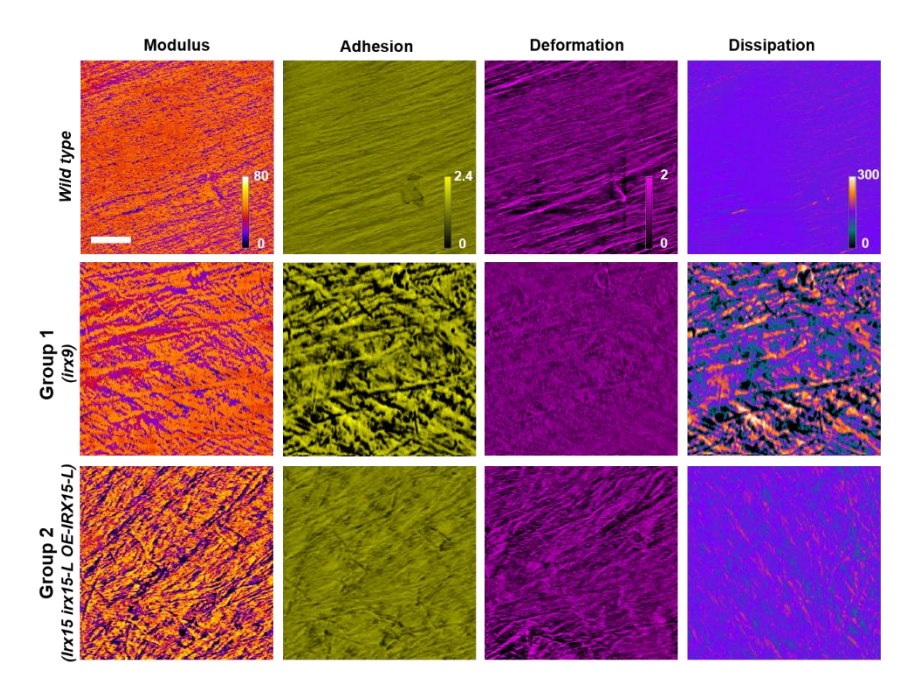


Figure 4.10 : Merged nanomechanical AFM imaging of *irx* **mutants.** Nanomechanical mapping of modulus (MPa), adhesion (nN), deformation (nm), and dissipation (eV) were scaled to the same absolute intensities for direct comparison of distributions. Groups were designated based upon qualitative features, with *irx9*, *irx10*, and *irx15 irx15-L* placed in group 1, and *irx15 irx15-L IRX15-L* and *irx15 irx15-L OE-IRX15-L* placed in group 2. Scale bar represents 200 nm, with all images corresponding to a 1.0 μm size.

Uniform features were generally observed in the wild type for all four properties, suggesting that an organized cellulose-hemicellulose network post chlorite delignification can induce mechanical uniformity. Nanomechanical images of *irx9*, *irx10*, and *irx15 irx15-L* (**Figure 4.10 Group1**) exhibited similar uneven distributions, specifically in modulus, adhesion, and dissipation. Spatial uniformity of adhesion and dissipation mostly restored in the *irx15 irx15-L IRX15-L* complementation lines (**Figure 4.10 Group2**), with uneven modulus and deformation

distributions likely corresponding to the wavy features observed in the height distribution profiles (**Figure 4.8**) limiting AFM tip interaction with the surface. The over-expressed complementation line (**Figure 4.10 Group2**) resembled a mix of features between *irx15 irx15-L* and the complementation lines, with similar modulus and deformation to the complementation line, while exhibiting minor heterogeneity in adhesion and dissipation.

Taken together, there is an apparent change in the electrostatic and surface strength environment of the *irx* mutants compared to wild type. Specifically, non-uniform modulus and deformation suggests microfibril defects induce reductions in cellulose microfibril surface strength, which extrapolated to the macroscale could result in reductions in compressive strength [26]. Stark contrasts of adhesion and dissipation profiles in the *irx* mutants also suggests that the chemical environment of the microfibril surface may also be altered, which could be a function of cellulose microfibril organization or of post-chlorite delignification hemicellulose localization along the microfibril surface [48]. In addition, the observation of a nanomechanical phenotype in *irx10* and to a lesser extent in *irx15 irx15-L IRX15-L* suggests altered xylan structure (DP) can induce altered xylan-cellulose interactions in the absence of lignin, however lignin likely acts as a stabilizer and maintains a normal cellulose microfibril structure as observed in the native SEM images (**Figure 4.5**) and the absence of a stem mechanical phenotype (**Figure 4.9**).

Discussion

The secondary cell wall is a complex system, with multiple interdependent components synthesized and coordinating in unison for precise control of nanoscale architecture promoting cell wall strength integrity. Xylan is an abundant component found in the secondary cell wall that plays an important role in promoting normal secondary cell wall organization, however, due to technological limitations as well as the complexity of cell wall biosynthesis, limited knowledge

is still known about specific interactions between cell wall components during both primary and secondary cell wall synthesis [75].

The root cause of irregular organization of the secondary cell wall in this study has been proposed to be directly linked to alterations in xylan content (**Figure 4.2A**), as evidenced by *irx9*, *irx15 irx15-L*, and *irx15 irx15-L OE-IRX15-L*, and to alterations in xylan structure, specifically xylan backbone DP (**Figure 4.2B**). In order to understand the impact of altered xylan on the cell wall, multiple indirect chemical and structural methods were used to elucidate structural changes imposed by altered xylan. Increased xylan epitopes recognition observed in the carbonate and 1M KOH extracts of *irx9* and *irx15 irx15-L* via glycome profiling (**Figure 4.3C**) revealed xylan was not as strongly integrated within the cell wall, and in the case of *irx9*, significantly higher pectin epitope recognition suggests pectin content may be increased as a cell wall compensation mechanism for altered xylan. Normal non-cellulosic carbohydrate extraction has been observed in *irx15 irx15-L IRX15-L*, suggesting a similar response to *irx10* for the complementation line [20].

RCIs determined from WAXS (**Figure 4.4**) provide direct evidence of irregular cellulose microfibril organization, with lower RCI in *irx9* and *irx15 irx15-L* suggesting less crystalline cellulose within the wall. Chemical analysis of crystalline cellulose content ruled out reductions in crystalline cellulose content contributing to a reduced RCI signal in *irx15 irx15-L*, and crystallite size ruled out changes in microfibril diameter, indicating that cellulose microfibril crystallization must be impacted [54]. Xylan chain length has been implicated in xylan adsorption to cellulose, which could alter the extent of xylan-cellulose hydrogen bonding, and impact hydrogen bonding between individual cellulose microfibrils [59]. Xylan structure (DP) in all the mutants observed are different, which implicates that a reduction in xylan content and

well as structure likely results in changes in cellulose crystallinity, however the specific mechanism altering cellulose crystallinity can only be speculated with the given results.

Ultrastructural characterization using SEM and AFM revealed overlapping, but distinct information supporting chemical analysis. In SEM, irx9, irx15 irx15-L, and irx15 irx15-L OE-IRX15-L displayed apparent alterations to inner cell wall shape at the whole cell level, while nuanced differences were observed in *irx10* and *irx15 irx15-L IRX15-L* upon closer inspection. The severity of cell wall irregularity observed in SEM was roughly correlated to extent of difference in chemical extractability observed in chemical analysis (Figure 4.3), as well as more importantly, related to irx mutants containing altered cell wall compositions. AFM images of delignified secondary cell wall microfibril surfaces showed irregular features in all genotypes, which implies phenotypes for irx mutants displaying altered xylan structure (irx10, irx15 irx15-L IRX15-L), but not altered xylan content are suppressed until the cell wall is delignified. Lignification occurs during SCW synthesis along with xylan deposition and cellulose microfibril layer synthesis, and with similar transcription factors governing expression of both xylan and lignin in interfascicular cells during SCW formation [76]. Lignin may play a parallel role to xylan within the cell wall, supplementing deficiencies in non-cellulosic components to maintain microfibril organization, which would explain altered lignin mutants also exhibiting irregular cellulose organization [38].

The complexity of features observed in AFM images (**Figure 4.5**) made a single metric to encapsulate microfibril surface irregularities unfeasible, however by measuring cell wall fibril bundle size (**Figure 4.6**), roughness (**Figure 4.7A,C**), microfibril dispersion (**Figure 4.7B**), and height topography (**Figure 4.8**) a few distinctions can be made between genotype microfibril surfaces. *Irx9* and *irx15 irx15-L* displayed aggregation of microfibrils originating from the

microfibril surface, into larger macrofibrils, traversing individual microfibril layers. This cell wall feature cannot be directly confirmed to exist in the native cell wall and may be the result of delignification and drying inducing aggregation [77], however is likely due to removal of lignin inducing cellulose aggregation in the absence of sufficient xylan to maintain microfibril organization. Roughness analysis was likely impacted by the height distribution profiles, resulting in the complementation lines having the highest roughness values, but were useful in demonstrating microfibril disorganization impacts surface uniformity in *irx9*, *irx15 irx15-L*, and to a lesser extent *irx10*. Similar deviations in microfibril orientation between all mutants compared to wild type does indicate that any change to xylan structure or content results in similar loss of orientation.

In addition to characterizing fundamental xylan-cellulose interaction, another major outcome of this study is the observation of previously invisible phenotypes using SEM and AFM to examine 3D topography. Identification of precise gene functions has been accelerated by the parallel development of analytical techniques to analyze cell wall structure [78], such as 3D electron tomography [79] and neutron scattering [80]. SEM and TEM are standard microscopy techniques for nanoscale characterization of plants [81], however TEM is usually employed to view changes within cell wall layers. From this work, we show that SEM can provide unique information on the integration of cell wall structures to observe phenotypes not obtainable using standard TEM alone, and propose broadening the application of SEM for plant cell wall phenotyping. AFM provides a broad range of tools to quantitatively characterize the cell wall landscape to supplement the observations from SEM, as well as provides the ability to probe nanomechanical properties of the cell wall surface. This is important and novel, as these microscopy in conjunction with one another, provide a route of direct measurements towards

connecting the role of nanoscale cell wall organization in macroscopic phenotypes observed (**Figure 4.11**).

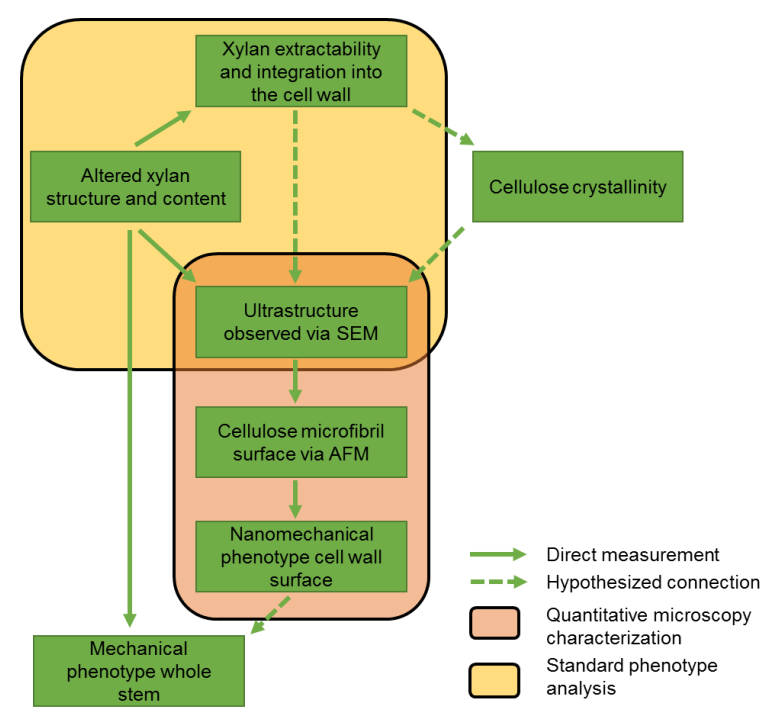


Figure 4.11: Schematic of analytical techniques utilized in this study, and proposed connections between individual techniques.

The loss of Arabidopsis stem mechanical integrity observed in *irx9*, *irx15 irx15-L* and *irx15 irx15-L OE-IRX15-L* (**Figure 4.9**) was comparable to similar mechanical phenotypes observed in xylan modified *irx9* mutants of rice properties [82], and of IRX8 homologs in poplar [83]. Mechanical phenotypes are not limited to xylan-deficient mutants, with mechanical deficiencies in cellulose deficient *brittle-culm1* [84] rice mutants that functions to crystallize cellulose [85]. Lignin deficient mutants such as *irx4* in Arabidopsis exhibit mechanical phenotypes [86], however reductions in other cell wall components convolute individual contributions to whole stem mechanical phenotypes. As an extended application of the results and techniques presented here, analysis of other Arabidopsis mutants may yield novel information relating to understanding cell wall polymer interactions. Specifically, investigation

of cellulose, and lignin deficient mutants, or combination mutants could help understand the role of lignin in maintaining normal cell wall structure with or without altered xylan structure.

Additional invisible phenotypes, such as altered xylan side chain substitution in the case of the *gux* mutants [23] or glucuronic acid methylation *gxmt* mutants [25] may be elucidated, and demonstrate the dynamic nature of the secondary cell wall in maintaining normal cell wall structure.

In summary, AFM height profiles and nanomechanical mapping demonstrate that cell wall topographical and organizational heterogeneity impact nanoscale mechanical properties, and together with SEM, tensile strength measurements, chemical analysis, and WAXS crystallinity measurements provide significant evidence that altered cell wall polymer abundance and structure can significantly impact cell wall organization at the nano and macroscale.

Conclusions

The secondary cell wall is a precise biological matrix that imparts cell wall rigidity, with loss of a single component resulting in dramatic phenotypic changes. This study investigated the effect of xylan deficient mutants in Arabidopsis on secondary cell wall organization to understand the role xylan plays in normal development. Reductions in relative crystallinity from WAXS diffraction patterns, coupled to increased extractability within the cell wall of *irx9* and *irx15 irx15-L* suggest altered hydrogen bonding between xylan and cellulose, and reduced cell wall integration of xylan. Nanoscale cell wall organization was impacted to some degree in all genotypes tested, and demonstrated altered xylan structure resulted in phenotypic changes that may have been masked by other cell wall components such as lignin.

Quantification of microfibril surface roughness, heterogeneity and orientation observed in AFM suggest normal cellulose deposition and organization is dependent in part upon non-covalent interactions with non-cellulosic polymers in the cell wall matrix. Cell wall defects

corresponded to nanomechanical heterogeneity in microfibril surface strength and chemical environment, with parallels between nanoscale and macroscale mechanical deficiencies in *irx9*, *irx15 irx15-L*, and *irx15 irx15-L OE-IRX15-L* displaying both altered xylan composition and structure. The analytical techniques presented demonstrate novel ways of characterizing invisible phenotypes to better understand the role of gene function impacting cell wall structure. Overall, irregular cell wall features observed from the *irx* mutants in this study are likely attributed to weakened cellulose-hemicellulose secondary cell wall matrix interfaces due to altered xylan content and structure, and highlight the fine-tuned complexity of the plant cell wall.

APPENDICES

APPENDIX C: Supplementary figures

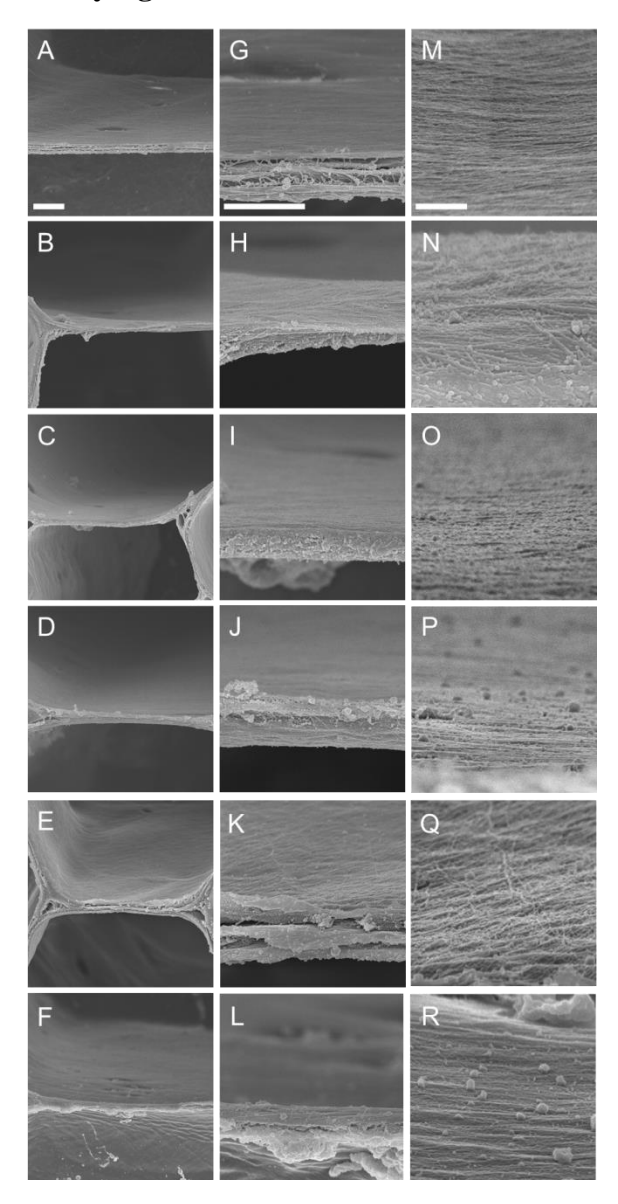


Figure 4.12 : SEM images of parenchyma cells surface texture in irx mutants. Wild type (**A,G,M**), *irx9* (**B,H,N**), *irx10* (**C,I,O**), *irx15 irx15-L* (**D,J,P**), *irx15 irx15-L IRX15-L* (**E,K,Q**), and *irx15 irx15-L OE-IRX15-L* (F,L,R) stems labeled. Scale bars are 2 μm for low magnification (A-E), 1 μm for intermediate magnification (G-L), and 200 nm for high magnification (M-R).

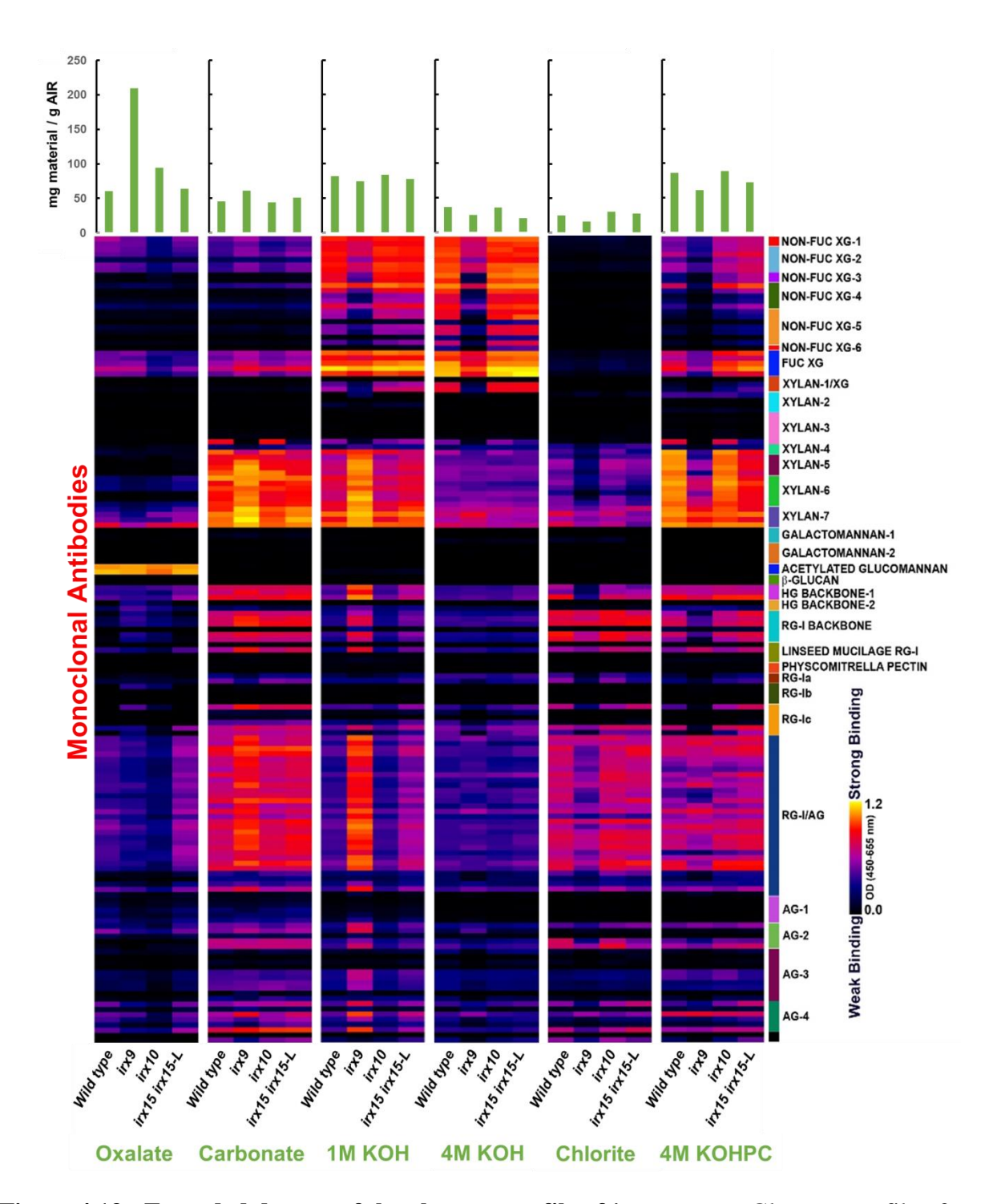


Figure 4.13 : Extended dataset of the glycome profile of *irx* **mutants.** Glycome profile of Arabidopsis cell wall material extracted sequentially with increasing chemical severity using oxalate, carbonate, 1M KOH, 4M KOH, acidic chlorite, and 4M KOHPC pretreatments as defined in materials and methods. Antibody binding strength is based upon optical density, with binding intensity presented as a color gradient from black (low binding) to red (intermediate binding), and yellow (strongest binding). Green bars on the top indicate the amount of carbohydrate recovered per gram of cell wall AIR for each extraction.

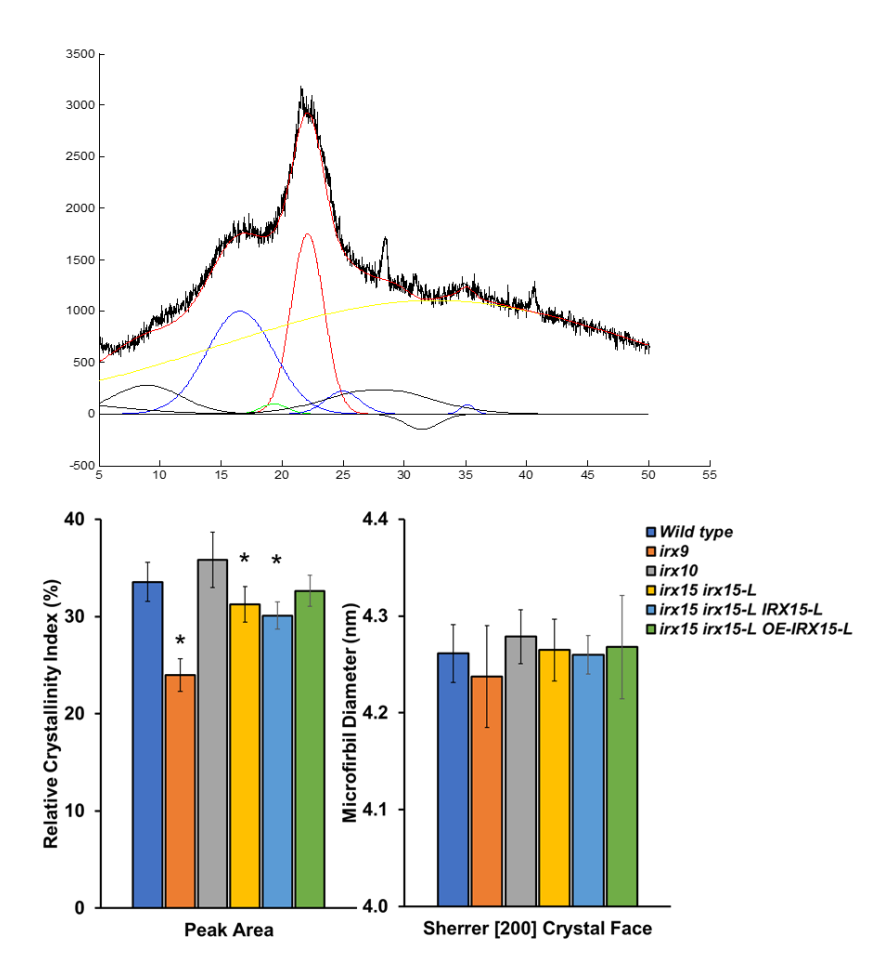


Figure 4.14: WAXS diffraction curve processing for crystallinity and microfibril diameter calculation. (A), WAXS diffraction curve fitting for quantification of relative crystallinity index, with ten Gaussian fits used to fit the major crystal faces and account for amorphous contributions. (B), Relative crystallinity index determined using the peak area method as described in the methods. (C), Sherrer microfibril diameter determined using the width at peak half height of the [200] crystal face.

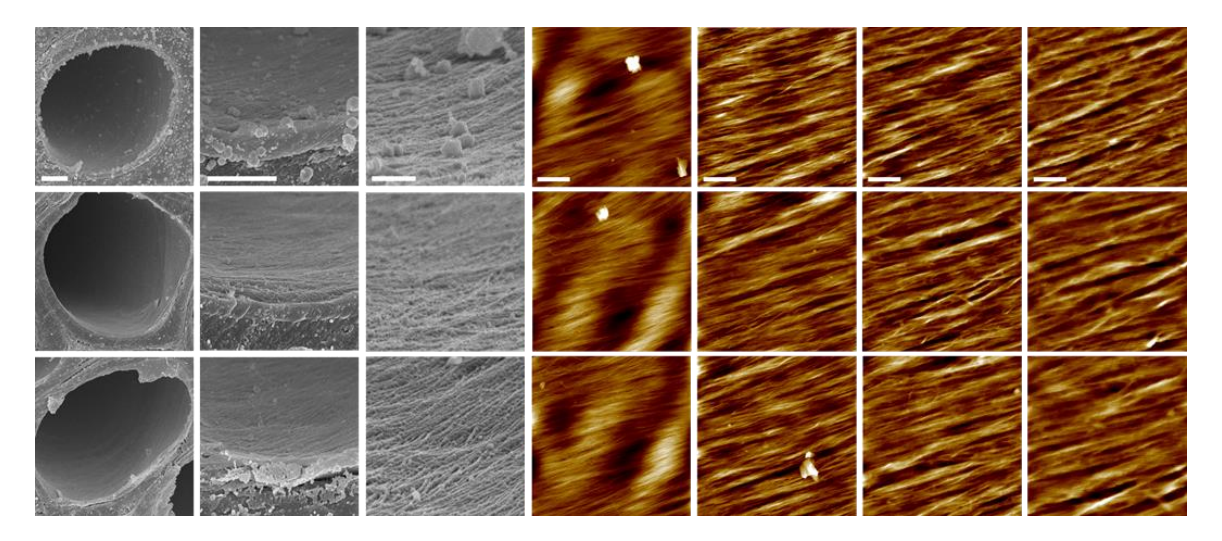


Figure 4.15 : Additional SEM and AFM images of sclerenchyma cell wall surface texture in Arabidopsis wild type. Scale bars for SEM are 2 μm for low magnification (left column), 1 μm for intermediate magnification (middle column), and 200 nm for high magnification (right column). Scale bars for AFM are 500 nm for the 2.5 μm images (first column), 200 nm for the 1.0 μm images (second column),100 nm for the 0.5 μm images (third column), and 50 nm for the 0.25 μm images (fourth column).

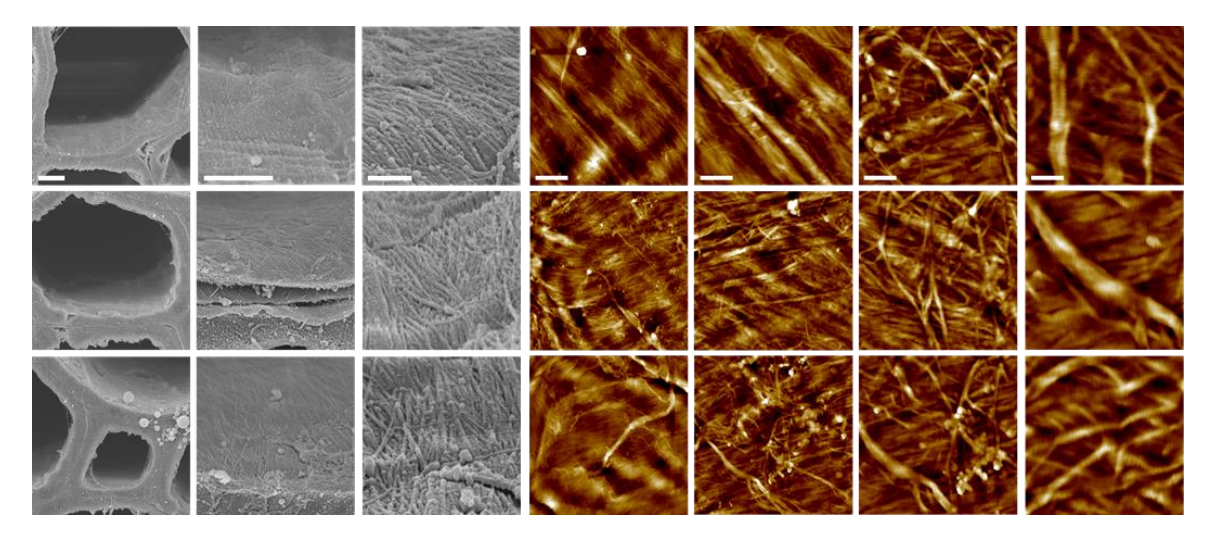


Figure 4.16: Additional SEM and AFM images of sclerenchyma cell wall surface texture in Arabidopsis *irx9*. Scale bars for SEM are 2 μ m for low magnification (left column), 1 μ m for intermediate magnification (middle column), and 200 nm for high magnification (right column). Scale bars for AFM are 500 nm for the 2.5 μ m images (first column), 200 nm for the 1.0 μ m images (second column),100 nm for the 0.5 μ m images (third column), and 50 nm for the 0.25 μ m images (fourth column).

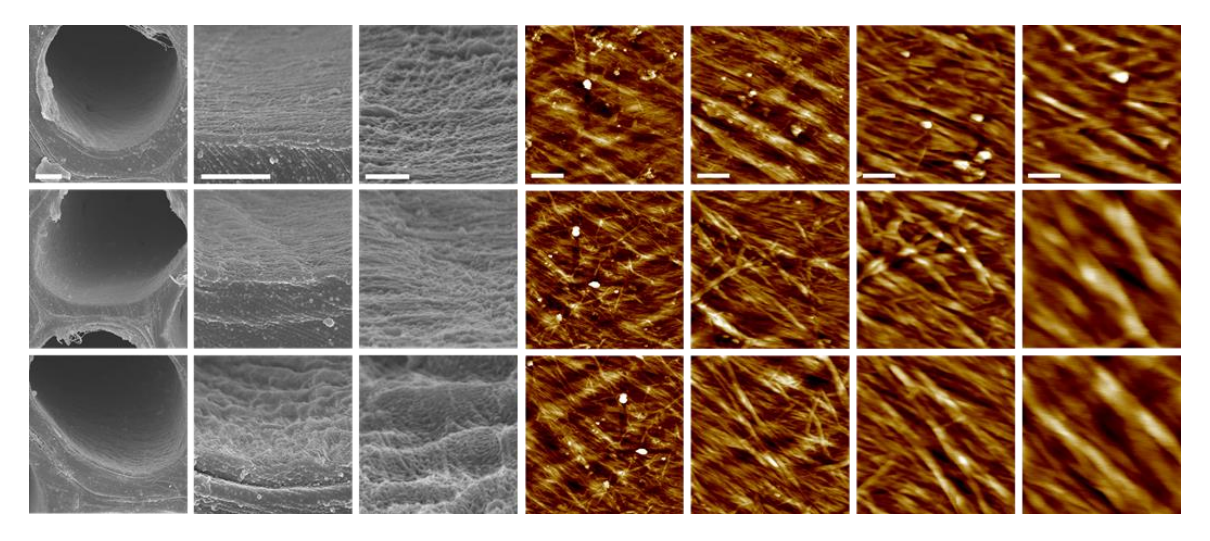


Figure 4.17: Additional SEM and AFM images of sclerenchyma cell wall surface texture in Arabidopsis irx10. Scale bars for SEM are 2 μm for low magnification (left column), 1 μm for intermediate magnification (middle column), and 200 nm for high magnification (right column). Scale bars for AFM are 500 nm for the 2.5 μm images (first column), 200 nm for the 1.0 μm images (second column),100 nm for the 0.5 μm images (third column), and 50 nm for the 0.25 μm images (fourth column).

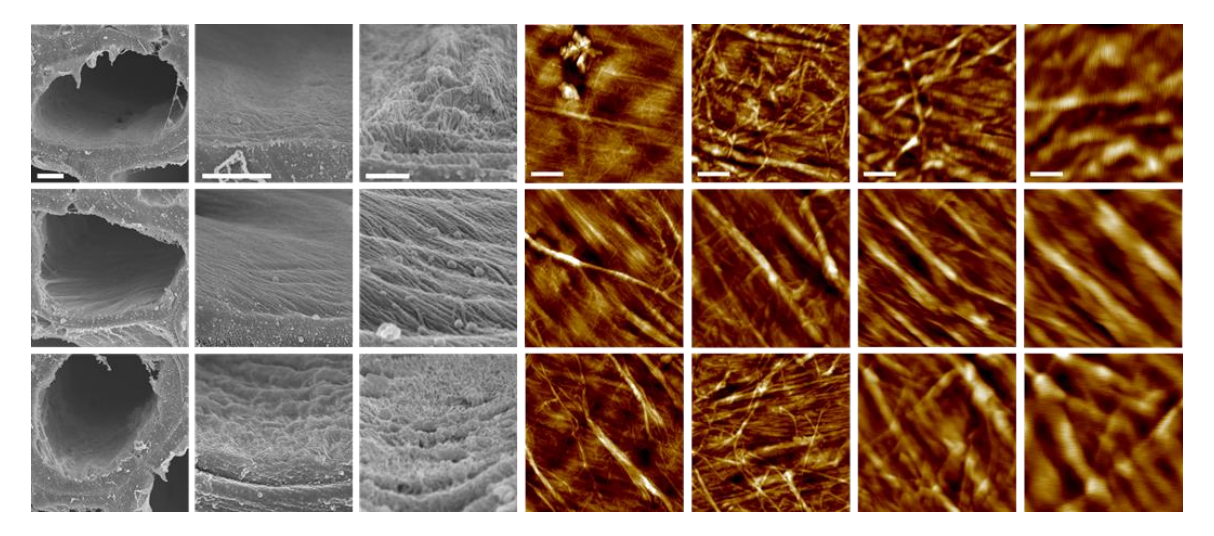


Figure 4.18: Additional SEM and AFM images of sclerenchyma cell wall surface texture in Arabidopsis irx15 irx15-L. Scale bars for SEM are 2 μ m for low magnification (left column), 1 μ m for intermediate magnification (middle column), and 200 nm for high magnification (right column). Scale bars for AFM are 500 nm for the 2.5 μ m images (first column), 200 nm for the 1.0 μ m images (second column), 100 nm for the 0.5 μ m images (third column), and 50 nm for the 0.25 μ m images (fourth column).

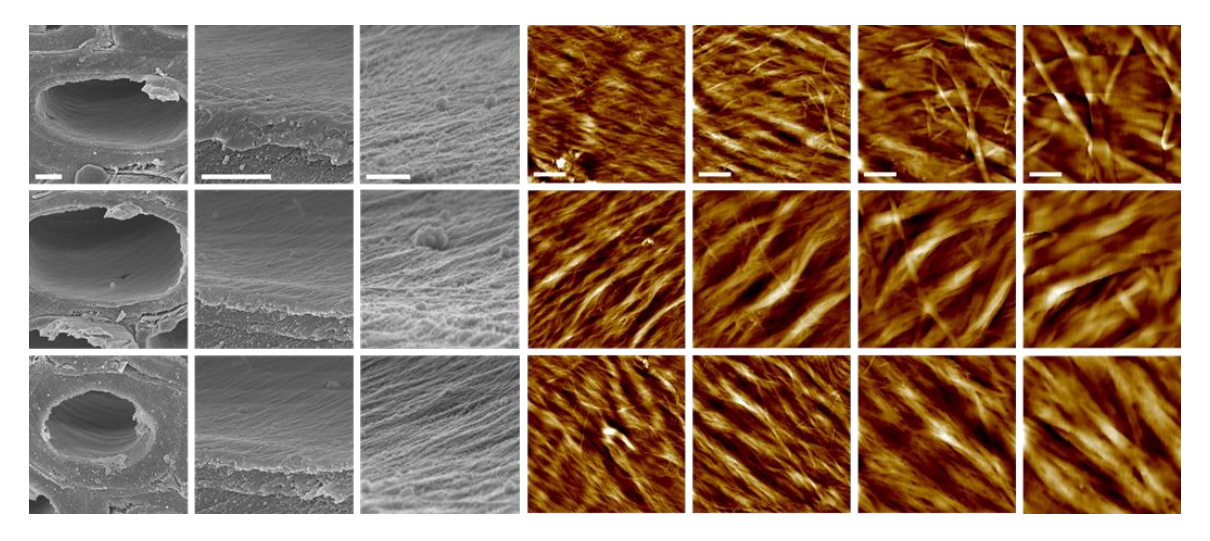


Figure 4.19: Additional SEM and AFM images of sclerenchyma cell wall surface texture in Arabidopsis irx15 irx15-L IRX15-L. Scale bars for SEM are 2 μm for low magnification (left column), 1 μm for intermediate magnification (middle column), and 200 nm for high magnification (right column). Scale bars for AFM are 500 nm for the 2.5 μm images (first column), 200 nm for the 1.0 μm images (second column), 100 nm for the 0.5 μm images (third column), and 50 nm for the 0.25 μm images (fourth column).

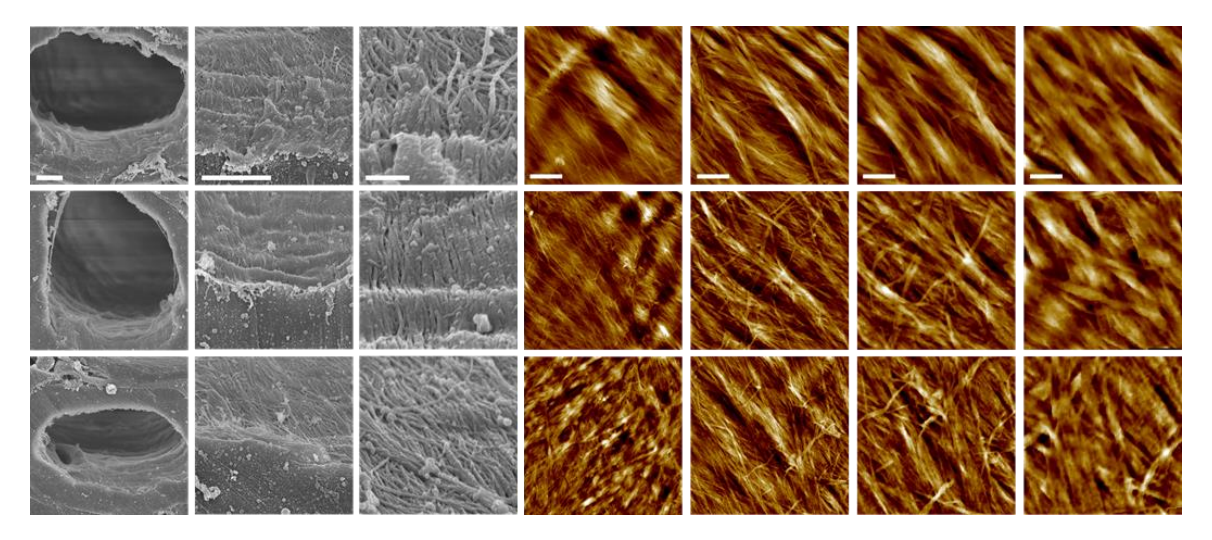


Figure 4.20: Additional SEM and AFM images of sclerenchyma cell wall surface texture in Arabidopsis *irx15 irx15-L OE-IRX15-L*. Scale bars for SEM are 2 μ m for low magnification (left column), 1 μ m for intermediate magnification (middle column), and 200 nm for high magnification (right column). Scale bars for AFM are 500 nm for the 2.5 μ m images (first column), 200 nm for the 1.0 μ m images (second column), 100 nm for the 0.5 μ m images (third column), and 50 nm for the 0.25 μ m images (fourth column).

Scale	R _a / nm					R _q / nm		
	2.5 µm	1.0 µm	0.5 μm	0.25 μm	2.5 µm	1.0 μm	0.5 µm	0.25 μm
Wild type	4.04 ± 0.25	0.49 ± 0.07	0.70 ± 0.02	1.18 ± 0.11	5.24 ± 0.34	0.63 ± 0.09	0.89 ± 0.03	1.51 ± 0.17
irx9	4.02 ± 1.04	0.77 ± 0.21	1.09 ± 0.18	2.16 ± 0.52	5.34 ± 1.43	0.98 ± 0.27	1.83 ± 0.73	2.76 ±0.65
	p = 0.97	p = 0.06	p = 0.08	p = 0.20	p = 0.92	p = 0.06	p = 0.09	p = 0.20
irx10	2.89 ± 0.68	0.67 ± 0.31	0.92 ± 0.05	1.38 ± 0.16	3.77 ± 0.87	0.86 ± 0.37	1.19 ± 0.04	1.77 ± 0.15
	p = 0.04	p = 0.26	p = 0.03	p = 0.36	p = 0.06	p = 0.25	p = 0.02	p = 0.33
irx15 irx15-L	3.68 ± 0.25	0.90 ± 0.47	1.11 ± 0.19	2.13 ± 0.79	4.82 ± 0.38	1.16 ± 0.64	1.41 ± 0.27	2.64 ± 1.02
	p = 0.03	p = 0.19	p = 0.06	p = 0.28	p = 0.06	p = 0.21	p = 0.09	p = 0.29
irx15 irx15-L	4.40 ± 0.91	0.99 ± 0.25	1.50 ± 0.33	2.13 ± 0.19	5.67 ± 1.05	1.25 ± 0.33	1.91 ± 0.40	2.72 ± 0.29
IRX15-L	p = 0.48	p = 0.01	p = 0.05	p = 0.10	p = 0.05	p = 0.02	p = 0.05	p = 0.11
irx15 irx15-L	4.45 ± 0.44	1.13 ± 0.37	1.43 ± 0.35	1.68 ± 0.29	5.97 ± 0.29	1.46 ± 0.45	1.82 ± 0.42	2.18 ± 0.31
OE-IRX15-L	p = 0.09	p = 0.09	p = 0.07	p = 0.08	p = 0.54	p = 0.06	p = 0.06	p = 0.07

Table 4.2: Roughness analysis and fiber width measurements of delignified irx mutant cell walls using AFM. Roughness parameters for average roughness (R_a) and root-mean-square roughness (R_q) measured on AFM height images at multiple image scales. Roughness is utilized in this case to measure cell wall uniformity. Roughness calculations were performed on three individual images for each scale (n = 3), with standard deviations shown in table. P values indicate statistical significance compared to wild type from t-test.

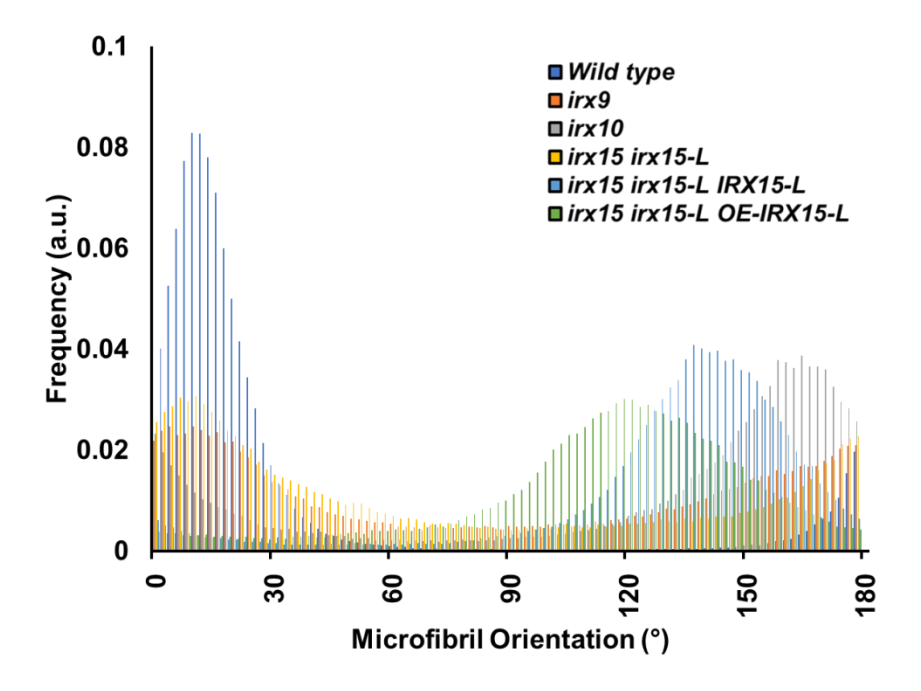


Figure 4.21 : Distribution profiles of microfibril orientations for an entire image. Sample image distribution profiles for each *irx* mutant and wild type. Dispersion was calculated based upon the width of the gaussian distribution.

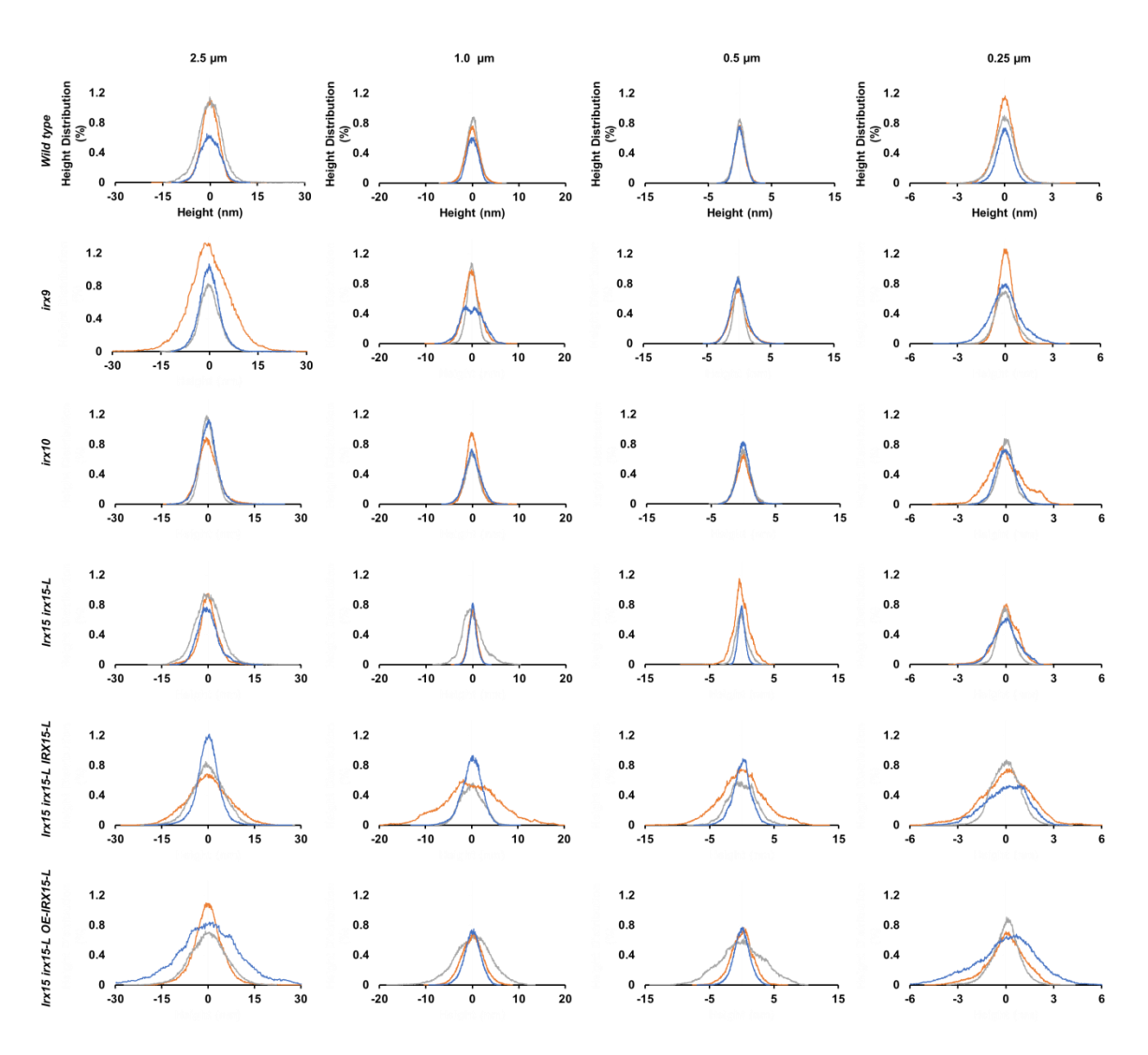


Figure 4.22 : Height distribution profiles of delignified *irx* **mutant cell walls using AFM.** Gaussian distributions of height ranges at each image scale are displayed as individual plots of three images for each sample.

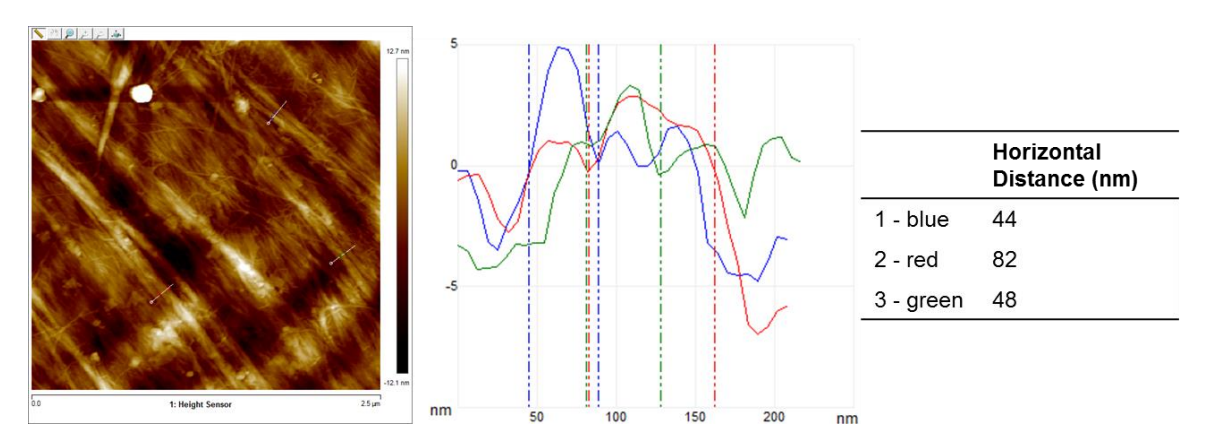


Figure 4.23 : Example calculation of microfibril width. Microfibril widths were calculated using the build in section Tool in Nanoscope. Well resolved microfibril features were used to determine horizontal fibril widths.

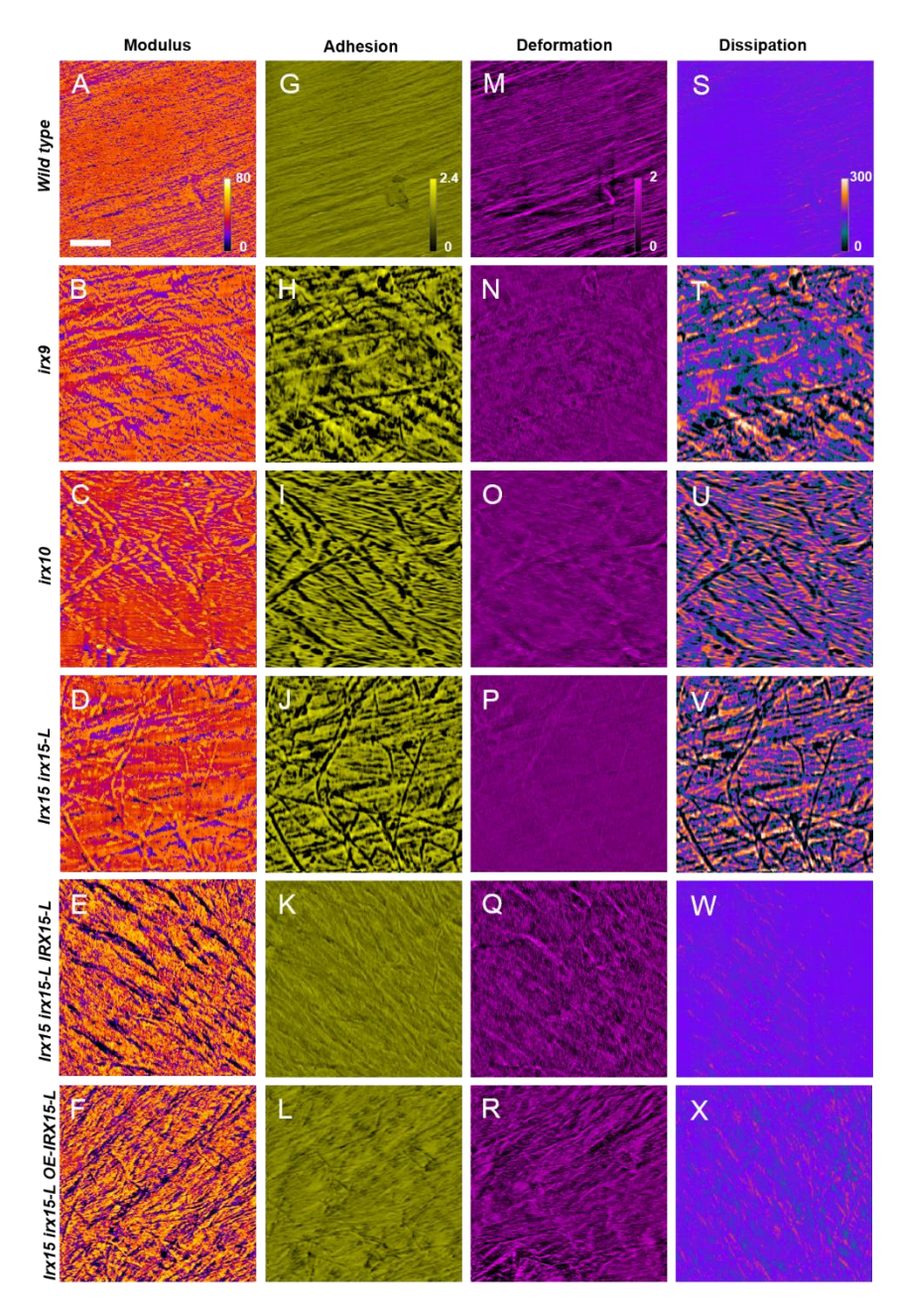


Figure 4.24 : Merged nanomechanical AFM imaging of all *irx* **mutants.** Nanomechanical mapping of modulus (MPa), adhesion (nN), deformation (nm), and dissipation (eV) were scaled to the same absolute intensities for direct comparison of distributions. Scale bar represents 200 nm, with all images corresponding to a 1.0 μm size.

APPENDIX D: Additional *irx* **experiments**

The following experiments were performed alongside other *irx* work, and were determined to not fit in the context of **Chapter 4**.

Additional methods

Water retention value

Water retention value (WRV) was determined according to a modified version of TAPPI UM 256, as previously described [87], with minor modifications. Briefly, 0.5g of milled AIR stems were soaked in 150ml of de-ionized water for 1 hour. After soaking for 1 hour, samples were rinsed with around 200 mL of de-ionized water and vacuum filtered using a 200 mesh Buchner filter. Washed biomass was inserted into a spin-column (Handee Spin Column Cs4, Thermo Scientific) with a 200 mesh stainless steel membrane, and centrifuged at 4000 x g for 15 minutes. Drained biomass was weighed on pre-massed aluminum trays, and dried in an oven at 105°C for at least 3 hours, then weighed again. The WRV is the ratio of the mass of water remaining in the biomass after centrifuging divided by the mass of dry biomass. Sequential extraction was performed using the same methodology as Glycome profiling. Water retention value was performed in technical triplicate of biological duplicates (n = 6) for each extraction.

Enzymatic hydrolysis

Enzymatic hydrolysis was performed at 1.0% solids loading (g AIR biomass/g solution) in 1.5 mL Posi-Click Tubes (Denville Scientific, Holliston, MA). Enzyme solutions were made at 30 mg protein/g glucan content using CTec3 (Novozymes A/S. Bagsværd, Denmark) and HTec3 (Novozymes A/S. Bagsværd, Denmark), with a ratio of 2:1 CTec3:HTec3. A buffer solution of 50 mM citric acid (pH 5.20) was used to maintain pH, and samples were incubated at 50°C with horizontal mixing at 180 rpm for 48 hr. Samples were centrifuged at 13000 x g for 3 min post-incubation and filtered using 22 μm mixed cellulose-ester filters (EMD Millipore,

Billerica, MA). Samples were quantified on the HPLC (Agilent 1100 Series) with an Aminex HPX-87H column (Bio-Rad, Hercules, CA, USA) with a mobile phase of 5 mM H₂SO₄. Glucose yield was determined based upon quantified glucose observed compared to total AIR cell wall glucan available (as glucose) including non-cellulosic glucan, while xylose yield was determined based upon total AIR cell wall xylan available (as xylose). Samples were performed in technical triplicate of biological duplicates (n = 6).

Additional results

Cell wall deconstruction measured by water retention value

Water retention value is metric that can be used quantify cell wall hydrophilicity, is often correlated with cell wall digestibility, and is dependent upon a cell wall composition as well as structure [87]. In the case of *irx* mutants, hydrophobic xylan, lignin and hydrophilic pectin content all contribute towards a sample bulk hydrophilicity. Sequential extraction can alter the impact of individual components and elucidate how residual cell wall components interact with an external variable. Water retention value was determined for initial AIR cell wall material, and after two increasingly harsher chemical extractions (**Fig. 4A**), along with chemical composition quantification of residue after all sequential extractions (EIC) (**Fig. 4B-D**).

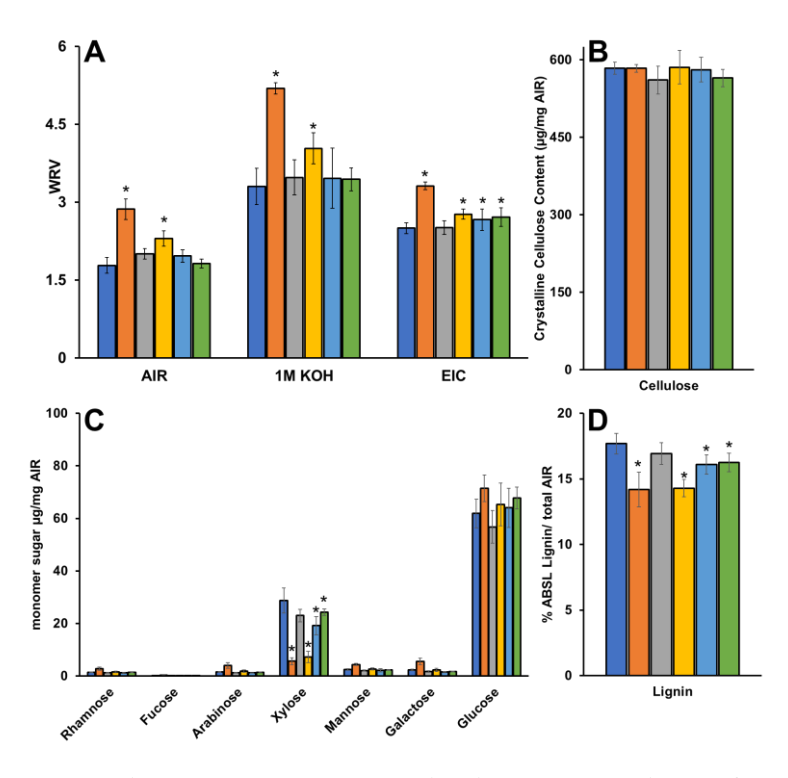


Figure 4.25 : Water retention values and extractive insoluble residue of cell wall material of *irx* **mutants.** (**A**), Water retention values (WRV) of alcohol insoluble residue (AIR) with and without chemical extraction with 1M KOH and extractive insoluble components (EIC) represents solid residue after sequential extraction with 4M KOH after chlorite delignification. (**B-D**), Composition of neutral monosaccharides, crystalline cellulose, and ABSL lignin content of residue remaining after 4M KOHPC extraction. Standard deviations are shown with two biological replicates with three technical replicates (n = 6).

Initial WRV of AIR samples showed higher values for *irx9* and *irx15 irx15-L*, which were most likely due to the decreased xylan (**Figure 4.2**) and lignin content (**Figure 4.3**). After 1M KOH, glycome profiles indicated similar extractions in the 4M KOH fraction for all but *irx9*, meaning that differences in lignin content most likely were the dominant composition variable dictating water retention, and the lower lignin in *irx9* and *irx15 irx15-L* resulted in higher WRV. WRV of the EIC residue resulted in a different trend however, with the complementation lines exhibiting increased WRV compared to wild type. Composition profiles (**Figure 4.25B-D**) indicated that the predominant difference between components in EIC is the residual xylan (0.3% total mass) and differences in lignin content. The likely explanation for the increases in water

retention observed after extractions in the complementation lines arises from the lower lignin content relative to wild type. This result indicates that the complementation lines do not fully revert to wild type, displaying similar characteristics to *irx15 irx15-L* after harsh extraction and may have subtle phenotypic differences compared to wild type that were not observed in initial phenotyping.

Enzymatic hydrolysis monomer sugar yields

After extensive investigation of the secondary cell wall ultrastructure and physical properties, enzymatic hydrolysis was performed to relate structural and compositional features to cell wall deconstruction.

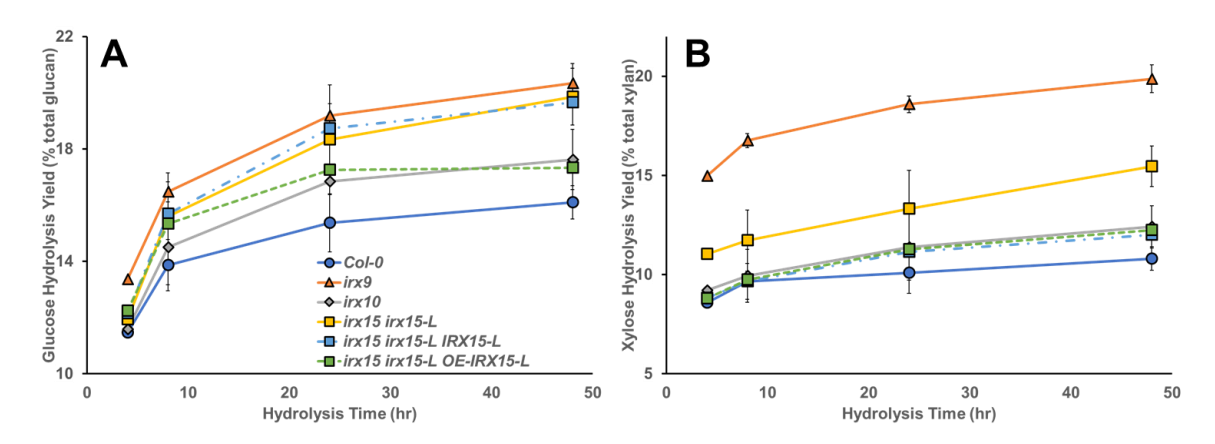


Figure 4.26: Enzymatic digestibility of cell wall material of *irx* mutant stems. Enzymatic hydrolysis monomeric sugar yields of glucose (**A**) and xylose (**B**) of unpretreated AIR on a basis of % monomeric sugar observed per total available polysaccharide (g/g*100). Standard deviations are shown (n = 6, biological duplicate with technical triplicate).

From the time course enzymatic hydrolysis results (**Figure 4.26**), glucose and xylose are more easily released for all the genotypes. Sugar yields *irx9* [51], *irx15 irx15-L*, and *irx15 irx15-L IRX15-L* [15] roughly correlate with prior studies utilizing pretreatments before hydrolysis, indicating increases in hydrolysis yields can be extrapolated outside of no pretreatment only. While the observed trend of glucose yields makes it hard to pinpoint the specific key contributor

to the improved yields, modifying xylan biosynthesis readily affects glucose yields in the positive direction. This compositional alteration, coupled with the observed mechanical changes argues for altered xylan plants as a viable route to improve feedstocks for biofuels production.

Understanding changes in cellulose RCI though alteration of xylan content

To further probe the hypothesis of xylan content impacting cellulose microfibril crystallinity and organization, sequential extraction was performed on wild type (**Fig. 5**) to observe composition and RCI changes in response to chemical extractions.

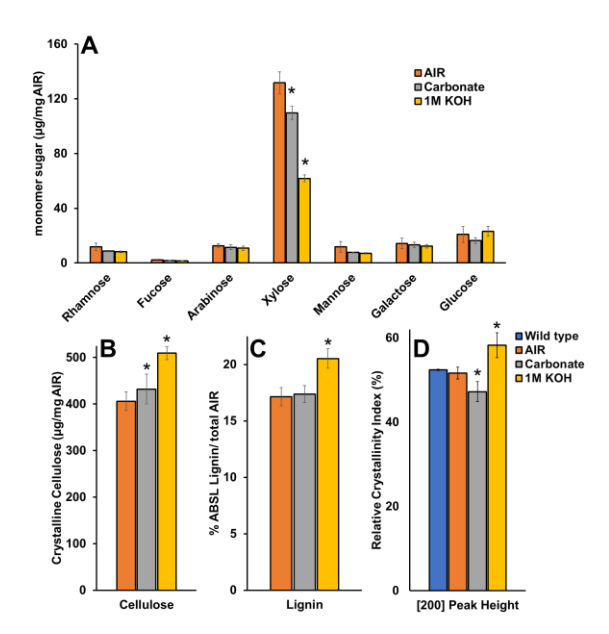


Figure 4.27: Cell wall compositions of Arabidopsis wild type and WAXS relative crystallinity index after chemical extraction. (A) cell wall neutral monosaccharide content determined from TFA hydrolysis, (B) crystalline cellulose content, and (C) ABSL lignin content of wild type AIR, and sequentially extracted with carbonate and 1M KOH. (D) Relative crystallinity indexes of the [200] peak face calculated from the WAXS diffraction patterns in wild type native, AIR, and sequentially extracted with carbonate and 1M KOH. Standard deviations are shown (n = 3, biological replicates. * indicates statistical significance compared to wild type (t-test, p < 0.05).

From the composition results (**Figure 4.27A-C**), carbonate (50 mM) removed hemicellulose and pectin components, with decreases in xylose (78% of AIR), rhamnose, and galactose content resulting in a small but statistical mass fraction increase in crystalline cellulose

content (7% increase from AIR). The 1M KOH extract was a significantly higher in concentration, and after pectin removal in the carbonate fraction, predominately resulted in the removal of xylans (xylose content was 47% of AIR) and xyloglucans, as observed in the composition profile (**Figure 4.27A**) and glycome profiling results (**Figure 4.13**), with an increase in the proportion of crystalline cellulose remaining (**Figure 4.27B**) in the residue (25% increase from AIR). From these chemical changes, WAXS was performed and RCIs were calculated, with a decrease in RCI after carbonate extraction, followed by a significant increase in RCI after 1M KOH extraction (**Figure 4.27D**). AIR RCI values were shown to be statistically equivalent to the native RCI, demonstrating that removal of non-structural components did not impact RCI.

While not definitive, changes in relative crystallinity observed following carbonate and 1M KOH extraction may be attributed to changes in cellulose microfibril hydrogen bonding within the cell wall. Specifically, chemical extraction would result in the removal of less structurally integrated hemicelluloses first, with the remaining hemicelluloses experiencing an altered chemical environment, as well as potentially altered structures due to chemical cleavage of some bonds. One potential outcome of this would be increased xylan-cellulose hydrogen bonding, resulting in lower observed crystallinities. Sufficient removal of non-cellulosic components (1M KOH) would result in the opposite observation, with increased inter-cellulose hydrogen bonding in the absence of spacer components. In more severe extractions such as 1M KOH however, RCI gets convoluted as cellulose constitutes a larger fraction of the total residue, which would also contribute to the proportional increase in observed RCI.

REFERENCES

REFERENCES

- 1. Cosgrove DJ: **Growth of the plant cell wall**. *Nat Rev Mol Cell Biol*. 2005, **6**:850-861.
- 2. Moon RJ, Martini A, Nairn J, Simonsen J, Youngblood J: **Cellulose nanomaterials review: structure, properties and nanocomposites**. *Chem Soc Rev.* 2011, **40**:3941-3994.
- 3. Persson S, Paredez A, Carroll A, Palsdottir H, Doblin M, Poindexter P, Khitrov N, Auer M, Somerville CR: Genetic evidence for three unique components in primary cellwall cellulose synthase complexes in Arabidopsis. *P Natl Acad Sci USA*. 2007, 104:15566-15571.
- Taylor NG, Howells RM, Huttly AK, Vickers K, Turner SR: Interactions among three distinct CesA proteins essential for cellulose synthesis. P Natl Acad Sci USA. 2003, 100:1450-1455.
- 5. Taylor NG: Cellulose biosynthesis and deposition in higher plants. *New Phytol.* 2008, **178**:239-252.
- 6. Li S, Bashline L, Zheng Y, Xin X, Huang S, Kong Z, Kim SH, Cosgrove DJ, Gu Y: Cellulose synthase complexes act in a concerted fashion to synthesize highly aggregated cellulose in secondary cell walls of plants. *P Natl Acad Sci USA*. 2016, 113:11348-11353.
- 7. Watanabe Y, Meents M, McDonnell L, Barkwill S, Sampathkumar A, Cartwright H, Demura T, Ehrhardt D, Samuels A, Mansfield S: **Visualization of cellulose synthases in Arabidopsis secondary cell walls**. *Science*. 2015, **350**:198-203.
- 8. Pauly M, Gille S, Liu L, Mansoori N, Souza A, Schultink A, Xiong G: **Hemicellulose biosynthesis**. *Planta*. 2013, **238**:627-642.
- 9. Ebringerova A, Hromadkova Z, Heinze T: **Hemicellulose**. In: *Polysaccharides 1: Structure, Characterization and Use*. Edited by Heinze T. 2005, **186**:1-67.
- 10. Gille S, Pauly M: **O-acetylation of plant cell wall polysaccharides**. *Frontiers Plant Sci.* 2012, **3**:12.
- 11. Pena MJ, Zhong R, Zhou G-K, Richardson EA, O'Neill MA, Darvill AG, York WS, Ye Z-H: **Arabidopsis irregular xylem8 and irregular xylem9: Implications for the complexity of glucuronoxylan biosynthesis**. *Plant Cell*. 2007, **19**:549-563.
- 12. York WS, O'Neill MA: **Biochemical control of xylan biosynthesis which end is up?** *Curr Opin Plant Biol.* 2008, **11**:258-265.

- 13. Wu A-M, Rihouey C, Seveno M, Hörnblad E, Singh SK, Matsunaga T, Ishii T, Lerouge P, Marchant A: **The Arabidopsis IRX10 and IRX10-LIKE glycosyltransferases are critical for glucuronoxylan biosynthesis during secondary cell wall formation**. *The Plant J.* 2009, **57**:718-731.
- 14. Wu A-M, Hörnblad E, Voxeur A, Gerber L, Rihouey C, Lerouge P, Marchant A: Analysis of the Arabidopsis IRX9/IRX9-L and IRX14/IRX14-L pairs of glycosyltransferase genes reveals critical contributions to biosynthesis of the hemicellulose glucuronoxylan. *Plant Physiol.* 2010, **153**:542-554.
- 15. Brown DM, Zhang Z, Stephens E, Dupree P, Turner SR: Characterization of IRX10 and IRX10-like reveals an essential role in glucuronoxylan biosynthesis in Arabidopsis. *Plant J.* 2009, **57**:732-746.
- 16. Jensen JK, Johnson NR, Wilkerson CG: **Arabidopsis thaliana IRX10 and two related proteins from psyllium and Physcomitrella patens are xylan xylosyltransferases**. *Plant J.* 2014, **80**:207-215.
- 17. Urbanowicz BR, Pena MJ, Moniz HA, Moremen KW, York WS: **Two Arabidopsis** proteins synthesize acetylated xylan in vitro. *Plant J.* 2014, **80**:197-206.
- 18. Rennie EA, Scheller HV: **Xylan biosynthesis**. Curr Opin Biotech. 2014, **26**:100-107.
- 19. Brown D, Wightman R, Zhang Z, Gomez LD, Atanassov I, Bukowski J-P, Tryfona T, McQueen-Mason SJ, Dupree P, Turner S: **Arabidopsis genes IRREGULAR XYLEM** (IRX15) and IRX15L encode DUF579-containing proteins that are essential for normal xylan deposition in the secondary cell wall. *Plant J.* 2011, 66:401-413.
- 20. Jensen JK, Kim H, Cocuron J-C, Orler R, Ralph J, Wilkerson CG: **The DUF579 domain containing proteins IRX15 and IRX15-L affect xylan synthesis in Arabidopsis**. *Plant J.* 2011, **66**:387-400.
- 21. Persson S, Caffall KH, Freshour G, Hilley MT, Bauer S, Poindexter P, Hahn MG, Mohnen D, Somerville C: **The Arabidopsis irregular xylem8 mutant is deficient in glucuronoxylan and homogalacturonan, which are essential for secondary cell wall integrity**. *Plant Cell*. 2007, **19**:237-255.
- 22. Lee C, O'Neill MA, Tsumuraya Y, Darvill AG, Ye ZH: **The irregular xylem9 mutant is deficient in xylan xylosyltransferase activity**. *Plant Cell Physiol*. 2007, **48**:1624-1634.
- 23. Mortimer JC, Miles GP, Brown DM, Zhang Z, Segura MP, Weimar T, Yu X, Seffen KA, Stephens E, Turner SR *et al*: **Absence of branches from xylan in Arabidopsis gux mutants reveals potential for simplification of lignocellulosic biomass**. *P Natl Acad Sci USA*. 2010, **107**:17409-17414.

- 24. Xiong G, Cheng K, Pauly M: **Xylan O-acetylation impacts xylem development and enzymatic recalcitrance as indicated by the Arabidopsis mutant tbl29**. *Mol Plant*. 2013, **6**:1373-1375.
- 25. Urbanowicz BR, Peña MJ, Ratnaparkhe S, Avci U, Backe J, Steet HF, Foston M, Li H, O'Neill MA, Ragauskas AJ *et al*: **4-O-methylation of glucuronic acid in Arabidopsis glucuronoxylan is catalyzed by a domain of unknown function family 579 protein**. *P Natl Acad Sci USA*. 2012, **109**:14253-14258.
- 26. Turner SR, Somerville CR: Collapsed xylem phenotype of Arabidopsis identifies mutants deficient in cellulose deposition in the secondary cell wall. *Plant Cell.* 1997, 9:689-701.
- 27. Hao Z, Mohnen D: A review of xylan and lignin biosynthesis: Foundation for studying Arabidopsis irregular xylem mutants with pleiotropic phenotypes. *Crit Rev Biochem Mol.* 2014, **49**:212-241.
- 28. Busse-Wicher M, Li A, Silveira RL, Pereira CS, Tryfona T, Gomes TCF, Skaf MS, Dupree P: **Evolution of xylan substitution patterns in gymnosperms and angiosperms: Implications for xylan interaction with cellulose**. *Plant Physiol*. 2016, **171**:2418-2431.
- 29. Busse-Wicher M, Grantham NJ, Lyczakowski JJ, Nikolovski N, Dupree P: **Xylan decoration patterns and the plant secondary cell wall molecular architecture**. *Biochem Soc T*. 2016, **44**:74-78.
- 30. Busse-Wicher M, Gomes TCF, Tryfona T, Nikolovski N, Stott K, Grantham NJ, Bolam DN, Skaf MS, Dupree P: **The pattern of xylan acetylation suggests xylan may interact with cellulose microfibrils as a twofold helical screw in the secondary plant cell wall of Arabidopsis thaliana**. *Plant J.* 2014, **79**:492-506.
- 31. Simmons TJ, Mortimer JC, Bernardinelli OD, Poppler AC, Brown SP, Deazevedo ER, Dupree R, Dupree P: **Folding of xylan onto cellulose fibrils in plant cell walls revealed by solid-state NMR**. *Nat Commun*. 2016, **7**:13902.
- 32. Bromley JR, Busse-Wicher M, Tryfona T, Mortimer JC, Zhang ZN, Brown DM, Dupree P: **GUX1** and **GUX2** glucuronyltransferases decorate distinct domains of glucuronoxylan with different substitution patterns. *Plant J.* 2013, **74**:423-434.
- 33. Xiong G, Dama M, Pauly M: Glucuronic acid moieties on xylan are functionally equivalent to O-acetyl-substituents. *Mol Plant*. 2015, 8:1119-1121.
- 34. Park YB, Lee CM, Kafle K, Park S, Cosgrove DJ, Kim SH: Effects of plant cell wall matrix polysaccharides on bacterial cellulose structure studied with vibrational sum frequency generation spectroscopy and X-ray diffraction. *Biomacromolecules*. 2014, 15:2718-2724.

- 35. Martínez-Sanz M, Lopez-Sanchez P, Gidley MJ, Gilbert EP: Evidence for differential interaction mechanism of plant cell wall matrix polysaccharides in hierarchically-structured bacterial cellulose. *Cellulose*. 2015, 22:1541-1563.
- 36. Whitney SEC, Brigham JE, Darke AH, Reid JSG, Gidley MJ: **Structural aspects of the interaction of mannan-based polysaccharides with bacterial cellulose**. *Carbohydr Res.* 1998, **307**:299-309.
- 37. Smith-Moritz AM, Hao Z, Fernandez-Nino SG, Fangel JU, Verhertbruggen Y, Holman HY, Willats WG, Ronald PC, Scheller HV, Heazlewood JL *et al*: **Structural characterization of a mixed-linkage glucan deficient mutant reveals alteration in cellulose microfibril orientation in rice coleoptile mesophyll cell walls.** *Front Plant Sci.* **2015, 6**:628.
- 38. Liu JL, Kim JI, Cusumano JC, Chapple C, Venugopalan N, Fischetti RF, Makowski L: The impact of alterations in lignin deposition on cellulose organization of the plant cell wall. *Biotechnol Biofuels*. 2016, 9.
- 39. Brown DM, Zeef LA, Ellis J, Goodacre R, Turner SR: Identification of novel genes in Arabidopsis involved in secondary cell wall formation using expression profiling and reverse genetics. *Plant Cell.* 2005, 17:2281-2295.
- 40. Foster CE, Martin TM, Pauly M: Comprehensive compositional analysis of plant cell walls (lignocellulosic biomass) part II: carbohydrates. *J Vis Exp.* 2010, 37.
- 41. Foster CE, Martin TM, Pauly M: Comprehensive compositional analysis of plant cell walls (Lignocellulosic biomass) part I: lignin. *J Vis Exp.* 2010, **37**.
- 42. DeMartini JD, Pattathil S, Avci U, Szekalski K, Mazumder K, Hahn MG, Wyman CE: Application of monoclonal antibodies to investigate plant cell wall deconstruction for biofuels production. *Energ Environ Sci.* 2011, 4:4332-4339.
- 43. Pattathil S, Avci U, Miller JS, Hahn MG: Immunological approaches to plant cell wall and biomass characterization: glycome profiling. In: *Biomass Conversion*. Springer; 2012: 61-72.
- 44. Pattathil S, Avci U, Baldwin D, Swennes AG, McGill JA, Popper Z, Bootten T, Albert A, Davis RH, Chennareddy C *et al*: A comprehensive toolkit of plant cell wall glycandirected monoclonal antibodies. *Plant Physiol.* 2010, **153**:514-525.
- 45. Pattathil S, Hahn MG, Dale BE, Chundawat SP: **Insights into plant cell wall structure**, **architecture**, **and integrity using glycome profiling of native and AFEXTM-pretreated biomass**. *J Exp Bot*. 2015, **66**:4279-4294.

- 46. Park S, Baker JO, Himmel ME, Parilla PA, Johnson DK: Cellulose crystallinity index: measurement techniques and their impact on interpreting cellulase performance. *Biotechnol Biofuels*. 2010, **3**:10.
- 47. Derjaguin BV, Muller VM, Toporov YP: **Effect of contact deformations on the adhesion of particles**. *J Colloid Interf Sci.* 1975, **53**:314-326.
- 48. Zhang T, Zheng Y, Cosgrove DJ: **Spatial organization of cellulose microfibrils and matrix polysaccharides in primary plant cell walls as imaged by multichannel atomic force microscopy**. *Plant J.* 2016, **85**:179-192.
- 49. Su C, Hu S, Hu Y, Erina N, Slade A: **Quantitative mechanical mapping of biomolecules in fluid**. *Mater Res Soc Symp P*. 2011, **1261**.
- 50. Landoulsi J, Dupres V: **Direct AFM force mapping of surface nanoscale organization and protein adsorption on an aluminum substrate**. *Phys Chem Chem Phys*. 2013, **15**:8429-8440.
- 51. Petersen PD, Lau J, Ebert B, Yang F, Verhertbruggen Y, Kim JS, Varanasi P, Suttangkakul A, Auer M, Loqué D *et al*: **Engineering of plants with improved properties as biofuels feedstocks by vessel-specific complementation of xylan biosynthesis mutants**. *Biotechnol Biofuels*. 2012, **5**:84.
- 52. Cheng G, Zhang X, Simmons B, Singh S: **Theory, practice and prospects of X-ray and neutron scattering for lignocellulosic biomass characterization: towards understanding biomass pretreatment**. *Energ Environ Sci.* 2015, **8**:436-455.
- 53. Harris DM, Corbin K, Wang T, Gutierrez R, Bertolo AL, Petti C, Smilgies DM, Estevez JM, Bonetta D, Urbanowicz BR *et al*: **Cellulose microfibril crystallinity is reduced by mutating C-terminal transmembrane region residues CESA1(A903V) and CESA3(T942I) of cellulose synthase**. *P Natl Acad Sci USA*. 2012, **109**:4098-4103.
- 54. Takahashi J, Rudsander UJ, Hedenström M, Banasiak A, Harholt J, Amelot N, Immerzeel P, Ryden P, Endo S, Ibatullin FM *et al*: **KORRIGAN1** and its Aspen homolog **PttCel9A1** decrease cellulose crystallinity in Arabidopsis stems. *Plant Cell Physiol*. 2009, **50**:1099-1115.
- 55. Somerville C: **Cellulose synthesis in higher plants**. *Annu Rev Cell Dev Biol*. 2006, **22**:53-78.
- 56. Lane DR, Wiedemeier A, Peng L, Höfte H, Vernhettes S, Desprez T, Hocart CH, Birch RJ, Baskin TI, Burn JE: **Temperature-sensitive alleles of RSW2 link the KORRIGAN endo-1, 4-β-glucanase to cellulose synthesis and cytokinesis in Arabidopsis**. *Plant Physiol.* 2001, **126**:278-288.

- 57. Fujita M, Himmelspach R, Ward J, Whittington A, Hasenbein N, Liu C, Truong TT, Galway ME, Mansfield SD, Hocart CH *et al*: **The** *anisotropy1* **D604N mmutation in the Arabidopsis cellulose synthase1 catalytic domain reduces cell wall crystallinity and the velocity of cellulose synthase complexes.** *Plant Physiol.* **2013, 162**:74-85.
- 58. Al-Haddad JM, Kang K-Y, Mansfield SD, Telewski FW: Chemical responses to modified lignin composition in tension wood of hybrid poplar (Populus tremula × Populus alba). *Tree Physiol.* 2013, **33**:365-373.
- 59. Kabel MA, van den Borne H, Vincken J-P, Voragen AGJ, Schols HA: **Structural differences of xylans affect their interaction with cellulose**. *Carbohyd Polym*. 2007, **69**:94-105.
- 60. Patterson AL: **The Scherrer formula for X-ray particle size determination**. *Phys Rev.* 1939, **56**:978-982.
- 61. Newman RH, Hill SJ, Harris PJ: Wide-angle x-ray scattering and solid-state nuclear magnetic resonance data combined to test models for cellulose microfibrils in mung bean cell walls. *Plant Physiol.* 2013, **163**:1558-1567.
- 62. Ding S-Y, Liu Y-S, Zeng Y, Himmel ME, Baker JO, Bayer EA: **How does plant cell wall nanoscale architecture correlate with enzymatic digestibility?** *Science.* 2012, **338**:1055-1060.
- 63. Chundawat SPS, Bellesia G, Uppugundla N, da Costa Sousa L, Gao D, Cheh AM, Agarwal UP, Bianchetti CM, Phillips GN, Langan P *et al*: **Restructuring the Crystalline Cellulose Hydrogen Bond Network Enhances Its Depolymerization Rate**. *Journal of the American Chemical Society* 2011, **133**(29):11163-11174.
- 64. Chundawat SPS, Donohoe BS, da Costa Sousa L, Elder T, Agarwal UP, Lu F, Ralph J, Himmel ME, Balan V, Dale BE: **Multi-scale visualization and characterization of lignocellulosic plant cell wall deconstruction during thermochemical pretreatment**. *Energ Environ Sci.* 2011, **4**:973-984.
- 65. Zhong R, Burk DH, Ye Z-H: **Fibers. A model for studying cell differentiation, cell elongation, and cell wall biosynthesis**. *Plant Physiol*. 2001, **126**:477-479.
- 66. Ding S-Y, Zhao S, Zeng Y: Size, shape, and arrangement of native cellulose fibrils in maize cell walls. *Cellulose*. 2014, **21**:863-871.
- 67. De Oliveira R, Albuquerque D, Cruz T, Yamaji F, Leite F: **Measurement of the nanoscale roughness by atomic force microscopy: basic principles and applications**. In: *Atomic Force Microscopy-Imaging, Measuring and Manipulating Surfaces at the Atomic Scale*. InTech; 2012.

- 68. Yan Y, Chibowski E, Szcześ A: Surface properties of Ti-6Al-4V alloy part I: Surface roughness and apparent surface free energy. *Mater Sci Eng.* 2017, **70**:207-215.
- 69. Xiao C, Zhang T, Zheng Y, Cosgrove DJ, Anderson CT: **Xyloglucan deficiency** disrupts microtubule stability and cellulose biosynthesis in Arabidopsis, altering cell growth and morphogenesis. *Plant Physiol.* 2016, **170**:234-249.
- 70. Adamcik J, Jung J-M, Flakowski J, De Los Rios P, Dietler G, Mezzenga R: Understanding amyloid aggregation by statistical analysis of atomic force microscopy images. *Nat Nano.* 2010, 5:423-428.
- 71. Schönberg C, Oksanen T, Suurnäkki A, Kettunen H, Buchert J: **The importance of xylan for the strength properties of spruce kraft pulp fibres**. *Holzforschung*. 2001, **55**:639-644.
- 72. Silveira RL, Stoyanov SR, Gusarov S, Skaf MS, Kovalenko A: **Plant biomass** recalcitrance: effect of hemicellulose composition on nanoscale forces that control cell wall strength. *J Am Chem Soc.* 2013, **135**:19048-19051.
- 73. Peng X-W, Ren J-l, Zhong L-X, Sun R-C: Nanocomposite films based on xylan-rich hemicelluloses and cellulose nanofibers with enhanced mechanical properties. *Biomacromolecules*. 2011, **12**:3321-3329.
- 74. Garcia R, Proksch R: **Nanomechanical mapping of soft matter by bimodal force microscopy**. *Eur Polym J*. 2013, **49**:1897-1906.
- 75. Mikkelsen D, Flanagan BM, Wilson SM, Bacic A, Gidley MJ: **Interactions of arabinoxylan and (1,3)(1,4)-β-glucan with cellulose networks**. *Biomacromolecules*. 2015, **16**:1232-1239.
- 76. Yang JH, Wang H: **Molecular mechanisms for vascular development and secondary cell wall formation**. *Front Plant Sci.* 2016, **7**:356.
- 77. Hult EL, Larsson PT, Iversen T: Cellulose fibril aggregation an inherent property of kraft pulps. *Polymer*. 2001, **42**:3309-3314.
- 78. Carpita NC, McCann MC: Characterizing visible and invisible cell wall mutant phenotypes. *J Exp Bot*. 2015, **66**:4145-4163.
- 79. Ciesielski PN, Matthews JF, Tucker MP, Beckham GT, Crowley MF, Himmel ME, Donohoe BS: **3D electron tomography of pretreated biomass informs atomic modeling of cellulose microfibrils**. *ACS Nano*. 2013, **7**:8011-8019.
- 80. Petridis L, O'Neill HM, Johnsen M, Fan B, Schulz R, Mamontov E, Maranas J, Langan P, Smith JC: **Hydration control of the mechanical and dynamical properties of cellulose**. *Biomacromolecules*. 2014, **15**:4152-4159.

- 81. Beecher JF, Hunt CG, Zhu JY: **Tools for the characterization of biomass at the nanometer scale**. In: *The Nanoscience and Technology of Renewable Biomaterials*. John Wiley & Sons, Ltd; 2009: 61-90.
- 82. Chiniquy D, Varanasi P, Oh T, Harholt J, Katnelson J, Singh S, Auer M, Simmons B, Adams PD, Scheller HV *et al*: **Three novel rice genes closely related to the Arabidopsis IRX9, IRX9L, and IRX14 genes and their roles in xylan biosynthesis.** *Front Plant Sci.* 2013, **4**:83.
- 83. Li Q, Min D, Wang JP-Y, Peszlen I, Horvath L, Horvath B, Nishimura Y, Jameel H, Chang H-M, Chiang VL *et al*: **Down-regulation of glycosyltransferase 8D genes in Populus trichocarpa caused reduced mechanical strength and xylan content in wood**. *Tree Physiol*. 2011, **31**:226-236.
- 84. Li Y, Qian Q, Zhou Y, Yan M, Sun L, Zhang M, Fu Z, Wang Y, Han B, Pang X *et al*: **BRITTLE CULM1, which encodes a COBRA-like protein, affects the mechanical properties of rice plants**. *Plant Cell*. 2003, **15**:2020-2031.
- 85. Liu L, Shang-Guan K, Zhang B, Liu X, Yan M, Zhang L, Shi Y, Zhang M, Qian Q, Li J et al: Brittle Culm1, a COBRA-like protein, functions in cellulose assembly through binding cellulose microfibrils. *PLOS Genet.* 2013, 9:e1003704.
- 86. Jones L, Ennos AR, Turner SR: Cloning and characterization of irregular xylem4 (irx4): a severely lignin-deficient mutant of Arabidopsis. *Plant J.* 2001, **26**:205-216.
- 87. Williams D, Hodge D: Impacts of delignification and hot water pretreatment on the water induced cell wall swelling behavior of grasses and its relation to cellulolytic enzyme hydrolysis and binding. *Cellulose*. 2014, 21:221-235.